



HAL
open science

Forced response and stability of mistuned structures subject to the Coriolis effect

Anthony Tacher

► **To cite this version:**

Anthony Tacher. Forced response and stability of mistuned structures subject to the Coriolis effect. Other. Ecole Centrale de Lyon, 2022. English. NNT : 2022ECDL0001 . tel-03969421

HAL Id: tel-03969421

<https://theses.hal.science/tel-03969421v1>

Submitted on 2 Feb 2023

HAL is a multi-disciplinary open access archive for the deposit and dissemination of scientific research documents, whether they are published or not. The documents may come from teaching and research institutions in France or abroad, or from public or private research centers.

L'archive ouverte pluridisciplinaire **HAL**, est destinée au dépôt et à la diffusion de documents scientifiques de niveau recherche, publiés ou non, émanant des établissements d'enseignement et de recherche français ou étrangers, des laboratoires publics ou privés.

École Centrale de Lyon

École doctorale **Mécanique Énergétique Génie civil Acoustique**

Unité de recherche **LTDS**

Thèse présentée par **Anthony TACHER**

Soutenue le **6 septembre 2022**

En vue de l'obtention du grade de docteur de l'École Centrale de Lyon

Discipline **Mécanique**

Spécialité **Dynamique des structures**

Forced response and stability of mistuned structures subject to the Coriolis effect

Thèse dirigée par Fabrice THOUVEREZ

Composition du jury

<i>Rapporteurs</i>	Scott COGAN Fabrizio SCARPA	Chargé de Recherche, FEMTO-ST, Univ. de Franche-Comté Professeur, University of Bristol
<i>Examineur</i>	Jason ARMAND	Ingénieur de Recherche, Safran Tech
<i>Présidente</i>	Marie-Annick GALLAND	Professeure, LMFA, École Centrale de Lyon
<i>Directeur de thèse</i>	Fabrice THOUVEREZ	Professeur, LTDS, École Centrale de Lyon

Cette thèse a été préparée chez les partenaires suivants

LTDS

LTDS UMR 5513
École Centrale de Lyon
36, avenue Guy de Collongue
69134 Ecully, France

Site <http://ltds.ec-lyon.fr/spip/>



Safran Tech

Digital Sciences & Technologies
Rue des Jeunes Bois, Châteaufort
78114 Magny-Les-Hameaux, France

Site <https://www.safran-group.com/fr>



Abstract

Turbomachinery architectures are continually evolving in order to reduce the carbon footprint while increasing performance. In particular, blisks are lighter than conventional designs by using a single-piece structure. As the technology has developed these blisks have increasingly larger diameters and a resulting strong coupling between the blades and the disc, which leads to the appearance of rotational effects, in particular the Coriolis effect. This phenomenon, historically neglected because of its small influence on the dynamics of previous conventional designs, must now be considered.

Cyclic symmetric structures generally exhibit mistuning, which is defined as structural or geometric differences between sectors due to manufacturing tolerances or in-service wear. Moreover, mistuning leads to vibrational changes in the structure which can interact with those of the Coriolis effect, thereby making the analysis of the vibrational behaviour more complex. Flutter, which is an aerodynamic instability phenomenon that can occur on bladed discs, can be avoided by introducing intentional mistuning, also known as detuning. However, when the Coriolis effect is significant, it can reduce the stabilising action of the detuning.

The objectives of this PhD work were to improve the understanding of the interaction between the Coriolis and mistuning effects, to better simulate the vibrational behaviour of bladed discs and to avoid any instability issues due to flutter. To do this, the objective was to first incorporate the rotational and mistuning effects into dynamic simulations of a lumped parameter model representing a blisk. Next, aeroelastic couplings were introduced onto this lumped parameter model to study the system stability in the presence of detuning and the Coriolis effect. Then, reduction methods allowing to take into account the Coriolis effect and mistuning were developed and validated. And finally, these methods were applied to a representative finite element model of a single piece bladed drum to study the interactions between the mistuning and Coriolis effects.

These studies have shown the influence of both mistuning and Coriolis effects for different frequency regions. The effects of mistuning, i.e. localisation and an amplitude magnification of the forced responses, appear when there is a strong participation of the blades. On the other hand, when the participation of the disc is predominant, the responses tend towards a tuned behaviour with the appearance of travelling waves. The results of the aeroelastic model studies have also shown that it is more difficult to stabilise flutter-prone modes using a specific detuning pattern when the Coriolis effect on the structure is significant.

Keywords : bladed drum, mistuning, Coriolis effect, cyclic symmetry, reduced-order model, rotational speed, vibrations, flutter

Résumé

Les architectures des turbomachines évoluent continuellement pour réduire les émissions de gaz à effet de serre tout en améliorant les performances de fonctionnement. Parmi les composants, les disques aubagés monoblocs (DAM) sont plus légers que les modèles classiques grâce à la fabrication d'une pièce en un seul élément. Avec l'évolution des technologies, ces DAM ont des diamètres de plus en plus grands, ce qui crée un fort couplage entre les aubes et le disque et entraîne l'apparition d'effets liés à la rotation, en particulier l'effet Coriolis. Ce phénomène, historiquement négligé en raison de sa faible influence sur la dynamique des pièces traditionnelles précédentes, doit maintenant être pris en compte.

Les roues aubagées présentent toujours du désaccordage induit par des différences structurales ou géométriques entre les secteurs dues aux tolérances de fabrication ou à l'usure en service. De plus, le désaccordage entraîne lui aussi des modifications vibratoires de la structure pouvant interagir avec celles de l'effet Coriolis ce qui rend l'analyse du comportement vibratoire plus complexe. Le flottement, qui est un phénomène d'instabilité aérodynamique pouvant apparaître sur les roues aubagées, peut être évité grâce à l'introduction d'un désaccordage intentionnel. Cependant, lorsque l'effet Coriolis est important, cela peut diminuer ce rôle stabilisateur.

Les enjeux de cette thèse sont d'améliorer la compréhension de l'interaction entre l'effet Coriolis et le désaccordage, afin de modéliser au mieux le comportement vibratoire des roues aubagées et éviter tout problème d'instabilité lié au flottement. Pour cela, l'objectif a tout d'abord été d'intégrer les effets liés à la rotation et au désaccordage dans les simulations dynamiques sur un modèle paramétrique représentatif d'une roue aubagée monobloc. Ensuite, les couplages aéroélastiques ont été introduits sur ce modèle paramétrique afin d'étudier la stabilité du système vis-à-vis du désaccordage intentionnel et de l'effet Coriolis. Puis, des méthodes de réduction permettant de prendre en compte le désaccordage et l'effet Coriolis ont été développées et validées. Pour finir, ces méthodes ont été appliquées sur un modèle éléments finis représentatif d'un tambour aubagé monobloc dans le but d'étudier les interactions entre le désaccordage et l'effet Coriolis.

Ces études ont permis de mettre en avant l'influence à la fois des effets du désaccordage et de l'effet Coriolis pour différentes plages fréquentielles. Les effets du désaccordage avec une localisation et une augmentation des amplitudes des réponses forcées apparaissent lorsqu'il y a une forte participation des aubes. En revanche, lorsque la participation du disque est considérable, les réponses tendent vers un comportement accordé avec l'apparition d'ondes tournantes. Les résultats des études sur le modèle aéroélastique ont aussi montré qu'il est plus difficile de stabiliser des modes sujets au flottement à l'aide d'un schéma de désaccordage intentionnel lorsque l'effet Coriolis est présent de façon non négligeable sur la structure.

Mots clés : tambour aubagé, désaccordage, effet Coriolis, symétrie cyclique, modèle réduit, vitesse de rotation, vibrations, flottement

Remerciements

Je tiens tout d'abord à remercier Scott Cogan et Fabrizio Scarpa de m'avoir fait l'honneur d'être rapporteurs de mes travaux de thèse et pour leurs remarques et échanges lors de la soutenance. Je remercie également Marie-Annick Galland d'avoir accepté de présider ce jury de thèse et pour son intérêt porté à mes travaux.

Je souhaite ensuite remercier mon directeur de thèse, Fabrice Thouverez, pour sa confiance et son accompagnement durant ces trois années de recherche. Toutes les discussions que nous avons pu avoir et ses précieux conseils m'ont permis d'orienter mes travaux dans les bonnes directions. Je ne peux être qu'admiratif de sa capacité et rapidité à trouver des solutions à tout type de problème.

Je tiens également à remercier Jason Armand pour son encadrement industriel, sa rigueur scientifique et ses précieux conseils, que ce soit sur les aspects techniques de la thèse, son déroulement mais aussi sur l'après-thèse. Sa relecture rigoureuse de mes articles, rapports et manuscrit ont permis d'en améliorer grandement la qualité scientifique et rédactionnelle. Merci aussi à Moustapha Mbaye qui a toujours suivi mes travaux avec grand intérêt et pour son expertise dans le domaine du désaccordage.

Je remercie aussi tous les collègues de Safran que j'ai pu rencontrer durant cette thèse et plus particulièrement l'équipe FSMS de Safran Tech pour leur accueil durant mes séjours à Saclay. Les différents échanges que nous avons pu avoir m'ont permis d'apporter une vision industrielle à mes travaux.

Je remercie chaleureusement mes collègues du LTDS, doctorants ou permanents, que j'ai pu côtoyer pendant ces trois années. Merci pour tous les moments d'entraide et les discussions scientifiques passionnantes que nous avons pu avoir. Je n'oublie pas non plus tous les bons moments passés ensemble que ce soit au bureau ou en dehors et qui ont permis de toujours garder une bonne ambiance. J'ai une pensée particulière pour Nicolas, Samuel et Hugo, je ne vous remercierai jamais assez pour tout ce que vous avez fait pour moi durant cette thèse.

J'adresse mes plus profonds remerciements à mes proches pour leur soutien lors de cette thèse. Merci plus particulièrement à mes parents qui m'ont toujours soutenu et aidé à accomplir mes projets aussi bien professionnels que personnels, je leur suis infiniment reconnaissant. Enfin merci à ma femme, Margot qui partage mon quotidien depuis 9 ans. Merci d'être à mes côtés depuis toutes ces années et pour tous les beaux moments que nous vivons. Je ne peux qu'être comblé d'être le papa de notre petite Louise grâce à toi.

Contents

Abstract	v
Remerciements	ix
Contents	xi
General introduction	1
I Turbomachinery dynamics	7
1 Description of jet engines	7
1.1 Components and working principle	8
1.2 Technological aspects	10
1.3 Sources of vibration and aeroelastic phenomena	13
2 Dynamics of an elastic body in rotation	15
2.1 Kinematics of a particle	15
2.2 Equations of motion	16
2.3 Linearisation of motion equations	20
3 Study of rotational cyclic-symmetric structures	21
3.1 Linear modal analysis of an undamped gyroscopic system	21
3.2 Properties of linear cyclic-symmetric structures	23
3.3 Nodal diameter and travelling-wave modes	27
3.4 Forced response	30
4 Vibration analysis of bladed disc	31
4.1 Coriolis force in bladed disc vibration	32
4.2 Mistuning and detuning	33
4.3 Dimensioning procedures	37
Chapter summary	40
II Lumped-parameter cyclic symmetric model	43
1 Perturbation method applied to a mistuned gyroscopic system	44
1.1 Formulating the eigenvalue system	44
1.2 Perturbation method	44
2 Cyclic symmetric structure	47
2.1 Description of the model	47
2.2 Expressions of the nonlinear restoring forces	48
2.3 Equations of motion	50
2.4 Nonlinear approximation	51
2.5 Mistuning introduction	52
3 Modal analyses	52
3.1 Modal analysis of the tuned bladed disc	53

3.2	Modal analysis of the mistuned bladed disc	55
3.3	Perturbation method comparison	59
4	Frequency response function	60
4.1	Forced response at rest	61
4.2	Forced response at high rotational velocity	64
	Chapter summary	66
III	Flutter stability study of a cyclic symmetric system	69
1	Aerodynamics forces	69
1.1	Expressions of the chordwise flow velocities	70
1.2	Calculation of the blade force	71
1.3	Matrix form of the aerodynamic coefficient C_f	73
1.4	Expression of aerodynamic force on the cyclic symmetric structure	74
1.5	Aerodynamic damping solution	75
2	Flutter instability and intentional mistuning optimisation	76
2.1	Aeroelastic stability of the tuned model	76
2.2	Subspace Optimisation Strategy	78
2.3	The genetic algorithm	79
2.4	Selection of detuning patterns without Coriolis effect	83
3	Coriolis influences on flutter stability	83
3.1	Detuned model with the Coriolis effect	83
3.2	Selection of detuning patterns with Coriolis effect	88
	Chapter summary	90
IV	Reduced-Order model for mistuning and Coriolis effects	91
1	Component Mode Synthesis (CMS)	92
1.1	Fixed-interface CMS: Craig-Bampton method	92
1.2	Free-interface CMS: Craig-Chang method	93
1.3	Reduction of the interface degrees of freedom	95
2	State of the art of existing reduction methods for mistuned models.	96
2.1	Subset of Nominal system Modes (SNM)	96
2.2	Component Mode Mistuning (CMM)	97
2.3	Integral Mode Mistuning (IMM)	99
3	Reduced-Order Model validation	101
3.1	Model description	101
3.2	Modal analysis	101
3.3	Free response	103
3.4	Forced response	107
4	Reduction with variable rotational speeds	111
4.1	Polynomial interpolation of the matrices	112
4.2	Parametric Reduced Order Model methodology	116
	Chapter summary	118
V	Analysis of a finite element model of a rotating bladed drum	121
1	Introduction of the finite element model	122
1.1	Geometry and materials	122
1.2	Centrifugal loading and boundary conditions	123
1.3	Finite element mesh	123
1.4	Modal analysis	124
1.5	Reduced Order Model	126

2 Preliminary simulations	126
2.1 Influence of the mistuning locations in the bladed drum	127
2.2 Coriolis requirement in the simulations	129
3 Dynamics evolution with the rotational speed	131
3.1 Low modal density region	131
3.2 High modal density region	133
3.3 Veering region	135
Chapter summary	138
Conclusion	141
List of Figures	147
List of Tables	153
Bibliography	155
A Nonlinear aspects and frequency analysis	171
B Expressions used in the calculation of the aerodynamic forces	187
C Matrices and vectors used to calculate the aerodynamic coefficient C_f	191
D Procedure for the matrices extraction	193
List of personal publications	195

General introduction

Industrial context

Like many sectors, the aeronautics industry must adapt to the challenges of sustainable development. This means reducing the carbon footprint with a goal of carbon neutrality in 2050. In addition to this major challenge, aircraft manufacturers must also reduce production and operating costs as well as noise pollution while maintaining high reliability. Significant progress has already been made in this area and the European Clean Sky research programme will continue to promote the development of technologies needed to meet all these objectives.

Many of these new technologies are associated with future engine developments, and the architectures of these new engines are intended to be slender and lighter in order to increase the performance and in particular the bypass ratio. One of the consequences is that these elements are more flexible and it is therefore important to ensure that they are not subject to damage such as high-cycle fatigue or aeroelastic with flutter for example.

Each new structure has to go through experimental testing phases to be validated and go into production. However, as these tests are very costly, computational methods have been developed over the years to assist in the development of these elements. These tools must be constantly improved in order to take into account the requirements brought by new technologies and to translate the physical behaviour of these components into real use.

Not all physical phenomena are taken into account in the current numerical tools in order to limit the computation time, as they are not necessary to have a good prediction. This is the case of the Coriolis effect, which is usually neglected, as the force generated by this phenomenon has been shown to be rather small in aircraft engines. This force acts on rotating objects in the perpendicular directions to the axis of rotation. On bladed discs, this leads to double frequency split and the appearance of rotating waves, which can cause instability due to aeroelastic interactions.

The main reason for omitting the Coriolis effect in turbomachinery is the strong rigidity of the various rotor components in the radial direction, thus preventing the Coriolis force from coupling the radial and tangential displacements. However, as mentioned earlier, new components are becoming increasingly flexible and it has already been shown experimentally that new turbomachinery structures exhibit a significant Coriolis effect. This suggests that it is becoming important to take this effect into account in the computational methods used to study the new architectures.

Another phenomenon that is also neglected in the early design phases is mistuning. This phenomenon refers to the material and geometric differences between the sectors of a bladed disc, which can significantly modify the dynamic response of the structure compared to

the tuned case. Historically, empirical coefficients were added to allow components pass certification tests. However, in order to avoid over-dimensioning engine or costly test phases, this mistuning phenomena is increasingly well modelled in numerical design tools.

Finally, detuning, which is an intentional mistuning, is increasingly considered in the aeronautical industry in order to reduce the mistuning effect and to address the flutter phenomenon. However, the Coriolis effect, which is starting to appear on new structures, can interact with mistuning and have a beneficial or detrimental effect.

It is in this context that the work presented in this manuscript is articulated, where the main objective is to improve the understanding of the interaction between the Coriolis and mistuning effect and the impact this interaction can have on flutter instability.

Scientific context

Studies on mistuning began in the late 1950s with the works of Armstrong [4] and Tobias [199] followed by the works of Whitehead [213], Wagner [210], Dye and Henry [51], and Ewins [54–56]. Many other works have been done to date and Castanier and Pierre [33] and Yuan [223] published comprehensive reviews on the subject, highlighting the progress already made and what still needs to be improved. Relevant to this work, some researchers are focused on using detuning to control response amplification due to mistuning [32, 37, 71]. Many of these methods are named parametric because one or more parameters of the system (such as the Young’s modulus) are modified to take into account the mistuning. Other methods are called nonparametric because they take into account the uncertainties on all the parameters of the system, as well as the modelling uncertainties. The work of Soize and Capiez-Lernout is a reference in this field [29, 30, 187, 188].

One of the major issues with mistuning is its correct modelling in numerical simulation. Currently, in order to be as realistic as possible, finite element models are widely used as they are faithful to real geometries. However, the numerical models can be large and reduction methods are necessary to save computation time. Classical methods using cyclic symmetry of bladed disc [198] are not applicable in the case of mistuning but classical sub-structuring methods such as Craig-Bampton [43] or [42] Craig-Chang can still be used. However, methods specifically developed for mistuned structures have emerged; the SMART of Bladh et al. [18, 19], Petrov’s method [150], the CMB and SNM of Yang and Griffin [221, 222], the FMM of Feiner and Griffin [57], the AMM of Martel et al. [126], the CMM of Lim et al. [119], the IMM of Vargiu et al. [207] and the NEWT of Fitzner et al. [59].

The Coriolis effect is usually considered to be negligible in the vibration analysis of bladed discs because it does not significantly change the natural frequencies or the forced response behaviour [191]. However, it has recently been shown that the Coriolis effect can lead to significant changes in the dynamic properties of bladed discs exhibiting a strongly coupled motion between the disc and the blades [64, 139]. The same applies to bladed drums with a relatively flexible drum and a large diameter [116, 155, 195]. More recently, Ruffini [165–168] showed numerically and experimentally that in periodic structures the Coriolis effect splits the natural frequencies of the twin modes in a forward travelling wave mode which propagates in the same direction as that of the rotational speed, and a backward travelling wave mode which propagates in the opposite direction.

Because the Coriolis effect is generally neglected in turbomachinery, the study of the interaction between the Coriolis and mistuning effects only began in the early 2000s with the works of Huang [80]. Other works were carried out later on, including those of Nikolic [139, 140], Xin [220] and Kan [86–88]. The influence of the Coriolis effect on the mistuning phenomena is still subject to discussion as some works show that the Coriolis effect enhances the localisation and amplitude magnification while others show that it reduces them, but in all cases the influence occurs mainly for low nodal diameter modes with a large blade-disc coupling.

Aeroelasticity is a branch of physics that is carefully studied in the aeronautics field and the unstable phenomenon of flutter was first studied on aircraft wings from 1920s [61, 62, 208] and shortly after on aircraft engines [104, 131, 202]. Theodersen’s theoretical work [197] is one of the main references on the subject. It has been shown that under certain conditions, the energy of the flow is absorbed by the structure and transformed into mechanical vibration energy, thus increasing the amplitude of the structural vibration which can lead to significant damage or even its destruction. In particular, in structures with cyclic symmetry such as bladed discs, the blades are placed in cascade, i.e. next to each other, and can interact with each other due to wakes created by the vibration of adjacent blades and create flutter. Notable developments on cascade flutter have been made by Lilley [118], Lane and Wang [106], Lane and Friedman [105] and Whitehead [215].

Cascade flutter can be limited by incorporating detuning as investigated by Whitehead [213], Kaza and Kielb [90, 91], and Bendiksen [13]. The goal is to break the natural cyclic symmetry of the bladed disc by defining a particular pattern consisting of two or more different types of blades, or with non-uniform circumferential spacing between blades. This is still a research topic as shown by the more recent works of Corral [40, 41], Siewert [184], and Martel and Rodriguez [126, 127, 161].

Studies have been done between mistuning and flutter as well as between mistuning and the Coriolis effect. In contrast, there are currently no studies that refer to the influence of the Coriolis effect on flutter, or that take mistuning into account. However, given the studies carried out to date on each of these phenomena, it is possible that the Coriolis effect could, under certain conditions, have a detrimental effect on flutter stability, even if the system has detuning to stabilise it.

Objectives

This thesis is based on the need to improve predictive dynamics tools for new bladed disc structures by taking into account phenomena such as the Coriolis effect, mistuning and flutter instability. Numerous studies have been and continue to be conducted on the stabilisation of flutter by detuning. Some research have been carried out over the last twenty years on the interaction between the Coriolis effect and mistuning but the understanding on this interaction is still poorly understood. Furthermore, no research has been done on the influence of the Coriolis effect on flutter stability.

The main objective of this thesis is to improve the understanding between the Coriolis and mistuning effects in order to estimate which phenomenon is predominant over the other and under which conditions. As the Coriolis effect is a fairly new phenomenon in the study of bladed disc dynamics, it will be important to model it well, especially during the model

reduction phase, which is absolutely necessary to decrease the computation time. Finally, this thesis should also provide new insights on the influence of the Coriolis effect on the flutter stability in the presence of detuning on the structure.

Thesis organization

This manuscript consists of five chapters, organised as follows. Chapter I presents the general context of the study by starting with brief descriptions of turbomachineries, some technological aspects particularly interesting for our study and the excitations to which they are subjected. The dynamic equations of an elastic body in rotation is then established, and the theory of cyclic symmetric structures is mentioned. Finally, this chapter ends with the presentation of different dimensioning tools related to the vibration analysis of bladed disc.

Chapter II is an investigation of the interaction between the Coriolis effect and mistuning on a cyclic symmetric structure. The sensitivity of the eigenvalues and eigenvectors to mistuning is first studied with the perturbation method. A lumped parameter model is used to perform a modal analysis using a numerical approach. Three different modes are thoroughly investigated for different rotational speeds, the first with an eigenvalue isolated from the others, the second in a frequency veering zone, and the third in a high modal density region. The studies are then carried out in forced responses with different forms of excitation and compared to the tuned case to deduce the influence of the Coriolis effect.

Chapter III presents an original study of the influence of the Coriolis effect on the aeroelastic stability of the same lumped parameter model as the previous chapter. This made it possible to highlight the complex interactions between flutter, mistuning and the Coriolis effect. The chapter begins with the theoretical development of the aerodynamics forces using Withehead's theory. Then, the subspace optimisation strategy and genetic algorithm are used to determine the best detuning pattern to stabilize the flutter-prone bladed disc. Lastly, the model is studied with and without the Coriolis effect in order to determine the Coriolis influence on flutter stability.

Chapter IV is devoted to the reduction of dynamic systems subject to both the Coriolis effect and mistuning. After a presentation of the classical component mode synthesis, a presentation of the reduced-order models for mistuned structure is given. The Subset of Nominal Modes, the Component Mode Mistuning and the Integral Mode Mistuning techniques have been chosen and adapted to consider the reduction of the Coriolis matrix. Both free and forced responses of the reduced-order models have been validated using the solutions obtained on the finite-element model of a simplified bladed drum compressor as a reference. Finally, the last part of this chapter is dedicated to reduction with variable rotational speeds using the polynomial interpolation of matrices and the parametric reduced order model methodology.

Chapter V uses an industrial model application to study the interaction between the Coriolis and mistuning effects in a stochastic manner. After a detailed presentation of the bladed drum compressor model, an analysis using Monte Carlo simulations has been performed to consider disc and blade mistuning independently, and to study the domination of one over the other. Then, the impact of the Coriolis effect has been highlighted through observation of the model with and without the Coriolis matrix. Finally, the evolution of the global dynamic behaviour with rotational speed has been investigated for different excitation frequencies and engine

orders in a low modal density, high modal density and veering regions.

Chapter I

Turbomachinery dynamics

This chapter introduces the different notions treated in this manuscript. How a turbine engine functions is presented at first with a particular focus on the vibratory issues to which the bladed discs are subjected. The classical dynamic equations for an elastic body in rotation are then established, followed by an introduction to the vibratory study of cyclic-symmetric structures. In this section, the specific vibratory characteristics of these structures are discussed, as well as the analytical and numerical tools which ensure an efficient resolution. Finally, the Coriolis and mistuning effects in bladed disk are discussed and tools for dimensioning the vibratory phenomena of these structures are presented.

Outline of the chapter

1 Description of jet engines	7
1.1 Components and working principle	8
1.2 Technological aspects	10
1.3 Sources of vibration and aeroelastic phenomena	13
2 Dynamics of an elastic body in rotation	15
2.1 Kinematics of a particle	15
2.2 Equations of motion	16
2.3 Linearisation of motion equations	20
3 Study of rotational cyclic-symmetric structures	21
3.1 Linear modal analysis of an undamped gyroscopic system	21
3.2 Properties of linear cyclic-symmetric structures	23
3.3 Nodal diameter and travelling-wave modes	27
3.4 Forced response	30
4 Vibration analysis of bladed disc	31
4.1 Coriolis force in bladed disc vibration	32
4.2 Mistuning and detuning	33
4.3 Dimensioning procedures	37
Chapter summary	40

1 Description of jet engines

The function of jet engines is to ensure the propulsion of aircraft in both civil and military sectors. Civil aircraft engine in particular, undergo constant changes to minimise their

environmental impact by lowering gas emissions and noise levels. Fuel consumption is also a great concern due to fluctuations in oil prices. To deal with these issues, manufacturers are developing more flexible and slender engine structures, leading to the need to account for new physical phenomena, which must be understood and modelled as realistically as possible.

There are different types of jet engines, the main ones being the turbojet and the turbofan, which are both composed of a core. The working principle of these two engines is the same: use Newton's third law by accelerating an air mass to cause a reaction force equal in magnitude but in the opposite direction to move the aircraft. This reaction force is called thrust.

1.1 Components and working principle

1.1.1 Main components of a turbojet

A core consists of three main components, namely the compressor, the combustion chamber and the turbine, in which the incoming fluid undergoes various transformations. All these components are illustrated in Fig. 1.1 for a simple representation of a turbojet. The compressor gives energy to the external air entering the engine via the air inlet to increase its pressure. This compressed air transverses the combustion chamber, where it is mixed with fuel such as kerosene, ignited and ejected. Most of this kinetic energy produced by the combustion is used to propel the engine and thus the aircraft. The other part of the energy is recovered by the turbine which, thanks to a transmission shaft, drives the compressor. The part consisting of the compressor, turbine and drive shaft of the engine is called the spool. An afterburner can also be added behind the turbine, which reheats the exhaust gases by injecting additional fuel in order to increase the thrust. This technology is mostly used in military supersonic aircraft.

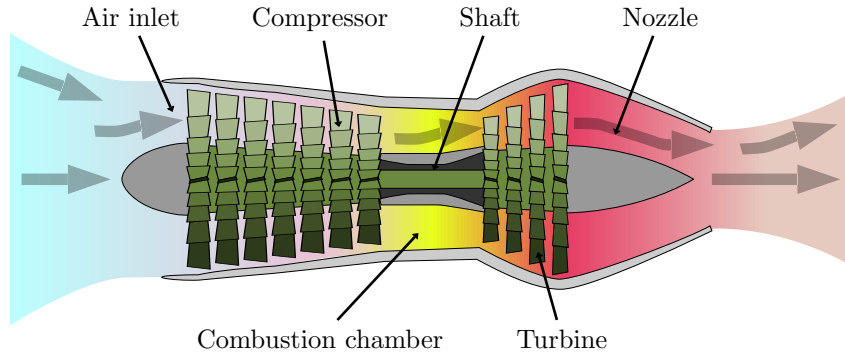


Figure I.1 – Schematic diagram of an axial flow turbojet [Wikipedia].

1.1.2 Main components of a turbofan

The major difference between a turbofan and a turbojet is the stream through the jet engine. For the turbojet, as illustrated in Fig. 1.1, all the air that enters passes through the core. For a turbofan the incoming air first goes through a fan and then the stream is split into two as shown in Fig. 1.2. The primary flow, also known as the core stream, goes through the core like in the turbojet, but the secondary flow, also known as the bypass stream, goes around the core and is only accelerated by the fan. The majority of the aircraft thrust is made by this bypass stream because the diameter of the fan is much larger than the diameter of the core and thus the volume of air delivered is much greater. It gives about 80% of the thrust while the core stream gives only 20%. The ratio of the bypass flow to the core flow is referred to as

the bypass ratio, and it is this value that engine manufacturers are mainly looking to improve in order to increase the performance of aircraft engines.

The turbofan configuration is the most common in civil aircraft engine because it is more fuel efficient and therefore less polluting. It is also less noisy than a turbojet configuration due to the bypass stream which considerably reduces the noise produced by the core.

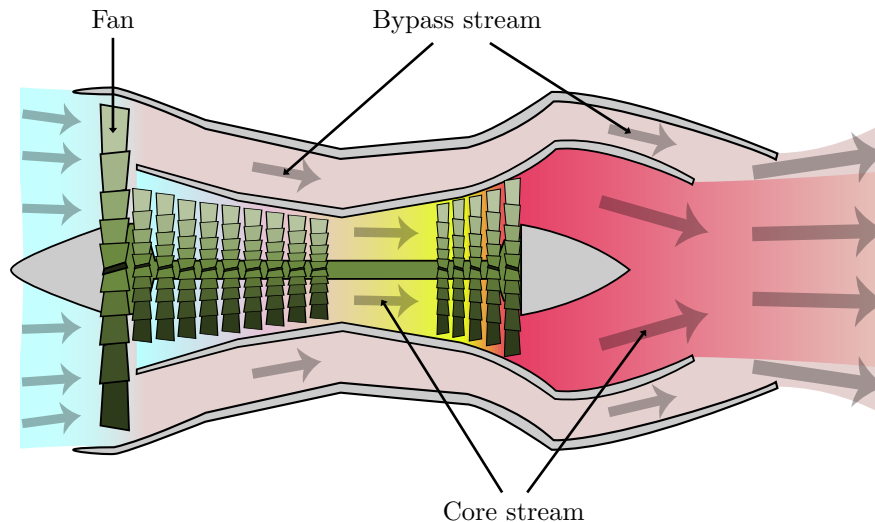


Figure I.2 – Schematic diagram of a separated-flow turbofan [Wikipedia].

1.1.3 Different configurations of a turbofan

The performance of a turbofan is related to its rotational speed but is limited by aerodynamic effects, especially for large fan diameter. In order to solve this problem the turbofan can be multi-spool. So far in this section, engines have been presented single-spool (Fig. I.1 and Fig. I.2) but they can also be double or triple-spool. The advantage is to have a higher speed for the high-pressure spool part with smaller bladed-disc diameter than the low-pressure spool. For a double-spool turbofan, the low-pressure spool also drives the fan and the high and low pressure shafts are concentric. A schematic diagram of a double-spool turbofan is shown in Fig. I.3.

1.1.4 Multi-stage structure

The engines presented in this section are axial because the air stream follows the rotational axis. Compressors and turbines consist of multiple stages, each of which has a moving part called rotor and a fixed part called stator. For a compressor stage (Fig. I.4a), the rotor accelerates the fluid and immediately afterwards the stator, also called stator vanes, redirect the flow direction to the rotational axis which has the effect of slowing down the fluid and increasing its pressure. For a turbine stage (Fig. I.4b), the stator, also called nozzle guide vanes, converts the pressure energy into kinetic energy by guiding the flow to enable the rotation of the downstream turbine rotating stage and thus make the whole spool rotate. A single compressor stage does not allow sufficient compression of the fluid and similarly a single turbine stage does not recover enough energy to run the engine efficiently, so both parts are composed of multiple stages.

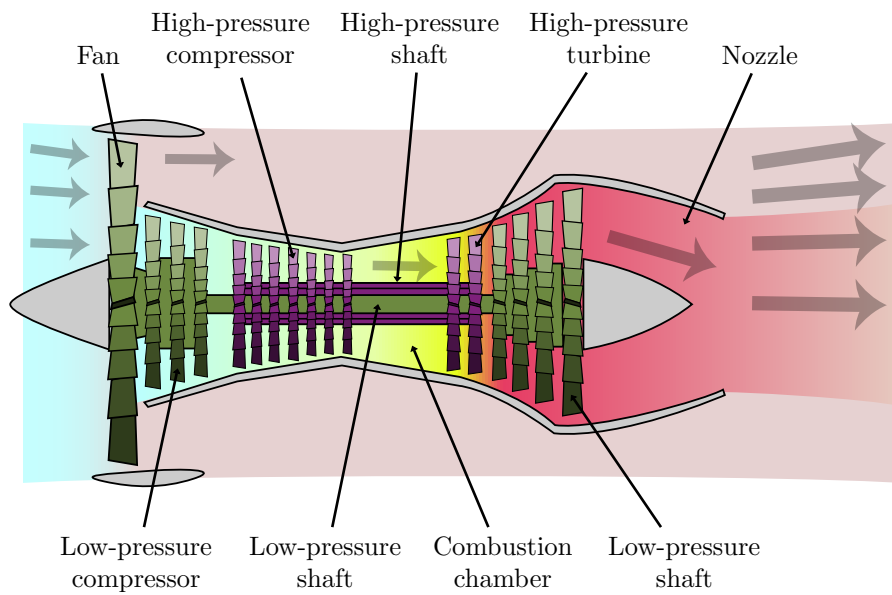


Figure I.3 – Schematic diagram of a double-spool turbofan [Wikipedia].

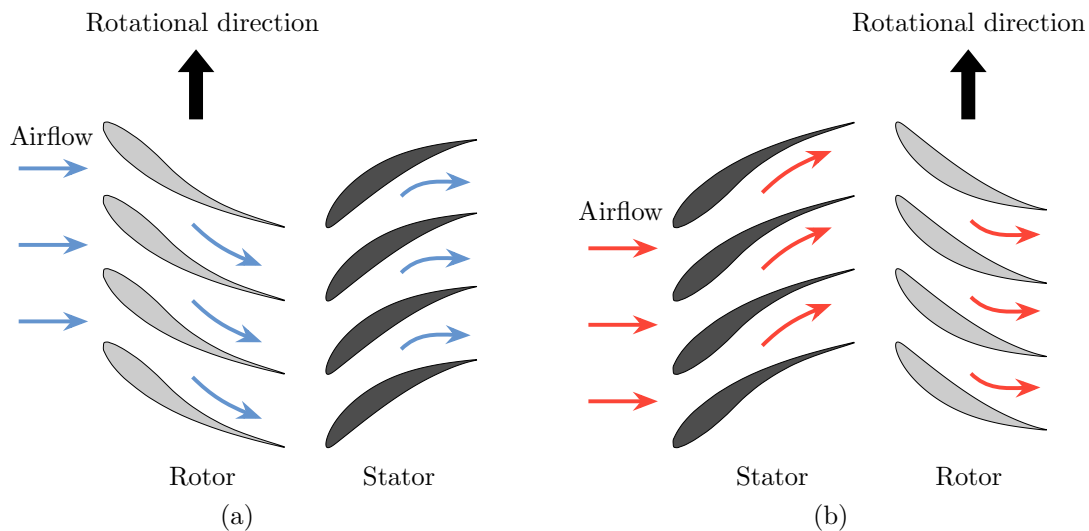


Figure I.4 – Schematic diagram of (a) compressor stage and (b) turbine stage.

1.2 Technological aspects

1.2.1 Technological evolution of turbofans.

As mentioned above, the most common aircraft engine in civil aviation is the dual-spool separated-flow turbofan, of which the best-selling model is the CFM56 shown in Fig. 1.5a. This engine powers short to medium-distance flights and is produced and marketed by CFM International, a joint venture between Safran Aircraft Engines and General Electric. The CFM56 began commercial flights in 1982 and has undergone various evolutions until the arrival of its successor in 2016, the LEAP (Leading Edge Aviation Propulsion) represented in Fig. 1.5b.

This engine was introduced to meet economic and environmental challenges to reduce fuel consumption and noise levels through new manufacturing processes, lighter materials and an

increase in fan diameter to improve the bypass ratio from around 6 for the CFM56 to almost 11 with the LEAP.

With the European Union's objective of becoming carbon neutral by 2050, aircraft manufacturers are already developing engines that will enable them to come closer to these objectives over a medium term horizon. For example, in the context of the Clean Sky programme, the UHPE (Ultra High Propulsive Efficiency) demonstrator is being developed. It is an Ultra High Bypass Ratio (UHBR) architecture, with an even larger fan size than the LEAP to achieve a bypass ratio of 15. A commercial version of this demonstrator is not expected before 2025.

Over the long term, other innovative engine architectures should make it possible to achieve the objectives, such as the open fan RISE (Revolutionary Innovation for Sustainable Engines) shown in Fig. I.5c. This engine should allow a fuel reduction of 20% compared to the current engines. However, the open fan conception requires rethinking the conventional architecture of aircraft, therefore its commercial introduction is not planned before 2035.

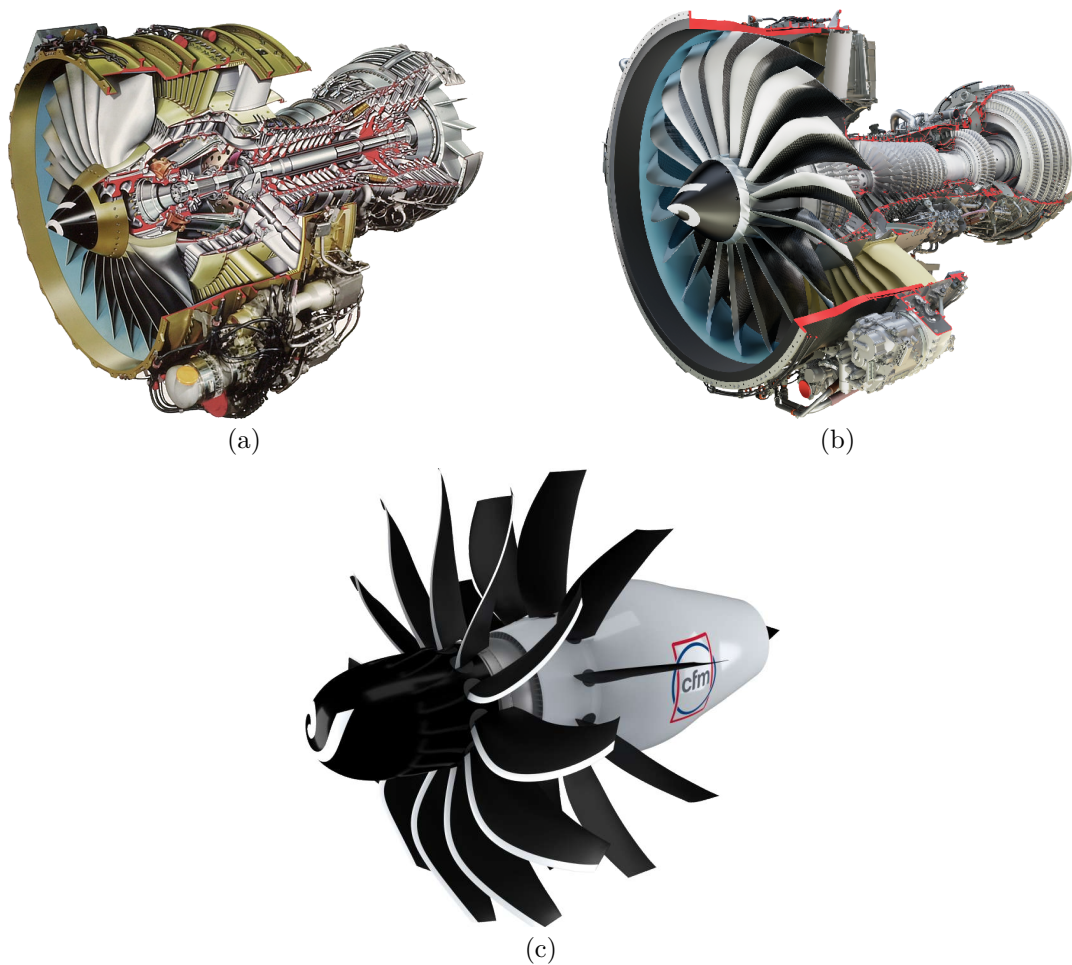


Figure I.5 – Turbofan of CFM International; past, present and future. (a) CFM56. (b) LEAP. (c) RISE. [CFM]

1.2.2 Low-pressure compressor design

The cross-section of the primary flow path changes as the flow progresses through the turbine engine. In particular, during the compression phase, the cross-section tends to decrease, which allows for an extended air inlet and an optimised compression ratio.

An axial compressor often consists of a drum, driven by a shaft, on which the different stages of blade rows are fixed. This drum can be made of one or more parts with a conical-shape to accommodate the changing diameter of the flowstream. For double-spool turbofans, the low-pressure compressor often consists of a single-piece drum, as represented in Fig. I.6a, on which the blades are mounted thanks to circumferential dovetail slots, as shown in Fig. I.6b.

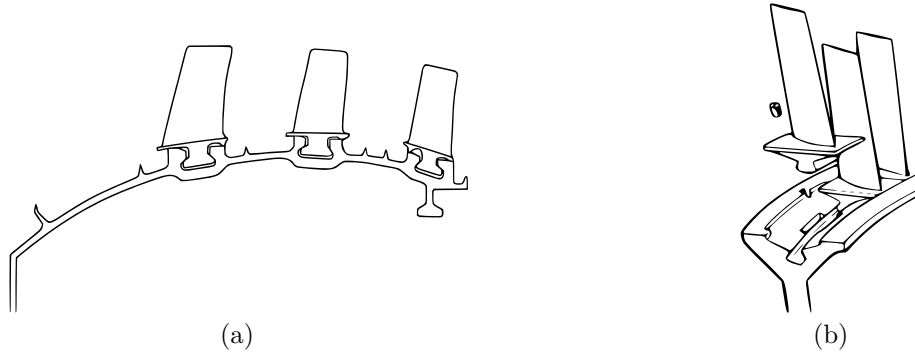


Figure I.6 – Schematic representation of (a) a 3-stage low-pressure compressor and (b) a circumferential dovetail [JetX Engineering].

The single-piece drum saves weight as it avoids the need for discs for each blade stage, which in addition have to be connected by drums with bolts. The single-piece drum is only attached to the shaft on the upstream side by bolts and the downstream side is free. The problem with this type of lightweight structure with a large diameter is that it can suffer significant vibrations depending on the radial displacement, which is not the case with a disc, as it is highly rigid in this direction. This radial displacement has a non-negligible consequence on the appearance of the Coriolis effect, as will be explained more precisely in Section I.4.1.

1.2.3 Single-piece technology

Historically, the blades and disc are manufactured separately and assembled via dovetail (Fig. I.7a) or fir tree profiles (Fig. I.7b). This method simplifies the manufacturing of the parts and allows easier maintenance of the blades, but results in blade/disc contact which induces non-linearities in the dynamics of the system [84, 114, 156]. The induced friction leads to faster wear of the elements, but also dissipates the vibratory energy and limits the amplitudes of vibrations.

Advances in manufacturing in recent years have made it possible to produce more complex structures and thus to have the blades and disc in a single-piece using machining or friction welding [120]. This technology allows a reduction in weight because less matter is needed at the blade/disc connection. It also improves aerodynamic performance by decreasing drag.

On the other hand, the single-piece structures have two major problems. The first one is the maintenance of the element which is much more complex than for inserted blades. The second is that the vibrations are no longer damped via the blade/disc contacts and the coupling is very strong, resulting in higher vibration levels. This second problem can be overcome by adding a friction ring damper into the disc [107, 192].

The single-piece technology is mainly used for bladed disc, also called blisk (Fig. I.8a), but is also starting to be considered for bladed drums [53] (Fig. I.8b). Without the presence of friction, the blade/disc coupling is important, which increases the appearance of Coriolis effect as explained in Section I.4.1. In addition to the radial displacement linked to the flexibility of the bladed drum, the evidence indicates that it is important to model and fully understand the Coriolis effect for future jet engine designs.



Figure I.7 – Schematic representation of (a) a dovetail root and (b) a fir tree root [JetX Engineering].

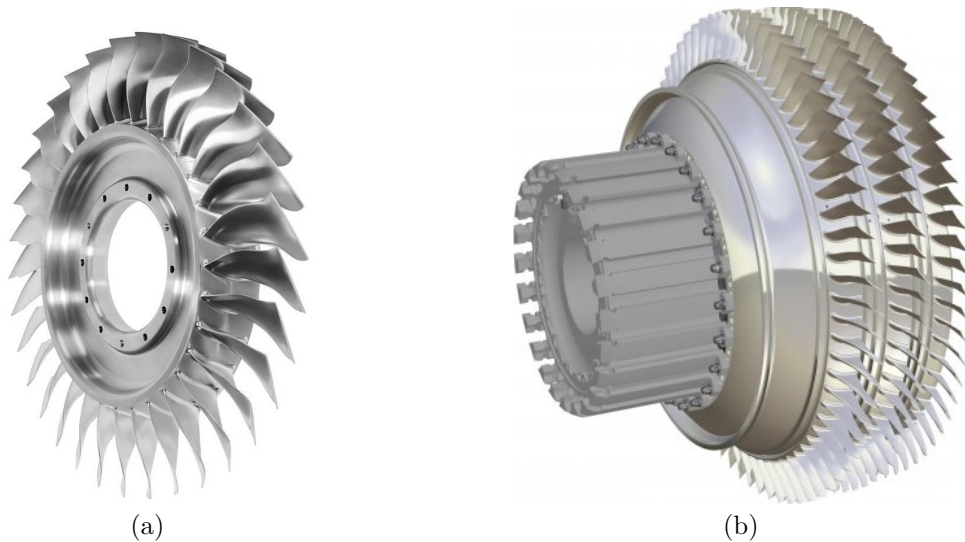


Figure I.8 – Single-piece technology. (a) Bladed disc [84]. (b) Bladed drum [Safran].

1.3 Sources of vibration and aeroelastic phenomena

It is important to understand and control vibration phenomena in jet engines as they can lead to a loss of performance and even damage some engine components. The sources of vibration excitations are numerous and can be separated into two categories: mechanical excitations and aerodynamic excitations.

1.3.1 Mechanical vibration excitation

A first source of mechanical vibration excitation is related to rotating imbalance. This phenomenon is specific to rotating machines and is due to an uneven distribution of the mass around the axis of rotation [206]. The consequence is that the centre of gravity is displaced from the rotational axis, which creates a periodic excitation with a frequency proportional to the rotational speed. The origins of the rotating imbalance can be linked to manufacturing defects of the components as well as bad balancing during the assembly of the different parts. In order to avoid excessive imbalance, the manufacturing tolerances of the elements are very strict and a balancing can be done after assembly, by adding weights or by removing material

with the help of machining in order to put the centre of gravity back on the rotational axis. Another cause of serious rotating imbalance is the loss of a blade, which can occur through fatigue or ingestion of a foreign object.

A second source of mechanical excitation is the rotor/stator contact. The clearances between the blades tip and casing are kept to a minimum in order to limit the flow bypassing the blades and to maximise the efficiency. However, the blades are subject to thermal and mechanical loads which can cause significant deformation of the blades and result in repeated contact between the blades and casing. This contact can lead to premature wear of the elements or to modal interaction between the blades and casing, resulting in an increase in vibration amplitudes until the elements break [7, 112]. In order to restrict this problem, it is possible to apply an abradable coating to the surface of the casing which will wear preferentially over the blades, protecting the blades from excessive wear [8, 110]. Moreover, an abradable coating is easily replaceable and less expensive than blades.

1.3.2 Aerodynamic excitation

The presence of obstacles in the flow path, such as stator vanes or nozzle guide vanes, causes fluctuations in the pressure field of the fluid [134], also called wakes, as shown in Fig. I.9. A rotor blade undergoes one excitation per wake and per revolution, which means that the total excitation on the blade has a frequency equal to the number of obstacles encountered by the fluid times the rotational speed. This phenomenon is called synchronous excitation because the frequency is proportional to the rotational speed and the number of obstacles corresponds to the engine order excitation term which will be developed later. This phenomenon can be particularly dangerous when a frequency excitation is close to a natural frequency, but these cases can be correctly predicted using design tools presented in Section I.4.3.

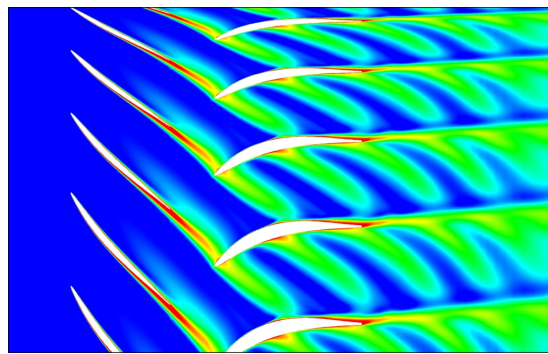


Figure I.9 – Wakes induced by stator vanes [183].

Flutter is an aeroelastic phenomenon caused by an interaction between blade vibrations and fluid energy [39]. Slight fluctuations in flow can lead to slight vibrations of the blades, which in turn can lead to more fluctuations in flow and so on. Depending on the energy exchange between the blades and the fluid, this can either reduce the vibration amplitudes or increase them. It is this second case that can lead to the phenomenon of flutter because the vibrations are self-excited. In the best case, the structure is able to saturate the vibration amplitudes due to non-linearities (fluid or structural), but in the worst case, the strong vibrations will lead to significant damage or even destruction of the mechanical elements.

Classical flutter is when two eigenfrequencies of two eigenmodes of a blade merge due to aerodynamic loading. Most commonly these are the bending and torsion modes, it appears

more often on wings but it can also appear on other slender blades like those of a fan. However, in turbomachinery this scenario is rare as the two eigenfrequencies are chosen during the design to be sufficiently far apart [104, 197].

The flutter that is most commonly encountered in turbomachinery is known as cascade flutter. It is characterised by a transfer of energy between adjacent blades via the fluid and a phase shift between their vibration. There are different types of flutter depending on the different operating conditions of the engine. More information can be found in [125, 215].

Unlike pressure fluctuations due to obstacles, the natural frequency of oscillation is not proportional to the rotational speed. This is called an asynchronous excitation and is much more difficult to anticipate.

2 Dynamics of an elastic body in rotation

In this section, the equations of motion for a rotating deformable structure are established with a discretised method and taking into account the phenomena related to rotation. First, the kinematics of a particle of a deformable solid is described. Then Hamilton's variational principle and a discretisation method are applied to determine the nonlinear equation of motion. Finally, the system is linearised around a static position in order to have a linear dynamic equation taking into account the rotational effects.

The developments in this section are mainly based on the work of Gmür [65] and Géradin and Rixen [63].

2.1 Kinematics of a particle

Consider a deformable solid with a volume \mathcal{V} , limited by a surface $\mathcal{S} = \partial\mathcal{V}$ in a fixed frame of reference $\mathcal{R}_f = \{0, X, Y, Z\}$ [65]. In its undeformed configuration of reference each particle P_f is identified by its position vector $\mathbf{x} = [x, y, z]_{\mathcal{R}_f}^T$ in the fixed frame of reference as shown in Fig. I.10a.

At time $t = 0$, the particle P_f is in P_0 with the position vector $\mathbf{v}_0(\mathbf{x})$ in the rotating frame of reference $\mathcal{R}_m = \{\bar{0}, \bar{X}, \bar{Y}, \bar{Z}\}$ which is coincident to the fixed frame of reference \mathcal{R}_f as shown in Fig. I.10b. When noting \mathbf{u}_0 the displacement vector from the configuration of reference, the vector $\mathbf{v}_0(\mathbf{x})$ can be defined as:

$$\mathbf{v}_0(\mathbf{x}) = \mathbf{x} + \mathbf{u}_0(\mathbf{x}). \quad (\text{I.1})$$

At time $t > 0$, due to the motion of the solid and its deformation each particle is moved to P identified by $\mathbf{y}(\mathbf{x}, t)$ in \mathcal{R}_f . These particles can also be defined in the rotating frame of reference with the vector \mathbf{v} :

$$\mathbf{v}(\mathbf{x}, t) = \mathbf{x} + \mathbf{u}(\mathbf{x}, t). \quad (\text{I.2})$$

The switch from the rotating to the fixed frame of reference can be decomposed in a translation $\mathbf{s}(t) = [s_x, s_y, s_z]_{\mathcal{R}_f}^T$ and a rotation designated by the rotation matrix $\mathbf{R}(t)$ which is orthogonal such as $\mathbf{R}^T\mathbf{R} = \mathbf{I}$ and $\mathbf{R}^T = \mathbf{R}^{-1}$. Therefore, the displacement of particles in \mathcal{R}_f can be expressed with the vector $\mathbf{y}(\mathbf{x}, t) = [y_x, y_y, y_z]_{\mathcal{R}_f}^T$ as shown in Fig. I.10c:

$$\begin{aligned} \mathbf{y}(\mathbf{x}, t) &= \mathbf{s}(t) + \mathbf{R}(t)\mathbf{v}(\mathbf{x}, t) \\ &= \mathbf{s}(t) + \mathbf{R}(t)(\mathbf{x} + \mathbf{u}(\mathbf{x}, t)). \end{aligned} \quad (\text{I.3})$$

It is possible to determine the velocity vector with a derivation but it is necessary to introduce the antisymmetric matrix $\mathbf{\Omega}(t)$ expressed with the components of the rotational

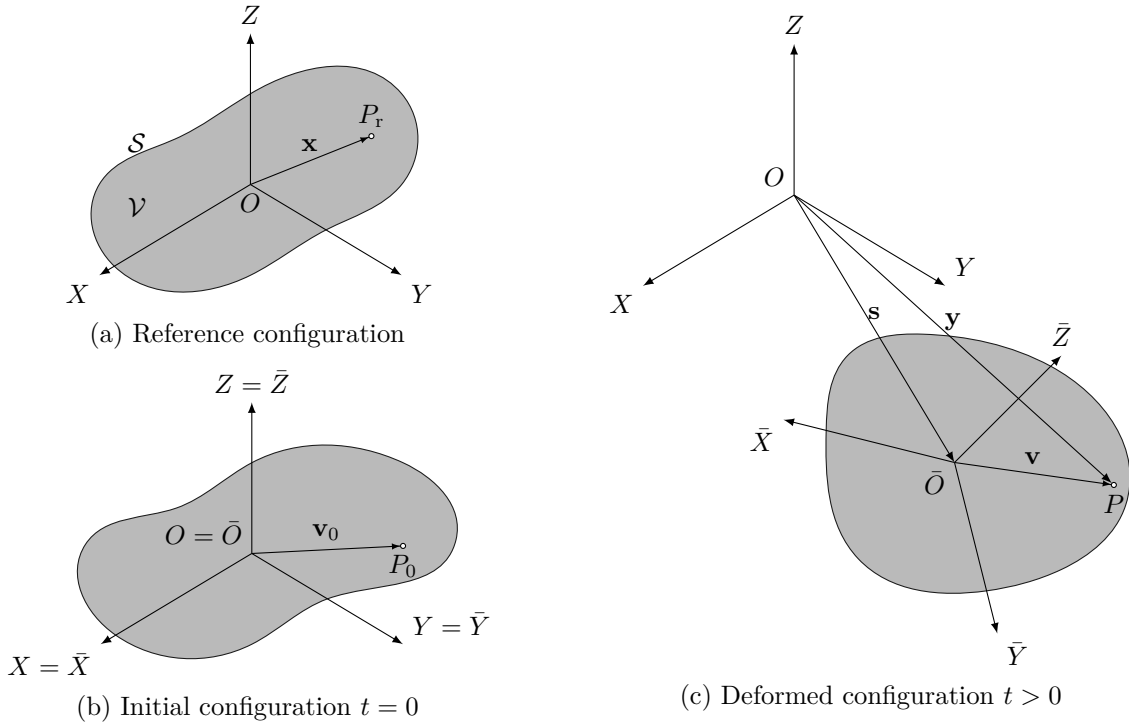


Figure I.10 – Configurations of a continuous system [63].

speed vector $\omega(t) = [\omega_x, \omega_y, \omega_z]^T_{\mathcal{R}_m}$ as follows:

$$\mathbf{\Omega} = \begin{bmatrix} 0 & -\omega_z & \omega_y \\ \omega_z & 0 & -\omega_x \\ -\omega_y & \omega_x & 0 \end{bmatrix}, \quad (\text{I.4})$$

so that the time derivation of the rotation matrix can be expressed with this antisymmetric matrix $\dot{\mathbf{R}}(t) = \mathbf{R}(t)\mathbf{\Omega}(t)$ and the velocity vector of a particle in \mathcal{R}_f

$$\dot{\mathbf{y}}(\mathbf{x}, t) = \dot{\mathbf{s}}(t) + \mathbf{R}(t)\mathbf{\Omega}(t)(\mathbf{x} + \mathbf{u}(\mathbf{x}, t)) + \mathbf{R}(t)\dot{\mathbf{u}}(\mathbf{x}, t). \quad (\text{I.5})$$

2.2 Equations of motion

The equations of motion can be found with the variational principle of Hamilton [9]. This principle specifies a stationarity of the total energy on a time interval $[t_1, t_2]$ which leads to:

$$\delta \int_{t_1}^{t_2} (\mathcal{T} - \mathcal{U} + \mathcal{W}) dt + \int_{t_1}^{t_2} \delta \mathcal{F} dt = 0, \quad (\text{I.6})$$

with \mathcal{T} the kinetic energy of the system, \mathcal{U} the total potential energy, \mathcal{F} the work of the dissipation and \mathcal{W} the work of the body and external forces.

By substituting the velocity vector with its expression Eq. (I.5), the kinetic energy expressed

in \mathcal{R}_f is as follows:

$$\begin{aligned}
\mathcal{T} &= \frac{1}{2} \int_{\mathcal{V}} \rho \dot{\mathbf{y}}^\top \dot{\mathbf{y}} \, d\mathcal{V} \\
&= \frac{1}{2} \int_{\mathcal{V}} \rho \dot{\mathbf{u}}^\top \dot{\mathbf{u}} \, d\mathcal{V} + \int_{\mathcal{V}} \rho \dot{\mathbf{u}}^\top \boldsymbol{\Omega} \mathbf{u} \, d\mathcal{V} + \frac{1}{2} \int_{\mathcal{V}} \rho \mathbf{u}^\top \boldsymbol{\Omega}^\top \boldsymbol{\Omega} \mathbf{u} \, d\mathcal{V} \\
&\quad + \int_{\mathcal{V}} \rho \mathbf{u}^\top \boldsymbol{\Omega}^\top (\mathbf{R}^\top \dot{\mathbf{s}} + \boldsymbol{\Omega} \mathbf{x}) \, d\mathcal{V} + \int_{\mathcal{V}} \rho \dot{\mathbf{u}}^\top (\mathbf{R}^\top \dot{\mathbf{s}} + \boldsymbol{\Omega} \mathbf{x}) \, d\mathcal{V} \\
&\quad + \frac{1}{2} \int_{\mathcal{V}} \rho (\dot{\mathbf{s}}^\top \dot{\mathbf{s}} + 2\dot{\mathbf{s}}^\top \mathbf{R} \boldsymbol{\Omega} \mathbf{x} + \mathbf{x}^\top \boldsymbol{\Omega}^\top \boldsymbol{\Omega} \mathbf{x}) \, d\mathcal{V}.
\end{aligned} \tag{I.7}$$

The potential energy of deformation is \mathcal{U}

$$\mathcal{U} = \frac{1}{2} \int_{\mathcal{V}} \boldsymbol{\sigma} : \boldsymbol{\varepsilon} \, d\mathcal{V} \tag{I.8}$$

To take into account the centrifugal stiffening and more generally geometrical nonlinearity due to large displacement, a material law such as Saint-Venant-Kirchhoff has to be taken into account [11]. This is the simplest hyperelastic material model because it is just an extension of the geometrically linear elastic material model to the geometrically nonlinear regime. This law expresses the second Piola-Kirchhoff stress tensor $\boldsymbol{\sigma}$ as a function of the Lagrangian Green strain tensor $\boldsymbol{\varepsilon}$ with the help of a fourth order tensor $\overline{\mathbf{D}}$.

$$\boldsymbol{\sigma} = \overline{\mathbf{D}} : \boldsymbol{\varepsilon} \tag{I.9}$$

Considering an isotropic material the relation can be simplified as a matrix expression:

$$\boldsymbol{\sigma} = \mathbf{D} \boldsymbol{\varepsilon}, \tag{I.10}$$

with $\boldsymbol{\sigma} = [\sigma_{11}, \sigma_{22}, \sigma_{33}, \sigma_{12}, \sigma_{23}, \sigma_{13}]^\top$ and $\boldsymbol{\varepsilon} = [\varepsilon_{11}, \varepsilon_{22}, \varepsilon_{33}, \varepsilon_{12}, \varepsilon_{23}, \varepsilon_{13}]^\top$ expressed in the Voigt notation and \mathbf{D} the matrix of elasticity

$$\mathbf{D} = \begin{bmatrix} \lambda + 2\mu & \lambda & \lambda & & & \\ \lambda & \lambda + 2\mu & \lambda & & & \\ \lambda & \lambda & \lambda + 2\mu & & & \\ & & & 2\mu & & \\ & & & & 2\mu & \\ & & & & & 2\mu \end{bmatrix}, \tag{I.11}$$

with λ and μ the Lamé parameters which can be expressed with the Young's modulus E and Poisson's ratio ν of the hyperelastic material such as:

$$\begin{aligned}
\lambda &= \frac{E\nu}{(1+\nu)(1-2\nu)}, \\
\mu &= \frac{E}{2(1+\nu)},
\end{aligned} \tag{I.12}$$

with the Saint Venant-Kirchhoff model the Lagrangian Green strain tensor is given by:

$$\begin{aligned}
\boldsymbol{\varepsilon} &= \frac{1}{2} ((\mathbf{grad} \mathbf{u})^\top + \mathbf{grad} \mathbf{u} + (\mathbf{grad} \mathbf{u})^\top \cdot \mathbf{grad} \mathbf{u}) \\
&= \frac{1}{2} (\boldsymbol{\nabla} + \boldsymbol{\nabla}_{\mathbf{u}}) \mathbf{u},
\end{aligned} \tag{I.13}$$

where \mathbf{grad} is the gradient operator, ∇ the linear differential operator and $\nabla_{\mathbf{u}}$ the nonlinear differential operator defined as follows:

$$\nabla = \begin{bmatrix} 2\frac{\partial}{\partial x} & 0 & 0 \\ 0 & 2\frac{\partial}{\partial y} & 0 \\ 0 & 0 & 2\frac{\partial}{\partial z} \\ \frac{\partial}{\partial y} & \frac{\partial}{\partial x} & 0 \\ 0 & \frac{\partial}{\partial z} & \frac{\partial}{\partial y} \\ \frac{\partial}{\partial z} & 0 & \frac{\partial}{\partial x} \end{bmatrix} \quad (\text{I.14})$$

and

$$\nabla_{\mathbf{u}} = \begin{bmatrix} \frac{\partial u_x}{\partial x} \frac{\partial}{\partial x} & \frac{\partial u_y}{\partial x} \frac{\partial}{\partial x} & \frac{\partial u_z}{\partial x} \frac{\partial}{\partial x} \\ \frac{\partial u_x}{\partial y} \frac{\partial}{\partial z} & \frac{\partial u_y}{\partial y} \frac{\partial}{\partial y} & \frac{\partial u_z}{\partial y} \frac{\partial}{\partial y} \\ \frac{\partial u_x}{\partial z} \frac{\partial}{\partial z} & \frac{\partial u_y}{\partial z} \frac{\partial}{\partial z} & \frac{\partial u_z}{\partial z} \frac{\partial}{\partial z} \\ \frac{\partial u_x}{\partial x} \frac{\partial}{\partial y} & \frac{\partial u_y}{\partial x} \frac{\partial}{\partial y} & \frac{\partial u_z}{\partial x} \frac{\partial}{\partial y} \\ \frac{\partial u_x}{\partial y} \frac{\partial}{\partial z} & \frac{\partial u_y}{\partial y} \frac{\partial}{\partial z} & \frac{\partial u_z}{\partial y} \frac{\partial}{\partial z} \\ \frac{\partial u_x}{\partial z} \frac{\partial}{\partial x} & \frac{\partial u_y}{\partial z} \frac{\partial}{\partial x} & \frac{\partial u_z}{\partial z} \frac{\partial}{\partial x} \end{bmatrix}. \quad (\text{I.15})$$

Therefore, using the relations Eq. (I.10) and Eq. (I.13) the potential energy of deformation becomes:

$$\mathcal{U} = \frac{1}{8} \int_{\mathcal{V}} \mathbf{u}^T (\nabla^T + \nabla_{\mathbf{u}}^T) \mathbf{D} (\nabla + \nabla_{\mathbf{u}}) \mathbf{u} \, d\mathcal{V}. \quad (\text{I.16})$$

The integral continuous forms of the energies are now determined but because of the complex shape of the bodies studied, an approximate solution will be developed with a decomposition of the displacement field $\mathbf{u}(\mathbf{x}, t)$ with a product of the chosen shape function $\mathbf{H}(\mathbf{x})$ and the generalised coordinates $\mathbf{q}(t)$ which will be the new unknowns of the problem,

$$\mathbf{u}(\mathbf{x}, t) = \mathbf{H}(\mathbf{x})\mathbf{q}(t). \quad (\text{I.17})$$

Due to this discretization of the displacement, the application of Hamilton's principle is equivalent to solving the Lagrange's equation defined by:

$$\frac{d}{dt} \left(\frac{\partial \mathcal{L}}{\partial \dot{\mathbf{q}}} \right) - \frac{\partial \mathcal{L}}{\partial \mathbf{q}} + \frac{\partial \mathcal{F}}{\partial \dot{\mathbf{q}}} = 0, \quad (\text{I.18})$$

where $\mathcal{L} = \mathcal{T} - \mathcal{U} + \mathcal{W}$ is the Lagrangian.

In the hypotheses of a viscous damping and an internal viscous damping, the work of the

dissipation forces is as follows:

$$\mathcal{F} = \frac{1}{2} \int_{\mathcal{V}} \eta_a \dot{\mathbf{u}}^\top \dot{\mathbf{u}} \, d\mathcal{V} + \frac{1}{2} \int_{\mathcal{V}} \eta_b (\nabla \dot{\mathbf{u}})^\top \mathbf{D} (\nabla \dot{\mathbf{u}}) \, d\mathcal{V}, \quad (\text{I.19})$$

with η_a the kinematics viscous damping and η_b the internal viscous damping.

Then, the work of the body and external surface forces is:

$$\mathcal{W} = \int_{\mathcal{V}} \mathbf{u}^\top \mathbf{f} \, d\mathcal{V} + \int_{\mathcal{S}} \mathbf{u}^\top \mathbf{t} \, d\mathcal{S} \quad (\text{I.20})$$

with \mathbf{f} the body forces and \mathbf{t} the external surface forces.

The application of the Lagrange's equations Eq. (I.18) using the energy expressions Eq. (I.7) and Eq. (I.8) with the nonlinear expression of the internal potential energy Eq. (I.16) and the work of the dissipation forces Eq. (I.19) leads to the equations of motion of the discretised system:

$$\mathbf{M} \ddot{\mathbf{q}}(t) + (\mathbf{C} + \mathbf{G}(t)) \dot{\mathbf{q}}(t) + (\mathbf{K} + \mathbf{P}(t) + \mathbf{N}(t)) \mathbf{q}(t) + \mathbf{f}^q(\mathbf{q}(t)) + \mathbf{f}^c(\mathbf{q}(t)) = \mathbf{f}^{\text{ext}}(t) + \mathbf{r}, \quad (\text{I.21})$$

with

$$\mathbf{M} = \int_{\mathcal{V}} \rho \mathbf{H}^\top \mathbf{H} \, d\mathcal{V}, \quad (\text{I.22})$$

$$\mathbf{C} = \int_{\mathcal{V}} \eta_a \mathbf{H}^\top \mathbf{H} \, d\mathcal{V} + \int_{\mathcal{V}} \eta_b (\nabla \mathbf{H})^\top \mathbf{C} (\nabla \mathbf{H}) \, d\mathcal{V}, \quad (\text{I.23})$$

$$\mathbf{G} = 2 \int_{\mathcal{V}} \rho \mathbf{H}^\top \boldsymbol{\Omega} \mathbf{H} \, d\mathcal{V}, \quad (\text{I.24})$$

$$\mathbf{K} = \int_{\mathcal{V}} (\nabla \mathbf{H})^\top \mathbf{C} (\nabla \mathbf{H}) \, d\mathcal{V}, \quad (\text{I.25})$$

$$\mathbf{P} = \int_{\mathcal{V}} \rho \mathbf{H}^\top \dot{\boldsymbol{\Omega}} \mathbf{H} \, d\mathcal{V}, \quad (\text{I.26})$$

$$\mathbf{N} = \int_{\mathcal{V}} \rho \mathbf{H}^\top \boldsymbol{\Omega}^2 \mathbf{H} \, d\mathcal{V}, \quad (\text{I.27})$$

$$\mathbf{f}^q(\mathbf{q}) = \int_{\mathcal{V}} (\nabla_{\mathbf{q}} \mathbf{H} \mathbf{q})^\top \mathbf{C} (\nabla \mathbf{H}) \mathbf{q} \, d\mathcal{V} + \frac{1}{2} \int_{\mathcal{V}} (\nabla \mathbf{H})^\top \mathbf{C} (\nabla_{\mathbf{q}} \mathbf{H} \mathbf{q}) \mathbf{q} \, d\mathcal{V}, \quad (\text{I.28})$$

$$\mathbf{f}^c(\mathbf{q}) = \frac{1}{2} \int_{\mathcal{V}} (\nabla_{\mathbf{q}} \mathbf{H} \mathbf{q})^\top \mathbf{C} (\nabla_{\mathbf{q}} \mathbf{H} \mathbf{q}) \mathbf{q} \, d\mathcal{V}, \quad (\text{I.29})$$

$$\mathbf{f}^{\text{ext}} = \int_{\mathcal{V}} \mathbf{H}^\top \mathbf{f} \, d\mathcal{V} + \int_{\mathcal{S}} \mathbf{H}^\top \mathbf{t} \, d\mathcal{S}, \quad (\text{I.30})$$

$$\mathbf{r} = \int_{\mathcal{V}} \rho \mathbf{H}^\top (\mathbf{R}^\top \ddot{\mathbf{s}} + \dot{\boldsymbol{\Omega}} \mathbf{x} + \boldsymbol{\Omega}^2 \mathbf{x}) \, d\mathcal{V}. \quad (\text{I.31})$$

\mathbf{M} , \mathbf{K} and \mathbf{C} are the mass, stiffness and damping matrices. \mathbf{M} is symmetric positive definite and \mathbf{K} is symmetric semi-definite. \mathbf{N} is the softening matrix and is negative semi-definite so it makes the rotating structure appear less stiff with a decrease of the eigenvalues when the rotational speed increases [159]. \mathbf{G} is the Coriolis matrix and is antisymmetric. This matrix represents the Coriolis effect which has specific consequences in turbomachinery dynamics as will later be explained in this chapter. The vectors \mathbf{f}^q and \mathbf{f}^c are the quadratic and cubic terms due to the hypothesis of large displacement and the nonlinear terms of the Lagrangian Green strain tensor. Finally, \mathbf{f}^{ext} is the vector of the external forces applied to the system from the body and surface forces.

Throughout the rest of the manuscript, the matrix of rotational speed $\boldsymbol{\Omega}$ is considered constant and the origins of the fixed frame of reference \mathcal{R}_f and the rotating frame of reference

\mathcal{R}_m are confounded. Therefore the matrix of angular acceleration \mathbf{P} disappears from the equations of motion Eq. (I.21) and the expression of the vector of indirect excitation \mathbf{r} is simplified as the vector of centrifugal forces:

$$\mathbf{r} = \int_{\mathcal{V}} \rho \mathbf{H}^T \Omega^2 \mathbf{x} \, d\mathcal{V}. \quad (\text{I.32})$$

2.3 Linearisation of motion equations

In turbomachinery dynamics, the hypothesis of large displacements can generally be reduced to originate from the centrifugal force only and leads to a static equilibrium position due to the centrifugal preload. It will now be assumed that the dynamics around the static position is linear and that the solution of the problem $\mathbf{q}(t)$ can be represented by an oscillation $\mathbf{q}_d(t)$ around a static equilibrium position \mathbf{q}_{st} :

$$\mathbf{q}(t) = \mathbf{q}_d(t) + \mathbf{q}_{st}. \quad (\text{I.33})$$

\mathbf{q}_{st} is solution of the nonlinear static equation:

$$(\mathbf{K} + \mathbf{N})\mathbf{q}_{st} + \mathbf{f}^q(\mathbf{q}_{st}) + \mathbf{f}^c(\mathbf{q}_{st}) = \mathbf{r}. \quad (\text{I.34})$$

Substituting Eq. (I.33) into the nonlinear dynamic equation Eq. (I.21) leads to:

$$\mathbf{M}\ddot{\mathbf{q}}_d + (\mathbf{C} + \mathbf{G})\dot{\mathbf{q}}_d + (\mathbf{K} + \mathbf{N})(\mathbf{q}_d + \mathbf{q}_{st}) + \mathbf{f}^q(\mathbf{q}_d + \mathbf{q}_{st}) + \mathbf{f}^c(\mathbf{q}_d + \mathbf{q}_{st}) = \mathbf{f}^{\text{ext}} + \mathbf{r}. \quad (\text{I.35})$$

Since the dynamic equation is supposed to be linear, a linear Taylor development around the static equilibrium position is used to linearise the nonlinear terms:

$$\mathbf{f}(\mathbf{q}_d + \mathbf{q}_{st}) \approx \mathbf{f}(\mathbf{q}_{st}) + \frac{\partial \mathbf{f}}{\partial \mathbf{q}}(\mathbf{q}_{st})\mathbf{q}_d. \quad (\text{I.36})$$

Using this expression in Eq. (I.35) leads to the following linear dynamic equation:

$$\mathbf{M}\ddot{\mathbf{q}}_d + (\mathbf{C} + \mathbf{G})\dot{\mathbf{q}}_d + (\mathbf{K} + \mathbf{N} + \mathbf{K}^t(\mathbf{q}_{st}))\mathbf{q}_d = \mathbf{f}^{\text{ext}}, \quad (\text{I.37})$$

with the stiffening matrix \mathbf{K}^t

$$\mathbf{K}^t(\mathbf{q}_{st}) = \frac{\partial \mathbf{f}^q}{\partial \mathbf{q}}(\mathbf{q}_{st}) + \frac{\partial \mathbf{f}^c}{\partial \mathbf{q}}(\mathbf{q}_{st}). \quad (\text{I.38})$$

It is necessary to solve the nonlinear static equation Eq. (I.34) first to determine the equilibrium position \mathbf{q}_{st} and evaluate the stiffening matrix \mathbf{K}^t . This matrix takes into account the geometric nonlinear effect of the centrifugal preload also known as the centrifugal stiffening effect. It makes the rotating structure appear more stiff with an increase of the eigenvalues and an increasing rotational speed [2]. This effect is opposed to the softening effect but it is difficult to know which effect will be predominant against the other because it depends on a lot of parameters like the geometry or the material properties. Finally, the global stiffness matrix is introduced as:

$$\mathbf{K}^g = \mathbf{K} + \mathbf{N} + \mathbf{K}^t. \quad (\text{I.39})$$

Note that for some structures there may be non-linearities to be taken into account in the dynamic equation. This is the case, for example, of friction between the blades and the disc when they are manufactured separately [84, 108, 156], to which the impact of fretting wear can also be added [3, 114, 174]. The rotor-stator contact can also lead to dynamic non-linearities [38,

115, 146]. Finally, very slender structures such as open-rotor blades can also have significant geometric non-linearities in dynamic response [50, 67, 128]. All these problems are not directly treated in this manuscript but the classical tools for studying nonlinear dynamics can be found in Appendix A.

3 Study of rotational cyclic-symmetric structures

This section focuses on the study of cyclic-symmetric structures such as bladed discs. First, the modal analysis of undamped gyroscopic system is reviewed in order to highlight the modal characteristics related to the Coriolis effect. Then, the theory of the reduced modelling of cyclic-symmetric structures will be developed in order to define the notions of modal diameter and travelling waves specific to these structures.

3.1 Linear modal analysis of an undamped gyroscopic system

Let us consider once more the linear dynamic equation of motion Eq. (I.37) set in the previous section but in free vibration so that there is no external forces and the system is undamped ($\mathbf{f}^{\text{ext}} = \mathbf{0}$ and $\mathbf{C} = \mathbf{0}$)

$$\mathbf{M}\ddot{\mathbf{q}}_d(t) + \mathbf{G}\dot{\mathbf{q}}_d(t) + \mathbf{K}^g\mathbf{q}_d(t) = \mathbf{0}. \quad (\text{I.40})$$

The real solution $\mathbf{q}_d(t)$ can be expressed in the exponential shape:

$$\mathbf{q}_d(t) = \frac{1}{2}(\mathbf{p}e^{\lambda t} + \text{c.c.}), \quad (\text{I.41})$$

where \mathbf{p} is the complex eigenvector, λ the complex eigenvalue and c.c. the complex conjugate part to obtain a real solution. Injecting this relation into Eq. (I.40) results in the following eigenproblem:

$$\frac{1}{2}([\lambda^2\mathbf{M} + \lambda\mathbf{G} + \mathbf{K}^g]\mathbf{p}e^{\lambda t} + \text{c.c.}) = \mathbf{0}. \quad (\text{I.42})$$

Projecting Eq. (I.42) onto $e^{-\lambda t}$ using the following scalar product:

$$\langle f(t), g(t) \rangle = \frac{2}{T} \int_0^T f(t)g(t)dt, \quad (\text{I.43})$$

leads to the complex eigenproblem:

$$[\lambda^2\mathbf{M} + \lambda\mathbf{G} + \mathbf{K}^g]\mathbf{p} = \mathbf{0}. \quad (\text{I.44})$$

At this stage, it is necessary to substitute this system of n second order differential equations by a system of $2n$ first order differential equations which is also called state-space representation:

$$[\mathbf{A} - \lambda\mathbf{B}]\mathbf{u} = \mathbf{0}, \quad (\text{I.45})$$

where,

$$\mathbf{A} = \begin{bmatrix} \mathbf{0} & \mathbf{K}^g \\ -\mathbf{K}^g & -\mathbf{G} \end{bmatrix}, \quad (\text{I.46})$$

$$\mathbf{B} = \begin{bmatrix} \mathbf{K}^g & \mathbf{0} \\ \mathbf{0} & \mathbf{M} \end{bmatrix}, \quad (\text{I.47})$$

$$\mathbf{u} = \begin{bmatrix} \mathbf{p} \\ \lambda \mathbf{p} \end{bmatrix}. \quad (\text{I.48})$$

\mathbf{A} and \mathbf{B} are respectively the stiffness and mass matrices of the augmented system. \mathbf{A} is an antisymmetric matrix and \mathbf{B} is a symmetric matrix. These properties can demonstrate that the augmented eigenproblem consists of n pairs of pure imaginary complex conjugate eigenvalues $\lambda_r = i\omega_r$ and $\bar{\lambda}_r = -i\omega_r$ and n pairs of complex conjugate eigenvectors \mathbf{u}_r and $\bar{\mathbf{u}}_r$ [130] where $r \in \llbracket 1, n \rrbracket$ and ω_r are the natural frequencies. To demonstrate these properties, let us consider the determinant of Eq. (I.45):

$$\det(\mathbf{A} - \lambda \mathbf{B}) = 0. \quad (\text{I.49})$$

The determinant of a matrix is equal to the determinant of the transposed matrix so

$$\det(\mathbf{A} - \lambda \mathbf{B})^\top = \det(\mathbf{A}^\top - \lambda \mathbf{B}^\top) = \det(-\mathbf{A} - \lambda \mathbf{B}) = 0. \quad (\text{I.50})$$

This demonstrates that if λ is an eigenvalue, then $-\lambda$ is also an eigenvalue. Now let us decompose the eigenvectors \mathbf{u} and $\bar{\mathbf{u}}$ with their real and imaginary parts \mathbf{y} and \mathbf{z} :

$$\mathbf{u} = \mathbf{y} + i\mathbf{z}, \quad (\text{I.51})$$

$$\bar{\mathbf{u}} = \mathbf{y} - i\mathbf{z}. \quad (\text{I.52})$$

Using the antisymmetric property of \mathbf{A} and the symmetric property of \mathbf{B} gives the following results:

$$\mathbf{y}^\top \mathbf{A} \mathbf{y} = (\mathbf{y}^\top \mathbf{A} \mathbf{y})^\top = \mathbf{y}^\top \mathbf{A}^\top \mathbf{y} = -\mathbf{y}^\top \mathbf{A} \mathbf{y} = 0, \quad (\text{I.53})$$

$$\mathbf{z}^\top \mathbf{A} \mathbf{z} = (\mathbf{z}^\top \mathbf{A} \mathbf{z})^\top = \mathbf{z}^\top \mathbf{A}^\top \mathbf{z} = -\mathbf{z}^\top \mathbf{A} \mathbf{z} = 0, \quad (\text{I.54})$$

$$\mathbf{y}^\top \mathbf{A} \mathbf{z} = (\mathbf{y}^\top \mathbf{A} \mathbf{z})^\top = \mathbf{z}^\top \mathbf{A}^\top \mathbf{y} = -\mathbf{z}^\top \mathbf{A} \mathbf{y}, \quad (\text{I.55})$$

$$\mathbf{y}^\top \mathbf{B} \mathbf{z} = (\mathbf{y}^\top \mathbf{B} \mathbf{z})^\top = \mathbf{z}^\top \mathbf{B}^\top \mathbf{y} = \mathbf{z}^\top \mathbf{B} \mathbf{y}. \quad (\text{I.56})$$

Multiplied Eq. (I.45) on the left by the complex conjugate $\bar{\mathbf{u}}^\top$ and using Eq. (I.53) to Eq. (I.56) gives:

$$\begin{aligned} \bar{\mathbf{u}}^\top (\mathbf{A} - \lambda \mathbf{B}) \mathbf{u} &= (\mathbf{y} - i\mathbf{z})^\top (\mathbf{A} - \lambda \mathbf{B}) (\mathbf{y} + i\mathbf{z}) \\ &= 2i\mathbf{y}^\top \mathbf{A} \mathbf{z} - \lambda (\mathbf{y}^\top \mathbf{B} \mathbf{y} + \mathbf{z}^\top \mathbf{B} \mathbf{z}). \end{aligned} \quad (\text{I.57})$$

This allows to be expressed as the eigenvalue λ considering \mathbf{B} as symmetric positive definite which is the general case:

$$\lambda = 2i \frac{\mathbf{y}^\top \mathbf{A} \mathbf{z}}{\mathbf{y}^\top \mathbf{B} \mathbf{y} + \mathbf{z}^\top \mathbf{B} \mathbf{z}}. \quad (\text{I.58})$$

Given that $\mathbf{y}^\top \mathbf{A} \mathbf{z}$ is a real value and $\mathbf{y}^\top \mathbf{B} \mathbf{y}$ and $\mathbf{z}^\top \mathbf{B} \mathbf{z}$ are strictly positive real values, then λ is a pure imaginary eigenvalue as $\lambda_r = i\omega_r$. Because $-\lambda$ is also an eigenvalue, the eigenproblem consist of n pairs of pure imaginary complex conjugates and thanks to Eq. (I.45), if (λ, \mathbf{u}) are

solutions of the eigenproblem $(\bar{\lambda}, \bar{\mathbf{u}})$ are also solutions. This leads to a solution of n pairs of complex conjugate eigenvectors \mathbf{u}_r and $\bar{\mathbf{u}}_r$.

This part gives us the tools to perform a linear modal analysis of a gyroscopic system. Because of the n pairs of solutions of the augmented system by the state space representation, it is only necessary to take the eigenvalue $\lambda_r = i\omega_r > 0$ with their associated eigenvector \mathbf{u} to have the n complex eigenvectors and natural frequencies of the eigenproblem Eq. (I.42). The previous demonstration shows that the eigenvalues of an undamped gyroscopic system are purely imaginary so this demonstrates that the Coriolis force is not dissipative. Indeed, it is well known that the real part of the eigenvalue of a damped system is proportional to the damping itself [65] so with a null real part the system is not dissipative. It should be noted that this modal analysis can also be conducted with the integration of a damped matrix. This will affect the eigenvectors and eigenvalues but there will still be a solution of n pairs of complex conjugate eigenvectors and eigenvalues.

3.2 Properties of linear cyclic-symmetric structures

One of the most interesting characteristics of a turbomachinery is its cyclic-symmetric geometry. The structure can be divided into N identical sectors such as the one in Fig. I.11a and can be generated from successive rotations of one sector of reference given in Fig. I.11b. This kind of structure is also called a tuned structure because each sector is identical. These types of structures have been studied intensively [198, 205, 217, 218]. These works provide the tools to study cyclic-symmetric structures with a wave model of only one reference sector, considerably reducing calculation time.

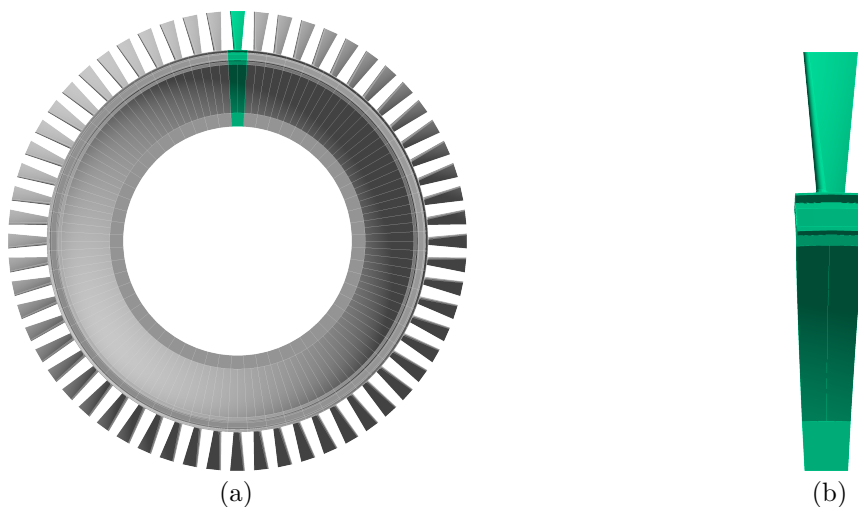


Figure I.11 – Example of a cyclic-symmetric structure. (a) Fully assembled structure composed of 60 sectors. (b) Reference sector.

3.2.1 Definition of cyclic components

The cyclic symmetry structure considered is composed of N sectors numbered from 0, for the reference sector, to $N - 1$. The cyclic symmetry axis is assumed to coincide with its axis of rotation. In what follows, it is important to precise the displacements of each sector, accordingly the vector of the unknown displacements \mathbf{q}_d in Eq. (I.37) is decomposed in N

vector of \mathbf{q}_j corresponding to the unknown displacement of the j^{th} sector

$$\mathbf{q}_d = [\mathbf{q}_0, \dots, \mathbf{q}_j, \dots, \mathbf{q}_{(N-1)}]^\top. \quad (\text{I.59})$$

Thanks to the linear representation theory of cyclic groups introduced in [205], the unknown displacement \mathbf{q}_j can be represented by a finite sum of harmonic functions:

$$\mathbf{q}_j = \sum_{k=0}^{N-1} \tilde{\mathbf{q}}_k e^{ijk\alpha}, \quad (\text{I.60})$$

where $\alpha = 2\pi/N$ is the space angle between each sector and $\tilde{\mathbf{q}}_k$ the complex amplitude of each harmonic function, also called k^{th} cyclic component. These components are linked to the unknown displacement by the inverse relation:

$$\tilde{\mathbf{q}}_k = \frac{1}{N} \sum_{j=0}^{N-1} \mathbf{q}_j e^{-ijk\alpha}. \quad (\text{I.61})$$

All the cyclic components are arranged in a vector $\tilde{\mathbf{q}}$

$$\tilde{\mathbf{q}} = [\tilde{\mathbf{q}}_0, \dots, \tilde{\mathbf{q}}_k, \dots, \tilde{\mathbf{q}}_{(N-1)}]^\top. \quad (\text{I.62})$$

The N relations Eq. (I.60) can be written in a matrix form:

$$\mathbf{q} = (\mathbf{F} \otimes \mathbf{I}_n) \tilde{\mathbf{q}}, \quad (\text{I.63})$$

where \otimes is the Kronecker product, n is the number of unknowns in one sector and \mathbf{I}_n the identity matrix of size n . \mathbf{F} is the discrete Fourier transform matrix:

$$\mathbf{F} = \begin{bmatrix} 1 & 1 & \dots & 1 \\ 1 & e^{i\alpha} & \dots & e^{i(N-1)\alpha} \\ \vdots & \vdots & \ddots & \vdots \\ 1 & e^{i(N-1)\alpha} & \dots & e^{i(N-1)^2\alpha} \end{bmatrix}. \quad (\text{I.64})$$

It should be noted that there are equivalent expressions in the real domain for Eq. (I.60) and Eq. (I.61) which replaces the complex cyclic component $\tilde{\mathbf{q}}_k$ by a real cyclic component. This notation is not developed in this manuscript as it has not been used but more informations can be found in the works of MacNeal [122] and Vakakis [204].

3.2.2 Problem formulation in cyclic basis

With Eq. (I.63), it has been seen that the physical unknowns of cyclic structure can be described in a cyclic basis thanks to cyclic components $\tilde{\mathbf{q}}$ and harmonic indexes k . It is now possible to project the complete system onto this cyclic basis in order to show that the problem Eq. (I.37) can be solved by a set of sub-problems on a reference sector for each k harmonic.

The matrices \mathbf{M} , \mathbf{G} , \mathbf{C} and \mathbf{K}^g are constructed in the same manner, so the developments will be made on the general matrix \mathbf{A} . As for the arrangement of the unknown vector in Eq. (I.59), the matrix \mathbf{A} dissociates the elements of each sub-structure, in order to have a block diagonal matrix with each block corresponding to a specific sector and where each one is

disjoint from the others:

$$\mathbf{A} = \text{diag}(\mathbf{A}_0, \dots, \mathbf{A}_j, \dots, \mathbf{A}_{N-1}) = \begin{bmatrix} \mathbf{A}_0 & \dots & 0 & \dots & 0 \\ \vdots & \ddots & & & \vdots \\ 0 & & \mathbf{A}_j & & 0 \\ \vdots & & & \ddots & \vdots \\ 0 & \dots & 0 & \dots & \mathbf{A}_{N-1} \end{bmatrix}. \quad (\text{I.65})$$

Thanks to the cyclic-symmetric hypothesis each sector is identical, i.e. $\mathbf{A}_j = \mathbf{A}_0$, so the matrices can be written in the compact form:

$$\mathbf{A} = \mathbf{I}_N \otimes \mathbf{A}_0. \quad (\text{I.66})$$

The projection of this matrix in the cyclic basis $\tilde{\mathbf{A}}$ is written with the help of the Fourier matrix as follows:

$$\tilde{\mathbf{A}} = (\mathbf{F}^H \otimes \mathbf{I}_n)(\mathbf{I}_N \otimes \mathbf{A}_0)(\mathbf{F} \otimes \mathbf{I}_n), \quad (\text{I.67})$$

with \mathbf{F}^H is the hermitian of the Fourier matrix. This expression can be simplified using the exponential property:

$$\sum_{k=0}^{N-1} e^{ikn\alpha} e^{-ikm\alpha} = N\delta_{n,m}, \quad (\text{I.68})$$

where $\delta_{n,m}$ is the Dirac Delta function equal to 1 if $n = m$ and 0 else. This gives the following relation:

$$\tilde{\mathbf{A}} = N\mathbf{A}. \quad (\text{I.69})$$

Thanks to this last expression, the formulation of the matrices projected in the cyclic basis does not involve the Fourier matrix and each harmonic is decoupled from the others. Moreover, each sub-matrix is equal to the reference sector matrix in the physical basis.

3.2.3 Cyclic boundary conditions

Up to now, the equations have been projected in the cyclic domain without taking into account the cyclic boundary conditions, so the vibration behaviour of the global structure cannot yet be characterized. It is therefore important to take into account these conditions at the interfaces between two adjacent sectors in the cyclic domain. These boundary conditions are illustrated in Fig. I.12.

In order to do this, the vector of unknown displacements has to be decomposed with the internal nodes \mathbf{q}_j^i , the left boundary nodes \mathbf{q}_j^l and the right boundary nodes \mathbf{q}_j^r such as:

$$\mathbf{q}_j = [\mathbf{q}_j^i, \mathbf{q}_j^l, \mathbf{q}_j^r]^T, \quad (\text{I.70})$$

and the same goes for the cyclic components:

$$\tilde{\mathbf{q}}_k = [\tilde{\mathbf{q}}_k^i, \tilde{\mathbf{q}}_k^l, \tilde{\mathbf{q}}_k^r]^T. \quad (\text{I.71})$$

To ensure the motion continuity at the interface between two sectors the following relation is imposed:

$$\mathbf{q}_j^l = \mathbf{q}_{j+1}^r, \quad (\text{I.72})$$

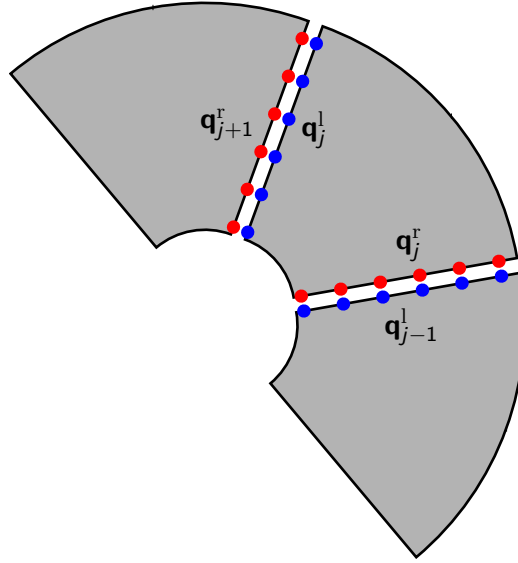


Figure I.12 – Boundary conditions between each sector of a cyclic-symmetric structure.

with $j \in \llbracket 0, N - 1 \rrbracket$. Then, using the relation Eq. (I.60) in Eq. (I.72) gives:

$$\sum_{k=0}^{N-1} \left(\tilde{\mathbf{q}}_k^l - e^{ik\alpha} \tilde{\mathbf{q}}_k^r \right) e^{ijk\alpha} = (\mathbf{F} \otimes \mathbf{I}_{n_b}) \mathbf{x} = \mathbf{0}, \quad (\text{I.73})$$

where n_b is the number of degrees of freedom of the right or left boundary and

$$\mathbf{x} = [\tilde{\mathbf{q}}_0^l - \tilde{\mathbf{q}}_0^r, \dots, \tilde{\mathbf{q}}_k^l - e^{ik\alpha} \tilde{\mathbf{q}}_k^r, \dots, \tilde{\mathbf{q}}_{N-1}^l - e^{i(N-1)\alpha} \tilde{\mathbf{q}}_{N-1}^r]^\top. \quad (\text{I.74})$$

Because \mathbf{F} has a non-zero determinant, the only solution of Eq. (I.73) is $\mathbf{x} = \mathbf{0}$, this leading to the following boundary conditions in the cyclic space:

$$\tilde{\mathbf{q}}_k^l = e^{ik\alpha} \tilde{\mathbf{q}}_k^r, \quad (\text{I.75})$$

with $k \in \llbracket 0, N - 1 \rrbracket$.

This allows the number of unknowns to be reduced to $\tilde{\mathbf{q}}^c = [\tilde{\mathbf{q}}_0^c, \dots, \tilde{\mathbf{q}}_k^c, \dots, \tilde{\mathbf{q}}_{(N-1)}^c]^\top$ with the help of the rectangular matrix \mathbf{B}

$$\tilde{\mathbf{q}} = \mathbf{B} \tilde{\mathbf{q}}^c, \quad (\text{I.76})$$

with $\mathbf{B} = \text{diag}(\mathbf{B}_0, \dots, \mathbf{B}_k, \dots, \mathbf{B}_{N-1})$ such as for the k^{th} component,

$$\begin{bmatrix} \tilde{\mathbf{q}}_k^i \\ \tilde{\mathbf{q}}_k^l \\ \tilde{\mathbf{q}}_k^r \end{bmatrix} = \begin{bmatrix} \mathbf{I}_{n_i} & 0 \\ 0 & e^{ik\alpha} \mathbf{I}_{n_b} \\ 0 & \mathbf{I}_{n_b} \end{bmatrix} \begin{bmatrix} \tilde{\mathbf{q}}_k^i \\ \tilde{\mathbf{q}}_k^r \end{bmatrix} = \mathbf{B}_k \tilde{\mathbf{q}}_k^c, \quad (\text{I.77})$$

with n_i the number of internal degrees of freedom. Accordingly, the application of the boundary

conditions for the matrices gives the following block diagonal matrices:

$$\tilde{\mathbf{A}}^c = \mathbf{B}^H \tilde{\mathbf{A}} \mathbf{B} = \begin{bmatrix} \tilde{\mathbf{A}}_0 & \dots & 0 & \dots & 0 \\ \vdots & \ddots & & & \vdots \\ 0 & & \tilde{\mathbf{A}}_k & & 0 \\ \vdots & & & \ddots & \vdots \\ 0 & \dots & 0 & \dots & \tilde{\mathbf{A}}_{N-1} \end{bmatrix}, \quad (\text{I.78})$$

with $\tilde{\mathbf{A}}_k = \mathbf{B}_k^H \mathbf{A}_0 \mathbf{B}_k$. For practical purposes, the matrices $\tilde{\mathbf{A}}^c$ will be noted $\tilde{\mathbf{A}}$ thereafter, as well as the cyclic components $\tilde{\mathbf{q}}^c$ will be noted $\tilde{\mathbf{q}}$.

Finally, the application of boundary conditions permits the reduction of the size of each sub-problem by n_b degrees of freedom while keeping them decoupled for each harmonic.

3.3 Nodal diameter and travelling-wave modes

3.3.1 Eigenmodes for a gyroscopic system

The modal analysis highlights the notion of nodal diameter modes of cyclic-symmetric structures with an index k representing the number of nodal diameter and included between $\llbracket 0, N/2 \rrbracket$ if N is even or $\llbracket 0, (N-1)/2 \rrbracket$ if N is odd.

Projecting the complex eigenproblem Eq. (I.44) on the cyclic basis using Eq. (I.63) and Eq. (I.76) for the boundary conditions gives the following sub-problem for the k^{th} harmonic:

$$[-\omega_k^2 \tilde{\mathbf{M}}_k - i\omega_k \tilde{\mathbf{G}}_k + \tilde{\mathbf{K}}_k^g] \tilde{\mathbf{p}}_k = \mathbf{0}. \quad (\text{I.79})$$

Because each sub-problem is solved independently, this means that the modes \mathbf{q}_k corresponding to the k^{th} harmonic have cyclic components only for $\tilde{\mathbf{q}}_k$ and that all other components are zero. Thanks to Eq. (I.60), the displacements of the modes \mathbf{q}_k can be rewritten:

$$\mathbf{q}_k = \tilde{\mathbf{q}}_k e^{ijk\alpha}. \quad (\text{I.80})$$

Substituting Eq. (I.41) in Eq. (I.80), the l^{th} dof of the k^{th} harmonic of the j^{th} sector can be written as:

$$q_{j,k}^l = \frac{1}{2} (\tilde{p}_k^l e^{-i\omega_k t} + \text{c.c.}) e^{ijk\alpha}. \quad (\text{I.81})$$

Knowing that \tilde{p}_k^l is a complex value, it can be rewritten in the following exponential form

$$\tilde{p}_k^l = r_k^l e^{i\theta_k^l}, \quad (\text{I.82})$$

with r_k^l the modulus and θ_k^l the argument of \tilde{p}_k^l . Injecting Eq. (I.82) in Eq. (I.81) gives

$$q_{j,k}^l = r_k^l \cos(\omega_k t - \theta_k^l - jk\alpha), \quad (\text{I.83})$$

where θ_k^l represents the phase between each dof of the same sector, and $jk\alpha$ the phase between each sector. With this expression, it is possible to see the appearance of k zero-displacement nodal lines also called nodal diameters around the structure. These modes are called travelling-wave modes because the nodal diameters travel around the structure due to the phase $jk\alpha$ between each sector.

With the help of Eq. (I.61), it can be deduced that $\overline{\tilde{\mathbf{p}}_k} = \tilde{\mathbf{p}}_{-k}$. Using this relation gives:

$$q_{j,-k}^l = r_k^l \cos(\omega_{-k} t + \theta_k^l + jk\alpha). \quad (\text{I.84})$$

The harmonic k has been restricted to $\llbracket 0, N-1 \rrbracket$ due to the cyclic symmetry of the system which requires that $\tilde{\mathbf{p}}_{N+k} = \tilde{\mathbf{p}}_k$, but it is also possible to show that $\tilde{\mathbf{p}}_{N-k} = \tilde{\mathbf{p}}_{-k}$ [156]. This relation imposes that the harmonics k are constrained between $\llbracket 0, K \rrbracket$ with $K = N/2$ if N is even or $K = (N-1)/2$ if N is odd. As will be shown later, this leads to harmonic folding when k is greater than K . There are still N different harmonics but they all lie between $\llbracket -K, K \rrbracket$.

Finally, the mode shapes of a cyclic-symmetric structure can be classified in three categories:

- $k = 0$: there is no nodal diameter, all the sectors vibrate with the same phase because $q_l^{j,0} = q_l^{j+1,0}$. These modes are called nondegenerate modes. An example is given in Fig. I.13a.
- $k = N/2$ if N is even: this is the highest number of nodal diameters, all the neighbouring sectors vibrate in opposition of phase because $q_l^{j,N/2} = -q_l^{j+1,N/2}$. As for $k = 0$, these modes are called nondegenerate modes. An example is given in Fig. I.13b.
- $k \in \llbracket 1, K \rrbracket$: there is k nodal diameters and due to the harmonic folding, there exists two modes with the same modal shape, one at the frequency ω_k and the other at the frequency ω_{-k} . These mode are called degenerate modes. Two examples are given for a one nodal diameter in Fig. I.14a and a two nodal diameters in Fig. I.14b.

Considering the natural frequencies as positive, the travelling waves with k nodal diameters propagate in opposite directions with one phase $jk\alpha$ for the mode with the frequency ω_k and the other phase $-jk\alpha$ for the frequency ω_{-k} , thanks to Eq. (I.84). In the following, the phase $jk\alpha$ will be associated to a forward wave because it moves with the structure rotation and a phase $-jk\alpha$ to a backward wave because it moves against the structure rotation. An example is given of the phase evolution for each blade over one period in Fig. I.15 for a degenerate mode of two nodal diameters with a forward wave in Fig. I.15a and a backward wave in Fig. I.15b.

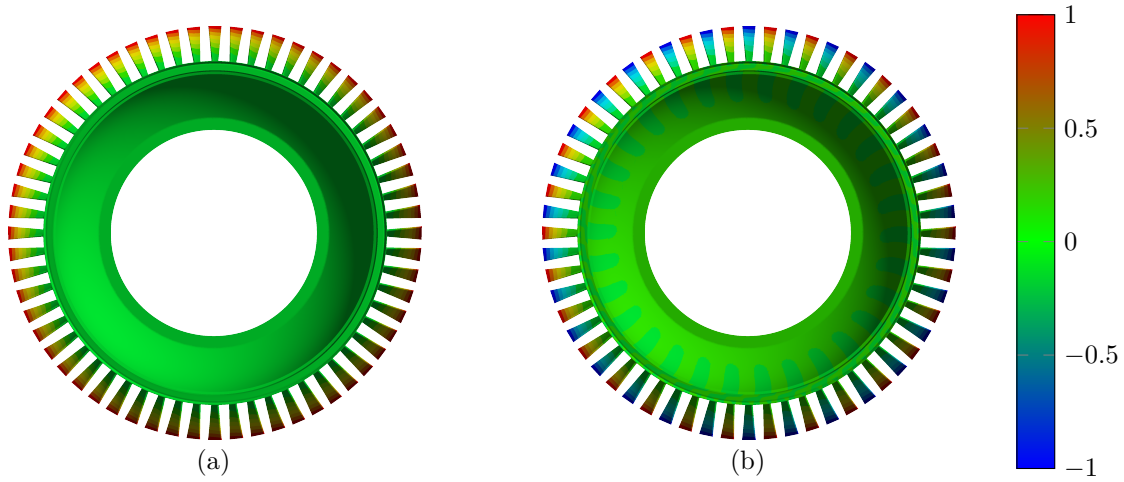


Figure I.13 – Nondegenerate modes of a cyclic structure with 60 sectors : (a) 0ND and (b) 30ND.

3.3.2 Specific case of a non-gyroscopic system

At rest or if the Coriolis effect is negligible, Eq. (I.79) becomes:

$$[-\omega_k^2 \tilde{\mathbf{M}}_k + \tilde{\mathbf{K}}_k^g] \tilde{\mathbf{p}}_k = \mathbf{0}. \quad (\text{I.85})$$

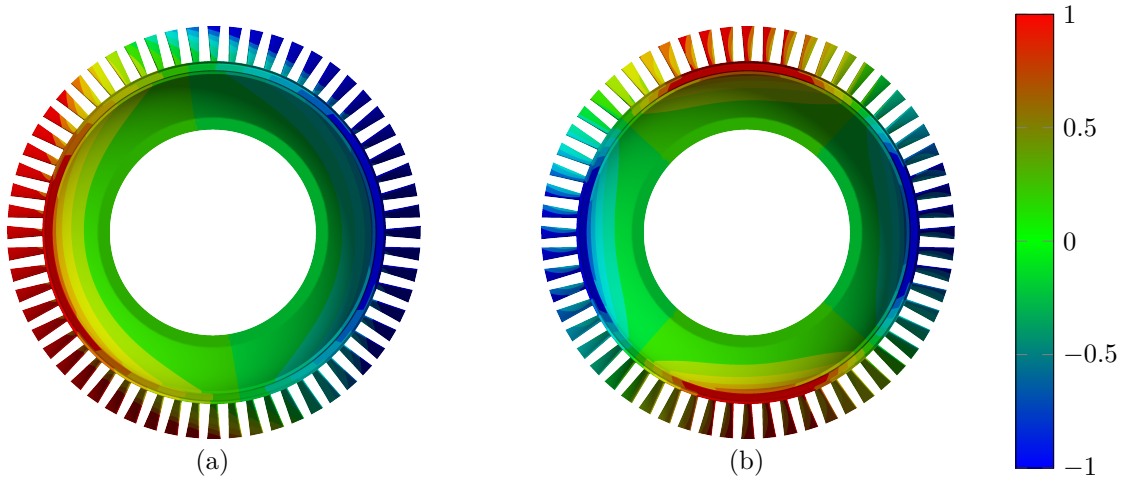


Figure I.14 – Degenerate modes of a cyclic structure with 60 sectors : (a) 1ND and (b) 2ND.

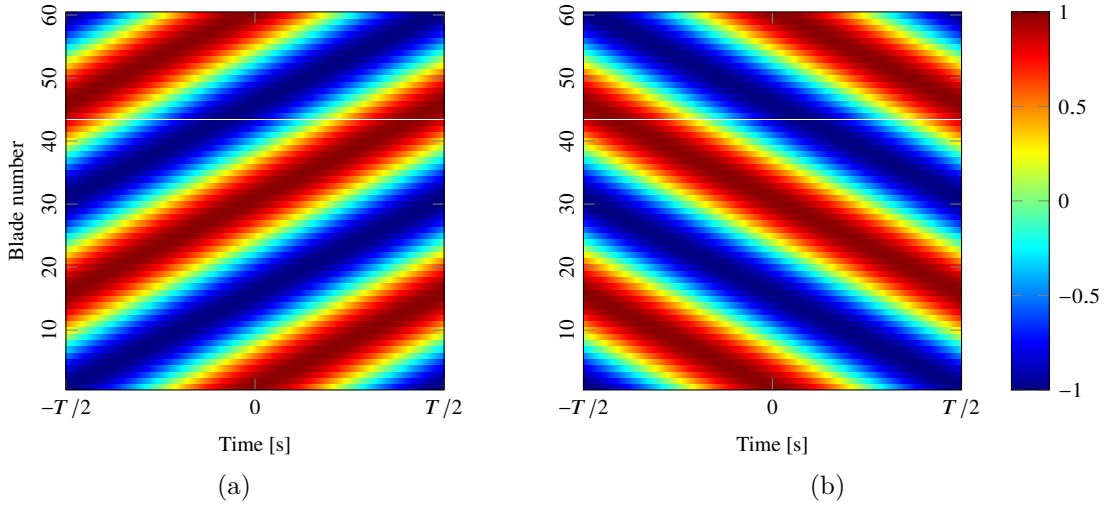


Figure I.15 – Blades phase over one period for a degenerate mode with 2 nodal diameters. (a) Forward wave and (b) Backward wave.

It was previously shown than $\overline{\tilde{\mathbf{p}}_k} = \tilde{\mathbf{p}}_{-k}$ and the same can be done for the matrices $\overline{\tilde{\mathbf{A}}_k} = \tilde{\mathbf{A}}_{-k}$, because $\overline{\tilde{\mathbf{B}}_k} = \tilde{\mathbf{B}}_{-k}$, thanks to Eq. (I.77). Using these relations in the complex conjugate of Eq. (I.85) for an harmonic $-k$ gives:

$$[-\omega_{-k}^2 \tilde{\mathbf{M}}_k + \tilde{\mathbf{K}}_k^g] \tilde{\mathbf{p}}_k = \mathbf{0}. \quad (\text{I.86})$$

Consequently, in this specific case, ω_k and ω_{-k} are eigenvalues of the eigenvector $\tilde{\mathbf{p}}_k$, and because of the uniqueness of the eigenvalue $\omega_k = \omega_{-k}$. Moreover, these two eigenvalues are associated to two eigenvectors $\tilde{\mathbf{p}}_k$ and $\tilde{\mathbf{p}}_{-k}$ orthogonal to each other, which are known as double eigenvectors.

For a double eigenvector all linear combinations of the two associated modes are also modes:

$$\gamma_k = a\mathbf{q}_k + b\mathbf{q}_{-k}, \quad (\text{I.87})$$

where a and b are real constants. If $a = b$ and using Eq. (I.83) and Eq. (I.84), this combined

mode γ_k at the l^{th} dof of the j^{th} sector can be written as:

$$\gamma_{j,k}^l = 2ar_k^l \cos(\theta_k^l + jk\alpha) \cos(\omega_k t). \quad (\text{I.88})$$

All the degrees of freedom vibrate in or out of phase depending on the sign of $\cos(\theta_k^l + jk\alpha)$ and the mode shape as the nodal diameters are locked in place. This type of mode shape is called standing wave. With the introduction of the antisymmetric Coriolis matrix, all the eigenvalues are different so all the degenerate modes are travelling waves for a gyroscopic tuned system.

3.4 Forced response

In the same way as the modal analysis, the forced response problems can be treated independently as sub-problems. In this case the damping matrix \mathbf{C} and the external force vector \mathbf{f}^{ext} must be added to the system.

3.4.1 Definition of the damping matrix

There are different models to introduce mechanical damping into system. The best known are modal and Rayleigh damping. The calculation of the damping matrix is done without taking into account the Coriolis matrix because this effect is only related to the inertial frame of reference and therefore has no influence on the mechanical damping of the structure as demonstrated in Section I.3.1.

The modal damping model allows the application of a ξ_i damping factor for each mode of the system. This coefficient can be different for each mode, therefore these factors are gathered in the diagonal matrix Ξ .

By solving the following system:

$$[-\omega_i^2 \mathbf{M} + \mathbf{K}] \phi = \mathbf{0}, \quad (\text{I.89})$$

it is possible to construct the diagonal matrix of eigenvalues Λ , as well as the complete modal basis Φ orthonormalised with respect to the mass matrix \mathbf{M} . The application of modal damping then assumes that:

$$\Phi^T \mathbf{C} \Phi = 2\Xi \sqrt{\Lambda}. \quad (\text{I.90})$$

Finally the expression of the damping matrix related to the modal damping model is written:

$$\mathbf{C} = 2\mathbf{M} \Phi \Xi \sqrt{\Lambda} \Phi^T \mathbf{M}. \quad (\text{I.91})$$

With the Rayleigh damping model, the damping matrix is expressed as a linear combination of the mass matrix \mathbf{M} and stiffness matrix \mathbf{K} :

$$\mathbf{C} = \alpha \mathbf{M} + \beta \mathbf{K}. \quad (\text{I.92})$$

Looking at the expression of the damping matrix in Eq. (I.23), it is possible to notice this same linear combination with the expression of the mass and stiffness matrix in Eq. (I.22) and Eq. (I.25) respectively.

It is possible to find a link between these two models by projecting Eq. (I.92) onto the modal basis Φ and equalising with Eq. (I.90) to obtain:

$$2\Xi \sqrt{\Lambda} = \alpha \mathbf{I}_n + \beta \Lambda, \quad (\text{I.93})$$

with n the total number of modes in the system. As Ξ and Λ are diagonal matrices, there is n

decoupled equation:

$$2\xi_i\omega_i = \alpha + \beta\omega_i^2. \quad (\text{I.94})$$

This makes it possible to deduce the expression of ξ_i :

$$\xi_i = \frac{1}{2} \left(\frac{\alpha}{\omega_i} + \beta\omega_i \right). \quad (\text{I.95})$$

As well as the expressions α and β :

$$\alpha = \xi_i\omega_i, \quad (\text{I.96})$$

$$\beta = \frac{\xi_i}{\omega_i}. \quad (\text{I.97})$$

The Rayleigh damping model is simpler to set up than the modal damping model because there is no need to calculate the modal basis ϕ , which is why this method will be retained for the definition of the damping matrix later. However, the equivalence between the two methods is used to calculate the coefficients α with Eq. (I.96) and β with Eq. (I.97) by fixing a damping factor ξ and a modal frequency ω_i .

Equation (I.92), can be used either in the physical basis with the complete matrices \mathbf{A} or in the cyclic basis with the block matrices $\tilde{\mathbf{A}}_k$.

3.4.2 Definition of the excitation force

As discussed in Section I.1.3, the bladed disc are subjected to rotating excitation forces with a frequency ω which depends on the rotational speed and the engine order h . The magnitude of the excitation force is the same for each sector and is denoted \mathbf{f}^{amp} . The expression of the excitation force for sector j in the exponential form is:

$$\mathbf{f}_j^{\text{ext}} = \frac{1}{2} \mathbf{f}^{\text{amp}} \left(e^{i(\omega t - jh\alpha)} + \text{c.c.} \right). \quad (\text{I.98})$$

By projecting this external force vector with the Fourier matrix such as $\tilde{\mathbf{f}}^{\text{ext}} = \mathbf{F}^H \mathbf{f}^{\text{ext}}$ and using the property in Eq. (I.68), it is possible to show that only the spacial harmonic $k = h$ responds

$$\tilde{\mathbf{f}}_k^{\text{ext}} = \frac{1}{2} \mathbf{f}^{\text{amp}} \left(e^{-i\omega t} + \text{c.c.} \right). \quad (\text{I.99})$$

Finally, for an excitation with an engine order h , only the sub-problem with the cyclic harmonic corresponding k needs to be solved. In this manuscript, the excitation will be done with one engine order at a time, but it is possible to have more complex excitations involving a decomposition of the external effort on several harmonics. The more harmonics there are, the greater the number of sub-problems to be solved, but thanks to the uncoupling, the time saving compared to solving the complete system remains significant.

4 Vibration analysis of bladed disc

This section further explores the notions of Coriolis effect and mistuning, which are central to this work. This section also presents some classical design tools to prevent vibration risks related to bladed disc.

4.1 Coriolis force in bladed disc vibration

The Coriolis force is acting perpendicularly to the direction of motion of an object in a rotating frame of reference. The displacements perpendicular to the axis of rotation will be coupled by the Coriolis force. With an in-plane tangential displacement, the Coriolis force will act radially and create an in-plane radial displacement. Inversely, with an in-plane radial displacement, the Coriolis force will act tangentially and create an in-plane tangential displacement. Finally, an out-of-plane displacement will not create Coriolis force. It is easy to confirm these remarks with the expression of the Coriolis force \vec{f}_c for a body of a mass m with a relative speed \vec{v} in the rotating frame at the rotational speed $\vec{\Omega}$:

$$\vec{f}_c = -2m\vec{\Omega} \times \vec{v}, \quad (\text{I.100})$$

where \times is the cross product.

Transposed to bladed discs vibrations, the two displacements perpendicular to the axis of rotation have to be significant in order to observe a Coriolis effect. For a blade the tension-compression stiffness is much more important than the flexural stiffness so there is only tangential displacement in classical blades because of the strong rigidity of discs in general, the Coriolis effect does not significantly alter the natural frequencies and modes shapes and thus can be considered negligible [191]. However, with the lightening of bladed disc and the increased complexity of blade geometry, the Coriolis effect will be greater for high rotational speeds. Indeed, it has been shown that the Coriolis effect can generate significant changes in the dynamic properties of bladed discs exhibiting a strong coupled motion between the disc and the blades in the plan perpendicular to the axis of rotation [64, 139].

The following example is a blisk model in which the blades and the disc are made in one piece so there is no damping between the disc and the blades due to friction. If the disc diameter is large enough with a small thickness, it will be less stiff and have a significant radial displacement and as mentioned above the blades will generate tangential displacement. Considering only the motion at the blade tip q_d , the displacement will describe an ellipse around a static position q_{st} . There are two possible configurations. In the first one, the blade tip travels the ellipse in the same direction as that of the rotation of the blisk (Fig. I.16a), it is the forward local displacement. In the second one, the blade tip travels the ellipse in the opposite direction of the rotation of the blisk (Fig. I.16b), it is the backward local displacement.

With a forward local displacement and according to Eq. (I.100), the Coriolis force is always directed toward the outside of the ellipse. The Coriolis effect in this case tends to soften the system because it takes away the dynamic point q_d from its static position q_{st} . As opposed to this, with a backward local displacement, the Coriolis force is always directed toward the inside of the ellipse. The Coriolis effect in this case tends to stiffen the system because it brings the dynamic point q_d closer to its static position q_{st} . Generally speaking, a forward local displacement is associated to a forward travelling wave and the backward local displacement to a backward travelling wave. This explains the split for the degenerate modes of a gyroscopic system, the forward travelling wave will go down in frequency and the backward travelling wave will go up in frequency with the increase of the rotational speed [25].

Finally, it is very important to not confuse the gyroscopic effect with the Coriolis effect. Indeed, the gyroscopic effect is especially observed in rotor dynamics where the disc is supposed to be rigid and the shaft flexible, the phenomenon appears for rotation of the shaft orthogonal to the engine rotational axis and creates a torque orthogonal to the shaft and the engine rotational axes. This creates a coupling between the two axes orthogonal to the engine rotational axis and the intensity of this coupling depends on the polar inertia of the disc. Moreover, because

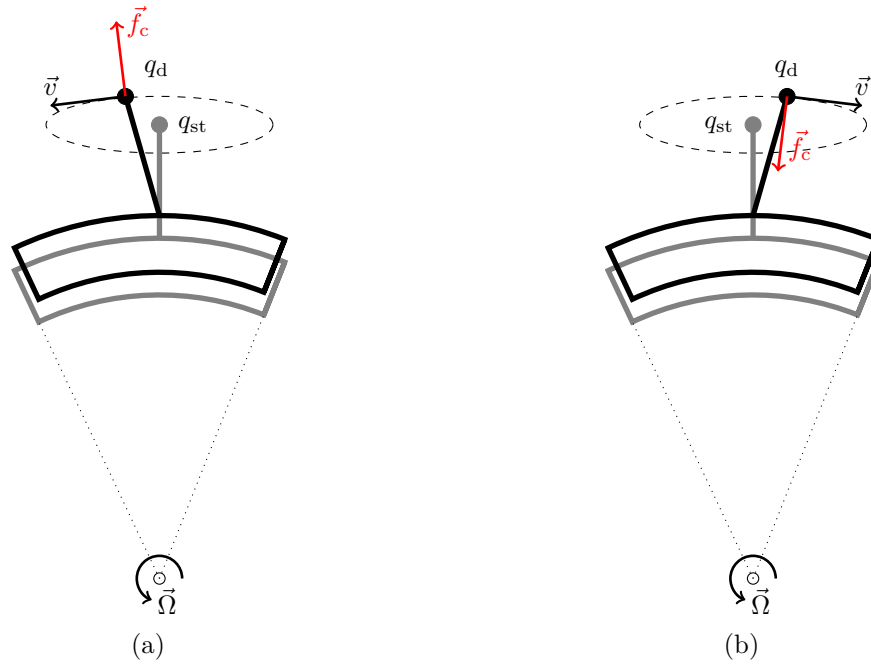


Figure I.16 – In-plane motion of a blade tip with the action of the Coriolis force. (a) Forward local displacement and (b) Backward local displacement

of the axisymmetric property of the structure analysed in rotor dynamics, the problem can be solved in the fixed reference frame and there is only the presence of a gyroscopic matrix \mathbf{G} . On the other hand, in the rotating frame of reference, it is the Coriolis matrix as in Eq. (I.24) where the terms associated to the gyroscopic effect are incorporated. For a bladed disc, the non-axisymmetric structure imposes that the problem be solved in the rotating frame of reference due to the time dependence of the different matrices ($\mathbf{M}, \mathbf{K}^g, \mathbf{C}$, etc.) in the fixed reference frame. The work in this manuscript is focused on rotating systems but only for Coriolis effect in bladed disc so the gyroscopic effect due to a flexible shaft will not be considered.

4.2 Mistuning and detuning

4.2.1 Mistuning

For analytical and numerical studies of bladed discs, cyclic symmetry assumptions are very helpful but this ideal geometry cannot be obtained on real structures due to deviation between sectors that result from manufacturing tolerances and natural wear. This physical phenomenon is called mistuning and leads to the splitting of double modes in symmetric structures, the occurrence of standing wave modes and the different vibration amplitudes for each sector [52, 211, 212].

The common point with the Coriolis and mistuning effects is the split frequency of the degenerate mode but in the mistuning case this split is independent of the rotational speed, as a consequence the split is already present at rest in contrast to the Coriolis effect. The second difference is the occurrence of standing wave modes instead of travelling wave modes with the Coriolis effect. The consequences are the localisation of vibrational energy in some blades and an increase of the maximal vibrational amplitude in some blades compared to the tuned case.

The deviation between frequencies with and without mistuning is defined as the standard deviation of random mistuning. The amplitude magnification factor, which corresponds to the

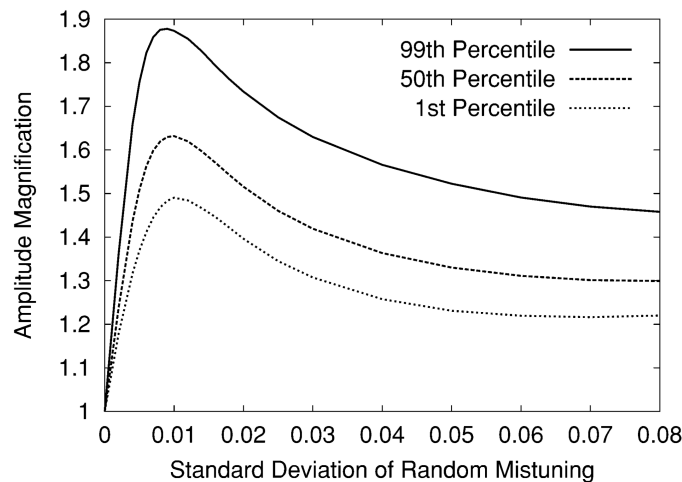


Figure I.17 – Amplitude magnification factor versus the standard deviation of random mistuning [33].

ratio between the maximum amplitude response of the mistuned and tuned cases, depends on this standard deviation, which can lead to response curves such as the ones in Fig. I.17. This plot can be decomposed into two areas: a first one before the peak with a steep slope and an increasing amplitude magnification factor with the increasing standard deviation and a second one after the peak with a softer slope and a decreasing amplitude magnification factor with the increasing standard deviation of random mistuning. Therefore, in this second area, the sensitivity to mistuning is lower.

4.2.2 Detuning

Mistuning is inevitable in turbomachinery and is usually in the first area of the curve in I.17 where the amplitude magnification factor can significantly change and reach critical levels. However, the second zone, where the amplification is smaller and more stable with small variations of the detuning level, can be done intentionally. This can be done with the help of detuning which consists in introducing mistuning intentionally [32, 37, 71, 157, 223]. This detuning can be introduced in different ways: by modifying the geometry of certain blades, by adding or removing mass, or by directly altering the material properties with a variation of the Young's modulus from one blade to another.

Detuning can also be used to increase stability margin with respect to flutter by introducing standing wave modes [13, 16, 40, 45, 79, 90, 96, 151, 175, 184, 229]. The goal is to break the natural cyclic symmetry of the bladed disc by defining a particular pattern consisting of two or more different types of blades, or with non-uniform circumferential spacing between blades. In this way, the vibration phase shifts between all the blades are different and the energy transfer through the fluid essential to the occurrence of flutter is limited. However, if the Coriolis effect becomes predominant over detuning at high speeds, it could potentially decrease the stability margin to flutter due to the occurrence of travelling wave modes as will be shown in Chapter III.

4.2.3 Coriolis and mistuning interaction

The interaction between Coriolis and mistuning effects has been studied in the past [140, 165]. Huang [80] investigated the effect of Coriolis force mode localisation due to mistuning and concluded from numerical results of an analytical model that the Coriolis forces tend

to enhance the localisation phenomenon in a mistuned system. Nikolic [139] used a lumped parameter spring mass model to study the effect of Coriolis forces with mistuning and it was found that the Coriolis effect can increase the maximum response level of a blade in a bladed disc with prominent radial flexibility. Xin [220] studied a finite element model of a realistic compressor bladed disc and concluded that large natural frequency splits due to the Coriolis effect are obtained for a low nodal diameter (ND), and that the Coriolis effect increases or reduces the mode localisation phenomenon depending on the mode. The same conclusions were reported by Kan [86, 88]. He was also the first to consider an intentionally mistuned bladed disc subject to the Coriolis effect [87].

Almeida [1] observed the evolution of modes from standing to travelling waves due to the Coriolis effect on an experimental rotating mistuned centrifugal compressor. Ruffini [166] made the same experimental observation as Almeida [1] on a simplified blisk. Fully-developed travelling waves were observed for low-mistuned modes, but highly-mistuned modes exhibited significant standing-wave components. All these contributions demonstrate that it is necessary to take Coriolis forces into account during the design stage of mistuned bladed discs. However, the coexistence of Coriolis and mistuning effects and the dominance of one over the other is not yet fully understood.

4.2.4 Monte Carlo simulation for forced response statistics

The main problem in the simulation of mistuning is to correctly determine the general trend of the vibration behaviour. A classical solution is to use a stochastic approach. For this purpose, the mistuning pattern is chosen randomly by changing a mechanical parameter, which is usually the Young's modulus or the natural frequency of the blade. This mistuning parameter is generated using a normal distribution with zero mean and standard deviation equal to the mistuning level σ .

For example in Fig. I.17, the amplification magnification curves are given for 3 different percentile which reflect the probability of a random mistuning pattern to be less than the amplification factor given at a specific mistuning level. These results are usually obtained using a Monte Carlo study. The principle of the simulation is to fix a standard deviation of random mistuning for the mistuning parameter with a standard normal distribution. This generates different random patterns of the mistuned bladed drum, for which a forced response is calculated. For each pattern, the largest amplitude response is recorded and divided by the maximum amplitude of the tuned case to find the amplitude magnification factor. A Monte Carlo simulation requires a large number of analyses to estimate precisely the statistics of forced response, which can be computationally expensive. Bladh and al. [20] estimated that 50,000 draws are necessary to have the 99.9 percentile curve.

Therefore, it is possible to accelerate the Monte Carlo simulation by estimating the amplitude magnification factor distribution [20]. This estimation is carried out using the cumulative distribution function of the three-parameter Weibull distribution for the largest value:

$$F(x) = e^{-((\lambda-x)/\delta)^\gamma}, \quad (\text{I.101})$$

where x is the random variable of the amplitude magnification, and δ , γ and λ are respectively the scale, shape and location parameters. To estimate these parameters, Eq. (I.101) has to be rearranged using the $\ln(-\ln(\cdot))$ operator:

$$\ln(\lambda - x) = \frac{1}{\gamma} \ln(-\ln(F)) + \ln(\delta). \quad (\text{I.102})$$

The location parameter λ describes the upper limit of x . In general, the approximation of λ is

given by a Whitehead approximation [213]:

$$\lambda = \frac{1}{2}(1 + \sqrt{N}). \quad (\text{I.103})$$

This approximation works well when there is only one family of modes in the frequency range of interest, since this assumption is made by Whitehead. However, in the veering region, this limit can be exceeded by the presence of several families of modes and the results seem to be case-dependent [74, 93, 219]. For these reasons and because the maximum amplitude magnification factor is difficult to generalise for every FEM, the value λ is assumed to be arbitrarily 20% above the maximum value x given by the simulation.

By sorting the x values of the simulation and determining the associated cumulative distribution function values, the two unknowns δ and γ in Eq. (I.102) can be estimated using a least-squares linear regression. Finally, the amplitude magnification factor can be calculated for every value of the cumulative distribution function using the operator $e^{(\cdot)}$ in Eq. (I.102).

$$x = \lambda - \delta(-\ln(F))^{\frac{1}{\gamma}}. \quad (\text{I.104})$$

An example of the cumulative distribution function given by the three-parameter Weibull distribution using a set of 50 mistuning patterns is plotted in Fig. I.18. Two curves correspond to two different limit amplitude magnification factor approximations, the blue one calculated using Whitehead's formula and the red one calculated using the 20% above the maximum value x of the simulation. This assumption does not change the Weibull curve significantly and allows to estimate the distribution even if the amplitude magnification factors are above the Whitehead's limit.

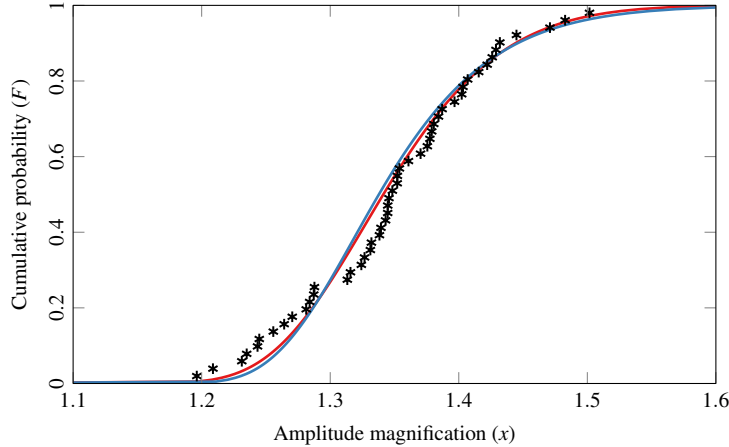


Figure I.18 – Cumulative distribution function for the accelerated Monte Carlo simulation. [*] Set of 50 mistuning patterns. [—] The three-parameter Weibull distribution using Whitehead's formula for λ . [—] The three-parameter Weibull distribution using the value 20% above the maximum for λ .

There are also non-stochastic methods to avoid stochastic calculus which can be time consuming and costly. Can be cited, the work of Klir [98] on the generalised information theory whose objective is to develop a broader treatment of information based on uncertainty. The interval arithmetic theory proposed by Moore [135] also makes it possible to define an interval, which includes all possibilities without using a stochastic method and has been applied to mechanical mistuned structures [49]. The fuzzy logic introduced by Zadeh [224], which contrasts with the Boolean logic and employs the concept of partial truth, has also been applied to

mistuned bladed discs [89]. Ben-Haim developed the Info-gap theory [12] which investigates the degree of lack of knowledge that can be tolerated while satisfying a critical level of performance [77].

4.3 Dimensioning procedures

The bladed disc dimensioning uses different diagram tools to define the excitability of a mode by a synchronous excitation source or to define the mechanical resistance of the components to cyclic loading.

4.3.1 Campbell diagram

The rotational effects of centrifugal stiffening and softening and the Coriolis effect cause the natural frequencies to change as a function of the rotational speed. This evolution can be represented by a Campbell diagram, which plots the natural frequencies as a function of the rotational speed. An example is given in Fig. I.19.

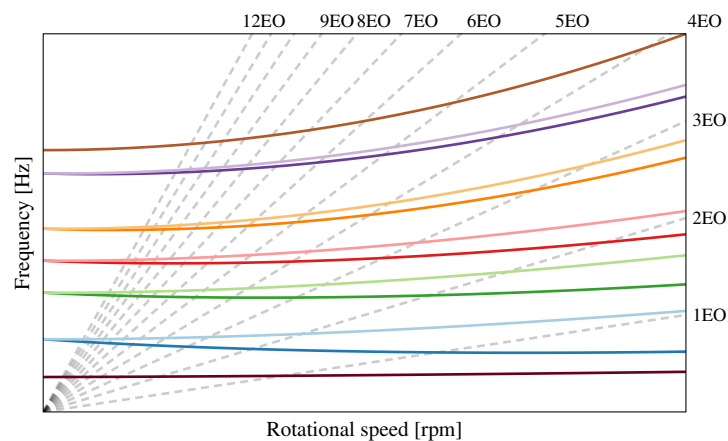


Figure I.19 – Campbell diagram

It can be seen that the frequencies of the degenerate modes are split into two due to the Coriolis effect with a forward travelling wave for the lower branches and backward travelling wave for the upper branches. In this case, as in the majority, the modes tend to increase with the rotational speed due to the stiffening effect, but in some other cases, the softening effect is predominant and the modes tend to decrease with the rotational speed.

On this diagram can also be represented in dashed line, the engine orders (EO) which are harmonics of the rotational speed, and as explained in Section I.1.3, these engine orders can be linked to synchronous excitations such as the number of wakes. A crossing between an engine order and an eigenfrequency indicates a risk of excitation of the mode which can lead to resonance and significant vibrations.

As observed in Fig. I.19, there is a significant number of crossings between the engine orders and the eigenfrequencies, but not all of these crossovers necessarily result in the structure being in resonance. For this, the engine order must coincide to the nodal diameter number of the mode it crosses, which is known as modal appropriation, and can be observed using a ZZENF diagram.

4.3.2 ZZENF diagram

In the development of cyclic symmetry in Section I.3.3, the folding phenomenon of spatial harmonics has been mentioned, and it is this property that allows to deduce the modal appropriation condition. It can be shown that the excitation of an N sector cyclic structure by an engine order h is only possible if one the following relations is satisfied [217]:

$$h - k = pN, \quad (\text{I.105})$$

$$h + k = pN, \quad (\text{I.106})$$

where k is the excited spatial harmonic between $[[0, K]]$ with $K = N/2$ if N is even or $K = (N - 1)/2$ if N is odd and p a natural number. The sign ahead of k gives information on the direction of the excited wave; with Eq. (I.105), it is a forward wave otherwise with Eq. (I.106), it is the backward wave. It should be noted that for nondegenerate modes, both equations are satisfied.

This condition can also be represented graphically with a ZZENF diagram (Zig Zag shaped Excitation line in the Nodal diameter versus Frequency diagram [218]). An example is given in Fig. I.20 for a bladed disc with 60 sectors. It should be noted that the blue curves correspond to Eq. (I.105) and thus to forward waves and the red curves to Eq. (I.106) and thus to backward waves. The green points are for nondegenerate modes.

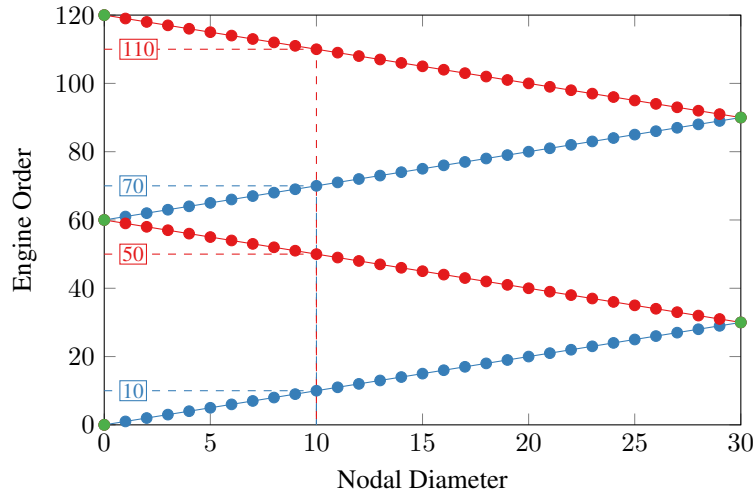


Figure I.20 – ZZENF diagram.

For example, it can be deduced that the forward modes with 10 nodal diameters are excited by the engine orders 10 and 70 and the backward modes by the engine orders 50 and 110.

4.3.3 Natural frequencies/nodal diameters diagram

The natural frequencies/nodal diameters diagram shows the evolution of natural frequencies as a function of the number of nodal diameters. It also allows the modes to be grouped into families according to their frequencies. These families are generally characterised by the deformation of the blades (bending, torsion, etc.). Unlike the Campbell diagram, this one is plotted for a given rotational speed. An example is given in Fig. I.21.

The first thing that can be observed with this diagram is the participation of the disc on the different modal families. The modes exhibiting slanted lines have an important participation of the disc [33]. It concerns the small diameters for the first families and then it increases for the families with higher frequencies.

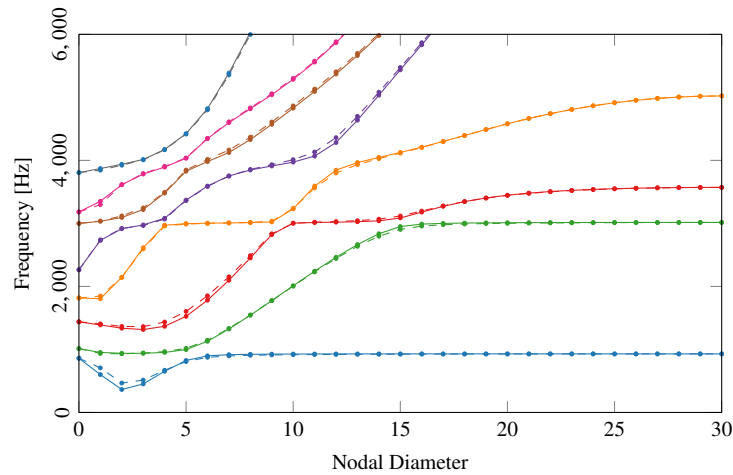


Figure I.21 – Natural frequencies/nodal diameters diagram.

On the other hand, the horizontal lines show blade modes without participation of the disc and with frequencies close to the modes of the clamped blade. It is at these levels that one can observe bending or torsion of the blades.

Finally, it is also possible to observe veering regions, which correspond to a convergence of the curves of two modal families [152]. It is preferable to avoid this type of zone during the design phase as this is where modes can exchange energy and in the case of mistuning, a very significant amplitude magnification of the response can be obtained [31].

4.3.4 S-N curve

The tools presented until now allow the risks of resonances to be anticipated in operation but do not take into account the vibratory fatigue of materials. This is defined as cyclic loading of the structure which depending on the stress level and the number of cycles, may lead to complete fracture of the structure.

The S-N curve, also known as Wöhler curve, allows to characterise materials' fatigue. It represents the cyclic stress σ_c against the number of loading cycle N_c (Fig. I.22). For 0 cycle, this corresponds to the tensile strength σ_u . This curve is usually obtained experimentally and is sometimes known as coupon testing.

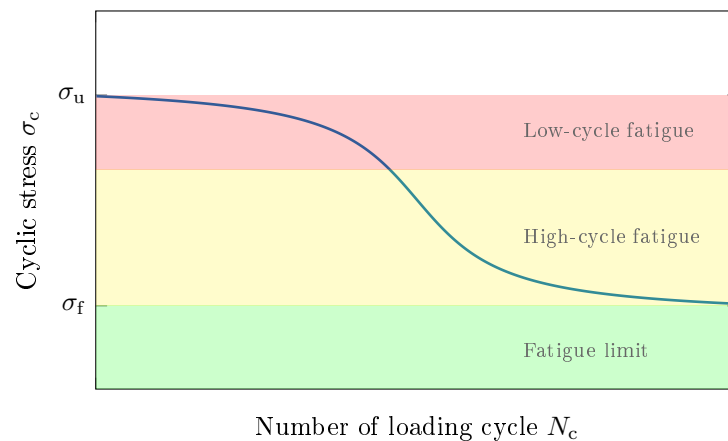


Figure I.22 – S-N curve.

Three areas can be distinguished in this diagram. The low-cycle fatigue area is characterised by a stress level which leads to fractures after a small number of load cycles and rupture after less than 100,000 cycles. Then, the rapidly falling curve in the high-cycle fatigue is where more stress cycles are possible. Finally, for some materials, such as steel, it is possible to observe a fatigue limit or endurance limit σ_f , which is shown on the diagram as a horizontal line where a stress level below this value will result in a theoretically infinite number of cycles.

4.3.5 Haigh diagram

The problem with the S-N curve is that it is only applied for a mean stress value σ_m , which is taken equal to zero, meaning that centrifugal loading is not taken into account, although its effect on material fatigue is often far from negligible. For this reason, there are diagrams that illustrate the influence of σ_m , such as the Haigh diagram (Fig. I.23).

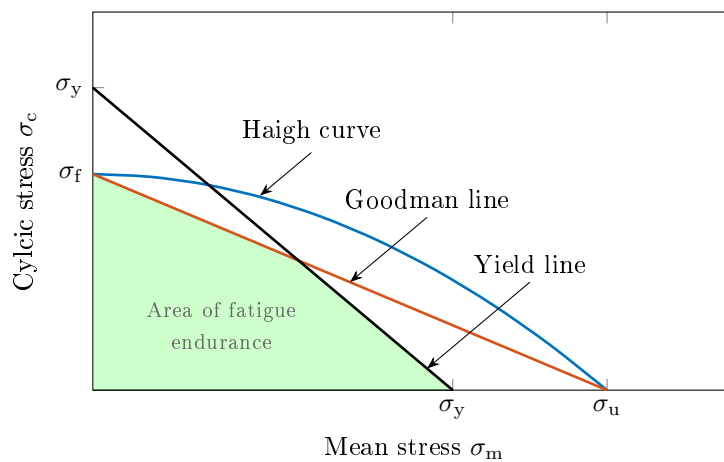


Figure I.23 – Haigh diagram.

It represents the cyclic stress against the mean stress. At mean stress zero ($\sigma_m = 0$), the cyclic stress is equal to the fatigue limit ($\sigma_c = \sigma_f$) and at cyclic stress zero $\sigma_c = 0$, the mean stress is equal to the tensile strength ($\sigma_m = \sigma_u$). The Haigh curve is used to connect these two points and theoretically any pair of points (σ_m, σ_c) under this curve is assumed to be acceptable for the design.

The actual Haigh diagram is hard to obtain, so there are models to simplify such as the Goodman line, which relates the fatigue limit to the tensile strength by a straight line. In order to avoid plastic deformation, the sum of cyclic stress and mean stress must never exceed the yield strength value σ_y , which limits the allowable zone to the area of fatigue endurance.

The Haigh diagram has only been presented here for tensile stress but the same reasoning can be used to extend the diagram to compressive stress with the value of the compressive yield strength.

Chapter summary

This chapter set out the theoretical framework necessary for the analysis of bladed discs subject to rotational effects and especially the Coriolis effect. In that way, the dynamic equations were developed as well as the theory of cyclic symmetry. Classical dimensioning tools were also presented.

This chapter also highlights some of the issues faced by aircraft manufacturers, who must constantly innovate to meet economic and environmental requirements. For this reason, the

various elements are redesigned to reduce the weight and increase the performance of engines. Some of these new technologies, due to their single-piece aspect, softness and large diameter such as bladed drums, can have a significant Coriolis effect. This effect is has been generally neglected during the design process. Combined with other phenomena such as mistuning or flutter, this can lead to undesired vibratory behaviour. It is therefore important to understand these different interactions in order to achieve the best possible design.

For this purpose, the following chapter proposes to use lumped-parameter model representative of bladed disc to highlight the interactions that may exist between Coriolis effects and mistuning.

Chapter II

Lumped-parameter cyclic symmetric model

In this chapter, a method based on the perturbation approach with an adaptation in the state-space representation is first developed to express the sensitivity of the eigenvalues and eigenvectors to mistuning. Secondly, a cyclically symmetric structure consisting of mass and springs is introduced to allow an in-depth study of the interaction between the Coriolis and mistuning effects. This simplified model is better suited than a numerical finite element model to explore the complex interaction between these two phenomena. After presenting the geometry of the model, its parameters and the geometrical nonlinearities, the modal analysis of the system will be performed and the perturbation method will be validated for different rotational velocities. Finally, the conclusions drawn from this modal analysis will be tested on the forced response system.

Outline of the chapter

1	Perturbation method applied to a mistuned gyroscopic system	44
1.1	Formulating the eigenvalue system	44
1.2	Perturbation method	44
2	Cyclic symmetric structure	47
2.1	Description of the model	47
2.2	Expressions of the nonlinear restoring forces	48
2.3	Equations of motion	50
2.4	Nonlinear approximation	51
2.5	Mistuning introduction	52
3	Modal analyses	52
3.1	Modal analysis of the tuned bladed disc	53
3.2	Modal analysis of the mistuned bladed disc	55
3.3	Perturbation method comparison	59
4	Frequency response function	60
4.1	Forced response at rest	61
4.2	Forced response at high rotational velocity	64
	Chapter summary	66

1 Perturbation method applied to a mistuned gyroscopic system

In this section, the sensitivity of the eigenvalues and eigenvectors to mistuning is studied using the perturbation method for a conservative rotating system. This provides analytical understanding of the mistuning effect on cyclic symmetric structures and particularly in the areas where two or more different modes have similar eigenvalues.

1.1 Formulating the eigenvalue system

Using the state-space representation developed in Section 1.3.1, decomposing the real and imaginary parts with the expression of the eigenvectors and knowing that for a conservative gyroscopic system the eigenvalues are purely imaginary leads to the following system

$$\begin{cases} \mathbf{A}\mathbf{x}_r + \omega_r\mathbf{B}\mathbf{y}_r = \mathbf{0} \\ \mathbf{A}\mathbf{y}_r - \omega_r\mathbf{B}\mathbf{x}_r = \mathbf{0} \\ (\mathbf{x}_r)^\top\mathbf{B}\mathbf{x}_r = 1 \\ (\mathbf{y}_r)^\top\mathbf{B}\mathbf{y}_r = 1, \end{cases} \quad (\text{II.1})$$

where the last two equations are the normalisation conditions of the vectors $(\mathbf{x}_r, \mathbf{y}_r)$ with respect to the matrix \mathbf{B} . As a reminder, \mathbf{x}_r and \mathbf{y}_r are respectively the real and imaginary parts of the complex eigenvector \mathbf{u}_r of the r^{th} mode such as:

$$\mathbf{u}_r = \mathbf{x}_r + i\mathbf{y}_r. \quad (\text{II.2})$$

Throughout the rest of the section, the tuned system will be identified with the superscript 0 . From an industrial point of view, the production of turbomachinery elements induces small material differences between sectors due to manufacturing tolerances or wear in service. The resulting mistuning will be considered weak enough to be treated as a disturbance of the mass and stiffness matrices of the tuned system without impacting the sector geometries, which is a good representation of this type of mistuning. However, the goal is to describe the global behaviour of the sensitivity of the eigenvalue with the perturbation method and not necessarily calculate the exact results.

$$\mathbf{A} = \mathbf{A}^0 + \varepsilon\delta\mathbf{A}, \quad (\text{II.3})$$

$$\mathbf{B} = \mathbf{B}^0 + \varepsilon\delta\mathbf{B}, \quad (\text{II.4})$$

where ε is the order parameter of the perturbation method and $\delta\mathbf{A}$ and $\delta\mathbf{B}$ the variations due to the mistuning from the tuned matrices \mathbf{A}^0 and \mathbf{B}^0 .

1.2 Perturbation method

The perturbation method applied to a mechanical undamped and non-gyroscopic system was first introduced in [35] and generalised in [186]. This section is an extension of this method for the gyroscopic system. Using the perturbation method, Eq. (II.3) and Eq. (II.4) in Eq.

(II.1) leads to

$$\begin{cases} [\mathbf{A}^0 + \varepsilon(\mathbf{A} - \mathbf{A}^0)]\mathbf{x}_r + \omega_r[\mathbf{B}^0 + \varepsilon(\mathbf{B} - \mathbf{B}^0)]\mathbf{y}_r = \mathbf{0} \\ [\mathbf{A}^0 + \varepsilon(\mathbf{A} - \mathbf{A}^0)]\mathbf{y}_r - \omega_r[\mathbf{B}^0 + \varepsilon(\mathbf{B} - \mathbf{B}^0)]\mathbf{x}_r = \mathbf{0} \\ (\mathbf{x}_r)^\top[\mathbf{B}^0 + \varepsilon(\mathbf{B} - \mathbf{B}^0)]\mathbf{x}_r = 1 \\ (\mathbf{y}_r)^\top[\mathbf{B}^0 + \varepsilon(\mathbf{B} - \mathbf{B}^0)]\mathbf{y}_r = 1, \end{cases} \quad (\text{II.5})$$

where \mathbf{x}_r , \mathbf{y}_r and ω_r are the unknowns of the perturbation method such as for $\varepsilon = 0$, Eq. (II.5) becomes the tuned system and for $\varepsilon = 1$, it becomes the mistuned system.

At this stage these unknowns are represented as power series with respect to ε .

$$\omega_r = \omega_r^0 + \sum_{p=1}^{\infty} \varepsilon^p \omega_r^p, \quad (\text{II.6})$$

$$\mathbf{x}_r = \mathbf{x}_r^0 + \sum_{p=1}^{\infty} \varepsilon^p \mathbf{x}_r^p, \quad (\text{II.7})$$

$$\mathbf{y}_r = \mathbf{y}_r^0 + \sum_{p=1}^{\infty} \varepsilon^p \mathbf{y}_r^p, \quad (\text{II.8})$$

when introducing Eq. (II.6), Eq. (II.7) and Eq. (II.8) in Eq. (II.5), the zeroth-order gives the tuned system and the next orders give:

Order 1:

$$\begin{cases} \mathbf{A}^0 \mathbf{x}_r^1 + \omega_r^0 \mathbf{B}^0 \mathbf{y}_r^1 = \mathbf{g}_r^1 \\ \mathbf{g}_r^1 = -\omega_r^1 \mathbf{B}^0 \mathbf{y}_r^0 - (\mathbf{A} - \mathbf{A}^0) \mathbf{x}_r^0 - \omega_r^0 (\mathbf{B} - \mathbf{B}^0) \mathbf{y}_r^0 \\ \mathbf{A}^0 \mathbf{y}_r^1 - \omega_r^0 \mathbf{B}^0 \mathbf{x}_r^1 = \mathbf{h}_r^1 \\ \mathbf{h}_r^1 = \omega_r^1 \mathbf{B}^0 \mathbf{x}_r^0 - (\mathbf{A} - \mathbf{A}^0) \mathbf{y}_r^0 + \omega_r^0 (\mathbf{B} - \mathbf{B}^0) \mathbf{x}_r^0 \\ (\mathbf{x}_r^0)^\top \mathbf{B}^0 \mathbf{x}_r^1 = \frac{1}{2} [1 - (\mathbf{x}_r^0)^\top \mathbf{B} \mathbf{x}_r^0] \\ (\mathbf{y}_r^0)^\top \mathbf{B}^0 \mathbf{y}_r^1 = \frac{1}{2} [1 - (\mathbf{y}_r^0)^\top \mathbf{B} \mathbf{y}_r^0], \end{cases} \quad (\text{II.9})$$

Order $p \geq 2$:

$$\begin{cases} \mathbf{A}^0 \mathbf{x}_r^p + \omega_r^0 \mathbf{B}^0 \mathbf{y}_r^p = \mathbf{g}_r^p \\ \mathbf{g}_r^p = -\omega_r^p \mathbf{B}^0 \mathbf{y}_r^0 - (\mathbf{A} - \mathbf{A}^0) \mathbf{x}_r^{p-1} - \sum_{k=1}^{p-1} \omega_r^k \mathbf{B}^0 \mathbf{y}_r^{p-k} - \sum_{k=0}^{p-1} \omega_r^k (\mathbf{B} - \mathbf{B}^0) \mathbf{y}_r^{p-1-k} \\ \mathbf{A}^0 \mathbf{y}_r^p - \omega_r^0 \mathbf{B}^0 \mathbf{x}_r^p = \mathbf{h}_r^p \\ \mathbf{h}_r^p = \omega_r^p \mathbf{B}^0 \mathbf{x}_r^0 - (\mathbf{A} - \mathbf{A}^0) \mathbf{y}_r^{p-1} + \sum_{k=1}^{p-1} \omega_r^k \mathbf{B}^0 \mathbf{x}_r^{p-k} + \sum_{k=0}^{p-1} \omega_r^k (\mathbf{B} - \mathbf{B}^0) \mathbf{x}_r^{p-1-k} \\ (\mathbf{x}_r^0)^\top \mathbf{B}^0 \mathbf{x}_r^p = -\frac{1}{2} \left[\sum_{k=0}^{p-1} (\mathbf{x}_r^k)^\top (\mathbf{B} - \mathbf{B}^0) \mathbf{x}_r^{p-1-k} + \sum_{k=1}^{p-1} (\mathbf{x}_r^k)^\top \mathbf{B}^0 \mathbf{x}_r^{p-k} \right] \\ (\mathbf{y}_r^0)^\top \mathbf{B}^0 \mathbf{y}_r^p = -\frac{1}{2} \left[\sum_{k=0}^{p-1} (\mathbf{y}_r^k)^\top (\mathbf{B} - \mathbf{B}^0) \mathbf{y}_r^{p-1-k} + \sum_{k=1}^{p-1} (\mathbf{y}_r^k)^\top \mathbf{B}^0 \mathbf{y}_r^{p-k} \right], \end{cases} \quad (\text{II.10})$$

1.2.1 Eigenvalues

The next step is to project the unknowns \mathbf{x}_r^p and \mathbf{y}_r^p onto the basis of the tuned eigenvectors to make it possible to find the eigenvalues expressions with the tuned eigenvectors and eigenvalues.

$$\mathbf{x}_r^p = \alpha_{r,r}^p \mathbf{x}_r^0 + \sum_{j=1, j \neq r}^n \alpha_{r,j}^p \mathbf{x}_j^0, \quad (\text{II.11})$$

$$\mathbf{y}_r^p = \beta_{r,r}^p \mathbf{y}_r^0 + \sum_{j=1, j \neq r}^n \beta_{r,j}^p \mathbf{y}_j^0. \quad (\text{II.12})$$

By multiplying the first Eq. (II.9) and Eq. (II.10) by $(\mathbf{y}_r^0)^\top$ and the second one by $(\mathbf{x}_r^0)^\top$, it is possible to determine the expression of ω_r^p so that:

Order 1:

$$\omega_r^1 = (\mathbf{x}_r^0)^\top \mathbf{A} \mathbf{y}_r^0 - \frac{\omega_r^0}{2} [(\mathbf{x}_r^0)^\top \mathbf{B} \mathbf{x}_r^0 + (\mathbf{y}_r^0)^\top \mathbf{B} \mathbf{y}_r^0]. \quad (\text{II.13})$$

Order $p \geq 2$:

$$\begin{aligned} \omega_r^p = & \frac{1}{2} [(\mathbf{x}_r^0)^\top (\mathbf{A} - \mathbf{A}^0) \mathbf{y}_r^{p-1} - (\mathbf{y}_r^0)^\top (\mathbf{A} - \mathbf{A}^0) \mathbf{x}_r^{p-1} - \sum_{k=1}^{p-1} \omega_r^k (\mathbf{y}_r^0)^\top \mathbf{B}^0 \mathbf{y}_r^{p-k} \\ & - \sum_{k=0}^{p-1} \omega_r^k (\mathbf{y}_r^0)^\top (\mathbf{B} - \mathbf{B}^0) \mathbf{y}_r^{p-1-k} - \sum_{k=1}^{p-1} \omega_r^k (\mathbf{x}_r^0)^\top \mathbf{B}^0 \mathbf{x}_r^{p-k} - \sum_{k=0}^{p-1} \omega_r^k (\mathbf{x}_r^0)^\top (\mathbf{B} - \mathbf{B}^0) \mathbf{x}_r^{p-1-k}]. \end{aligned} \quad (\text{II.14})$$

1.2.2 Eigenvectors

To find the eigenvectors expressions, one only needs to find the expressions of $\alpha_{r,j}^p$ and $\beta_{r,j}^p$ and then use Eq. (II.11) and Eq. (II.12). There are two cases:

- $j = r$: Using the normalisation conditions of Eq. (II.9) and Eq. (II.10) with Eq. (II.11) and Eq. (II.12).

Order 1:

$$\alpha_{r,r}^1 = \frac{1 - (\mathbf{x}_r^0)^\top \mathbf{B} (\mathbf{x}_r^0)}{2}, \quad (\text{II.15})$$

$$\beta_{r,r}^1 = \frac{1 - (\mathbf{y}_r^0)^\top \mathbf{B} (\mathbf{y}_r^0)}{2}. \quad (\text{II.16})$$

Order $p \geq 2$:

$$\alpha_{r,r}^p = -\frac{1}{2} \left[\sum_{k=0}^{p-1} (\mathbf{x}_r^k)^\top (\mathbf{B} - \mathbf{B}^0) \mathbf{x}_r^{p-1-k} + \sum_{k=1}^{p-1} (\mathbf{x}_r^k)^\top \mathbf{B}^0 \mathbf{x}_r^{p-k} \right], \quad (\text{II.17})$$

$$\beta_{r,r}^p = -\frac{1}{2} \left[\sum_{k=0}^{p-1} (\mathbf{y}_r^k)^\top (\mathbf{B} - \mathbf{B}^0) \mathbf{y}_r^{p-1-k} + \sum_{k=1}^{p-1} (\mathbf{y}_r^k)^\top \mathbf{B}^0 \mathbf{y}_r^{p-k} \right]. \quad (\text{II.18})$$

- $j \neq r$: Multiplying the first Eq. (II.9) and Eq. (II.10) by $(\mathbf{y}_j^0)^\top$ and the second one by

$(x_j^0)^\top$ with Eq. (II.11) and Eq. (II.12).

$$\alpha_{r,j}^p = \frac{\omega_r^0(\mathbf{x}_j^0)^\top \mathbf{h}_r^p - \omega_j^0(\mathbf{y}_j^0)^\top \mathbf{g}_r^p}{(\omega_j^0)^2 - (\omega_r^0)^2}, \quad (\text{II.19})$$

$$\beta_{r,j}^p = \frac{\omega_j^0(\mathbf{x}_j^0)^\top \mathbf{h}_r^p - \omega_r^0(\mathbf{y}_j^0)^\top \mathbf{g}_r^p}{(\omega_j^0)^2 - (\omega_r^0)^2}. \quad (\text{II.20})$$

It is now possible to express the eigenvectors and eigenvalues of the mistuned system with the eigenvalues and eigenvectors of the tuned one based on a p^{th} order approximation.

The mistuning effect results in a significant interaction between the tuned modes and thanks to the analytical expressions in Eq. (II.19) and Eq. (II.20) it is possible to know in which cases mistuning has a high or low chance of occurring. When the coefficients $\alpha_{r,j}^p$ and $\beta_{r,j}^p$ (with $j \neq r$) are negligible compared to the coefficients $\alpha_{r,r}^p$ and $\beta_{r,r}^p$, the mistuned eigenvector is similar to the tuned one and thus the mistuning effect is negligible. In contrast, when the coefficients $\alpha_{r,j}^p$ and $\beta_{r,j}^p$ (with $j \neq r$) are of the same order or greater than the coefficients $\alpha_{r,r}^p$ and $\beta_{r,r}^p$, the mistuning effect can be important due to the superposition of tuned modes in the modal shape of the detuned case which will prevent pure rotating waves that are observed in the tuned case.

There are two main sources for the increase of the coefficients $\alpha_{r,j}^p$ and $\beta_{r,j}^p$. The most obvious is the increase in the level of mistuning. The larger the perturbations $\delta\mathbf{A}$ and $\delta\mathbf{B}$ are, the larger the coefficients $\alpha_{r,j}^p$ and $\beta_{r,j}^p$ are with $j \neq r$. The second case is when $(\omega_j^0)^2 \approx (\omega_r^0)^2$, $\alpha_{r,j}^p$ and $\beta_{r,j}^p$ can be significant due to an asymptotic discontinuity in the calculations of these coefficients. This leads to a strong contribution of the mode shape of the j^{th} tuned mode to the mode shape of the r^{th} mistuned mode and this could lead to a standing wave.

Finally, when the Coriolis effect is large enough, the double modes are separated and the effect of the small random mistuning becomes insignificant. In the case of detuning, the $\delta_{r,j}^p$ and $\delta_{r,j}^p$ perturbations will be larger and the $\alpha_{r,j}^p$ and $\beta_{r,j}^p$ coefficients will never be negligible, thus increasing the localisation and amplification effects. However, as for the case of small random mistuning, due to the separation of the double modes with the Coriolis effect, the detuning effect will have a smaller influence in the area where the modes are well isolated in frequency from each other.

A numerical validation of these formulations will be carried out later in this chapter with the modal analysis of the lumped parameter model.

2 Cyclic symmetric structure

The model used for the study is described in this section. It is built to simplify the numerical analysis while reproducing the classical dynamics of a bladed disc. The number of degrees of freedom (dofs) is reduced to a minimum, with one dof for the bending motion of the blade, and two dofs by disc sector, allowing a radial and tangential displacement of the latter. The radial flexibility of the disc and the strong coupling between the blades and the disc are important factors for the presence of the Coriolis effect on the structure.

2.1 Description of the model

The model in Fig. II.1 contains N sectors with two masses m^b and m^d respectively for the blade and the disc sector. Each disc mass is coupled side-by-side with springs which reflect the coupling rigidity k^c between each sector of disc, with a length l^c at rest. The radial flexibility of the disc is represented by the k^r spring while the tangential k^t spring allows to avoid rigid body

modes. The k^b spring represents the bending stiffness of the blade. Finally, it is assumed that the blades are infinitely rigid along the elastic axis, which implies that the radial displacement of the blade is equal to the radial displacement of the disc. The geometry of the lumped parameter model is given in Fig. II.1. The parameters were chosen to be representative of a compressor stage composed of 60 blades of length $l^b = 0.080$ m and a disc of radius $r = 0.320$ m. The disc rotates at a nominal value of 5,000 rpm. All numerical values are shown in Table II.1. The length l^c is expressed as a function of the length r ,

$$l^c = 2r \sin(\pi/N). \quad (\text{II.21})$$

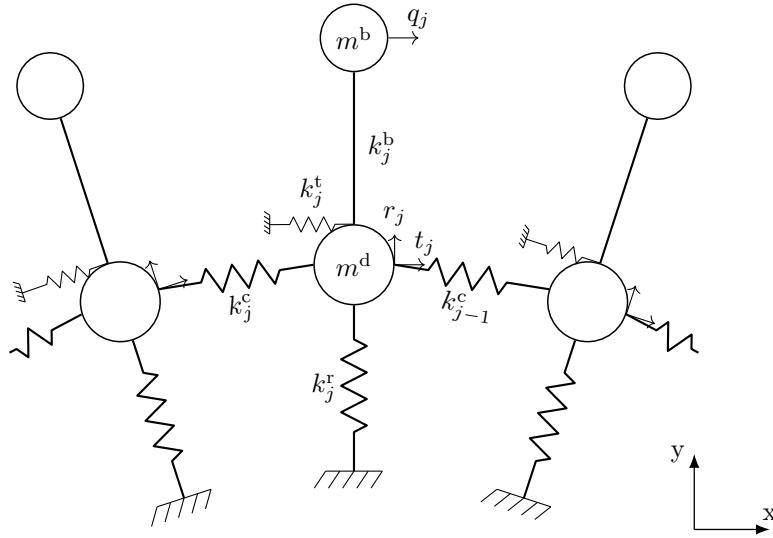


Figure II.1 – Cyclic symmetric lumped parameter model

Table II.1 – Numerical values of the bladed disc

Parameter	Value	Unit
N	60	-
m^b	0.090	kg
m^d	0.295	kg
k^c	1.26×10^9	N/m
k^r	6.84×10^6	N/m
k^t	4.02×10^7	N/m
k^b	4.06×10^6	N/m
l^b	0.080	m
r	0.320	m
Ω	5,000	rpm

2.2 Expressions of the nonlinear restoring forces

The displacement of the mass is not perfectly radial or tangential but is a displacement in both directions. To account for this 2D motion, the expressions of the forces due to the coupled and radial springs are nonlinear. These nonlinear forces on the tangential t_j and radial r_j dofs of the j^{th} disc sector are expressed as follows

$$f_{t_j}^{k_j^r}(t_j, r_j) = -k^r \frac{r - \sqrt{(r+r_j)^2 + t_j^2}}{\sqrt{(r+r_j)^2 + t_j^2}} t_j, \quad (\text{II.22})$$

$$f_{r_j}^{k_j^r}(t_j, r_j) = -k^r \frac{r - \sqrt{(r+r_j)^2 + t_j^2}}{\sqrt{(r+r_j)^2 + t_j^2}} (r+r_j), \quad (\text{II.23})$$

$$f_{t_j}^{k_j^c}(t_j, r_j, t_{j+1}, r_{j+1}) = -k^c \frac{l^c - \sqrt{(t_j + \sin(\alpha)(r+r_{j+1}) - \cos(\alpha)t_{j+1})^2 + (r+r_j - \cos(\alpha)(r+r_{j+1}) - \sin(\alpha)t_{j+1})^2}}{\sqrt{(t_j + \sin(\alpha)(r+r_{j+1}) - \cos(\alpha)t_{j+1})^2 + (r+r_j - \cos(\alpha)(r+r_{j+1}) - \sin(\alpha)t_{j+1})^2}} \cdot (r+r_j - \cos(\alpha)(r+r_{j+1}) - \sin(\alpha)t_{j+1}), \quad (\text{II.24})$$

$$f_{r_j}^{k_j^c}(t_j, r_j, t_{j+1}, r_{j+1}) = -k^c \frac{l^c - \sqrt{(t_j + \sin(\alpha)(r+r_{j+1}) - \cos(\alpha)t_{j+1})^2 + (r+r_j - \cos(\alpha)(r+r_{j+1}) - \sin(\alpha)t_{j+1})^2}}{\sqrt{(t_j + \sin(\alpha)(r+r_{j+1}) - \cos(\alpha)t_{j+1})^2 + (r+r_j - \cos(\alpha)(r+r_{j+1}) - \sin(\alpha)t_{j+1})^2}} \cdot (t_j + \sin(\alpha)(r+r_{j+1}) - \cos(\alpha)t_{j+1}), \quad (\text{II.25})$$

$$f_{t_j}^{k_{i-1}^c}(t_j, r_j, t_{j-1}, r_{j-1}) = -k^c \frac{l^c - \sqrt{(t_j - \sin(\alpha)(r+r_{j-1}) - \cos(\alpha)t_{j-1})^2 + (r+r_j + \sin(\alpha)t_{j-1} - \cos(\alpha)(r+r_{j-1}))^2}}{\sqrt{(t_j - \sin(\alpha)(r+r_{j-1}) - \cos(\alpha)t_{j-1})^2 + (r+r_j + \sin(\alpha)t_{j-1} - \cos(\alpha)(r+r_{j-1}))^2}} \cdot (r+r_j + \sin(\alpha)t_{j-1} - \cos(\alpha)(r+r_{j-1})), \quad (\text{II.26})$$

$$f_{r_j}^{k_{i-1}^c}(t_j, r_j, t_{j-1}, r_{j-1}) = -k^c \frac{l^c - \sqrt{(t_j - \sin(\alpha)(r+r_{j-1}) - \cos(\alpha)t_{j-1})^2 + (r+r_j + \sin(\alpha)t_{j-1} - \cos(\alpha)(r+r_{j-1}))^2}}{\sqrt{(t_j - \sin(\alpha)(r+r_{j-1}) - \cos(\alpha)t_{j-1})^2 + (r+r_j + \sin(\alpha)t_{j-1} - \cos(\alpha)(r+r_{j-1}))^2}} \cdot (t_j - \sin(\alpha)(r+r_{j-1}) - \cos(\alpha)t_{j-1}), \quad (\text{II.27})$$

where $\alpha = 2\pi/N$.

It may be noted that the nonlinear expressions of the forces induced by the coupled springs are even more complex because of the coupling with the dofs of the adjacent sectors. The force induced by the tangential spring of the j^{th} sector is considered linear because its role is only to prevent a rigid body of the structure by an angular movement around the axis of rotation. For this reason, this spring only acts on the tangential dof t_j so that

$$f_{t_j}^{k_j^t} = -k^t t_j. \quad (\text{II.28})$$

Since it is assumed that the blades are infinitely stiff along the elastic axis, the force induced by the bending stiffness of the blade k^b acts only on the dofs t_j and q_j :

$$f_{t_j}^{k_j^b} = -k^b (t_j - q_j), \quad (\text{II.29})$$

$$f_{q_j}^{k_j^b} = -k^b(q_j - t_j). \quad (\text{II.30})$$

Finally, the complete nonlinear restoring forces expressions of the tangential and radial disc dofs of the j^{th} sector are respectively:

$$f_{t_j}^{\text{nl}} = f_{t_j}^{k_j^r} + f_{t_j}^{k_j^c} + f_{t_j}^{k_j^{c-1}}, \quad (\text{II.31})$$

$$f_{r_j}^{\text{nl}} = f_{r_j}^{k_j^r} + f_{r_j}^{k_j^c} + f_{r_j}^{k_j^{c-1}}. \quad (\text{II.32})$$

It is important to have these nonlinear expressions because, as it will be shown in the following, these nonlinearities represent the geometrical nonlinearities of the structure and allow, for example, to show the phenomenon of centrifugal stiffening inherent to rotating bladed disc.

2.3 Equations of motion

Now that the balance of forces acting on each dof of the model has been made it is possible to determine the equations of motion of the system using Newton's second law. The origins of the fixed and rotating frames of reference are considered to coincide with the centre of the structure. To determine the global equations of motion of the system, the study is focused on the two masses of the j^{th} sector of the system and their positions are identified by the vector \mathbf{y}_j^{d} for the disc and \mathbf{y}_j^{b} for the blade in the fixed reference frame and \mathbf{v}_j^{d} and \mathbf{v}_j^{b} in the rotating reference frame. In its undeformed configuration of reference the masses are identified by the vector \mathbf{x}_j^{d} and \mathbf{x}_j^{b} such as $\mathbf{v}_j^{\text{d}} = \dot{\mathbf{x}}_j^{\text{d}} + \mathbf{u}_j^{\text{d}}$ with $\mathbf{u}_j^{\text{d}} = [t_j, r_j]^{\text{T}}$ and $\mathbf{x}_j^{\text{d}} = [0, r]^{\text{T}}$ and $\mathbf{v}_j^{\text{b}} = \dot{\mathbf{x}}_j^{\text{b}} + \mathbf{u}_j^{\text{b}}$ with $\mathbf{u}_j^{\text{b}} = [q_j, r_j]^{\text{T}}$ and $\mathbf{x}_j^{\text{b}} = [0, r + l^{\text{b}}]^{\text{T}}$.

Using the Newton's second law separately on the disc and blade masses of the j^{th} sector gives:

$$m^{\text{d}} \ddot{\mathbf{y}}_j^{\text{d}} = \mathbf{f}_j^{\text{d}} + \mathbf{f}_j^{\text{ext,d}}, \quad (\text{II.33})$$

$$m^{\text{b}} \ddot{\mathbf{y}}_j^{\text{b}} = \mathbf{f}_j^{\text{b}} + \mathbf{f}_j^{\text{ext,b}}, \quad (\text{II.34})$$

with $\mathbf{f}_j^{\text{d}} = [f_{t_j}^{\text{nl}} + f_{t_j}^{k_j^t} + f_{t_j}^{k_j^b}, f_{r_j}^{\text{nl}}]^{\text{T}}$ and $\mathbf{f}_j^{\text{b}} = [f_{q_j}^{k_j^b}, 0]^{\text{T}}$. The external forces $\mathbf{f}_j^{\text{ext}}$ applied on the j^{th} sector will be considered rotating for the same reasons as mentioned in Section I.3.4 and its expression will be as developed in Eq. (I.98). For each sector only the dof related to the bending of the blade q_j is excited with an amplitude $f_a = 0.5 \text{ N}$.

Moreover, by calculating the acceleration vector in the fixed frame and knowing that the rotating velocity is constant

$$\ddot{\mathbf{y}}_i^{\text{d}} = \ddot{\mathbf{u}}_i^{\text{d}} + 2\boldsymbol{\Omega}\dot{\mathbf{u}}_i^{\text{d}} + \boldsymbol{\Omega}^2\mathbf{u}_i^{\text{d}} + \boldsymbol{\Omega}^2\mathbf{x}_i^{\text{d}}, \quad (\text{II.35})$$

$$\ddot{\mathbf{y}}_i^{\text{b}} = \ddot{\mathbf{u}}_i^{\text{b}} + 2\boldsymbol{\Omega}\dot{\mathbf{u}}_i^{\text{b}} + \boldsymbol{\Omega}^2\mathbf{u}_i^{\text{b}} + \boldsymbol{\Omega}^2\mathbf{x}_i^{\text{b}}, \quad (\text{II.36})$$

where

$$\boldsymbol{\Omega} = \begin{bmatrix} 0 & -\omega \\ \omega & 0 \end{bmatrix}. \quad (\text{II.37})$$

This gives the equations of motion of the j^{th} sector

$$\mathbf{M}_0 \ddot{\mathbf{u}}_j + \mathbf{G}_0 \dot{\mathbf{u}}_j + (\mathbf{N}_0 + \mathbf{K}_0) \mathbf{u}_j + \mathbf{f}_j^{\text{nl}}(\mathbf{u}_{j-1}, \mathbf{u}_j, \mathbf{u}_{j+1}) = \mathbf{r}_0 + \mathbf{f}_j^{\text{ext}}, \quad (\text{II.38})$$

with

$$\mathbf{M}_0 = \begin{bmatrix} m^b & 0 & 0 \\ 0 & m^d & 0 \\ 0 & 0 & m^d + m^b \end{bmatrix}, \quad (\text{II.39})$$

$$\mathbf{G}_0 = \begin{bmatrix} 0 & 0 & -2m^b\omega \\ 0 & 0 & -2m^d\omega \\ 2m^b\omega & 2m^d\omega & 0 \end{bmatrix}, \quad (\text{II.40})$$

$$\mathbf{N}_0 = \begin{bmatrix} -m^b\omega^2 & 0 & 0 \\ 0 & -m^d\omega^2 & 0 \\ 0 & 0 & -(m^d + m^b)\omega^2 \end{bmatrix}, \quad (\text{II.41})$$

$$\mathbf{K}_0 = \begin{bmatrix} k^b & -k^b & 0 \\ -k^b & k^t & 0 \\ 0 & 0 & 0 \end{bmatrix}, \quad (\text{II.42})$$

$$\mathbf{f}_j^{\text{nl}} = \begin{bmatrix} 0 \\ f_{t_j}^{\text{nl}} \\ f_{r_j}^{\text{nl}} \end{bmatrix}, \quad (\text{II.43})$$

$$\mathbf{r}_0 = \begin{bmatrix} 0 \\ 0 \\ 2((m^b + m^d)r + m^b l^b)\omega^2 \end{bmatrix}, \quad (\text{II.44})$$

$$\mathbf{u}_j = \begin{bmatrix} q_j \\ t_j \\ r_j \end{bmatrix}. \quad (\text{II.45})$$

It is now possible to determine the global equation of motion of the system

$$\mathbf{M}\ddot{\mathbf{u}} + (\mathbf{G} + \mathbf{C})\dot{\mathbf{u}} + (\mathbf{N} + \mathbf{K})\mathbf{u} + \mathbf{f}^{\text{nl}}(\mathbf{u}) = \mathbf{r} + \mathbf{f}^{\text{ext}}, \quad (\text{II.46})$$

with the matrices \mathbf{M} , \mathbf{G} , \mathbf{N} and \mathbf{K} constructed with the same general shape \mathbf{A} such as $\mathbf{A} = (\mathbf{I}_N) \otimes \mathbf{A}_0$ where \mathbf{A}_0 is the matrix for one sector.

The damping matrix \mathbf{C} is introduced in the dynamic equation of motion. As developed in Section I.3.4, the damping can be expressed as a Rayleigh damping with the mass \mathbf{M} and stiffness \mathbf{K} matrices:

$$\mathbf{C} = \alpha\mathbf{M} + \beta\mathbf{K}. \quad (\text{II.47})$$

Where the coefficients α and β are calculated using a damping ratio $\xi = 5e^{-4}$ and the first natural frequency of the tuned model $\omega_0 = 791.24$ Hz.

$$\alpha = 2\pi\xi\omega_0, \quad (\text{II.48})$$

$$\beta = \frac{\xi}{2\pi\omega_0}. \quad (\text{II.49})$$

2.4 Nonlinear approximation

The equation of motion defined in Eq. (II.46) is close to the equation of motion defined in Eq. (I.21) of Section I.2.2 except for the nonlinear terms which have complex expressions as can be seen from Eq. (II.22) to Eq. (II.27). To further simplify the geometrical nonlinearity terms, a Taylor development is carried out around a static position \mathbf{u}_0 for the vector of the nonlinear expressions \mathbf{f}^{nl} . The development is truncated at the first order because it is sufficient

to obtain a converged linear response. The nonlinearities are not taken into account in the dynamic equation because the vibrational levels studied later are not high enough to activate them and higher levels would not be realistic. In addition, nonlinear modal analysis on a similar structure was studied in [193] and showed very little influence on the observed interactions between the Coriolis and mistuning effects. The tools used to solve the nonlinear dynamic equation in this article are presented in Appendix A.

To specify the static position, the displacement \mathbf{u} is expanded as a static part \mathbf{u}_0 and a dynamic part \mathbf{q} such that $\mathbf{u} = \mathbf{u}_0 + \mathbf{q}$. Then, as mentioned above, a first-order Taylor development is carried out for the vector of the nonlinear expressions \mathbf{f}^{nl}

$$\mathbf{f}^{\text{nl}}(\mathbf{u}) = \mathbf{f}^{\text{nl}}(\mathbf{u}_0) + \mathbf{K}^{\text{t}}(\mathbf{u}_0)\mathbf{q}, \quad (\text{II.50})$$

where

$$\mathbf{K}^{\text{t}}(\mathbf{u}_0) = \frac{\partial \mathbf{f}^{\text{nl}}}{\partial \mathbf{u}}(\mathbf{u}_0). \quad (\text{II.51})$$

Finally, Eq. (II.46) can be expressed as a static and a dynamic equation:

$$\begin{cases} (\mathbf{N} + \mathbf{K})\mathbf{u}_0 + \mathbf{f}^{\text{nl}}(\mathbf{u}_0) = \mathbf{r} \\ \mathbf{M}\ddot{\mathbf{q}} + (\mathbf{G} + \mathbf{C})\dot{\mathbf{q}} + (\mathbf{N} + \mathbf{K} + \mathbf{K}^{\text{t}}(\mathbf{u}_0))\mathbf{q} = \mathbf{f}^{\text{ext}}. \end{cases} \quad (\text{II.52})$$

The static nonlinear equation permits the determination of the static position \mathbf{u}_0 due to the centrifugal force \mathbf{r} and to calculate the stiffening matrix \mathbf{K}^{t} of the dynamic equation which gives the dynamic behaviour of the system \mathbf{q} around its static position. For the simplicity of the future development, the global stiffness matrix is defined as $\mathbf{K}^{\text{g}} = \mathbf{N} + \mathbf{K} + \mathbf{K}^{\text{t}}(\mathbf{u}_0)$.

2.5 Mistuning introduction

As mentioned in Section I.4.2, mistuning can be random or intentional and can occur in different ways, but in the present chapter and the next one, it will be introduced as blade stiffness variations, which is one of the most classical ways of introducing mistuning [18, 119, 150, 214, 222].

$$k_j = k_o(1 + \delta_j), \quad (\text{II.53})$$

where k_j corresponds to the stiffness of the mistuned spring of the j^{th} sector, δ_j the perturbation stiffness and k_o the stiffness of the tuned spring. The perturbations due to inherent mistuning of structures will be considered here using a normal distribution function with zero mean and $\pm 1\%$ standard deviation of the stiffness of each spring. This mistuning pattern, represented in Fig. II.2, will be the same for all numerical simulations in this chapter.

3 Modal analyses

This section concerns a modal analysis of the lumped parameter model so there is no external forces applied on the masses and the Rayleigh damping is not considered, which simplifies Eq. (II.52) as follows:

$$\begin{cases} (\mathbf{N} + \mathbf{K})\mathbf{u}_0 + \mathbf{f}^{\text{nl}}(\mathbf{u}_0) = \mathbf{r} \\ \mathbf{M}\ddot{\mathbf{q}} + \mathbf{G}\dot{\mathbf{q}} + \mathbf{K}^{\text{g}}\mathbf{q} = \mathbf{0}. \end{cases} \quad (\text{II.54})$$

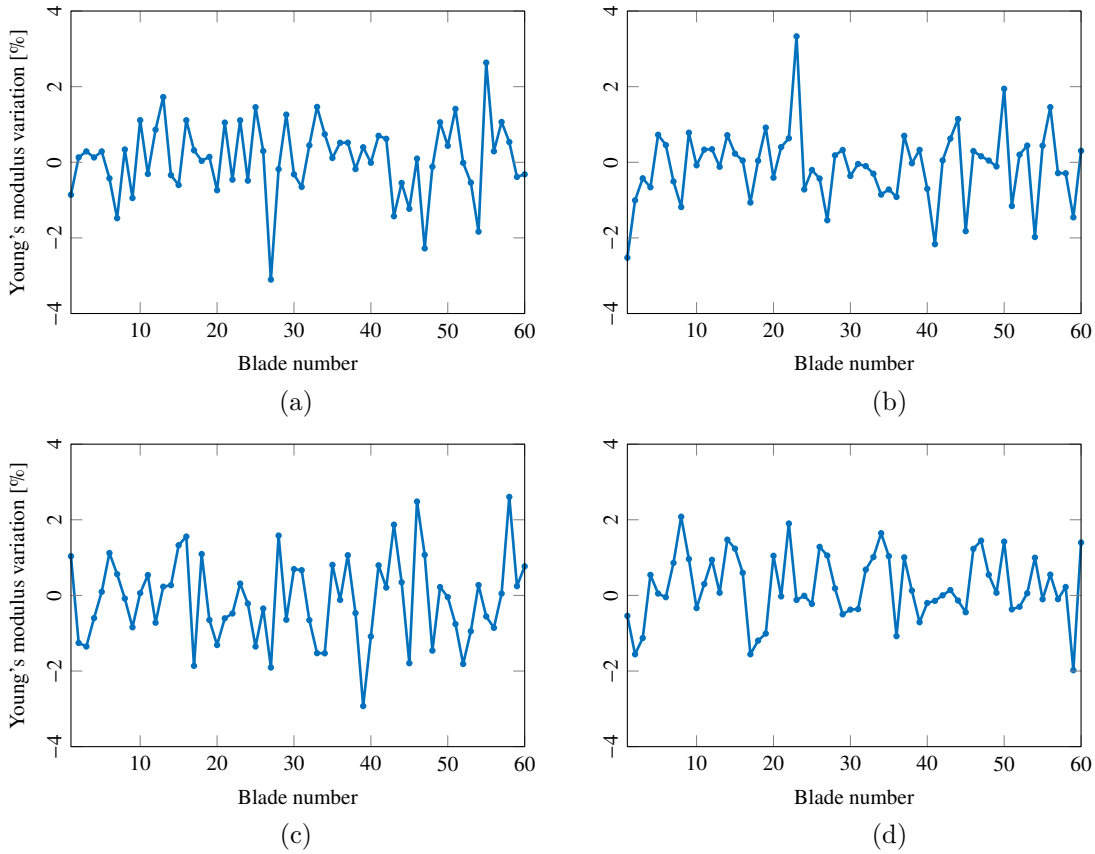


Figure II.2 – Mistuning pattern using a normal distribution function with zero mean and $\pm 1\%$ standard deviation for each spring. (a) Blade spring k^b . (b) Radial spring k^r . (c) Coupling spring k^c . (d) Tangential spring k^t .

3.1 Modal analysis of the tuned bladed disc

Before looking at the interaction between the Coriolis effect and mistuning, this subsection focuses only on the evolution of the linear modes of the tuned case in order to determine which modes will be of interest for further studies in the mistuned case. The system in Eq. (II.54) is solved without taking the mistuning into account. The static equation is nonlinear but it can be easily solved using the trust-region dogleg algorithm [136, 154] for a given rotational speed, after which it is possible to estimate the mistuned stiffness matrix \mathbf{K} . The eigenvalues and eigenvectors of the dynamic equation can be found using the state-space method set out in Section I.3.1.

Although the eigenvalues of the system are between 789 Hz and 147 kHz for $\Omega = 5,000$ rpm, the study will be focused between 750 Hz and 1,400 Hz because all the interesting phenomenologies are in this range. The frequencies of these modes are represented in Fig. II.3 versus their number of nodal diameters. There is the presence of two families represented by two different colours. The frequencies of the third modal family are not shown because they are well above 3,000 Hz. The disc modes are represented by slanted lines and the blade bending modes by the horizontal line around 1,050 Hz. There is also the presence of a veering region at the crossings of the first two families marked by a red rectangle. In this way, the modes above 1,400 Hz are disc modes and there is no interest in studying them because they present neither a very pronounced Coriolis effect –with a significant frequency split between FW and BW modes– nor a mistuning sensitivity as it will be shown later in this chapter.

The backward travelling wave (BW) modes are represented by dashed lines while the forward travelling wave (FW) modes are represented by solid lines. The split observed at some nodal diameters between the FW and BW modes is due to the Coriolis effect.

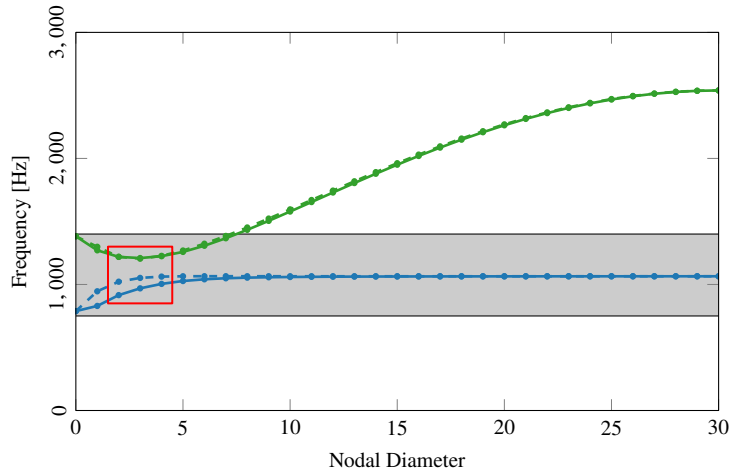


Figure II.3 – Natural frequencies versus number of nodal diameter at 5,000 rpm. All different modal families are represented with different colours. [—]: Forward wave modes. [--]: Backward wave modes. [□]: Veering regions. [■]: Studied region for the numerical simulations.

Thereafter and to simplify the description of the tuned modes, they will be defined by their number X of nodal diameters (ND) followed by the direction of the rotating wave FW or BW. In addition, as each modal family has the same nodal diameters, the Y family membership will be placed at the end. For example, the mode of the first modal family with 2 nodal diameters and a forward travelling wave will be defined as 2ND-FW 1.

The evolution of these modes as a function of the rotational speed is represented by the Campbell diagram in Fig. II.4. The high density of modes in this region makes it very difficult to clearly recognise all the modes but it is still possible to identify 3 regions with different behaviour.

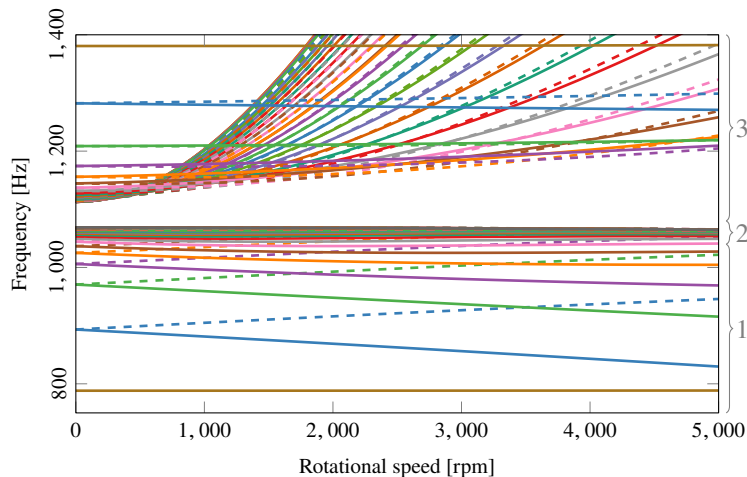


Figure II.4 – Campbell diagram of the tuned bladed disc between 750 Hz and 1,400 Hz. [—]: Forward wave modes. [--]: Backward wave modes.

The first region, tagged '1' in Fig. II.4 corresponds to the modes below 1,040 Hz. These modes have few nodal diameters (all less than 6ND) and a participation of both the blades

and the disc. An example of the modal shape encountered in this area is given in Fig. II.5a, which corresponds to the 2ND-FW 1 at 5,000 rpm. The nodal diameters can be identified by the zero displacement of the blue coloured blades. The green ones correspond to a positive q_j displacement and the red ones to a negative displacement. The deformation of the disc can be observed by comparing it with the undeformed shape represented by a grey circle. The participation of both the blades and the disc creates a strong Coriolis effect with an important frequency split of the double modes at high speed (Fig. II.4).

The second region is for the modes between 1,040 Hz and 1,070 Hz and are blade modes with small disc participation. This represents all the modes with a number of nodal diameters greater than 6 and which are on the horizontal line around 1,050 Hz of Fig. II.3. They have little or no disc participation, are very close in frequency, and the Coriolis effect is barely present. Figure II.5b shows an example of the modes in this region with the shape 10ND-BW 1.

Finally, the third region represents the modes above 1,070 Hz which are disc-dominated as it can be observed in Fig. II.5c with the modal shape 3ND-BW 2 of the second modal family. Most of these modes have a high sensitivity to the centrifugal effect as can be observed in Fig. II.4 with a fast frequency increase of the modes with respect to the rotational speed.

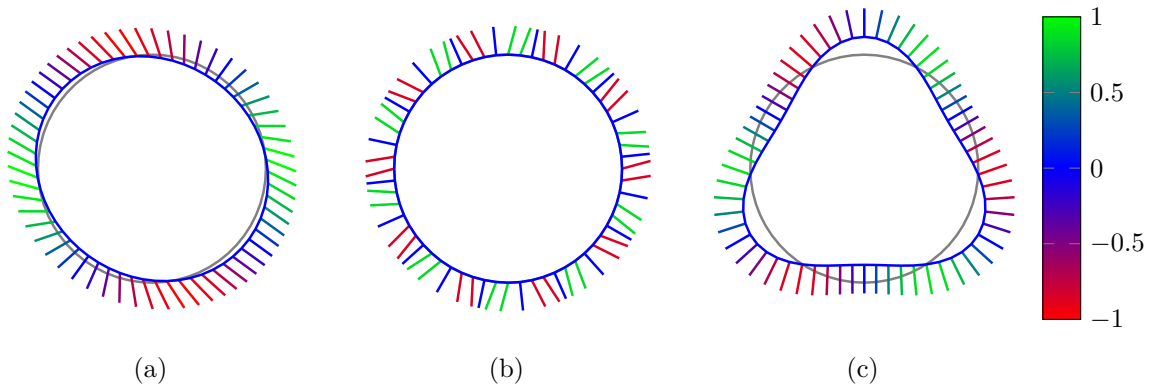


Figure II.5 – Modal shape of three modes in each different regions. (a) First region: 2ND-FW 1. (b) Second region: 10ND-BW 1. (c) Third region: 3ND-BW 2

For the rest of the modal analysis, the study will focus on the modes given as examples from the first and second region. The third region is not retained because the modes of interest for the study are those with blades participation and blade-disc participation but the modes with only disc participation do not provide any additional phenomenology of interest. To the 2ND-FW 1 and 10ND-BW 1 modes will be added the 1ND-FW 1 mode of the first modal family represented by the line [—] around 900 Hz on Fig. II.4. This mode located in the first region does not cross any other mode with the evolution of the rotational speed and becomes strongly frequency isolated. According to the perturbation method developed previously, this mode should not be sensitive to the effect of mistuning.

3.2 Modal analysis of the mistuned bladed disc

The study is now focused on the numerical results of the linear mistuned system in Eq. (II.54). Firstly, the Campbell diagram of the mistuned case is given in Fig. II.6. This diagram is very similar to the one of the tuned case in Fig II.4 as it is still possible to identify the 3 regions defined in the previous section and the frequency values are only modified by 0.2 % on average. As will be shown later, it is mainly the modal shapes that are modified by mistuning.

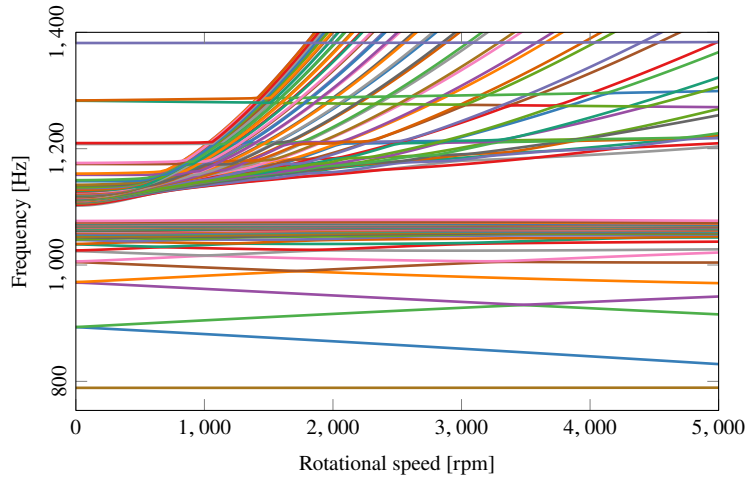


Figure II.6 – Campbell diagram of the mistuned bladed disc between 750 Hz and 1,400 Hz.

On a Campbell diagram of a tuned structure, there are many areas where the frequencies of different modes intersect. In a mistuned structure, the crossings no longer appear and instead there is veering regions, giving the impression that the two branches are pushing each other away — an example is given in Fig. II.7 on a restricted area of the Campbell diagram, the veering areas are circled in red. Crossings between modes can still occur, but they are rarer than veering zones. It is important to distinguish these veering regions from those mentioned above in Fig. II.3. For the present one, the veering region occurs between two modes depending on the rotational speed whereas for the other one the rotational speed is constant and the veering zone occurs between two modal family according to the number of nodal diameters.

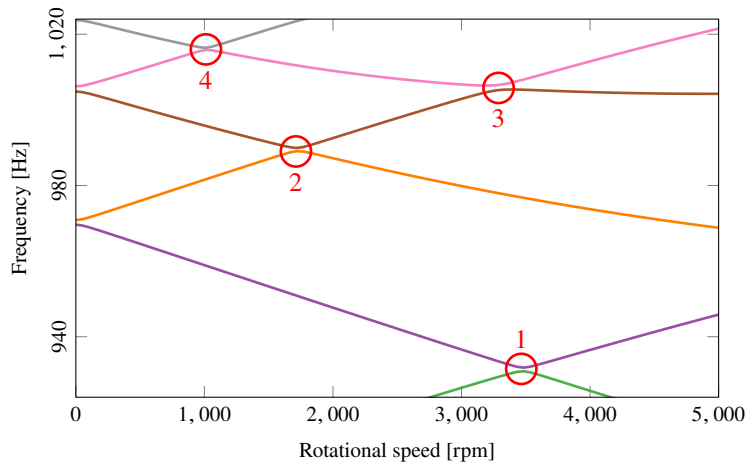


Figure II.7 – Zoom on the Campbell diagram of the mistuned bladed disc between 925 Hz and 1,025 Hz. [○]: Veering regions.

Nodal diameters may no longer appear when mistuning is too strong. For that reason, the general term *modes* is preferred over *nodal diameter modes* in what follows. Moreover, due to the veering regions, it is difficult to follow the target tuned modes identified in the previous section but at rest the 1ND-FW 1, 2ND-FW 1 and 10ND-BW 1 are respectively the 2nd, 4th and 21th modes when sorted by eigenvalues. Therefore, the target modes in the mistuned case will be the 2nd, 4th and 21th modes at rest, referred to as M2, M4 and M21 respectively.

The aim of this section is to look at the evolution of the target modes versus the rotational

speed and more specifically the mistuning effect using two criteria. The first criterion is the average change of amplitude (ACA):

$$\mu = \frac{\sum_{j=1}^N |a_j - a_{\max}| / a_{\max}}{N} \cdot 100, \quad (\text{II.55})$$

where a_j is the bending amplitude of the j^{th} sector and a_{\max} the maximal bending amplitude of the mode. This criterion is used to quantify the phenomenon of localisation since it measures the difference between the amplitude of each sector and the maximum sector amplitude. Thus, an ACA close to 100 % means that only one sector vibrates with a large amplitude compared to the other sector, and an ACA close to 0 % means that all the sectors vibrate at the same amplitude, which is specific to travelling waves or nondegenerate modes. The second criterion is a discrete Fourier transform (DFT).

$$d_l = \frac{1}{N} \sum_{j=1}^N q_j e^{ijl\theta}, \quad (\text{II.56})$$

where $\theta = 2\pi/N$, d_l is the coefficient of the l nodal diameter(s) component. A positive index l corresponds to a FW travelling wave, and a negative l corresponds to a BW travelling wave. q_j is the complex bending amplitude of the j^{th} sector. In the presence of a perfect travelling wave response of l nodal diameters –which is the case of a tuned system– the coefficient d_l is equal to 1, and all the other coefficients different to l are equal to 0. When the mode has a strongly mistuned behaviour, there is the superposition of multiple travelling waves, and quite a few coefficients are different than 0.

Table II.2 presents the ACA for the target modes at different rotational speeds. At rest, the modes are standing waves so the average values are high because each sector vibrates at a different amplitude, but for mode M2 this ACA value decreases with an increasing rotational speed to become lower than 6% at 5,000 RPM. This behaviour is an indication that a travelling wave forms at high speed, which is confirmed by the evolution of the spatial DFT components in Fig. II.8a. At rest, the DFT components of the 1ND-FW and BW components are almost equal, constituting a standing wave, whereas when the speed increases, the 1ND-BW component decreases until it becomes negligible and the 1ND-FW component increases, which means that at high speed a forward travelling wave mode is predominant.

For the M4 mode, a high ACA value appears at 3,500 RPM in Table II.2 and above this speed the values are smaller but never below 9%, which indicates that a travelling wave starts forming at high speed far from the veering area but never fully develops. This veering can be observed as the first veering region in Fig. II.6. Figure II.8b confirms this behaviour: at rest the DFT components of the 2ND-FW and BW are almost equal, then the 2ND-FW component is predominant until the veering area at 3,500 RPM. In this area the 1ND-BW component becomes as significant as the 2ND-FW component, and becoming predominant at higher speeds.

Finally, for the M21 mode, there is no doubt that the effect of mistuning is predominant because the ACA levels are very high in Table II.2 which means that one blade responds more strongly than the others and there is no DFT component greater than 0.1 in Fig. II.8c which means that no rotating wave is present even partially for the M21 mode.

In this section, it was observed that a mode which is completely isolated in frequency from the other modes, such as the M2 mode, tends towards a tuned behaviour with the appearance of a rotating wave and similar vibration amplitudes for all sectors. The veering regions tend to reduce this tuned behaviour with exchanges of shape from one tuned mode to another and the more veering zones there are, the more difficult it is to tend towards a tuned behaviour as

Table II.2 – Average change of amplitude at different rotational speeds for different mistuned linear modes

Ω	0	500	1,000	1,500	2,000	2,500	3,000	3,500	4,000	4,500	5,000
M2	38.96	7.24	7.09	6.92	6.72	6.53	6.35	6.18	6.02	5.89	5.78
M4	44.77	13.66	12.72	11.85	10.92	9.68	11.4	34.88	9.76	9.22	10.35
M21	75.5	75.05	77.4	74.55	78.33	73.62	70.34	79.51	87.78	88.51	85.46

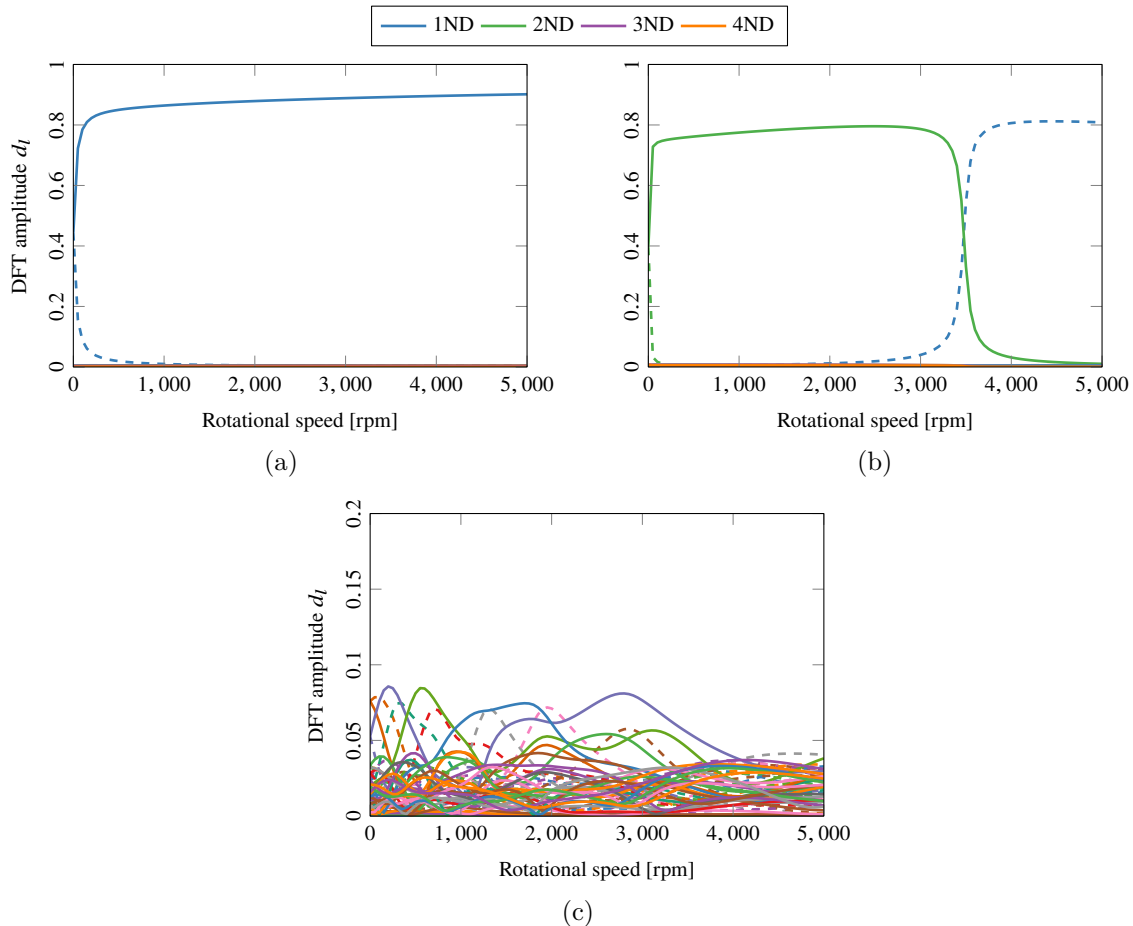


Figure II.8 – Evolution of the DFT components with speed for the modes; (a) M2, (b) M4 and (c) M21. The DFT components represent the participation of the different travelling waves on the dynamic response of the structure. The solid curves represent the forward wave [—] and the dashed curves represent the backward wave [--].

observed with the M4 mode. Finally, when a mode is in a zone of high modal density such as region 2 in Fig. II.4 and the M21 mode, the effect of mistuning is predominant with a very pronounced localisation.

All these observations confirm the conclusions made during the development of the perturbation method in Section II.1: when the mistuning is present on a bladed disc, all the tuned modes which are close in frequency will tend to interact with each other to create the mistuned modes. This is why, the mistuning has an impact on the behaviour of the system only when two modes are close to each other, as otherwise the mistuning is too small to significantly modify the modal shapes. Due to the rotational effects and in particular the Coriolis effect,

some modes can be separated from the others by increasing the rotational speed and thus exhibit a tuned behaviour.

3.3 Perturbation method comparison

The perturbation method was applied at the beginning of this chapter to analytically express the mistuned eigenvectors on the basis of the tuned eigenvectors and conduct a sensitivity analysis of the eigenvectors against mistuning. Now that the linear modal analysis of the lumped parameter model has been performed, the derived analytical expressions will be compared numerically in this section with the target modes M2, M4 and M21 previously defined. The accuracy of the perturbation method is evaluated using the following error measure for the eigenvalues

$$e_r = \frac{|\omega_r - \omega_r^e|}{\omega_r^e}, \quad (\text{II.57})$$

where ω_r is an eigenvalue calculated using the analytical approach and ω_r^e is the same eigenvalue but directly calculated from the numerical system in Eq. (II.54) and will be set as reference.

The eigenvectors will be compared using the Modal Assurance Criterion (MAC) [203].

$$\text{MAC}_r = \frac{|\mathbf{u}_r^H \mathbf{u}_r^e|^2}{|\mathbf{u}_r^H \mathbf{u}_r| |\mathbf{u}_r^e H \mathbf{u}_r^e|}, \quad (\text{II.58})$$

where \mathbf{u}_r is the eigenvector of the analytical approach and \mathbf{u}_r^e the eigenvector of the numerical system. As a reminder, the perturbation method was developed using the state-space representation, thus the modes \mathbf{u}_r and \mathbf{u}_r^e are also in the state-space representation.

The numerical application requires to truncate the power series at an order P in Eq. (II.6), Eq. (II.7) and Eq. (II.8). The order does not need to be very high to give good results far from the frequency crossover zones as it is mainly the tuned mode that responds. Conversely, when approaching the crossover areas there is a discontinuity phenomenon which brings all the tuned modes close in frequency into the mistuned mode and therefore it is important to use a high order P . It was chosen to take $P = 50$ as a compromise between good accuracy of the results and reasonable calculation times of about one hour.

The errors for the eigenvalues is given in Table II.3 and are all under than 0.05 percent, which gives a good prediction of the eigenvalues using the perturbation method. However, some values are not provided in the table because they are close to the crossover of tuned modes and therefore to the discontinuities mentioned above. As a results, it is not possible to obtain these eigenfrequencies with a sufficient accuracy. For mode M4 this corresponds to the crossover between modes 2ND-FW 1 and 1ND-BW 1 at 3,500 rpm and for mode M21, which is in zone 2 of the Campbell diagram Fig. II.4, there are crossovers between a very large number of modes between 0 rpm and 5,000 rpm which does not permit the estimation of this mode's eigenvalue using the perturbation method.

Table II.3 – Accuracy evaluation of the eigenvalues for different rotational speeds using the ACA criterion.

Ω	1,000	1,500	2,000	2,500	3,000	3,500	4,000	4,500	5,000
e_2	< 0.01	< 0.01	< 0.01	< 0.01	< 0.01	< 0.01	< 0.01	< 0.01	< 0.01
e_4	0.01	0.01	0.01	< 0.01	< 0.01	—	< 0.01	0.01	0.01
e_{21}	—	—	—	—	—	—	—	—	—

The evaluation of the MAC is given in Table II.4 and gives the same conclusions for the

evaluation of the errors for the eigenvalues. The MAC values are never lower than 0.99 except near the crossing zones which is at 3,500 rpm for the M4 mode and over the whole rotational speed range for the M21 mode.

Table II.4 – Accuracy evaluation of the eigenvectors for different rotational speeds using the MAC criterion.

Ω	1,000	1,500	2,000	2,500	3,000	3,500	4,000	4,500	5,000
MAC ₂	> 0.99	> 0.99	> 0.99	> 0.99	> 0.99	> 0.99	> 0.99	> 0.99	> 0.99
MAC ₄	> 0.99	> 0.99	> 0.99	> 0.99	> 0.99	0.61	> 0.99	> 0.99	> 0.99
MAC ₂₁	0.26	0.09	0.01	0.08	0.01	0.03	0.01	0.04	0.02

However, the modal shapes given near the crossing areas by the perturbation method are not totally inconsistent. Indeed, when looking at the ACA criterion in Table II.5 the values given by the perturbation method are of the same order of magnitude as the one given by the benchmark and reflect a strong localisation. Then, looking at the DFT components in Fig. II.9, the M4 mode has only two main components which are the 1ND-BW and 2ND-FW travelling waves like the benchmark (Fig. II.9a). For the M21 mode, almost all the DFT components respond whether it is with the perturbation method or the benchmark (Fig. II.9b). In all cases, even if the levels are not identical with the benchmark, the perturbation method captures the behaviour of the system reasonably well even close to the crossover areas.

Table II.5 – Comparison of the average change of amplitude between the perturbation method (ACA P. M.) and the benchmark (ACA B.) for the M4 and M21 modes.

Mode	Ω	ACA P. M.	ACA B.
M4	3,500	36.08	34.88
M21	5,000	72.30	85.46

The evaluation of the error for the eigenvalues and of the MAC for the eigenvectors in this section allows the validation of the analytical developments of the perturbation method realised in Section II.1. Even if this method is not directly applicable in the region where frequencies cross tuned modes due to discontinuity issues, it is still possible to capture the mistuned behaviour around these areas with significant localisation and the predominance of multiple travelling waves leading to a standing wave.

4 Frequency response function

This section investigates the frequency response function (FRF) for different kinds of excitation shapes at different rotational velocities. In the same way as for the previous modal analysis, the phenomena resulting from the Coriolis and mistuning effects will be highlighted. The deformed shape around the resonance peaks will be investigated in the linear case to validate the conclusions of the modal analysis on the mode shapes around the eigenfrequency.

The system to be solved is the same as for the modal analysis (Eq. (II.54)) to which is added a damping matrix \mathbf{C} and an excitation force \mathbf{f}^{ext}

$$\begin{cases} (\mathbf{N} + \mathbf{K})\mathbf{u}_0 + \mathbf{f}^{\text{nl}}(\mathbf{u}_0) = \mathbf{r} \\ \mathbf{M}\ddot{\mathbf{q}} + (\mathbf{G} + \mathbf{C})\dot{\mathbf{q}} + \mathbf{K}^g\mathbf{q} = \mathbf{f}^{\text{ext}}. \end{cases} \quad (\text{II.59})$$

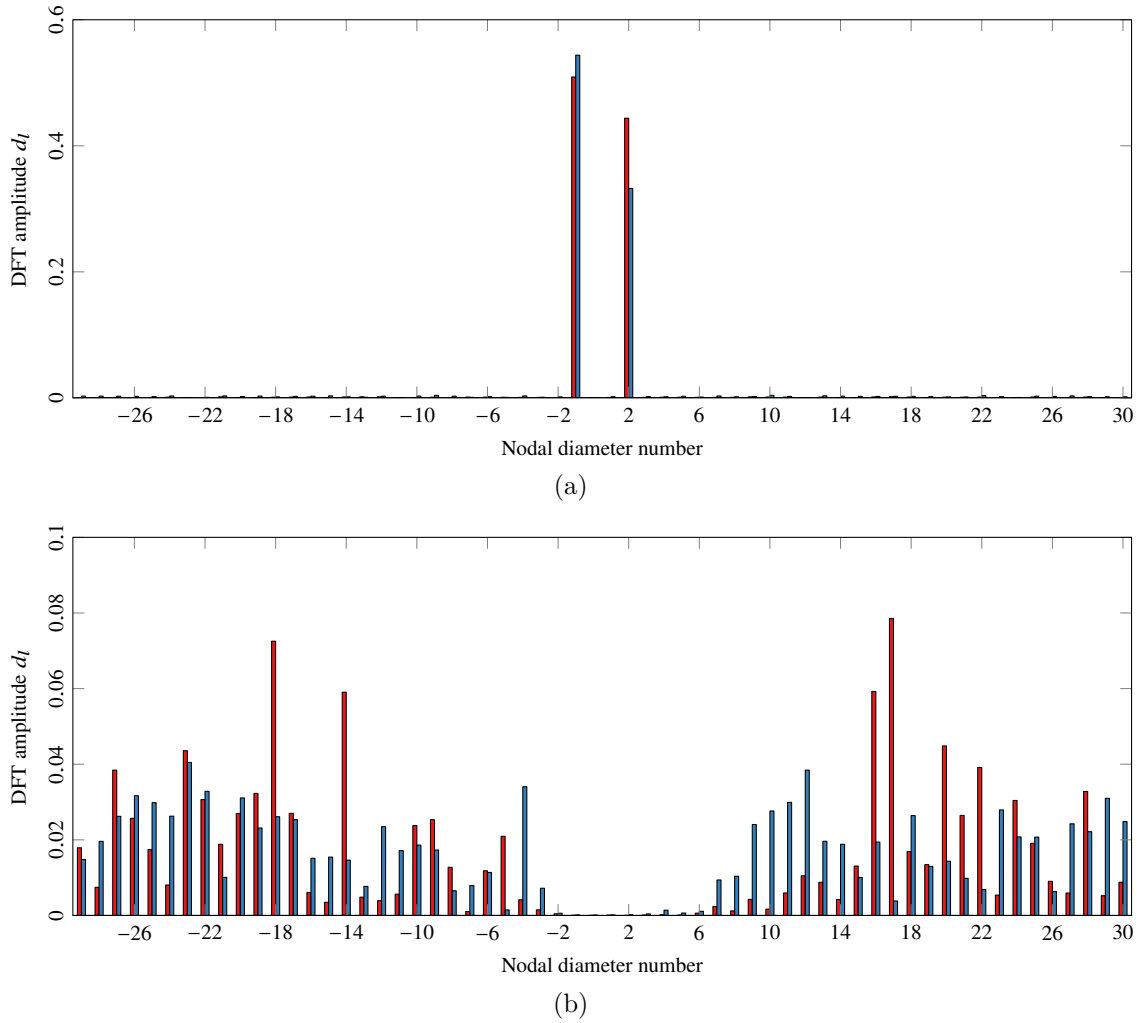


Figure II.9 – Comparison of the DFT components for the modes; (a) M4 at 3,500 rpm and (c) M21 at 5,000 rpm. [■]: Perturbation method. [■]: Benchmark.

4.1 Forced response at rest

The first simulation is focused around the eigenvalue of the M2 mode at rest and the frequency excitation is between 392 Hz and 395 Hz. Because the tuned mode corresponding to the M2 mode has a 1ND-FW travelling wave, the excitation is a 1EO-FW travelling wave. The results are presented in Fig. II.10, in which full blue curve represents a bending dof of the mistuned system. Each curve has a different maximum amplitude and resonant frequency which is characteristic of mistuning. Some curves have two resonance peaks related to the frequency split of the 1ND double mode due to mistuning but this is not present on all curves because the eigenvalues of the two modes are close: the M2 mode has an eigenvalue of 893.15 Hz and the M3 mode of 893.69 Hz. The ACA criterion representing the localisation of the response can be evaluated at the frequency of the maximum amplitude (893.48 Hz). The ACA value is $\mu = 36.72\%$, which is close to the value found during the modal analysis (38.96% in Table II.2) and shows a strong localisation.

The dashed curve in Fig. II.10 represents the tuned system, where each curve is perfectly superimposed with the same amplitude due to the perfect 1ND-FW travelling wave response. The maximal amplitude of the mistuned case is above the maximal amplitude of the tuned

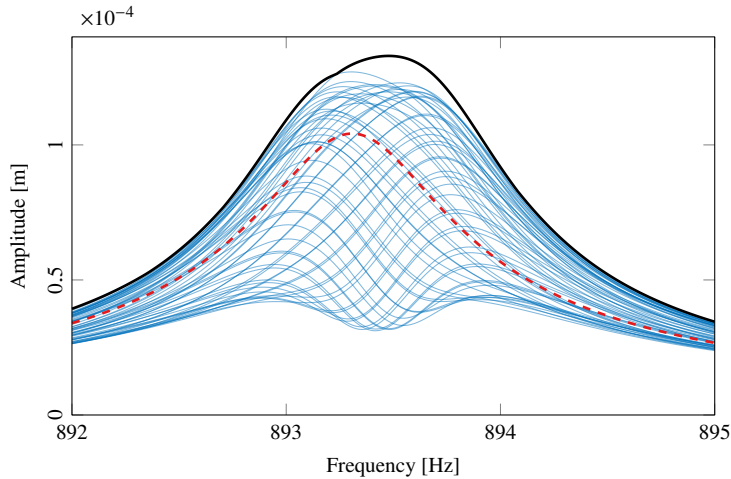


Figure II.10 – FRF around the mode M2 at rest with a 1EO-FW excitation. [—]: FRF of one dof of each sector. [—]: Maximum amplitude response. [- -]: Tuned case.

case, referred to as 'amplitude magnification'. This phenomenon can be quantified using the ratio of the maximum amplitude of the detuned case to that of the tuned one, which is equal to 1.28 in the present case.

Finally, the DFT of this response is shown in Fig. II.11. Away from the resonance peak, the response tends to be of the shape of the excitation with a predominance of the 1ND-FW travelling wave but at the resonance peak there is an increase in the participation of the 1ND-BW component which reinforces the mistuning response of the structure with the formation of a standing wave. This validates what has already been observed in the modal analysis with the presence of these two waves at rest in the M2 mode (Fig. II.8a).

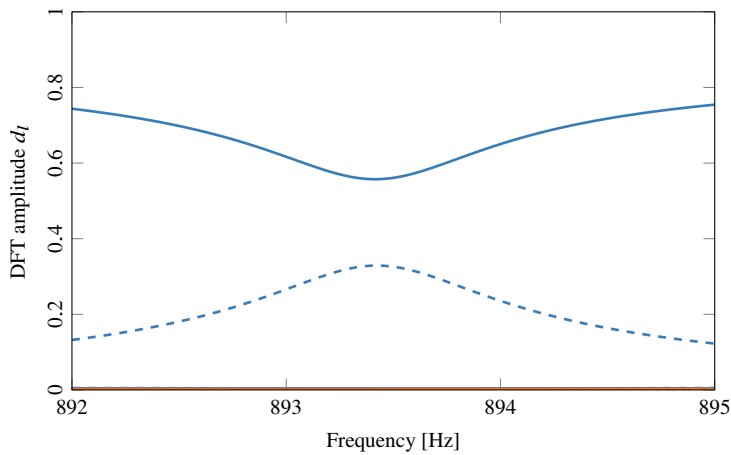


Figure II.11 – DFT around the mode M2 at rest with a 1EO-FW excitation. [—]: 1ND-FW. [- -]: 1ND-BW.

The M4 and M5 modes are associated with the 2ND double mode, and as for the M2 and M3 modes, the frequency split due to mistuning is small and the eigenvalues of the other modes are far apart. For this reason, the behaviour at rest of the M4 mode with a 2EO-FW excitation is very similar to Fig. II.10 and will not be shown here.

The second simulation is focused on the eigenvalue of the mode M21 at rest and the frequency excitation is between 1,030 Hz and 1,080 Hz. The frequency range is larger than for

the first simulation because this mode is in the high modal density region where many modes respond. The tuned mode corresponding to the M21 mode has a 10ND-BW travelling wave so the excitation is a 10EO-BW travelling wave. The results are presented in Fig. II.12.

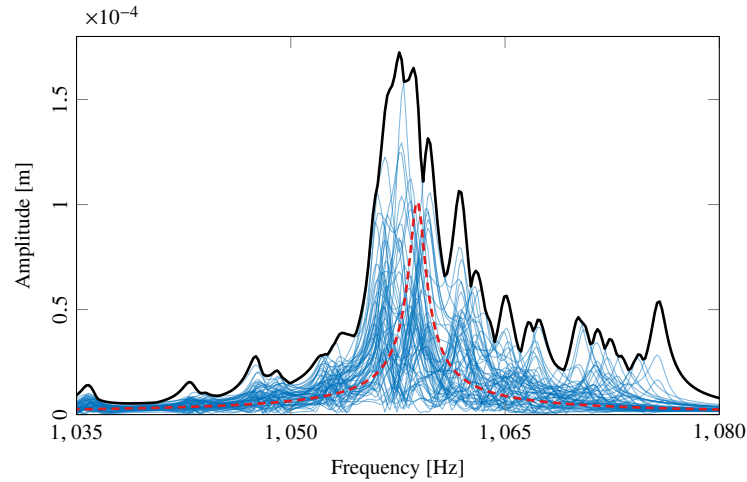


Figure II.12 – FRF around the mode M21 at rest with a 10EO-BW excitation. [—]: FRF of one dof of each sector. [—]: Maximum amplitude response. [--]: Tuned case.

The FRF of the tuned case presents only one peak at the resonance of the 10ND-BW mode but the mistuned one presents multiple peaks corresponding to all the mistuned modes present in this area with amplitudes that are more or less significant depending on the sectors. The ACA criterion at the maximum amplitude is $\mu = 75.65\%$ which represents once again the phenomenon of localisation related to the mistuning. In addition, as in the first simulation, there is a phenomenon of amplitude magnification with a ratio of 1.71.

The DFT of this response has been represented in Fig. II.13, and as for the first simulation, the predominant wave far from the resonance peaks is the same as the excitation. However, in the high modal density regions, there is no longer a predominant DFT component and all waves are present. This reinforces the observation made in Fig. II.8c, that in a high modal density region, no rotating waves are predominant.

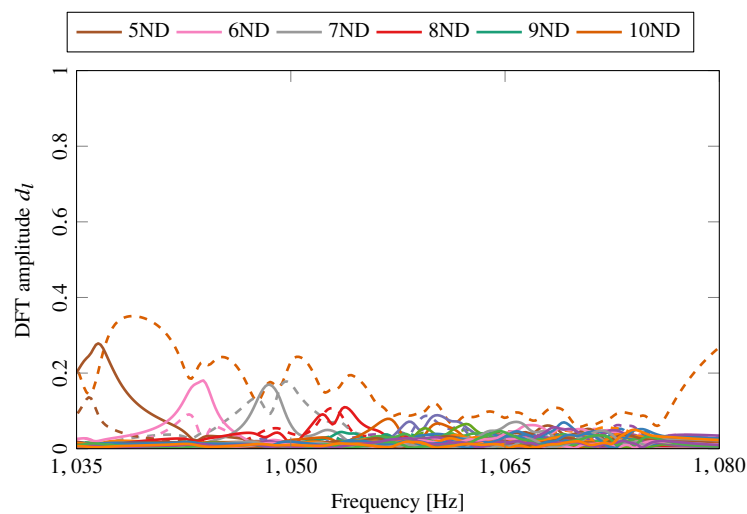


Figure II.13 – DFT around the mode M21 at rest with a 10EO-BW excitation. [—]: Forward wave. [--]: Backward wave.

This section has shown that the target modes have strong mistuning phenomena at rest with response amplification, localisation and the presence of standing waves due to the superposition of multiple rotating waves. This phenomenon is even more pronounced when there is the presence of many modes in a restricted frequency range as it is the case for the M21 mode.

4.2 Forced response at high rotational velocity

The simulations carried out in this section are the same as those carried out previously but at a rotational speed of 5,000 rpm. For the mode M2 at 5,000 rpm, the frequency excitation has changed compared to at rest due to the rotational effects: it is now between 829.5 Hz and 831 Hz. The results are presented in Fig. II.14 and are similar to the tuned case with each dof vibrating at very close amplitudes giving an ACA criterion of $\mu = 5.78\%$ against $\mu = 36.72\%$ at rest, which means that there is no longer a localisation phenomenon. The maximal amplitude is also close to the maximal amplitude of the tuned case with an amplification factor of 1.06 against 1.28 at rest. Finally, the response shape at the resonance is a predominant 1ND-FW travelling wave as shown with the spatial DFT in Fig. II.15 which is the same as the one observed with the modal analysis at high speed in Fig II.8a and confirms that the behaviour of the mistuned structure around the M2 mode eigenvalue at high speed is close to that of the tuned case.

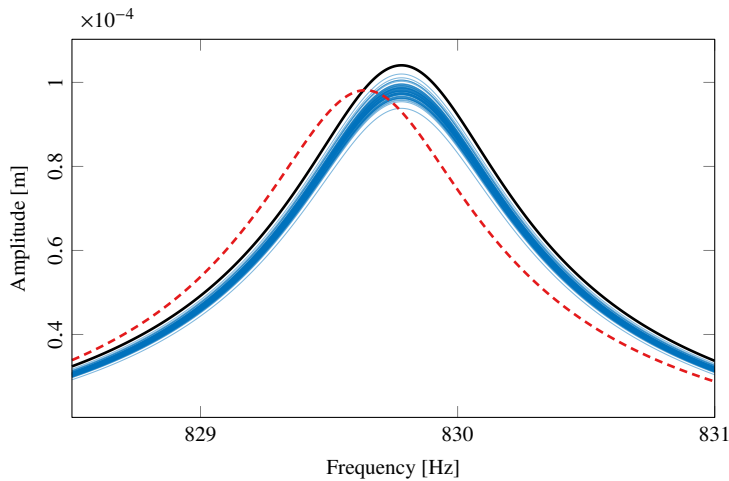


Figure II.14 – FRF around the mode M2 at 5,000 rpm with a 1EO-FW excitation. [—]: FRF of one dof of each sector. [—]: Maximum amplitude response. [--]: Tuned case.

The forced response around the eigenvalue of the M21 mode at 5,000 rpm and a 10ND-BW excitation is presented in Fig. II.16. For this simulation, even if the maximum amplitude response curve is different from the one at rest in Fig. II.12, the vibratory behaviour of the structure remains similar with predominant mistuning effects. The localisation is still very strong with an ACA of $\mu = 72.50\%$ against $\mu = 75.65\%$ at rest. The amplification factor has decreased from 1.71 at rest to 1.28 at 5,000 rpm but the maximum amplitude of the mistuned case is still much larger than that of the tuned case. As for the DFT components in Fig. II.17, the behaviour has not changed, with a slight predominance of the 10ND-BW excitation wave outside the resonance areas but inside it remains a superposition of all the rotating waves that gives a stationary appearance to the response.

For the M4 mode with 2ND-FW excitation, the evolution is more varied than for the M2 and M21 modes. The M4 mode, like the M2 mode, becomes frequency isolated with increasing rotational speed and tends towards the tuned behaviour up to 2,500 rpm as can be

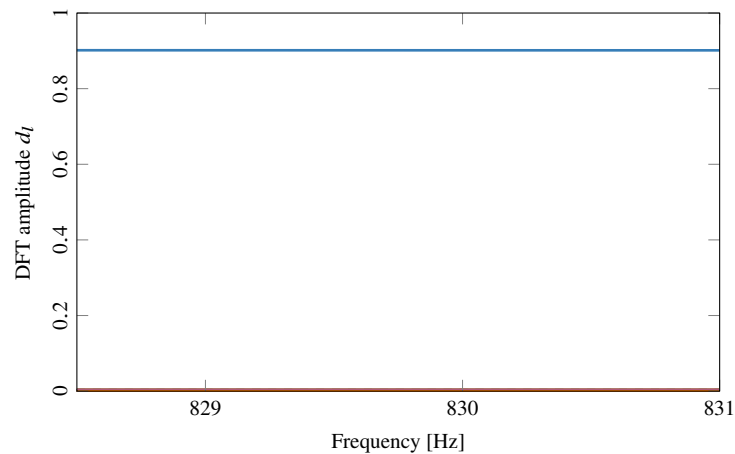


Figure II.15 – DFT around the mode M2 at 5,000 rpm with a 1EO-FW excitation. [—]: 1ND-FW.

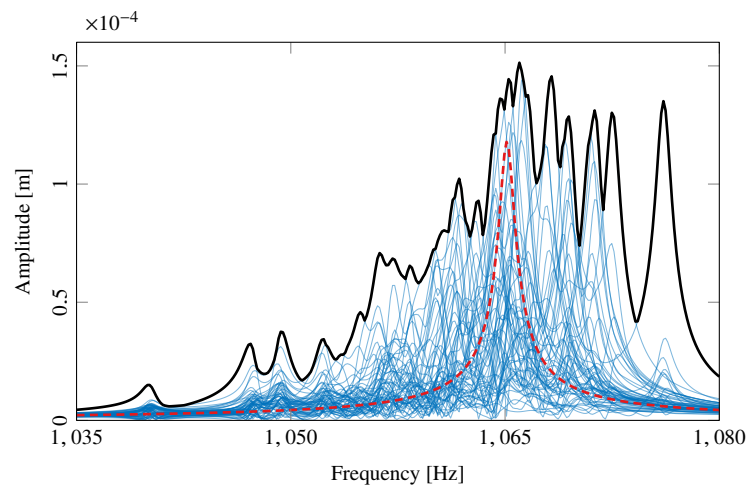


Figure II.16 – FRF around the mode M21 at 5,000 rpm with a 10EO-BW excitation. [—]: FRF of one dof of each sector. [—]: Maximum amplitude response. [--]: Tuned case.

observed on the forced response in Fig. II.18a. However, at 3,500 rpm, the mode is in a veering zone and the mistuning is more predominant as shown in Fig. II.18b. The localisation and amplitude magnification increase from $\mu = 9.72\%$ and 1.10 at 2,500 rpm to $\mu = 40.21\%$ and 1.38 at 3,500 rpm, respectively. Finally, at 2,500 rpm, the predominant DFT component is the 2ND-FW over the whole FRF (Fig. II.19a) whereas in the resonance zone at 3,500 rpm, the predominance of the 2ND-FW component decreases and that of the 1ND-BW increases to give a standing wave in this area (Fig. II.19b).

This section shows that for the area close to the M2 mode which, thanks to the Coriolis effect, is frequency isolated, the forced response of the mistuned case is similar to that of the tuned one. On the other hand, for the M21 mode, which remains in the zone of high modal density, rotational speed increasing does not bring any significant evolution to the forced response and the effect of the mistuning remains predominant. Finally, for modes such as M4, the behaviour is close to that of the tuned case when the mode is frequency isolated but in the veering areas, the mistuning effects are predominate.

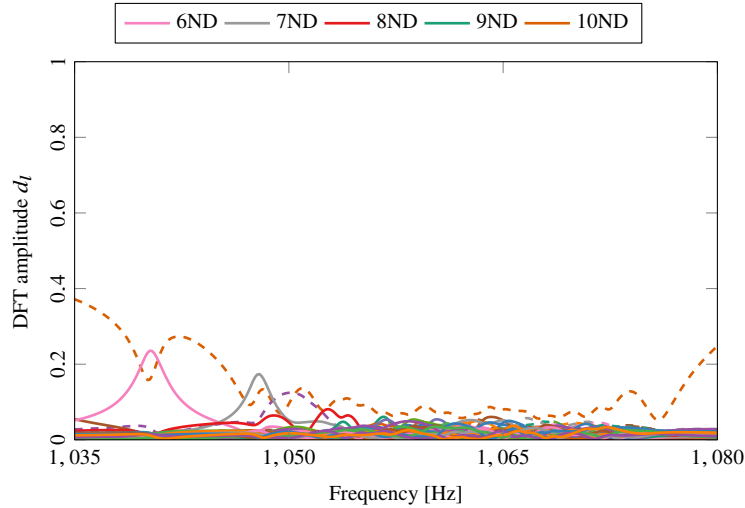


Figure II.17 – DFT around the mode M21 at 5,000 rpm with a 10EO-BW excitation. [—]: Forward wave. [--]: Backward wave.

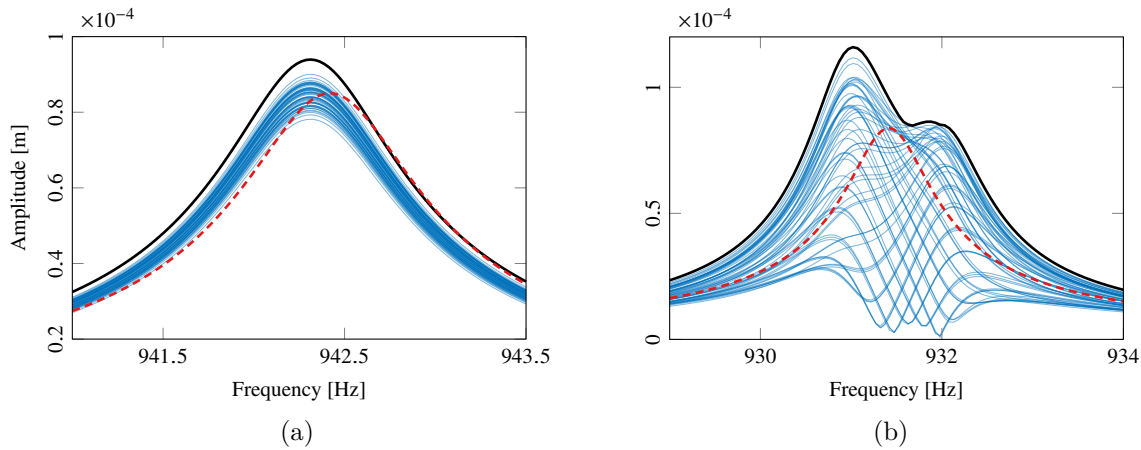


Figure II.18 – FRF around the mode M4 at (a) 2,500 rpm and (b) 3,500 rpm with a 2EO-FW excitation. [—]: FRF of one dof of each sector. [—]: Maximum amplitude response. [--]: Tuned case.

Chapter summary

In this chapter, the interaction between the Coriolis and mistuning effects in cyclic symmetric structures was investigated with an analytical perturbation method. This method allowed expressing the eigenvalues and eigenvectors of the mistuned system with the eigenvalues and eigenvectors of the tuned system. The difficulty of predicting the eigenvectors around the areas where two modes have the same eigenvalue was highlighted and an explanation of the standing wave modes present in the frequency veering zones was given by the proposed analytical approach. Moreover, in a cyclic symmetric structure, the standing wave double modes are split into two travelling wave modes due to the Coriolis effect, so if the mode is sufficiently frequency isolated, its interaction with the other modes becomes weaker and the blade behaviour should be close to the tuned case.

This phenomenon was then modelled using a numerical approach on a lumped parameter model representative of a bladed disc, by first performing a modal analysis and then a forced response around three target modes. For the isolated mode, a standing wave mode was observed

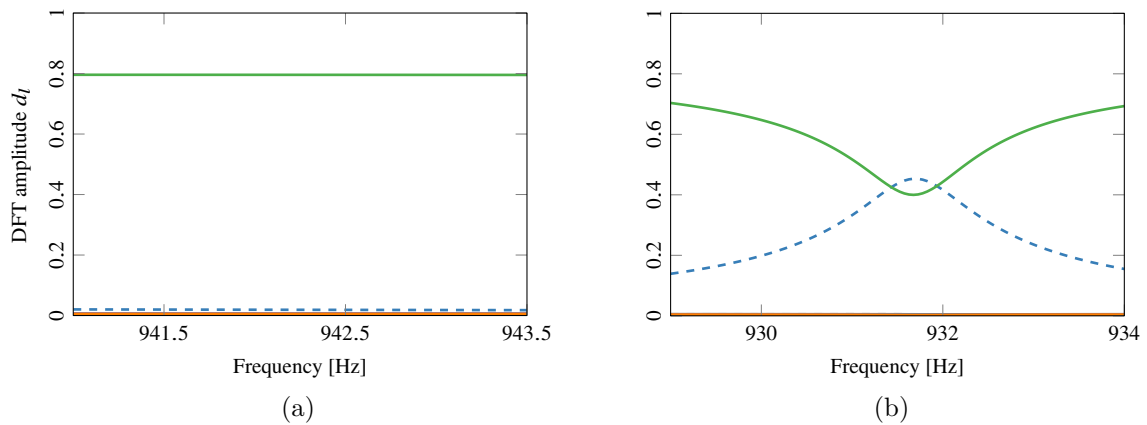


Figure II.19 – DFT around the mode M4 at (a) 2,500 rpm and (b) 3,500 rpm with a 2EO-FW excitation. [—]: 2ND-FW. [--]: 1ND-BW.

at rest before becoming a full travelling wave mode at high speeds. For the mode in a veering area, the two tuned mode shapes coexisted and a considerable change of amplitude occurred between each sector, interpreted as a localisation phenomenon due to a standing wave. Finally, for the mode in the high modal density region, the mistuned behaviour predominates with significant localisation and response amplification over the entire rotational speed range.

Chapter III

Flutter stability study of a cyclic symmetric system

In this chapter, aerodynamic loads are introduced to the lumped mass-spring model of Chapter II using Whitehead’s theory for a cascade of blades in an incompressible flow [216]. This allows to set up a simple model of the bladed disc which can be used for extensive parametric studies. Firstly, the equations to calculate the aerodynamic forces are developed. Then, a study will be performed on the aeroelastic stability of the tuned model without the Coriolis effect to then propose a method to stabilise the model through detuning and two different optimisation strategies to find the best detuning pattern. Finally, the results are discussed with a particular focus on the influence of the Coriolis effect on the aeroelastic stability of the system.

Outline of the chapter

1 Aerodynamics forces	69
1.1 Expressions of the chordwise flow velocities	70
1.2 Calculation of the blade force	71
1.3 Matrix form of the aerodynamic coefficient C_f	73
1.4 Expression of aerodynamic force on the cyclic symmetric structure	74
1.5 Aerodynamic damping solution	75
2 Flutter instability and intentional mistuning optimisation	76
2.1 Aeroelastic stability of the tuned model	76
2.2 Subspace Optimisation Strategy	78
2.3 The genetic algorithm	79
2.4 Selection of detuning patterns without Coriolis effect	83
3 Coriolis influences on flutter stability	83
3.1 Detuned model with the Coriolis effect	83
3.2 Selection of detuning patterns with Coriolis effect	88
Chapter summary	90

1 Aerodynamics forces

This section introduces the aerodynamic model used for the flutter stability study of the cyclic symmetric system used in Section II.2. The aerodynamic loads were established using

the Whitehead model for the analysis of the bending flutter of unstalled cascade blades [216]. This approach is an extension of Theodorsen's theory derived from study of a two-dimensional fluid [197] enabling cascade effects to be taken into account as well as the deflection of steady flow, which was not presented in [215]. The assumptions of this model are the following:

- Only translational motions perpendicular to the chord line are considered;
- The fluid is incompressible and inviscid;
- No blade stall, the flow always follows the blade surface;
- The blades are assumed to be flat plates (no blade camber or thickness);
- The amplitude of vibration is assumed to be small, in accordance with linear theory;
- Cyclic symmetric structure (no mistuning or detuning);
- The wakes are assumed to lie in straight lines, in line with the blades.

Moreover, due to the time periodicity of the solution and the linearity of the dynamic equations the response at the j^{th} blade can be expressed as:

$$q_j = p_j e^{i\omega t} + \text{c.c.}, \quad (\text{III.1})$$

where p_j is the complex amplitude, ω the frequency and c.c. corresponds to the complex conjugate.

1.1 Expressions of the chordwise flow velocities

This part is not intended to be exhaustive on the development of the aerodynamic model as the calculations are rather lengthy but will give a good overview of the method used to obtain the aerodynamic force expression acting on the blades. Only the main expressions will be given in this section, the others can be found in Appendix B. The blades and their wakes are replaced by vortex sheets thanks to the flat plate hypothesis and the vorticities have two components, a steady one ζ , and a fluctuating one γ . Once these components have been found, the force f_j^a on the j^{th} blade can be calculated using the following expression:

$$f_j^a e^{i\omega t} = \int_0^c (p^-(x') - p^+(x')) dx', \quad (\text{III.2})$$

where ω is the frequency of vibration, x' the coordinate on the chord axis and c the chord length. p^- and p^+ are the pressures slightly above and below the blade and it requires to know the velocities (u, v) induced by the vorticities to calculate them.

All parameters of the aerodynamic model are shown in Fig. III.1. The freestream velocity relative to the blades is illustrated by U , and its air inlet angle is considered as α . The stagger angle of the blades is θ . In terms of structural characteristics, the cascade spacing is represented by s . Thereafter, it will be more convenient to use the variable τ to specify the incidence of the steady flow rather than α and θ , its expression is given in Eq. (B.1):

The velocities induced by the vorticity on the other blades at points just above and below the reference blade, denoted (u^+, v^+) and (u^-, v^-) respectively, are expressed as follows:

$$u^+ = U + i\omega p_j u_p e^{i\omega t} + \tau(U u_0 + i\omega p_j u_\tau e^{i\omega t}) - \frac{1}{2}(\zeta + (\gamma + \epsilon)e^{i\omega t}), \quad (\text{III.3})$$

$$u^- = U + i\omega p_j u_p e^{i\omega t} + \tau(U u_0 + i\omega p_j u_\tau e^{i\omega t}) + \frac{1}{2}(\zeta + (\gamma + \epsilon)e^{i\omega t}), \quad (\text{III.4})$$

$$v^+ = v^- = i\omega p_j e^{i\omega t}, \quad (\text{III.5})$$

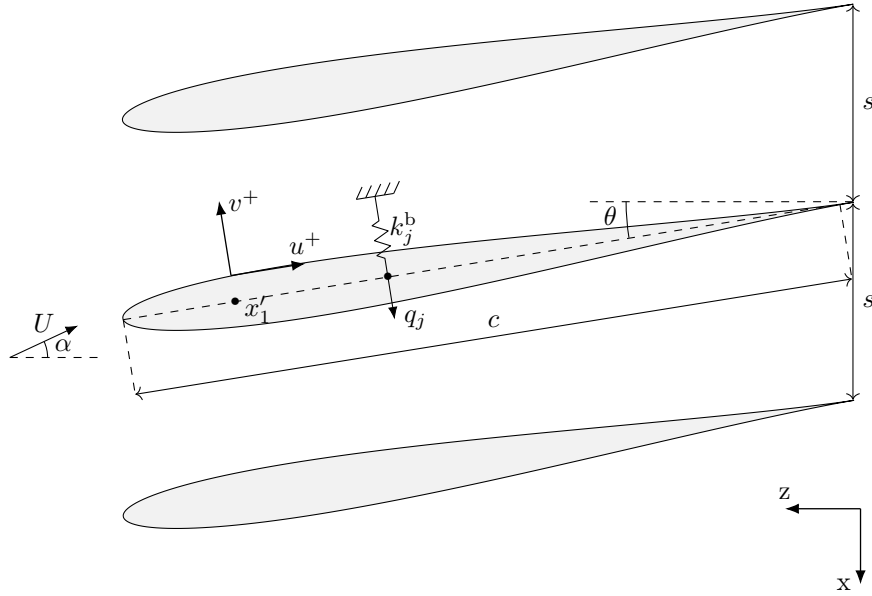


Figure III.1 – Blade geometry and aerodynamic model.

where ϵ is the free vorticity which is always carried downstream at the velocity U from the bound vorticity γ , its expression can be found in Eq. (B.7). Finally, the coefficients u_0 , u_p and u_τ are given in Eq. (B.23), Eq. (B.24) and Eq. (B.25) respectively.

1.2 Calculation of the blade force

Now that the chordwise flow velocities have been given, it is possible to use the unsteady Bernoulli equation to calculate the pressure p^+ above the reference blade:

$$\frac{\partial \phi^+}{\partial t} + \frac{1}{2}u^{+2} + \frac{1}{2}v^{+2} + \frac{p^+}{\rho} = F(t), \quad (\text{III.6})$$

where ρ is the air density and $F(t)$ an arbitrary function of time. ϕ^+ is the potential velocity such as:

$$\frac{\partial \phi^+}{\partial x'} = u^+. \quad (\text{III.7})$$

Integrating Eq. (III.7) over x' at the point x'_1 , then deriving this new expression by time and using Eq. (III.3) gives

$$\frac{\partial \phi^+}{\partial t} = i\omega e^{i\omega t} \int_0^{x'_1} \left(i\omega p_j u_p + i\omega p_j \tau u_\tau - \frac{1}{2}(\gamma + \epsilon) \right) dx', \quad (\text{III.8})$$

By injecting Eq. (III.3), Eq. (III.5) and Eq. (III.8) in Eq. (III.6), it is now possible to give the pressure above the blade at point x'_1 :

$$p^+(x'_1) = -\rho \left(\frac{1}{2}u_s^{+2} + u_s^+ u_d^+ e^{i\omega t} + \frac{1}{2}u_d^{+2} e^{2i\omega t} - \frac{1}{2}\omega^2 p_j^2 e^{2i\omega t} + i\omega e^{i\omega t} \int_0^{x'_1} u_d^+ dx' - F(t) \right), \quad (\text{III.9})$$

with

$$u_s^+ = U + \tau U u_0 - \frac{1}{2}\zeta, \quad (\text{III.10})$$

$$u_d^+ = i\omega p_j u_p + i\omega p_j \tau u_\tau - \frac{1}{2}(\gamma + \epsilon). \quad (\text{III.11})$$

Due to the hypothesis of small amplitude of vibration, the second order terms can be neglected in Eq. (III.9), which gives:

$$p^+(x'_1) = -\rho \left(u_s^+ u_d^+ + i\omega \int_0^{x'_1} u_d^+ dx' - F(t) \right) e^{i\omega t}. \quad (\text{III.12})$$

The same procedure is used to calculate the pressure p^- below the reference blade:

$$p^-(x'_1) = -\rho \left(u_s^- u_d^- + i\omega \int_0^{x'_1} u_d^- dx' - F(t) \right) e^{i\omega t}, \quad (\text{III.13})$$

with

$$u_s^- = U + \tau U u_0 + \frac{1}{2}\zeta, \quad (\text{III.14})$$

$$u_d^- = i\omega p_j u_p + i\omega p_j \tau u_\tau + \frac{1}{2}(\gamma + \epsilon). \quad (\text{III.15})$$

Using Eq. (III.12) and Eq. (III.13), the pressure difference between the pressure and suction sides of the blade at the point x'_1 can be calculated:

$$p^-(x'_1) - p^+(x'_1) = \rho \left(u_s^+ u_d^+ - u_s^- u_d^- + i\omega \int_0^{x'_1} (u_d^+ - u_d^-) dx' \right) e^{i\omega t}. \quad (\text{III.16})$$

Substituting from Eq. (III.10), Eq. (III.11), Eq. (III.14) and Eq. (III.15) gives:

$$p^-(x'_1) - p^+(x'_1) = -\rho \left(U\gamma + \tau U u_0(\gamma + \epsilon) + i\omega p_j \zeta (u_p + \tau u_\tau) + U\epsilon + i\omega \int_0^{x'_1} (u_d^+ - u_d^-) dx' \right) e^{i\omega t}. \quad (\text{III.17})$$

Moreover, integrating Eq. (B.9) with respect to the variable x' at the point x'_1 gives:

$$\epsilon(x'_1) + \frac{i\omega}{U} \int_0^{x'_1} (\gamma(x') + \epsilon(x')) dx' = K, \quad (\text{III.18})$$

where K is a constant, and thanks to Eq. (B.7), it is possible to determine that $\epsilon(0) = 0$, which necessarily implies that $K = 0$. Equation (III.17) can then be simplified thanks to Eq. (III.18).

$$p^-(x'_1) - p^+(x'_1) = -\rho (U\gamma + \tau U u_0(\gamma + \epsilon) + i\omega p_j \zeta (u_p + \tau u_\tau)) e^{i\omega t}, \quad (\text{III.19})$$

Substituting Eq. (III.19) into Eq. (III.2), it is possible to express the aerodynamic force f_j^a :

$$f_j^a = -\rho \int_0^c (U\gamma + \tau U u_0(\gamma + \epsilon) + i\omega p_j \zeta (u_p + \tau u_\tau)) dx'. \quad (\text{III.20})$$

Using the non-dimensional expressions Eq. (B.3), Eq. (B.6) and Eq. (B.8) of ζ , γ and ϵ

respectively, and using the change of variables $z = x'/c$ leads to:

$$f_j^a = i\omega\rho cUC_f p_j, \quad (\text{III.21})$$

where

$$C_f = \int_0^1 \left\{ -\gamma_p + \tau [-\gamma_\tau - u_0(\gamma_p + \epsilon_p) + u_p\zeta_0] + \tau^2 [-u_0(\gamma_\tau + \epsilon_\tau) + u_\tau\zeta_0] \right\} dz. \quad (\text{III.22})$$

1.3 Matrix form of the aerodynamic coefficient C_f

The coefficient C_f in the form given in Eq. (III.22) is difficult to estimate numerically due to the different integrals present in the expression. In order to evaluate this coefficient more easily, it was proposed in [215] to use the trapezoidal rule to evaluate the integrals, which allows the equations to be written using matrices.

First of all, in usual thin-aerofoil theory for single aerofoils, the equations are based on angular positions (ψ, ϕ) rather than an exact surface location (x', η) to facilitate integration. The following change of variable is therefore applied:

$$x = \frac{1}{2}(1 - \cos(\psi)), \quad (\text{III.23})$$

$$\eta = \frac{1}{2}(1 - \cos(\phi)). \quad (\text{III.24})$$

Due to the trapezoidal rule, the velocities functions are specified at n points for $\psi = \frac{\pi l}{n}$ and $\phi = \frac{\pi(2m+1)}{2n}$, where l and m are integer taking values from 0 to $n-1$. The choice of these expressions is made so that the values of ϕ are halfway between the values of ψ in order to avoid problems of function definitions and discontinuities.

It is now possible to express Eq. (III.22) in vector form:

$$C_f = -\mathbf{D}^T \mathbf{\Gamma}_p + \tau \left[-\mathbf{D}^T \mathbf{\Gamma}_\tau - \mathbf{Y}_0^T (\mathbf{\Gamma}_p + \mathbf{E}_p) + \mathbf{Y}_p^T \mathbf{Z} \right] + \tau^2 \left[-\mathbf{Y}_0^T (\mathbf{\Gamma}_\tau + \mathbf{E}_\tau) + \mathbf{Y}_\tau^T \mathbf{Z} \right], \quad (\text{III.25})$$

where the expressions of the vectors are given in Appendix C.

The problem with the above expression is that the unknown variables $\zeta_0, \gamma_p, \gamma_\tau, \epsilon_p, \epsilon_\tau, u_0, u_p, u_\tau$ are in the unknown vectors $\mathbf{Z}, \mathbf{\Gamma}_p, \mathbf{\Gamma}_\tau, \mathbf{E}_p, \mathbf{E}_\tau, \mathbf{Y}_0, \mathbf{Y}_p, \mathbf{Y}_\tau$ respectively. However, thanks to the expressions from Eq. (B.18) to Eq. (B.25), it is possible to express these unknown vectors using matrices:

$$\mathbf{Z} = \mathbf{A}_0^{-1}\mathbf{D}, \quad (\text{III.26})$$

$$\mathbf{\Gamma}_p = \mathbf{A}^{-1}\mathbf{D}, \quad (\text{III.27})$$

$$\mathbf{\Gamma}_\tau = \mathbf{A}^{-1}\mathbf{Q}\mathbf{Z} = \mathbf{A}^{-1}\mathbf{Q}\mathbf{A}_0^{-1}\mathbf{D}, \quad (\text{III.28})$$

$$\mathbf{E}_p = \mathbf{H}\mathbf{\Gamma}_p = \mathbf{H}\mathbf{A}^{-1}\mathbf{D}, \quad (\text{III.29})$$

$$\mathbf{E}_\tau = \mathbf{H}\mathbf{\Gamma}_\tau = \mathbf{H}\mathbf{A}^{-1}\mathbf{Q}\mathbf{A}_0^{-1}\mathbf{D}, \quad (\text{III.30})$$

$$\mathbf{Y}_0 = \tan(\theta)\mathbf{D} - \mathbf{B}_0\mathbf{Z} = \tan(\theta)\mathbf{D} - \mathbf{B}_0\mathbf{A}_0^{-1}\mathbf{D}, \quad (\text{III.31})$$

$$\mathbf{Y}_p = \mathbf{B}\mathbf{\Gamma}_p = \mathbf{B}\mathbf{A}^{-1}\mathbf{D}, \quad (\text{III.32})$$

$$\mathbf{Y}_\tau = \mathbf{B}\mathbf{\Gamma}_\tau - \mathbf{P}\mathbf{Z} = (\mathbf{B}\mathbf{A}^{-1}\mathbf{Q} - \mathbf{P})\mathbf{A}_0^{-1}\mathbf{D}, \quad (\text{III.33})$$

$$(\text{III.34})$$

where the expressions of the matrices are also given in Appendix C.

Finally, it is possible to determine the aerodynamic coefficient C_f as a function of the vibration frequency ω and the interblade phase angle $\beta_k = 2\pi k/N$:

$$\begin{aligned} C_f(\omega, \beta_k) = & -\mathbf{D}^\top \mathbf{A}^{-1} \mathbf{D} + \tau \left[\mathbf{D}^\top \left((\mathbf{A}_0^\top)^{-1} \mathbf{B}_0^\top - \mathbf{I} \tan(\theta) \right) (\mathbf{H} + \mathbf{I}) \mathbf{A}^{-1} \mathbf{D} + \right. \\ & \left. \mathbf{D}^\top \left((\mathbf{A}^\top)^{-1} \mathbf{B}^\top - \mathbf{A}^{-1} \mathbf{Q} \right) \mathbf{A}_0^{-1} \mathbf{D} \right] + \\ & \tau^2 \left[\mathbf{D}^\top \left((\mathbf{A}_0^\top)^{-1} \mathbf{B}_0^\top - \mathbf{I} \tan(\theta) \right) (\mathbf{H} + \mathbf{I}) \mathbf{A}^{-1} \mathbf{Q} \mathbf{A}_0^{-1} \mathbf{D} + \right. \\ & \left. \mathbf{D}^\top (\mathbf{A}_0^\top)^{-1} \left(\mathbf{Q}^\top (\mathbf{A}^\top)^{-1} \mathbf{B}^\top - \mathbf{P}^\top \right) \mathbf{A}_0^{-1} \mathbf{D} \right]. \end{aligned} \quad (\text{III.35})$$

1.4 Expression of aerodynamic force on the cyclic symmetric structure

Due to the high density and stiffness of turbomachinery blades, aerodynamic forces are generally assumed to be linear with regard to displacement and velocity [14]. Moreover, the generalised aerodynamic forces related to the vibration only occur in the case of dynamic displacement \mathbf{q} of the structure, which gives:

$$\mathbf{f}^a(\mathbf{q}, \dot{\mathbf{q}}) = \mathbf{A}^a \mathbf{q} + \mathbf{B}^a \dot{\mathbf{q}}, \quad (\text{III.36})$$

where \mathbf{A}^a is the aerodynamic stiffness matrix and \mathbf{B}^a is the aerodynamic damping matrix.

To be able to express the aerodynamic forces on the complete system \mathbf{f}^a from the aerodynamic force applied to a reference blade f_j^a in Eq. III.21, the system has to be considered tuned. Accordingly, the response at the j^{th} blade can be expressed as follows using the cyclic symmetry theory:

$$p_j = \sum_{k=0}^{N-1} \tilde{p}_k e^{ij\beta_k}, \quad (\text{III.37})$$

where \tilde{p}_k is the complex cyclic amplitude.

Thanks to Eq. (III.21), it is possible to express the aerodynamic force applied to a blade in the cyclic domain for each cyclic harmonic k .

$$f_k^a(\omega, \tilde{p}_k, \beta_k) = l(\omega, \beta_k) \tilde{p}_k, \quad (\text{III.38})$$

where $l(\omega, \beta_k) = i\omega\rho cUC_f(\omega, \beta_k)$. Due to the nonlinear expression of the coefficient C_f ,

a linearisation of the aerodynamic force around the frequency in vacuum ω_0 is necessary to obtain an equivalent formulation to that in Eq. (III.36).

$$\begin{aligned} f_k^a(\omega, \tilde{p}_k, \beta_k) &\approx \left[l_k(\omega_0, \beta_k) + \frac{\partial l_k(\omega_0, \beta_k)}{\partial \omega} (\omega - \omega_0) \right] \tilde{p}_k \\ &\approx [a_k(\omega_0, \beta_k) + i\omega b_k(\omega_0, \beta_k)] \tilde{p}_k, \end{aligned} \quad (\text{III.39})$$

with $a_k(\omega_0, \beta_k) = l_k(\omega_0, \beta_k) - \frac{\partial l_k(\omega_0, \beta_k)}{\partial \omega} \omega_0$ and $b_k(\omega_0, \beta_k) = -i \frac{\partial l_k(\omega_0, \beta_k)}{\partial \omega}$.

In the cyclic domain the matrices $\tilde{\mathbf{A}}$, $\tilde{\mathbf{B}}$ of the matrices \mathbf{A}^a , \mathbf{B}^a in the physical domain are block diagonal and each $\tilde{\mathbf{A}}_k$, $\tilde{\mathbf{B}}_k$ have only one term a_k , b_k on the dof related to blade flexion.

$$\tilde{\mathbf{A}} = \begin{bmatrix} \tilde{\mathbf{A}}_0 & & & \\ & \tilde{\mathbf{A}}_1 & & \\ & & \ddots & \\ & & & \tilde{\mathbf{A}}_{N-1} \end{bmatrix}, \quad \tilde{\mathbf{B}} = \begin{bmatrix} \tilde{\mathbf{B}}_0 & & & \\ & \tilde{\mathbf{B}}_1 & & \\ & & \ddots & \\ & & & \tilde{\mathbf{B}}_{N-1} \end{bmatrix}, \quad (\text{III.40})$$

with

$$\mathbf{A}_k = \begin{bmatrix} a_k & 0 & 0 \\ 0 & 0 & 0 \\ 0 & 0 & 0 \end{bmatrix}, \quad \mathbf{B}_k = \begin{bmatrix} b_k & 0 & 0 \\ 0 & 0 & 0 \\ 0 & 0 & 0 \end{bmatrix}. \quad (\text{III.41})$$

To find the expressions of the matrices \mathbf{A}^a and \mathbf{B}^a it is necessary to go back into the physical domain:

$$\mathbf{A}^a = \mathbf{F} \tilde{\mathbf{A}} \mathbf{F}^H, \quad (\text{III.42})$$

$$\mathbf{B}^a = \mathbf{F} \tilde{\mathbf{B}} \mathbf{F}^H, \quad (\text{III.43})$$

where \mathbf{F} is the discrete Fourier transform matrix (its expression is given Eq. (I.64)) and \mathbf{F}^H its Hermitian matrix.

Finally, using the dynamic equation in the frequency domain is expressed as follows:

$$\left[-\omega^2 \mathbf{M} + i\omega(\mathbf{G} - \mathbf{B}^a) + (\mathbf{K}^g - \mathbf{A}^a) \right] \mathbf{p} = \mathbf{0}. \quad (\text{III.44})$$

1.5 Aerodynamic damping solution

To simplify the resolution of the eigenvalue problem Eq. (III.44), it has been decided to separate the real and the imaginary parts of \mathbf{A}^a and \mathbf{B}^a to obtain two real matrices \mathbf{C}^a and \mathbf{D}^a such as:

$$\mathbf{C}^a = \text{Re}(\mathbf{A}^a) - \omega \text{Im}(\mathbf{B}^a), \quad (\text{III.45})$$

$$\mathbf{D}^a = \frac{\text{Im}(\mathbf{A}^a)}{\omega} + \text{Re}(\mathbf{B}^a). \quad (\text{III.46})$$

The new eigenvalue problem is then:

$$\left[-\omega^2 \mathbf{M} + i\omega(\mathbf{G} - \mathbf{D}^a) + (\mathbf{K}^g - \mathbf{C}^a) \right] \mathbf{p} = \mathbf{0}. \quad (\text{III.47})$$

With this formulation, the matrices \mathbf{C}^a and \mathbf{D}^a depend on ω . For this reason, the assumption

has been made to evaluate these matrices at ω_0 , then use the new natural frequency ω to recalculate the matrices \mathbf{C}^a and \mathbf{D}^a and repeat this procedure until a converged value ω is obtained. This iterative method is principally used to solve modal analysis of structures with frequency-dependent non-proportional linear damping [230]. Finally, aerodynamic damping can be determined with the following formulation:

$$\xi_n = \frac{\text{Im}(\omega_n)}{2\text{Re}(\omega_n)}. \quad (\text{III.48})$$

The stability of the system can be determined from this definition and the expression in Eq. (III.1). If ξ_n is positive then the system is stable, whereas if it is negative the system is unstable.

2 Flutter instability and intentional mistuning optimisation

The lumped mass-spring model used for the numerical application is the same as the one used in Section II.2 with the same parameters provided in Table II.1. The characteristics of the fluid were determined for an engine operating at 10,000 m of altitude and an aircraft flying at Mach 0.74. The considered compressor is located directly behind the fan which gives an air density of $\rho = 0.496 \text{ kg/m}^3$ and a freestream velocity relative to the blades of $U = 300 \text{ m/s}$. In terms of structural characteristics needed for the aerodynamical model, the cascade spacing is estimated to be $s = 0.042 \text{ m}$ with a chord length of $c = 0.040 \text{ m}$, and the stagger angle of the blade is $\theta = 30^\circ$. All parameters of the aerodynamic model are summarised in Table III.1.

Table III.1 – Numerical values for the aerodynamic model.

Parameter	Value	Unit
ρ	0.496	kg/m^3
U	300	m/s
c	0.040	m
s	0.042	m
θ	0.524	rad

2.1 Aeroelastic stability of the tuned model

To determine the aeroelastic stability of the modes, it is necessary to solve the eigenvalue problem Eq. (III.44). Since the matrices \mathbf{C} and \mathbf{D} are evaluated from a vacuum frequency $\omega_{0,n}$, the aerodynamic damping ξ_n is determined only for this mode. This implies solving an eigenvalue problem for each mode of interest. The focus will be made only on the modes present in the area between 750 Hz and 1,400 Hz, which is represented in grey on Fig. II.3.

Firstly, the model will be considered tuned in order to ensure that it does exhibit flutter. It is mentioned in [216] that the case of zero-deflection flow which is treated in [215] does not allow for the appearance of flutter on the bending mode of the cascade blades. More precisely, the zero-deflection flow is for an air inlet angle equal to the stagger angle which means $\alpha = \theta$. A parametric study of the air inlet angle is carried out to determine under which condition the flutter phenomenon is the most likely to occur. The study will be limited between -90 and 90 degrees because beyond these values the direction of the fluid is reversed which is beyond the scope of this research.

The damping coefficients are displayed in Fig. III.2 versus the nodal diameter index for the modes of interest for different values of α . In Fig. III.2a, these are the damping coefficients for

the first modal family and in Fig. III.2b these are those for the second modal family, for the latter the nodal diameters are restricted between -8 and 8 because beyond that, the modes have values greater than $1,400$ Hz and are therefore not taken into account. Whether it is for the first modal family or the second, only $\alpha = -85^\circ$ and $\alpha = 85^\circ$ present negative damping coefficients and therefore a flutter phenomenon. All values of α between -68° and 68° have small positive aerodynamic damping values, thus the flutter phenomenon can only occur between -90° and -70° or between 70° and 90° .

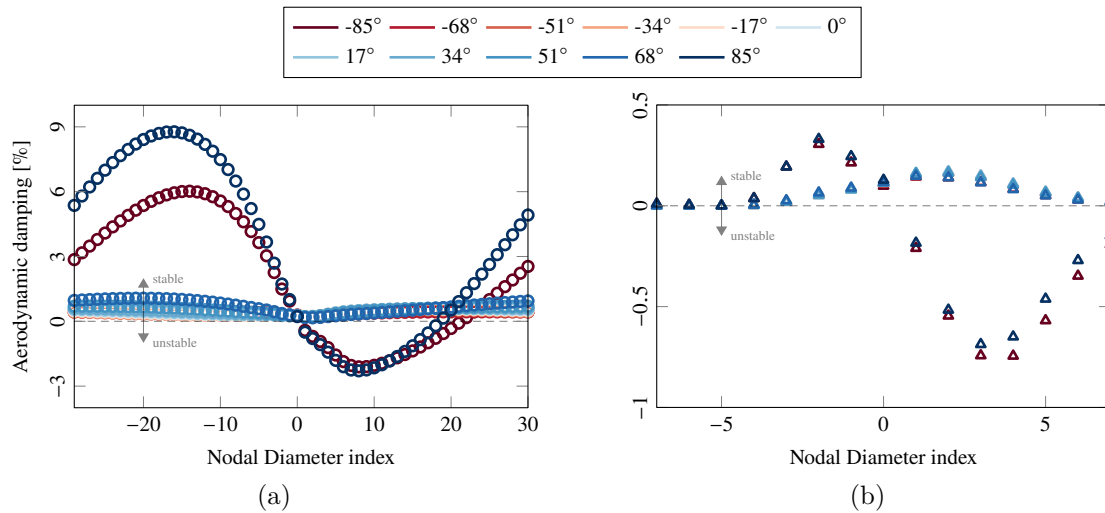


Figure III.2 – Aerodynamic damping versus the nodal diameter index for air inlet angle between -85° and 85° . (a) First modal family. (b) Second modal family.

For the rest of the study, it was decided to focus on the range between 70° and 90° because it is preferable to keep the angular deviation between α and θ reasonable to remain close to a realistic configuration. Figure III.3 is similar to Fig. III.2 but with a zoom on the α range from 70° to 80° . Thanks to Fig. III.3a, it is possible to see that the flutter phenomenon starts from $\alpha = 78^\circ$. In order to keep reasonable values of aerodynamic damping coefficients, the value of the air inlet angle will be $\alpha = 79^\circ$ for the rest of the flutter stability study.

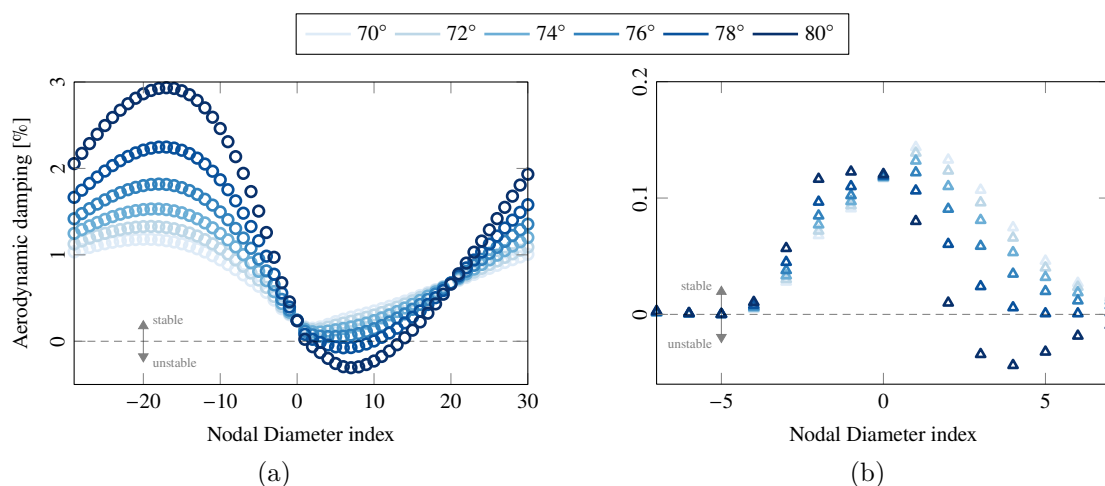


Figure III.3 – Aerodynamic damping versus the nodal diameter index for air inlet angle between 70° and 80° . (a) First modal family. (b) Second modal family.

The damping coefficients for $\alpha = 79^\circ$ are displayed in Fig. III.4. In Fig. III.4a the

calculation was made with the Coriolis matrix factored in, while in the second case in Fig. III.4b, it was not considered, to allow a comparison of the aerodynamic coefficients with and without the Coriolis effect. For both figures, the results are very similar, there are 15 unstable modes, all between the nodal diameter indexes 2 and 11. Minimum aerodynamic damping occurs at $\xi_7 = -0.174\%$ with the Coriolis effect and $\xi_7 = -0.177\%$ without.

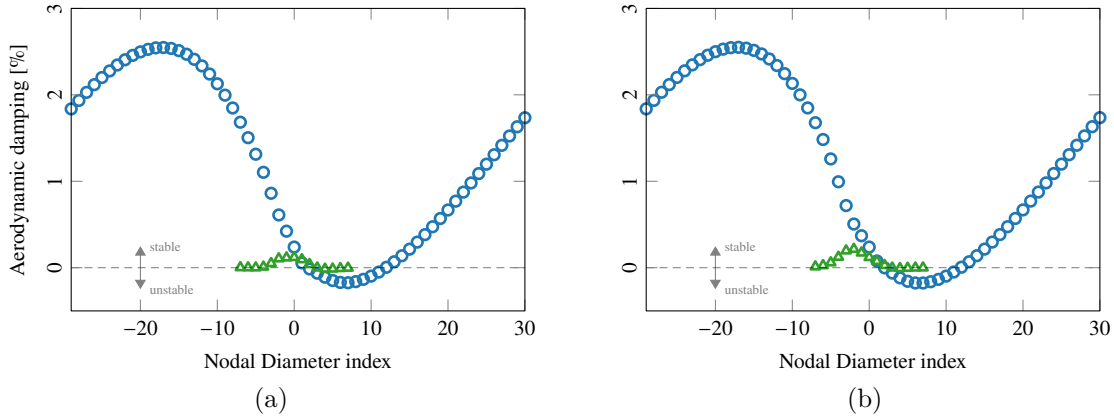


Figure III.4 – Aerodynamic damping versus the nodal diameter index. \circ : first modal family. \triangle : second modal family. (a) With the Coriolis effect. (b) Without the Coriolis effect.

2.2 Subspace Optimisation Strategy

Now that it has been demonstrated that the tuned lumped mass-spring model presents flutter instabilities on 15 modes, this section will focus on stabilising the model using detuning. The goal is to break the natural cyclic symmetry of the bladed disc by defining a particular pattern consisting of two or more different types of blades or with non-uniform circumferential spacing between blades [45, 60, 79, 96, 175].

To show the interactions between the Coriolis effect and detuning and particularly the negative effect that the former can exercise on the latter, the Coriolis effect will not be considered when choosing the best detuning pattern, but will be taken into account after looking at the changes that can be enabled.

In this manuscript, detuning will be carried out using two different types of blades A and B [16, 151, 171–173]. The first type of blade corresponds to a variation of x percent of Young’s modulus and the second to a variation of y percent. The choice of its values will be discussed later in this section. By combining these two types of blades, it is possible to create different detuning patterns and break the natural cyclic symmetry of the bladed disc.

The number of detuning patterns can be approximated by $2^N/N$ [71] which for 60 blades gives more than $1.92e^{16}$ possible combinations. It is therefore impossible to test all these combinations. The first solution considered is to use the subspace optimisation strategy [71].

This method consists of reducing the space of combinations by defining groupings of p blades to have $M = N/p$ sectors (with M rounds to the nearest integer less than or equal to N/p). This subspace must be small enough to consider all possible combinations. It has been chosen to take $p = 4$ to have only $M = 15$ sectors and 2,192 possible combinations. Eight different groupings of blades have been tested, which gives a total of 17,536 patterns to test. The eight pairs of groupings tested are as follows:

- | | | | |
|-----------------|-----------------|-----------------|-----------------|
| (a) AAAA / BBBB | (c) ABBA / BAAB | (e) AAAB / BBBA | (g) AABA / BBAB |
| (b) AABB / BBAA | (d) ABAB / BABA | (f) ABAA / BABB | (h) BAAA / ABBB |

The assumption of this method is that by testing all possible combinations of these subspaces, the best detuning pattern that emerges will be close enough or equal to that of the full space. This method was originally used to find the detuning pattern which minimises the amplification factor of the forced response due to mistuning, but is fully applicable to aerodynamic stabilisation as shown in [58].

All these patterns have been tested by choosing arbitrarily blade A as a variation of 5% of Young's modulus and blade B as a variation of -5% . The best detuning patterns given by each pair of groupings are depicted in Fig. III.5 and the associated minimum damping coefficients are as follows:

- | | | | |
|-------------|----------------|-------------|-------------|
| (a) 0.001 % | (c) 0.002 % | (e) 0.004 % | (g) 0.001 % |
| (b) 0.005 % | (d) -0.001% | (f) 0.001 % | (h) 0.004 % |

For all these patterns, the minimum damping coefficient is greater than 0 except for the (d) grouping which means that all these groupings allow a stabilisation of the model except the (d). In each case the alternating between A and B blades seems to be strong enough to break the symmetry, but in a contradictory way the (d) grouping which has the most important variation with an almost perfect alternate arrangement ABAB is the one that does not stabilise the system. This is because the coupling between the blades is strong due to the flexibility of the disc and for that kind of coupling, the optimal pattern does not present much AB alternation [160].

From this optimisation strategy, it appears that the best detuning pattern is the one represented in Fig. III.5b with a minimum damping coefficient of 0.005% whereas in the tuned case it was -0.177% . The choice of the values the Young's modulus of A and B made it possible to find a pattern allowing to stabilise the system but these values were chosen arbitrarily and are not necessarily optimal. It may be possible to find values with a smaller Young's modulus deviation that would stabilise the structure as well.

One strategy could be to use the subspace optimisation method with arbitrarily values of Young's modulus for A and B to find the best performing pattern, and afterwards, change the values of A and B to optimise this detuning pattern. The problem with this strategy is that it does not ensure that the best performing pattern for a given values of A and B is the same for other values, which is why this strategy has not been retained thereafter.

2.3 The genetic algorithm

An other approach to limit the number of simulations is to use a genetic algorithm [10, 37]. The principle of this method is inspired by Darwin's theory of natural evolution [46] and consists in the evolution of a population from one generation to the next by favouring the reproduction of the best individuals and creating mutations that allow these individuals to upgrade over the generations. With this solution, the patterns and Young's modulus are modified at the same time in each generation.

The first step of the genetic algorithm is to generate a random population of n_{ind} individuals also called chromosomes. An individual is composed of $N + 2$ genes, the first N genes are of type A or B which represent the two types of blades, and the last two genes are percentage values which represent the variation of the Young's modulus of type A and B blades. In order to avoid an excessive deviation between Young's modulus of the two blades, the variation value is limited. The next step is to define for each of its individuals a selection probability p_s which

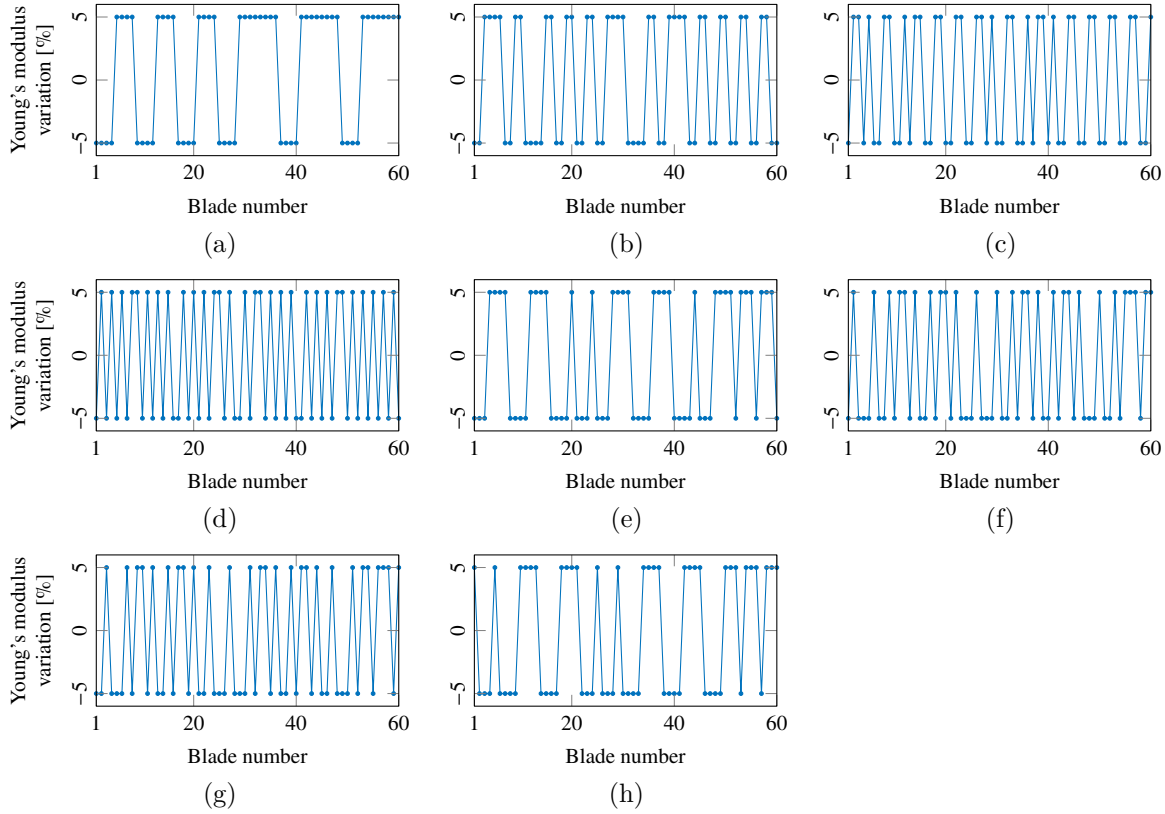


Figure III.5 – Best detuning patterns given by the subspace optimisation strategy for the eight subspace without the Coriolis effect. The eight letters correspond to the eight pairs of grouping.

must be high if the detuning pattern allows a good stabilisation of the system and low in the opposite case. This probability is based on the fitness function, which determines the ability of an individual to compete with other individuals. In this case, the value of the minimum aerodynamic coefficient of the detuning pattern must be maximum. The selection probability is defined as follows:

$$p_s(i) = \frac{\Xi(i) - \min(\Xi)}{\sum_{k=1}^q \Xi(k) - n * \min(\Xi)}, \quad (\text{III.49})$$

where $\Xi(i)$ is the smallest ξ_n of the i^{th} pattern and $\min(\Xi)$ is the minimum value among all $\Xi(i)$. It has been shown in the tuned case that the minimum aerodynamic coefficient is negative, which means that if the ξ_n minimum is greater than zero for a particular pattern, it is globally stabilising against flutter and the higher the value, the more stabilising it is. Once the selection probability has been defined for all the individuals of the generation, it is time to select $n_{\text{ind}}/2$ pairs of individuals using this selection probability. These selected pairs of individuals are called parents and will give rise to $n_{\text{ind}}/2$ pairs of children (also called offspring) through the crossover phase.

For a pair of parents the crossover has a probability p_c of occurring. If this does not happen, then the children are identical to the parents. Otherwise, a randomly chosen crossover point between the genes must be defined and the children are then created by exchanging the genes of the parents up to the crossover point.

Finally, the last step before the new generation can be created is mutation. Each gene of each offspring chromosome has a mutation probability p_m . If the mutation occurs in one of the

first 60 genes, it switches from type A to type B or vice versa, but if it is one of the last two genes then the percentage value is changed to another random value. The mutation process is very important in a genetic algorithm as it maintains diversity within the population and prevents premature convergence. At the beginning of the algorithm, it is convenient to have a high mutation probability to properly cover the space of possible solutions, but towards the end of the process, a high mutation rate may force the disappearance of the optimum solution. To avoid this kind of situation, Choi proposed an exponentially decreasing function on the number of generations g [37]:

$$p_m(g) = p_m(0)e^{-\tau g/g_t}, \quad (\text{III.50})$$

where $p_m(0)$ is the initial mutation probability, g_t the total number of generations, and τ the rate of decay.

Once this step is finished, the new generation $g + 1$ has been created and it is necessary to repeat the whole process until the g_t^{th} generation is reached.

Finally, in order to avoid losing the best detuning pattern from one generation to the next, because it would not have been selected or would have undergone crossover and mutation, the "one elite reservation" strategy is adopted. The aim is to keep the individual with the best selection probability from one generation to the next without any change. Accordingly, the total number of individuals from the second generation until the last generation is $n_{\text{ind}} + 1$.

In order to run this algorithm, many different parameters must be defined. The first parameter is the number of individuals n_{ind} , in order to have a sufficiently large population to take into account a maximum of diversity, this one is chosen as three times the number of sectors, that is $n_{\text{ind}} = 180$. Then, the probability of crossover $p_c = 0.7$, the initial mutation probability $p_m(0) = 0.99$ and the rate of decay $\tau = 5$ are chosen as in [37] where a quick convergence of the algorithm was shown with these values. The last parameter to choose is the total number of generations g_t , this parameter is important because it defines the number of patterns that will be computed (which is g_t multiplied by n_{ind}) and therefore the computation time of the algorithm.

Three different values will be tested: $g_t = 100$ to have a number of patterns tested around that of the subspace optimisation strategy, $g_t = 500$ which is the number chosen in [37] and $g_t = 2,500$ which will be considered as a reference to evaluate the performance of the two others because it will allow for a rather important diversity of patterns which should allow for a convergence towards one of the most optimal detuning patterns.

The best detuning pattern for the three genetic algorithms are given in Fig. III.6 and the minimum damping coefficients are 0.003 %, 0.004 % and 0.005 %, respectively. The detuning patterns have different distributions of A and B blades but the detuning levels are similar and close to the limit given by the genetic algorithm of $\pm 5\%$, which suggests that the greater the Young's modulus, the greater the stabilisation.

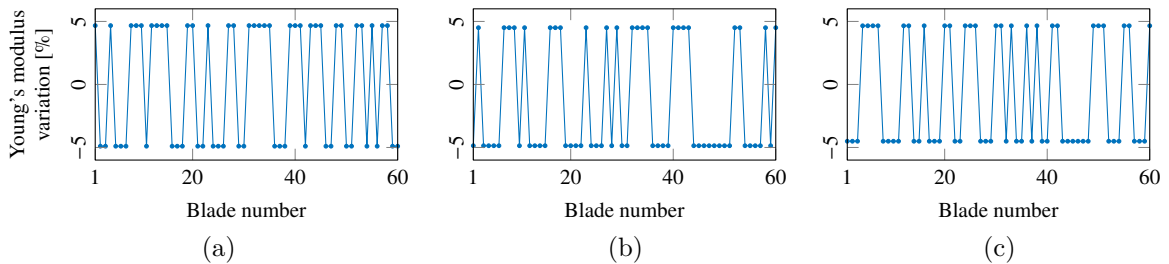


Figure III.6 – Best detuning patterns given by the the genetic algorithm for different number of generation without the Coriolis effect. (a): $g_t = 100$. (b): $g_t = 500$. (c): $g_t = 2500$.

Then, the convergence of the algorithms as a function of the number of generations are shown in Fig. III.7 with three different indications. The blue curve gives the information on the minimum damping coefficient of the best detuning pattern of a generation while the red curve gives that of the worst one. The green curve gives the average value of the minimum damping coefficient of all detuning patterns of a generation.

The three figures have very similar behaviours and suggest that an algorithm with 100 generations is sufficient to find a suitable detuning pattern with this method, even if in this case the minimum damping coefficient for 100 generations is slightly smaller than for 500 and 2500 generations. In any case, the minimum damping coefficient of the best detuning pattern is very close to zero from the beginning to the end and has difficulty increasing over generation. As will be observed later, some modes have a low damping coefficient because of their small blade participation. It is therefore difficult to increase the minimum damping coefficient and it remains close to zero.

As for the worst detuning pattern, its value tends to remain around -0.2% which is close from the one of the tuned case with -0.177% . Finally, progressive increasing of the average value is observed to approach the maximum value towards the last generations. This reflects an overall improvement of the population over the generations and therefore increases the chances of converging to an optimal solution but the lack of significant improvement in the minimum value of the worst detuning pattern, shows that the best elements are still very sensitive to crossover and mutation.

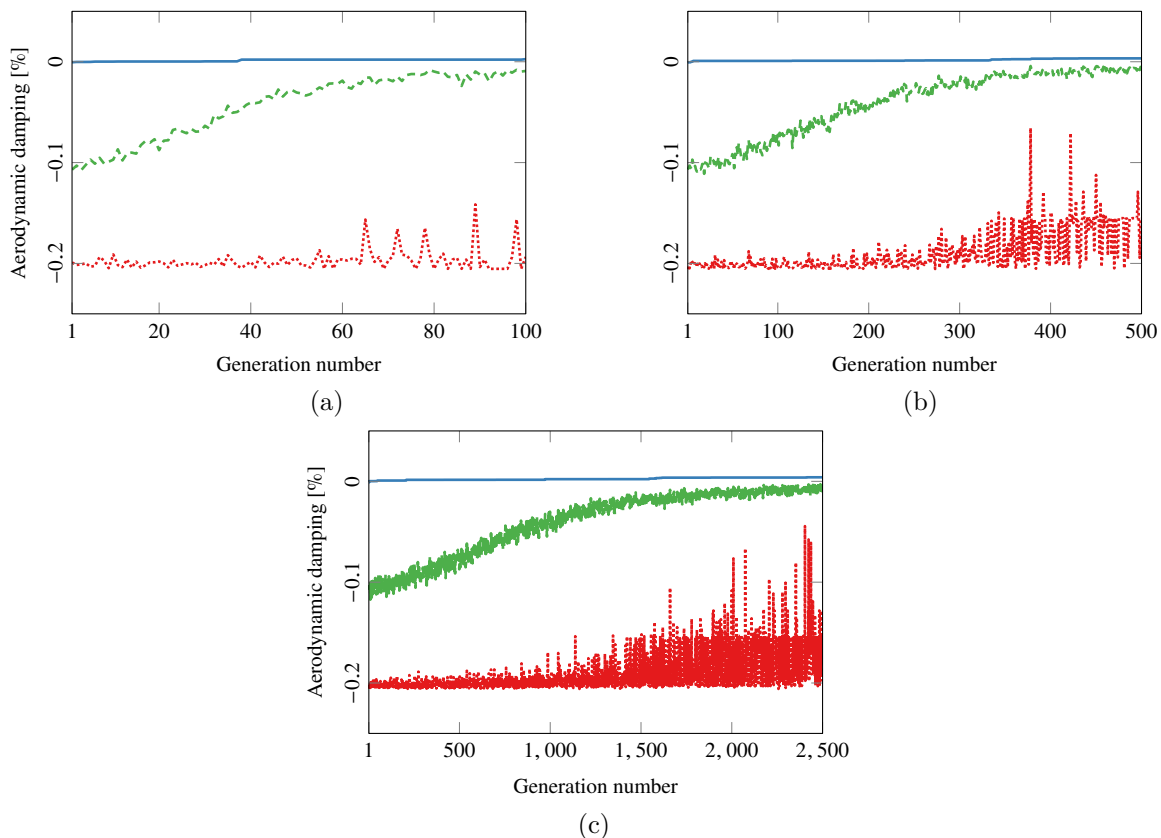


Figure III.7 – Convergence of the genetic algorithm for different number of generation without the Coriolis effect. (a): $g_t = 100$. (b): $g_t = 500$. (c): $g_t = 2500$. [—]: Maximum. [--]: Mean. [....]: Minimum.

2.4 Selection of detuning patterns without Coriolis effect

From the subspace optimisation strategy and the genetic algorithm, it is the first one that allowed to find the best detuning pattern with a reduced number of simulations. The pattern chosen to stabilise the model without taking into account the Coriolis effect is the one presented in Fig. III.5b with a minimum damping coefficient of 0.005 %. In order to better present the effectiveness of this one, the smallest aerodynamic damping coefficients versus their associated frequency have been plotted in Fig. III.8 for both the tuned and detuned cases. It can be seen that many modes are in the unstable zone in the tuned case (circle marker) while none are in this zone for the detuned case (stars marker).

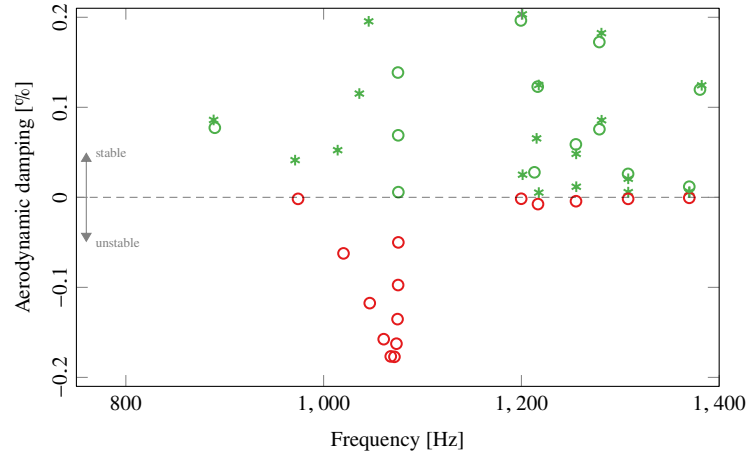


Figure III.8 – Aerodynamic damping versus the model frequency without the Coriolis effect in the tuned case [○] and in the detuned case [*]. The negative aerodynamic damping coefficients are represented in red and the positive ones in green.

3 Coriolis influences on flutter stability

The choice of detuning pattern has been made in the previous section to allow stabilisation of the model without the Coriolis effect. This section will be focused on the detuned model with the Coriolis effect taken into account in order to study its influence.

3.1 Detuned model with the Coriolis effect

The inclusion of the Coriolis effect now gives a minimum aerodynamic damping of $\xi_n = -0.027\%$ and as observed in Fig. III.9, there are five modes with negative damping, meaning that some modes which were stabilised by detuning without taking the Coriolis effect into account are actually unstable. For better readability, these modes will be sorted by frequency and named M6, M8, M67, M71 and M73 as in Section II.3.

To better understand this phenomenon, a continuity coefficient was added before the Coriolis matrix and the calculations performed by varying this coefficient from $c_{\text{cont}} = 0$ (Coriolis effect not taken into account) to $c_{\text{cont}} = 1$ (Coriolis effect fully accounted for). Then, a mode-sorting algorithm was used to follow the evolution of the modes from the state without Coriolis to the state with Coriolis, according to a consistency criterion of the modes.

Thanks to this method it is now possible to plot the evolution of the damping coefficient from the state without Coriolis to the state with Coriolis. The damping coefficients of the five modes with a negative value due to the impact of the Coriolis effect are recorded in Fig. III.10.

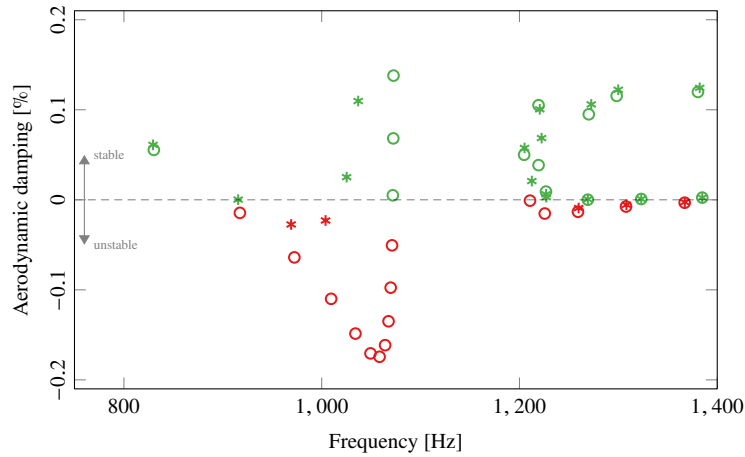


Figure III.9 – Aerodynamic damping versus the frequency for the model with the Coriolis effect in the tuned case [O] and in the detuned case [*]. The negative aerodynamic damping coefficients are represented in red and the positive ones in green.

M6 and M8 modes seem to have a very strong dependence on the Coriolis effect since their aerodynamic damping coefficients vary a lot with the continuation parameter. These modes have a damping coefficient of 0.052% and 0.115% without the Coriolis matrix which evolve respectively to -0.027% and -0.023% with it. As for the other three modes, their evolutions are less significant and their values remain very close to zero.

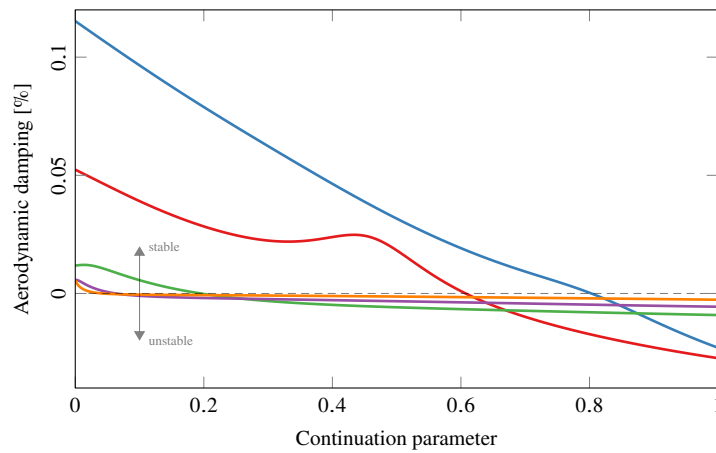


Figure III.10 – Aerodynamic damping versus the continuation parameter (0 / 1: case without / with Coriolis). [—]: M6 mode. [—]: M8 mode. [—]: M67 mode. [—]: M71 mode. [—]: M73 mode.

Each mode can be identified by the predominant travelling wave in its deformation using a DFT (Eq. (II.56)) that computes the projection of each mode onto the travelling waves. Subsequent to the DFT on the M6, M8, M67, M71 and M73 unstable modes, it can be observed that all these modes have a predominant travelling wave, which are 3ND-FW, 4ND-FW, 5ND-FW, 6ND-FW and 7ND-FW, respectively. This predominance can also be observed through the deformations of these modes in Fig. III.11.

With these figures, it can be seen that the detuning effect is small because even if they are not perfect, the nodal diameters are clearly perceptible. However, for M6 and M8 modes in Fig. III.11a and Fig. III.11b, detuning can be observed with heterogeneous amplitudes on

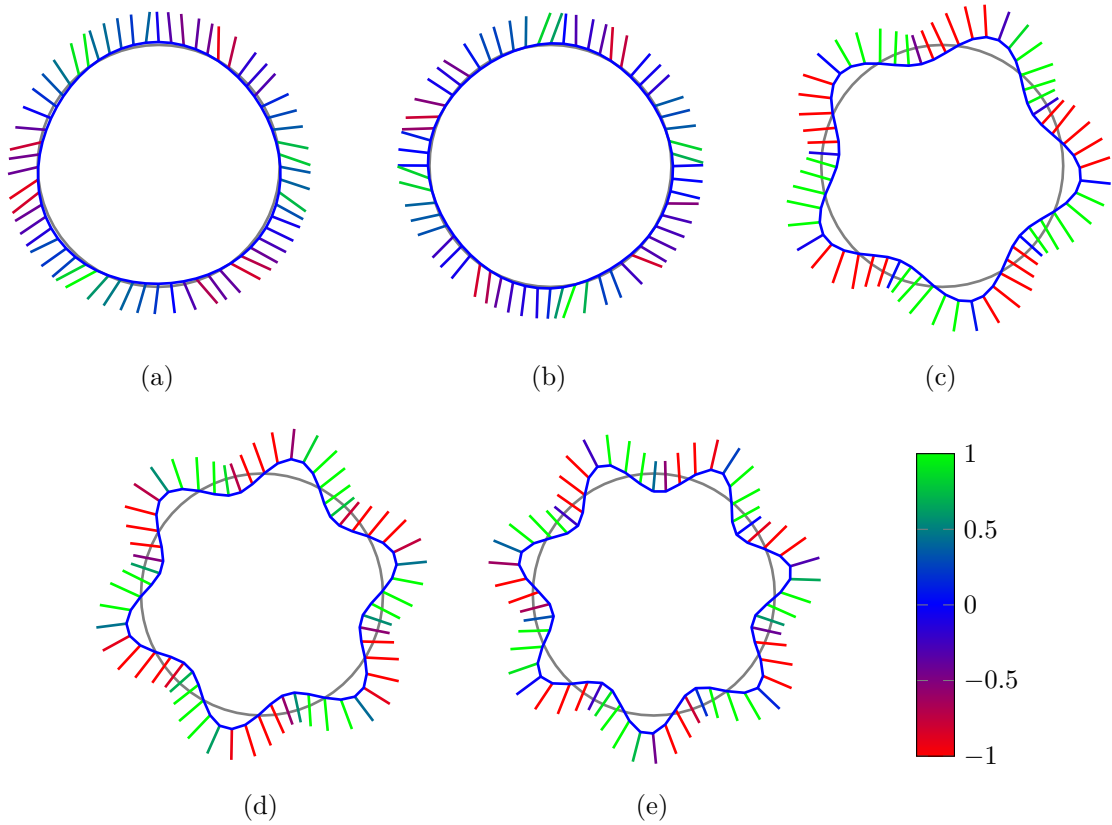


Figure III.11 – Modal shape of the five unstable modes. (a) M6 mode. (b) M8 mode. (c) M67 mode. (d) M71 mode. (e) M73 mode.

the blades. For these two modes, the participation is both on the blades and the disc and their frequencies are lower than 1,040 Hz, which corresponds to the first zone mentioned in Section II.3. For the other three modes, these are at frequencies higher than 1,070 Hz and are disc-dominated, which corresponds to the third zone and the second modal family.

The sensitivity of these modes to the Coriolis effect is better understood thanks to these last observations. All these modes have a disc participation, which allows a non-negligible Coriolis effect development and accordingly, a behaviour which tends towards the tuned case. Moreover, the 3ND-FW 1, 4ND-FW 1, 5ND-FW 2, 6ND-FW 2 and 7ND-FW 2 modes, which correspond to the predominant travelling wave of the detuned modes, are unstable as seen in Fig. III.4. Furthermore, the fact that the M67, M71 and M73 modes are disc-dominated also explains why these modes are weakly sensitive to aerodynamic load and therefore have an aerodynamic coefficient close to zero.

In Chapter II and also in other publications [1, 166, 193, 194], it has been shown that the Coriolis effect tends to bring the detuned modes closer to their tuned state when the modes are sufficiently isolated from other modes. Detuning is predominant when several modes are close in frequency because they interact with each other due to detuning. However, when the Coriolis effect tends to isolate a mode in frequency, then its behaviour is close to that of the tuned case because it cannot interact with another mode.

To better understand this, the evolutions of the DFT components of the detuned case are shown in Fig. III.12 for the five modes of interest. At $c_{\text{cont}} = 0$, the M67, M71 and M73 modes have two predominant components which are forward and backward waves with 5ND, 6ND and 7ND, respectively. Then, with the increasing of the continuation coefficient, the forward wave

becomes predominant over the backward wave, until it reaches a maximum and remains the only predominant component. This evolution is due to a frequency isolation of these modes with the Coriolis effect as can be seen in the Campbell diagram in Fig. III.13b and thus a behaviour close the tuned case as it has already been shown in Chapter II. However, the tuned behaviour is not as obvious here due to the detuning level which is greater than the mistuning level in the previous chapter.

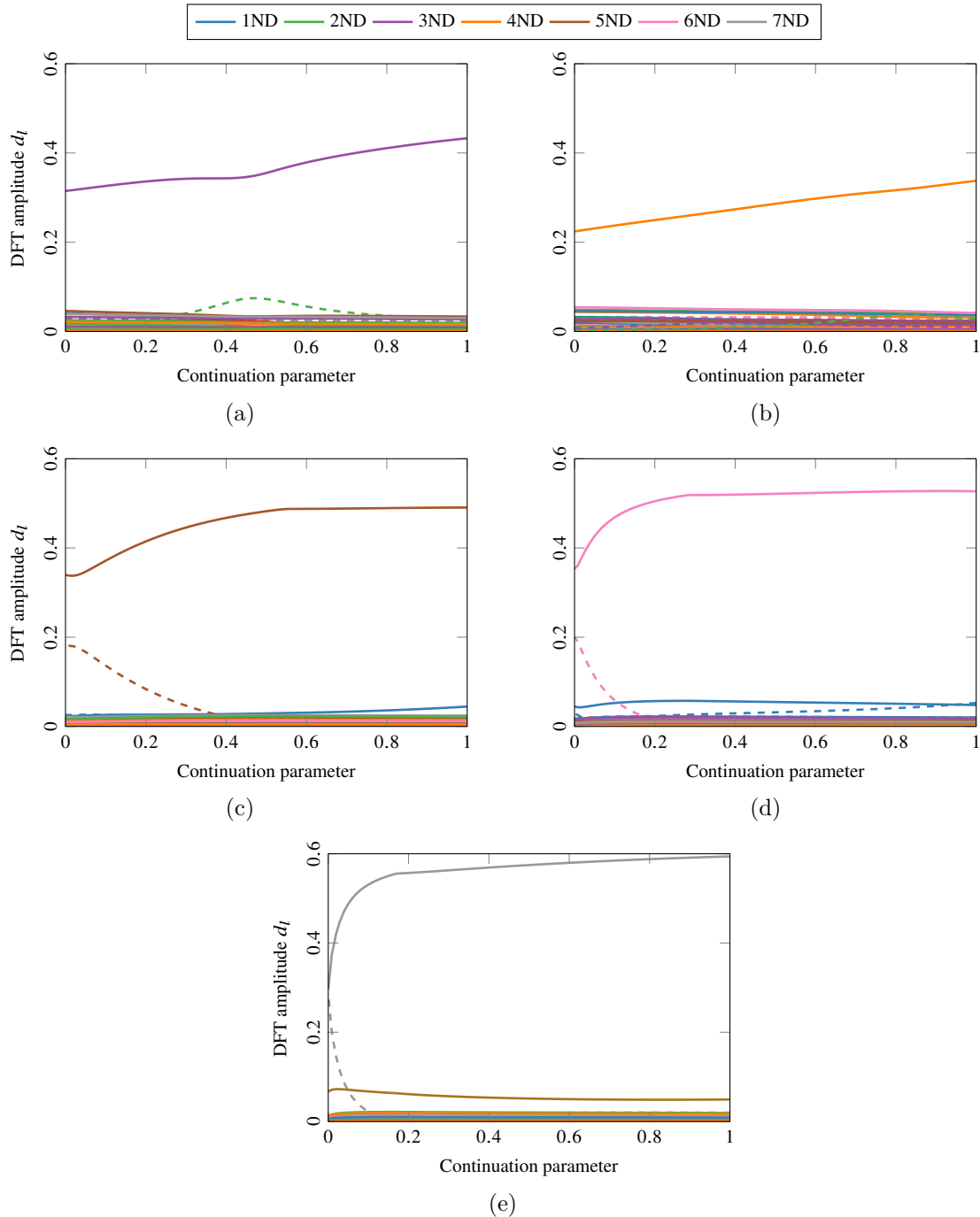


Figure III.12 – Evolution of the DFT components with the continuation parameter in the tuned case (0 / 1: case without / with Coriolis). [—]: Forward waves. [---]: Backward waves. (a) M6 mode. (b) M8 mode. (c) M67 mode. (d) M71 mode. (e) M73 mode.

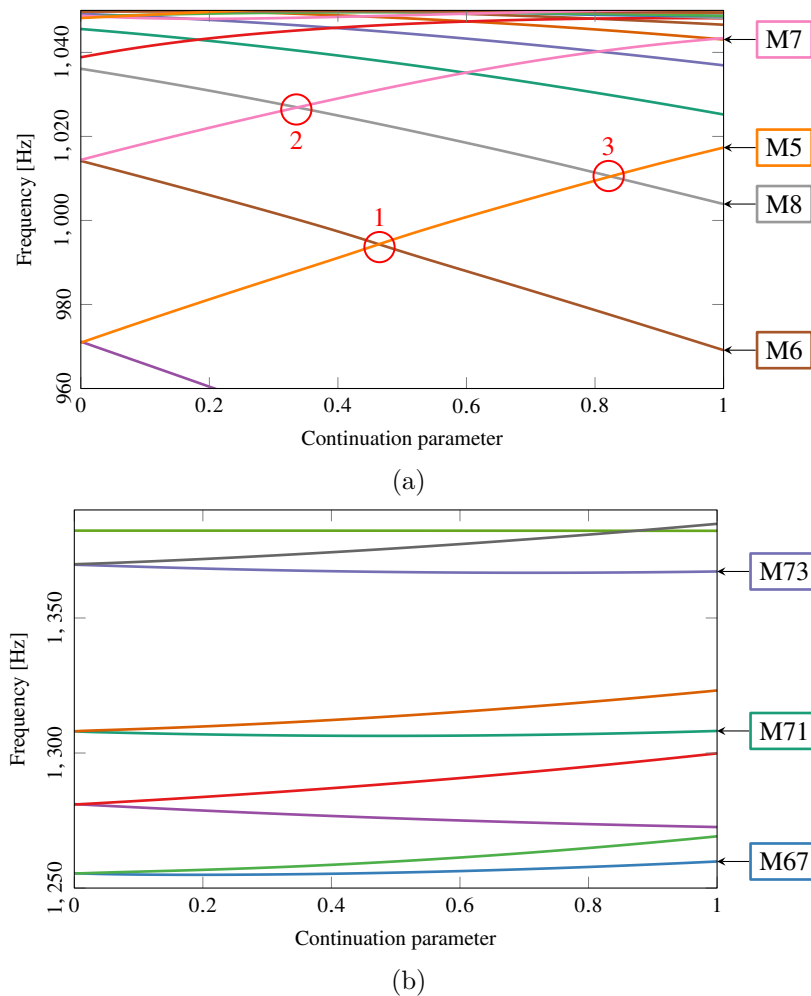


Figure III.13 – Campbell diagram of the mistuned bladed disc with the aerodynamic forces. (a) Zoom between 960 Hz and 1,040 Hz for the M6 and M8 modes. (b) Zoom between 1,250 Hz and 1,390 Hz for the M67, M71 and M73 modes. [○]: Crossing regions.

For M6 and M8 modes, the behaviour is different, as there is no backward wave without the Coriolis effect, but only a forward wave which increases progressively with the continuation coefficient until it reaches a level large enough for the damping coefficients of these modes to return to negative values. For the M6 mode in Fig. III.11a, a local increase of the 2ND-BW component can be observed at $c_{cont} = 0.45$ which is also observed in Fig. III.10. This local increase is explained by a frequency crossing between the M5 (which has a predominant 2ND-FW travelling wave) and M6 modes as shown in Fig. III.13a and an interaction of these two shapes, which creates more localisation and increases the flutter stability.

The M8 mode also crosses M5 and M7 modes with the continuation parameter. However, this does not create interaction between the modes with variations in DFT components and therefore does not create a variation in the damping coefficient either. This behaviour is different from that observed in Chapter II, i.e. when mistuning is added, the modes interact strongly with each other and no longer cross as observed in Fig. II.7. This difference is explained by the inclusion of the aerodynamic matrices \mathbf{C}^a and \mathbf{D}^a in the equation of motion, because if Fig. III.13a is plotted without these two matrices, there is the presence of veering region, as observed in Fig. III.14. This highlights a limitation of the model: the aerodynamic forces were created assuming the tuned system which could explain the similarity of this behaviour to the

tuned case.

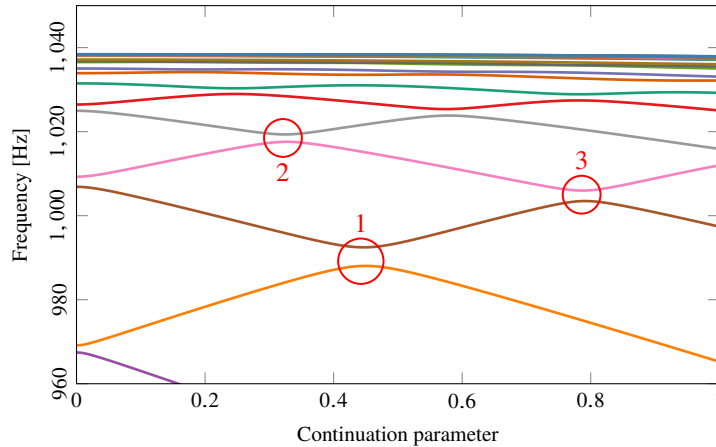


Figure III.14 – Campbell diagram of the mistuned bladed disc without the aerodynamic forces between 960 Hz and 1,040 Hz for the M6 and M8 modes. [○]: Veering regions.

3.2 Selection of detuning patterns with Coriolis effect

In the previous subsection, it was demonstrated that the optimum detuning pattern obtain without taking into account the Coriolis effect was ineffective when this one is introduced in the model. It is therefore important to examine whether there is still a pattern allowing the system to be stabilised when taking the Coriolis effect into account. For this purpose, the same strategies have been applied as for the selection of the detuning pattern without the Coriolis effect using subspace optimisation and a genetic algorithm with $g_t = 500$. However, the limitation in variation value of Young's modulus to $\pm 5\%$ does not facilitate the finding of a satisfactory pattern (even with $g_t = 2500$).

First the subspace optimisation strategy has been used for different Young's modulus variation and the minimum damping coefficient of the best detuning pattern is given in Fig. III.15. It is only by pushing the limits to $\pm 10\%$ that a pattern allowing the stabilisation of the model is found. With the subspace optimisation strategy, the minimum damping coefficients for each pair of groupings are as follows:

- | | | | |
|---------------------------|--------------------------|---------------------------|---------------------------|
| (a) $-2 \times 10^{-4}\%$ | (c) $5 \times 10^{-4}\%$ | (e) $-1 \times 10^{-4}\%$ | (g) $2 \times 10^{-4}\%$ |
| (b) $2 \times 10^{-4}\%$ | (d) $6 \times 10^{-4}\%$ | (f) $2 \times 10^{-4}\%$ | (h) $-1 \times 10^{-4}\%$ |

However, the genetic algorithm gives a better detuning pattern with a minimum damping coefficient of $\xi_n = 0.001\%$. Again, the best pair of blades to stabilise this model has Young's modulus values close to the given limits with a variation of -9.62% for the first blade and 9.27% for the second, the model is given in Fig III.16.

It can be observed in Fig. III.17 that there are no more unstable modes thanks to this new pattern and that the minimum damping coefficient is $\xi_n = 0.001\%$. It is therefore still possible to stabilise the model even if the Coriolis effect is present. However, it is necessary to use a pattern with a higher level of detuning to compensate for frequency separations due to the Coriolis effect and still allow modal interactions of the tuned modes to obtain a stabilising effect against flutter.

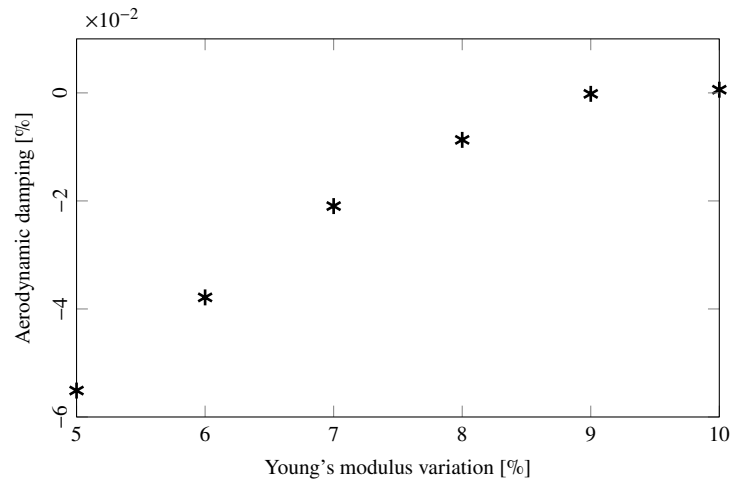


Figure III.15 – Minimum damping coefficient of the best detuning pattern for different Young's modulus variation.

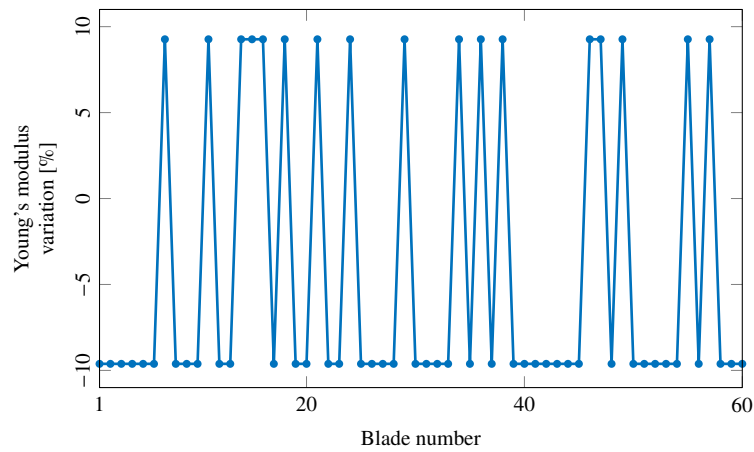


Figure III.16 – Best detuning pattern given by a genetic algorithm with the Coriolis effect.

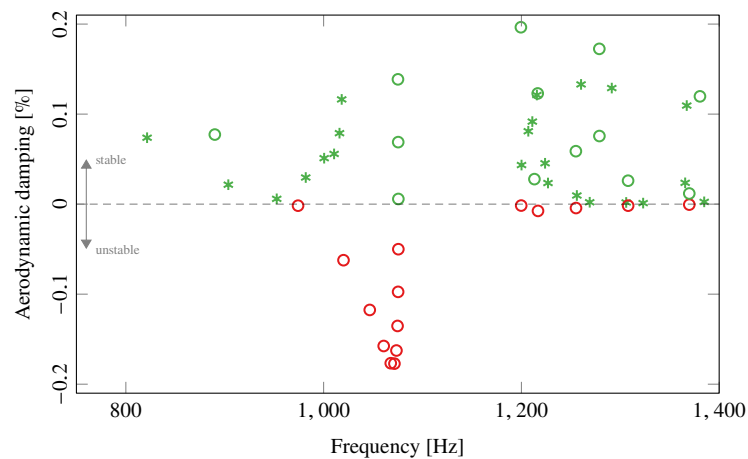


Figure III.17 – Aerodynamic damping versus the frequency for the model with the Coriolis effect in the tuned case [O] and in the detuned case [*]. The negative aerodynamic damping coefficients are represented in red and the positive ones in green.

Chapter summary

The objective of this chapter was to improve the understanding of the aerodynamic stability of bladed discs subject to the Coriolis effect combined with detuning. The approach of the problem was simplified using Whitehead's theory of incompressible flow on cascade blades and a lumped mass-spring model. This enabled the modeling of a bladed disc subjected to flutter instability. At this stage, the addition, or omission, of the Coriolis effect in a tuned structure seems to have a weak influence on the aerodynamic coefficients of the system.

A detuning pattern was used to allow the stabilisation of the modes subjected to flutter. This pattern was chosen without taking the Coriolis effect into account and using two different strategies, the first one was the subspace optimisation strategy and the second one was a genetic algorithm. The two methods appear to be roughly equivalent, although the advantage of the genetic algorithm is that it can vary the values of the Young's modulus of the blades, but the calculation time is greater because of the larger number of simulations.

Once the Coriolis effect was activated, some modes became unstable due to the frequency separation of the modes, which did not allow sufficient interaction to create stability. It has been shown that these interactions are due to the Coriolis effect, which in some cases tends to isolate the modes in frequency (especially with strong participation of the disc). After using the same genetic algorithm, taking into account the Coriolis effect, it was possible to find a model that stabilises the system against flutter. But this was achievable only because detuning was increased, otherwise it was impossible to stabilise the system. This indicates the importance of taking into account the Coriolis effect when choosing detuning patterns when the model is sensitive to it.

Chapter IV

Reduced-Order model for mistuning and Coriolis effects

The finite element method allows to predict with good accuracy the behaviour of complex industrial system. In Section 1.3.2 was mentioned the cyclic symmetry method which allows to limit the modelling to a single sector. However, the analysis of a mistuned structure implies the need to model the full structure with all the sectors, which can significantly increase the computational cost. It is possible to avoid this by using general linear reduction methods such as Craig-Bampton [43] or Craig-Chang [42].

This chapter first reviews the classical methods of modal synthesis as well as those specific to mistuned models. The focus is to adapt these different existing methods to consider the Coriolis effect and to compare the accuracy and efficiency of the different methods. The study is focused on the SNM [222], the CMM [119] and the IMM [207], the results of which are compared to those obtained on a reference mistuned model for validation. These methods have been chosen for their simplicity of implementation, robustness, popularity in the literature and adaptability to the Coriolis matrix. The considered model is a FEM representative of a simplified industrial low pressure compressor bladed drum presenting a strong Coriolis effect and in which mistuning is randomly distributed among the blades. Finally, as the Coriolis and global stiffness matrices depend on the rotational speed, the last section of this chapter is devoted to multi-speed reduction models.

Outline of the chapter

1 Component Mode Synthesis (CMS)	92
1.1 Fixed-interface CMS: Craig-Bampton method	92
1.2 Free-interface CMS: Craig-Chang method	93
1.3 Reduction of the interface degrees of freedom	95
2 State of the art of existing reduction methods for mistuned models.	96
2.1 Subset of Nominal system Modes (SNM)	96
2.2 Component Mode Mistuning (CMM)	97
2.3 Integral Mode Mistuning (IMM)	99
3 Reduced-Order Model validation	101
3.1 Model description	101
3.2 Modal analysis	101
3.3 Free response	103
3.4 Forced response	107

4 Reduction with variable rotational speeds	111
4.1 Polynomial interpolation of the matrices	112
4.2 Parametric Reduced Order Model methodology	116
Chapter summary	118

1 Component Mode Synthesis (CMS)

Component mode synthesis (CMS) also called dynamic sub-structuring methods allows to compute structural models of large size in a suitable time. The first step consists of dividing the total structure into several substructures with interfaces between each substructure. Then, these substructures are reduced using a projection basis and finally reassembled using the defined interfaces to obtain the reduced model. Existing sub-structuring methods can be divided into two distinct groups: fixed-interface methods [81], of which the Craig-Bampton method [43] is the most popular; and free-interface methods [78], of which the Craig-Chang method [42] is one.

In order to facilitate the theoretical development of the CMS methods, the interface dofs \mathbf{p}_f in each substructures are separated from the interior dofs \mathbf{p}_i in the unknowns vector \mathbf{p} . In the same way, the structural matrices are organised to separate the components of the interface dofs from the internal ones. The equation of motion given in Eq. (I.37) is then rewritten for a single substructure as:

$$\left(-\omega^2 \begin{bmatrix} \mathbf{M}_{ii} & \mathbf{M}_{if} \\ \mathbf{M}_{fi} & \mathbf{M}_{ff} \end{bmatrix} + i\omega \begin{bmatrix} \mathbf{G}_{ii} & \mathbf{G}_{if} \\ \mathbf{G}_{fi} & \mathbf{G}_{ff} \end{bmatrix} + \begin{bmatrix} \mathbf{K}_{ii} & \mathbf{K}_{if} \\ \mathbf{K}_{fi} & \mathbf{K}_{ff} \end{bmatrix} \right) \begin{bmatrix} \mathbf{p}_i \\ \mathbf{p}_f \end{bmatrix} = \begin{bmatrix} \mathbf{f}_i^{\text{ext}} \\ \mathbf{f}_f^{\text{ext}} \end{bmatrix}. \quad (\text{IV.1})$$

1.1 Fixed-interface CMS: Craig-Bampton method

The most widely used method for system reduction in the field of structural dynamics is the Craig-Bampton method [43], which is a fixed-interface CMS. The projection basis is composed of normal modes Φ^{CB} and constraint modes Ψ^{CB} . The first allow to define the displacements associated with the internal degrees of freedom and the latter allow the kinematic compatibility between the different substructures.

The normal modes Φ^{CB} are defined as the modes of the substructure when the interface dofs \mathbf{p}_f are clamped. They are the solution of the following eigenvalue problem:

$$\left(-\omega^2 \mathbf{M}_{ii} + \mathbf{K}_{ii} \right) \Phi^{\text{CB}} = \mathbf{0}. \quad (\text{IV.2})$$

To allow for a reduction in size, not all modes are taken into account in the Φ^{CB} matrix, only specific modes are retained by using a frequency criterion or modal effective mass [63].

The constraint modes Ψ^{CB} are obtained by imposing unit displacements to each dof of the interface while keeping the other dofs fixed. Thanks to Eq. (IV.1) with $\omega = 0$ and $\mathbf{f}_i^{\text{ext}} = \mathbf{0}$, it is possible to define the constraint modes as follows:

$$\Psi^{\text{CB}} = -\mathbf{K}_{ii}^{-1} \mathbf{K}_{if}. \quad (\text{IV.3})$$

The number of constraint modes is equal to the number of interface dofs and cannot be reduced because all of these modes must be taken into account in the reduction basis. This number is generally much higher than the number of normal modes selected and it is therefore this

number that defines the size of the reduction basis. The fewer interface dofs, the smaller the ROM.

The reduction matrix associated to a substructure is finally written:

$$\mathbf{R} = \begin{bmatrix} \mathbf{\Phi}^{\text{CB}} & \mathbf{\Psi}^{\text{CB}} \\ \mathbf{0} & \mathbf{I} \end{bmatrix}, \quad (\text{IV.4})$$

which gives the following reduction matrices:

$$\mathbf{M}^{\text{CB}} = \mathbf{R}^{\text{H}}\mathbf{M}\mathbf{R} = \begin{bmatrix} \mathbf{I} & \mathbf{M}_{\text{if}}^{\text{CB}} \\ \mathbf{M}_{\text{fi}}^{\text{CB}} & \mathbf{M}_{\text{ff}}^{\text{CB}} \end{bmatrix}, \quad (\text{IV.5})$$

$$\mathbf{G}^{\text{CB}} = \mathbf{R}^{\text{H}}\mathbf{G}\mathbf{R} = \begin{bmatrix} \mathbf{G}_{\text{ii}}^{\text{CB}} & \mathbf{G}_{\text{if}}^{\text{CB}} \\ \mathbf{G}_{\text{fi}}^{\text{CB}} & \mathbf{G}_{\text{ff}}^{\text{CB}} \end{bmatrix}, \quad (\text{IV.6})$$

$$\mathbf{K}^{\text{CB}} = \mathbf{R}^{\text{H}}\mathbf{K}\mathbf{R} = \begin{bmatrix} \mathbf{\Lambda}^{\text{CB}} & \mathbf{0} \\ \mathbf{0} & \mathbf{K}_{\text{ff}}^{\text{CB}} \end{bmatrix}. \quad (\text{IV.7})$$

where $\mathbf{\Lambda}^{\text{CB}}$ is a diagonal matrix containing the eigenvalues associated to the normal modes $\mathbf{\Phi}^{\text{CB}}$.

After applying this reduction method on each substructure, it is possible to rebuild the complete system using an assembly matrix to connect the interface dofs from one substructure to another. In this manuscript, the Craig-Bampton method has been developed in the classical way without taking into account the Coriolis matrix in the calculation of the normal modes and with a reduction on the Coriolis matrix in the same way as the mass and stiffness matrices. This method has already been used in [34, 225, 227, 228] and is sufficient for the case study in this manuscript as will be shown in the following. Nonetheless, other extensions of the Craig-Bampton method exist for more general systems which allow to take into account the Coriolis matrix in the construction of the reduction matrix [99, 100, 179].

1.2 Free-interface CMS: Craig-Chang method

Craig-Chang's method [42] is one of the free interface modal synthesis methods. The first step is to determine the free interface modes $\mathbf{\Phi}^{\text{CC}}$ of each substructure using the following eigenvalue problem:

$$\left(-\omega^2\mathbf{M} + \mathbf{K}\right)\mathbf{\Phi}^{\text{CC}} = \mathbf{0}. \quad (\text{IV.8})$$

As for the Craig-Bampton method, this matrix $\mathbf{\Phi}^{\text{CC}}$ of free vibration modes is truncated by keeping only a certain number $\mathbf{\Phi}_{\text{k}}$ of them in order to allow a reduction of the model, the modes which are not kept will be noted $\mathbf{\Phi}_{\text{a}}$ and the basis of these modes is arranged such as $\mathbf{\Phi}^{\text{CC}} = [\mathbf{\Phi}_{\text{k}} \ \mathbf{\Phi}_{\text{a}}]$. The projection of the displacements \mathbf{p} on this basis of the free vibration modes gives:

$$\mathbf{p} = \mathbf{\Phi}^{\text{CC}}\mathbf{u} = \mathbf{\Phi}_{\text{k}}\mathbf{u}_{\text{k}} + \mathbf{\Phi}_{\text{a}}\mathbf{u}_{\text{a}}, \quad (\text{IV.9})$$

where \mathbf{u} are the generalised coordinates associated with the modes $\mathbf{\Phi}^{\text{CC}}$.

Next, attachment modes $\mathbf{\Psi}^{\text{CC}}$ must be calculated to take into account the influence of adjacent substructures. They are defined as the response of the substructure to a set of unit forces applied on each interface dof:

$$\mathbf{K}\mathbf{\Psi}^{\text{CC}} = \begin{bmatrix} \mathbf{0} \\ \mathbf{I} \end{bmatrix} = \mathbf{F}. \quad (\text{IV.10})$$

Assuming that the free vibration modes are orthonormalised with respect to the mass matrix and premultiplying Eq. (IV.10) by Φ_k^H gives:

$$\begin{aligned} \mathbf{u}_k &= \left(\Phi_k^H \mathbf{K} \Phi_k \right)^{-1} \Phi_k^H \mathbf{F} \\ &= \Lambda_k^{-1} \Phi_k^H \mathbf{F}, \end{aligned} \quad (\text{IV.11})$$

where Λ_k is a diagonal matrix containing the eigenvalues of the kept free vibration modes. Injecting Eq. (IV.10) and Eq. (IV.11) in Eq. (IV.9) gives:

$$\begin{aligned} \Phi_a \mathbf{u}_a &= \Psi - \Phi_k \mathbf{u}_k \\ &= \left(\mathbf{K}^{-1} - \Phi_k \Lambda_k^{-1} \Phi_k^H \right) \mathbf{F} \\ &= \mathbf{G} \mathbf{F}. \end{aligned} \quad (\text{IV.12})$$

Equation (IV.9) can be rewritten:

$$\mathbf{p} = \Phi_k \mathbf{u}_k + \mathbf{G} \mathbf{F}. \quad (\text{IV.13})$$

Taking into account the internal and interface dofs gives:

$$\begin{bmatrix} \mathbf{p}_i \\ \mathbf{p}_f \end{bmatrix} = \begin{bmatrix} \Phi_{k,i} \\ \Phi_{k,f} \end{bmatrix} \mathbf{u}_k + \begin{bmatrix} \mathbf{G}_{ii} & \mathbf{G}_{if} \\ \mathbf{G}_{fi} & \mathbf{G}_{ff} \end{bmatrix} \begin{bmatrix} \mathbf{0} \\ \mathbf{I} \end{bmatrix}. \quad (\text{IV.14})$$

This allows to express the internal displacements \mathbf{p}_i in terms of interfaces displacements \mathbf{p}_f and generalised coordinates \mathbf{u}_k :

$$\mathbf{p}_i = \left(\Phi_{k,i} - \mathbf{G}_{if} \mathbf{G}_{ff}^{-1} \Phi_{k,f} \right) \mathbf{u}_k + \mathbf{G}_{if} \mathbf{G}_{ff}^{-1} \mathbf{p}_f. \quad (\text{IV.15})$$

It is now possible to express the reduction matrix in the same way as in the Craig-Bampton method:

$$\mathbf{R} = \begin{bmatrix} \Phi_{k,i} - \mathbf{G}_{if} \mathbf{G}_{ff}^{-1} \Phi_{k,f} & \mathbf{G}_{if} \mathbf{G}_{ff}^{-1} \\ \mathbf{0} & \mathbf{I} \end{bmatrix}. \quad (\text{IV.16})$$

One of the difficulties of this method is when the stiffness matrix of the substructure is not invertible due to rigid-body modes. For this, it is necessary to use an alternative formulation which was first proposed in MacNeal method [123].

Firstly, the equation of motion project on the rigid-body modes gives:

$$\ddot{\mathbf{u}}_r = \Phi_r^H \mathbf{F}, \quad (\text{IV.17})$$

where Φ_r are the rigid-body modes and \mathbf{u}_r the related generalised coordinates such as:

$$\ddot{\mathbf{p}}_r = \Phi_r \ddot{\mathbf{u}}_r. \quad (\text{IV.18})$$

Secondly, the inertia force \mathbf{F}_I due to the applied force \mathbf{F} gives:

$$\mathbf{F}_I = -\mathbf{M} \ddot{\mathbf{p}}_r, \quad (\text{IV.19})$$

and using Eq. (IV.17) and Eq. (IV.18):

$$\mathbf{F}_I = -\mathbf{M} \Phi_r \Phi_r^H \mathbf{F}. \quad (\text{IV.20})$$

As for the normal modes of the Craig-Bampton's method, only certain modes will be kept in the basis in order to guarantee a reduction of the model size. These modes are called branch modes in [15, 83] or interface modes in [200]. The transformation matrix of this method is then:

$$\mathbf{T}_s = \begin{bmatrix} \mathbf{I}_{i,1} & & & \\ & \ddots & & \\ & & \mathbf{I}_{i,N} & \\ & & & \Phi \end{bmatrix}. \quad (\text{IV.26})$$

In the literature, reducing the interfaces in addition to a sub-structuring method such as Craig-Bampton or Craig-Chang is generally referred to as double modal synthesis. These methods have been shown to have a strong reduction potential in the study of cyclic symmetric structures [201].

2 State of the art of existing reduction methods for mistuned models.

Among all the ROMs that have been developed for linear mistuned bladed discs, one can mention the Secondary Modal Analysis Reduction Technique (SMART) proposed by Bladh et al. [18, 19], which uses the Craig-Bampton method and condenses the interface degrees of freedom (dofs) using cyclic symmetric properties. Petrov et al. [150] developed a method in which the mistuning is introduced by lumped masses, dampers and springs attached to some degrees of freedom of the blades. Yang and Griffin [221, 222] presented the Component Mode Based (CMB) and the Subset of Nominal Modes (SNM) which uses a subset of the tuned mode shapes to represent the mistuned mode shape. Feiner and Griffin [57] suggested a simplification of the SNM with the Fundamental Mistuning Model (FMM) for an isolated family, and Martel et al. [126] provided the Asymptotic Mistuning Model (AMM) which selects only the active modes of a family. Lim et al. [119] proposed the Component Mode Mistuning (CMM), which draws on the SNM and Craig-Bampton principles and is used to quickly generate a mistuned ROM. Vargiu et al. [207] extended the CMM method with the Integral Mode Mistuning to allow for mistuning on the entire sector and not only on the blade. Fitzner et al. [59] suggested the Nodal Energy Weighted Transformation (NEWT), which is a method derived from the CMM and which differs from it by the mistuning projection approach. This section presents the SNM, CMM and IMM methods for a mistuned bladed disc system considering the classical equation of motion:

$$\left(-\omega^2 \mathbf{M} + i\omega(\mathbf{C} + \mathbf{G}) + \mathbf{K}\right) \mathbf{p} = \mathbf{f}_{\text{ext}}. \quad (\text{IV.27})$$

2.1 Subset of Nominal system Modes (SNM)

One of the first methods developed for the reduction of small mistuned bladed disc models was the Subset of Nominal system Modes (SNM) established by Yang and Griffin [222]. For the simplicity of the future development and in the same way as in Chapter II and III, let us consider the case of stiffness mistuning only:

$$\mathbf{K} = \mathbf{K}^0 + \Delta \mathbf{K}, \quad (\text{IV.28})$$

where \mathbf{K}^0 is the stiffness matrix of the tuned model and $\Delta \mathbf{K}$ is the stiffness perturbation. This last matrix is often computed as a variation of Young's modulus in different parts of the model. For the mass, damping, and Coriolis matrices, they are the same for the tuned and mistuned models.

The SNM method is based on the assumption that the unknown displacement vector for a small mistuned model can be approximated as a subset of the tuned modes

$$\mathbf{p} \approx \Phi^0 \mathbf{u}. \quad (\text{IV.29})$$

where \mathbf{u} is the new reduced unknown vector and in which each term determines the contribution of each tuned mode in the response. Φ^0 and Λ^0 are the chosen eigenvectors and eigenvalues used for the subset of nominal modes and which satisfy the system

$$\mathbf{K}^0 \Phi^0 = \mathbf{M} \Phi^0 \Lambda^0. \quad (\text{IV.30})$$

Thus, the equation of motion of the mistuned system Eq. (IV.27) can be reduced on a subset of nominal modes composed of the tuned modes present in a frequency range of interest and by premultiplying Eq. (IV.27) by Φ^{0H} the Hermitian of Φ^0

$$\left(-\omega^2 \mathbf{I} + i\omega(\hat{\mathbf{C}} + \hat{\mathbf{G}}) + \Lambda^0 + \Phi^{0H} \Delta \mathbf{K} \Phi^0 \right) \mathbf{u} = \hat{\mathbf{f}}_{\text{ext}}, \quad (\text{IV.31})$$

where

$$\Phi^{0H} \mathbf{M} \Phi^0 = \mathbf{I}, \quad (\text{IV.32})$$

$$\Phi^{0H} \mathbf{C} \Phi^0 = \hat{\mathbf{C}}, \quad (\text{IV.33})$$

$$\Phi^{0H} \mathbf{G} \Phi^0 = \hat{\mathbf{G}}, \quad (\text{IV.34})$$

$$\Phi^{0H} \mathbf{K}^0 \Phi^0 = \Lambda^0, \quad (\text{IV.35})$$

$$\Phi^{0H} \mathbf{f}_{\text{ext}} = \hat{\mathbf{f}}_{\text{ext}}. \quad (\text{IV.36})$$

The advantages of this method are that the blades and the disc are treated as a single structure, the tuned mode can be calculated using the cyclic symmetry properties to accelerate the computing time of the reduction basis and the reduced model has as many degrees of freedom as the number of retained modes. There is no need to calculate the reduced tuned mass and stiffness matrices as there are directly the identity and diagonal eigenvalues matrices. The weak point of this method is the calculation of the reduced perturbation matrix, because it is a matrix operation of the same size as the full model which can be very time-consuming for a Monte Carlo simulation.

2.2 Component Mode Mistuning (CMM)

The Component Mode Mistuning method (CMM) was first proposed by Lim and al. [119]. In this method, the system is divided into different substructures. The first substructure is the whole tuned bladed disc, in which the ROM is generated using the tuned modes as in the SNM method. The other substructures are the blade mistuning components defined by the difference between the mistuned blades and the tuned blades. The mistuning can be introduced in mass or stiffness, but as for the SNM, the development here will be focused on the stiffness. However, in this method, the mistuning can only be considered for the blades as represented in Fig. IV.1 and in a proportional manner, as follows:

$$\Delta \mathbf{K}_n^b = \delta_n \mathbf{K}^b. \quad (\text{IV.37})$$

At rest (0 rpm), this definition of proportional mistuning may be due to a variation of Young's modulus [18].

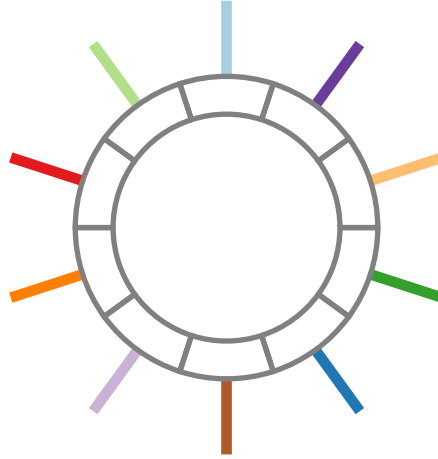


Figure IV.1 – Representation of a cyclic structure with blade mistuning as introduced with the CMM method.

For small mistuning, the CMM and SMM are very similar in the reduced equation of motion, even though for the CMM the mistuning can only be located on the blades. The difference stems from the mistuning projection, introduced by Bladh et al. [17]. By assuming that the mode shapes of the tuned and mistuned blades are the same, the mistuned matrix is projected onto the chosen eigenvectors Φ_{CB} of the cantilevered tuned blade fixed at the blade-disc interface. However, these modes are not sufficient to describe the displacements at the blade-disc interface. If these displacements are not small, it is necessary to introduce constraint modes Ψ_{CB} , which are obtained by applying a unit displacement to each dof of the blade-disc interface while keeping the other dofs fixed. It follows that they can be determined using the following equation:

$$\Psi_{CB} = -\mathbf{K}_{ii}^{b-1} \mathbf{K}_{if}^b, \quad (\text{IV.38})$$

where superscript b illustrates the tuned blade and subscripts i and f indicate the internal blade dofs and the boundary blade dofs. The projection is very similar to the Craig-Bampton transformation [43].

$$\Phi_n^b = \begin{bmatrix} \Phi_{n,i}^b \\ \Phi_{n,f}^b \end{bmatrix} \approx \begin{bmatrix} \Phi_{CB} & \Psi_{CB} \\ \mathbf{0} & \mathbf{I} \end{bmatrix} \begin{bmatrix} \mathbf{Q}_n^{\Phi_{CB}} \\ \mathbf{Q}_n^{\Psi_{CB}} \end{bmatrix} = \mathbf{T}_{CB} \mathbf{Q}_n \quad (\text{IV.39})$$

where Φ_n^b is the matrix of the tuned modes limited to the blade dofs of the n^{th} sector. $\mathbf{Q}_n^{\Phi_{CB}}$ and $\mathbf{Q}_n^{\Psi_{CB}}$ are respectively the modal participation factors of the cantilevered tuned blade modes and constraint modes for the blade of the n^{th} sector. The participation factors matrix can be found directly with Eq. (IV.39)

$$\mathbf{Q}_n^{\Psi_{CB}} = \Phi_{n,f}^b. \quad (\text{IV.40})$$

Premultiplying Eq. (IV.39) by $\begin{pmatrix} \left[\Phi_{CB} \\ \mathbf{0} \right]^H & \mathbf{K}^b \end{pmatrix}$ and using the orthogonality of the modes allows to determine the expression of $\mathbf{Q}_n^{\Phi_{CB}}$

$$\mathbf{Q}_n^{\Phi_{CB}} = \Lambda_{CB}^{-1} \begin{bmatrix} \Phi_{CB} \\ \mathbf{0} \end{bmatrix}^H \mathbf{K}^b \Phi_n^b, \quad (\text{IV.41})$$

where $\mathbf{\Lambda}_{\text{CB}}$ is the diagonal matrix of the cantilevered tuned blade eigenvalues. As the mistuning is only considered for the blade stiffening perturbation, the matrix $\Delta\mathbf{K}$ is block diagonal and its reduction can be expressed as the following sum:

$$\mathbf{\Phi}^{0\text{H}} \Delta\mathbf{K} \mathbf{\Phi}^0 = \sum_{n=1}^N \mathbf{\Phi}_n^{\text{bH}} \Delta\mathbf{K}_n^{\text{b}} \mathbf{\Phi}_n^{\text{b}}, \quad (\text{IV.42})$$

where $\Delta\mathbf{K}_n^{\text{b}}$ is the stiffness mistuning perturbation of the n^{th} blade. Substituting Eq. (IV.39) in Eq. (IV.42) gives

$$\mathbf{\Phi}^{0\text{H}} \Delta\mathbf{K} \mathbf{\Phi}^0 \approx \sum_{n=1}^N \mathbf{Q}_n^{\text{H}} \mathbf{T}_{\text{CB}}^{\text{H}} \Delta\mathbf{K}_n^{\text{b}} \mathbf{T}_{\text{CB}} \mathbf{Q}_n. \quad (\text{IV.43})$$

Using the assumption that the mistuning is proportional on the blades (Eq. (IV.37)), it is now possible to simplify Eq. (IV.43)

$$\mathbf{\Phi}^{0\text{H}} \Delta\mathbf{K} \mathbf{\Phi} \approx \sum_{n=1}^N \delta_n \mathbf{Q}_n^{\text{H}} \mathbf{T}_{\text{CB}}^{\text{H}} \mathbf{K}^{\text{b}} \mathbf{T}_{\text{CB}} \mathbf{Q}_n. \quad (\text{IV.44})$$

One advantage of this method compared to the SNM is that the mistuning parameters δ_n are expressed directly in the reduced space, and the expression $(\mathbf{Q}_n^{\text{H}} \mathbf{T}_{\text{CB}}^{\text{H}} \mathbf{K}^{\text{b}} \mathbf{T}_{\text{CB}} \mathbf{Q}_n)$ has to be calculated only once for each tuned sector and a given subset of nominal system modes. This allows fast generation of ROMs with different mistuning patterns without going back to the full model, which is really useful for Monte Carlo simulations.

In many articles referring to the CMM [102, 119, 141, 207], there is an assumption that the displacements at the blade-disc interface are very small, so that only the dominant cantilever blade modes are sufficient to project the mistuning. Accordingly, Eq. (IV.44) becomes:

$$\mathbf{\Phi}^{0\text{H}} \Delta\mathbf{K} \mathbf{\Phi} \approx \sum_{n=1}^N \delta_n \mathbf{Q}_n^{\Phi_{\text{CB}}} \mathbf{\Lambda}_{\text{CB}} \mathbf{Q}_n^{\Phi_{\text{CB}}}. \quad (\text{IV.45})$$

But in the case of a blade disc model with a strong Coriolis effect, the interaction between the blades and the disc is very strong and the displacement at the blade-disc interface is not negligible, so this assumption will not be done in what follows.

2.3 Integral Mode Mistuning (IMM)

The Integral Mode Mistuning proposed by Vargui and al. [207] is an extension of the CMM to take into account sector mistuning instead of blade mistuning, as shown in Fig. IV.2. As for the SNM and CMM, the IMM uses the small mistuning approximation to write Eq. (IV.31). The mistuning stiffness matrix $\Delta\mathbf{K}$ is no longer block diagonal, but it is still possible to express its reduction as a sum:

$$\mathbf{\Phi}^{0\text{H}} \Delta\mathbf{K} \mathbf{\Phi}^0 = \sum_{n=1}^N \mathbf{\Phi}_n^{\text{sH}} \Delta\mathbf{K}_n^{\text{s}} \mathbf{\Phi}_n^{\text{s}}, \quad (\text{IV.46})$$

where $\Delta\mathbf{K}_n^{\text{s}}$ is the stiffness perturbation matrix, and $\mathbf{\Phi}_n^{\text{s}}$ the subset of tuned modes matrix restrained to the n^{th} sector, including the left (l) and right (r) interfaces dofs.



Figure IV.2 – Representation of a cyclic structure with sector mistuning as introduced with the IMM method.

$$\Phi_n^s \text{H} \Delta \mathbf{K}_n^s \Phi_n^s = \begin{bmatrix} \Phi_{n,r}^s \\ \Phi_{n,i}^s \\ \Phi_{n,l}^s \end{bmatrix}^{\text{H}} \begin{bmatrix} \Delta \mathbf{K}_{n,rr}^s & \Delta \mathbf{K}_{n,ri}^s & \mathbf{0} \\ \Delta \mathbf{K}_{n,ir}^s & \Delta \mathbf{K}_{n,ii}^s & \Delta \mathbf{K}_{n,il}^s \\ \mathbf{0} & \Delta \mathbf{K}_{n,li}^s & \Delta \mathbf{K}_{n,ll}^s \end{bmatrix} \begin{bmatrix} \Phi_{n,r}^s \\ \Phi_{n,i}^s \\ \Phi_{n,l}^s \end{bmatrix} \quad (\text{IV.47})$$

The mistuning matrix is no longer projected onto the cantilevered blade modes. They are replaced by the modes of a whole tuned sector with free interfaces. Then, the tuned modes Φ_n^s are expressed as a linear combination of the free-interface sector modes Φ^{FS} using participation factors \mathbf{Q}_n

$$\Phi_n^s \approx \Phi^{\text{FS}} \mathbf{Q}_n. \quad (\text{IV.48})$$

Premultiplying Eq. (IV.48) with $(\Phi^{\text{FSH}} \mathbf{K}^{\text{FS}})$ where \mathbf{K}^{FS} is the stiffness matrix of the tuned free-interface sector, and using the orthogonality of the modes allows to determine the expression of \mathbf{Q}_n

$$\mathbf{Q}_n = \Lambda^{\text{FS}-1} \Phi^{\text{FSH}} \mathbf{K}^{\text{FS}} \Phi_n^s, \quad (\text{IV.49})$$

where Λ^{FS} is the diagonal matrix of the free-interface sector eigenvalues. Replacing Eq. (IV.48) in Eq. (IV.46), and using proportional mistuning gives

$$\Phi^{0\text{H}} \Delta \mathbf{K} \Phi^0 \approx \sum_{n=1}^N \delta_n \mathbf{Q}_n \text{H} \Lambda^{\text{FS}} \mathbf{Q}_n. \quad (\text{IV.50})$$

The advantages of the IMM are the same as those of the CMM: the mistuning parameters δ_n are expressed directly in the reduced space, and the expressions $\mathbf{Q}_n \text{H} \Lambda^{\text{FS}} \mathbf{Q}_n$ have to be calculated only once. However, with the full CMM developed here, there is a need to calculate constraint modes, which is not the case for the IMM. In contrast, the cantilevered blade mode shapes are well suited to the mode shapes of the whole tuned structure, which is not necessarily the case of the free-interface modes, where the free interface allows more flexibility on the disc than in the whole structure. As a consequence, it requires more free-interface modes with the IMM than cantilevered blade modes with the CMM.

3 Reduced-Order Model validation

Now that the different reduction methods have been presented, it is necessary to validate them for the numerical model used in the analysis of the interaction between the Coriolis effect and mistuning. First, the numerical model will be presented, then the validation will be done for the three different reduction methods in the case of free response and in the case of a forced response.

3.1 Model description

The model chosen to study the interaction between the Coriolis effect and mistuning is a simplified industrial bladed drum of a low-pressure compressor, with a single stage of blades and 20 sectors. This model presents a high sensitivity to the Coriolis effect over some modes because of the drum flexibility [195]. The numerical simulations were carried out at 10,000 rpm as the Coriolis effect is significant at this level of rotational speed. The FEM has been realised with ANSYS and the procedure of extraction of the matrices with a centrifugal preload is presented in Appendix D.

The FEM was generated from a reference sector and using the cyclic symmetry section represented by a blue surface in Fig. IV.3a. The full FEM is presented in Fig. IV.3b and was set as the benchmark for the comparison with the ROM. It is discretised using 33,140 quadratic elements with 107,520 nodes. The drum is clamped on the 3,200 backside nodes, represented by a yellow surface in Fig. IV.3a, which gives a full-size model of 312,960 dofs. The material used for the modelling is a standard steel of which the properties are listed in Table IV.1.

Table IV.1 – Material properties of the standard steel.

Material property	Value	Unit
Mass density (ρ)	7850	kg/m ³
Young's modulus (E)	200	GPa
Poisson's ratio (ν)	0.3	-

3.2 Modal analysis

The evolution of the modes with the rotational speed can be summarised in a Campbell diagram (Fig. IV.4). It can be observed that some modes are split in frequency due to the Coriolis effect, especially for the 1ND and 2ND modes of the first family and the 3ND of the second family. All of these modes are disc-dominated modes except for the 1ND-BW mode of the first family, which is a blade-disc mode. The accumulation of modes above the 1ND-BW 1 are blade-dominated modes with a first flexural mode and different nodal diameter numbers.

The modes of the tuned structure at 10,000 rpm are shown in Fig. IV.5a, representing their frequency versus their nodal diameter number. Disc-dominated modes are represented by slanted lines; by contrast, the horizontal lines represent blade-dominated modes. Around 700 Hz, it is dominated by the first flexural mode (1F) (Fig. IV.6a), around 2,000 Hz, it is the first torsional mode (1T) (Fig. IV.6b), and around 2,500 Hz, it is the second flexural mode (2F) (Fig. IV.6c). At the crossing between two modal families, there is what appears to be a veering region: the blade and disc-dominated modes veer away from each other, and the modes in this region are a combination of blade and disc motions. Three of these regions are surrounded by squares in Fig. IV.5a. Only the veering for the 1ND between the first and the second families will be studied later on in this chapter due to the proximity of the modes as

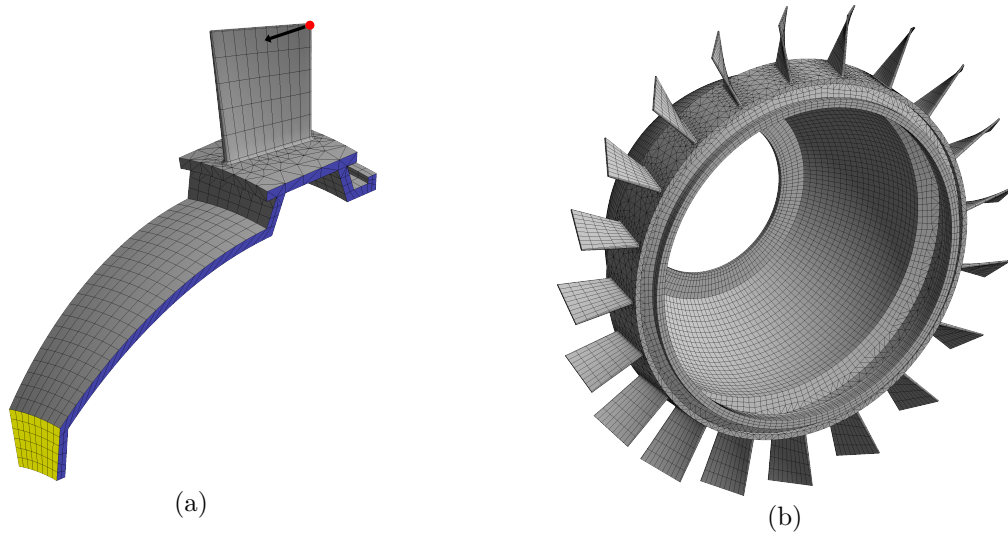


Figure IV.3 – Finite element mesh for the 20-sector bladed drum. (a) Reference sector. (b) Full assembly model. [■]: Clamped surface. [■]: Cyclic symmetric section. [●]: Excitation node. [→]: Excitation vector.

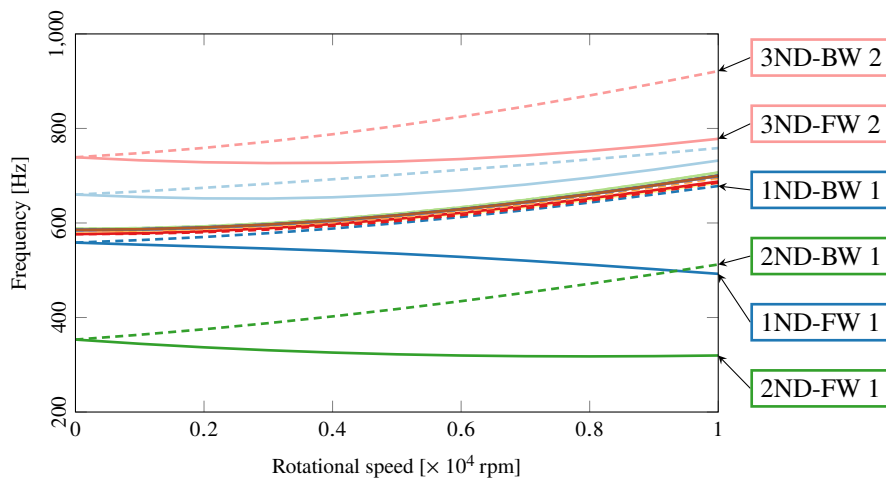


Figure IV.4 – Campbell diagram of the tuned bladed drum between 200 Hz and 1,000 Hz. [—]: Forward wave modes. [---]: Backward wave modes.

shown in Fig. IV.5b. It is known that localisation due to mistuning can be strong in these regions [20, 82, 152].

The force response study will be focused on three different regions and EOs, which are surrounded by circles in Fig. IV.5a. These regions will be named from left to right: the veering region, the low modal density region and the high modal density region.

Each of these regions were chosen for their different characteristics. The low modal density region was chosen because the sensitivity to the Coriolis effect is important with a strong disc participation as can be seen in Fig. IV.7a. The high modal density region has a predominant blade participation on the first bending mode as shown in Fig. IV.7b and a lot of modes close in frequency mode which means that mistuning effects may be dominating. And finally the veering region, with a mixed blade-disc mode as observed in Fig. IV.7c where both the Coriolis and mistuning effects are present with a strong amplification of the response [31]. The characteristics of each region will be developed further in Chapter V.

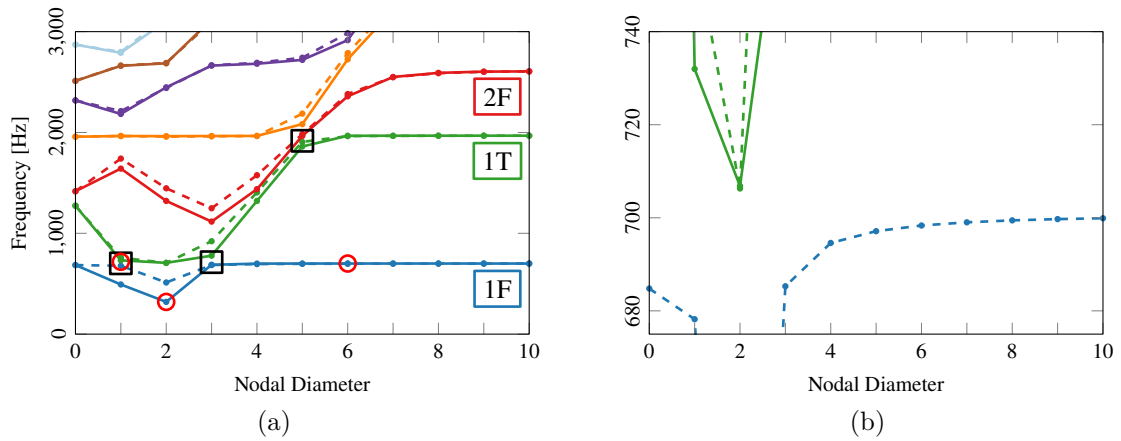


Figure IV.5 – Natural frequencies versus number of nodal diameter at 10,000 rpm. All different modal families are represented with different colours. [—]: Forward wave modes. [--]: Backward wave modes. [□]: Veering regions. [○]: Studied modes for the numerical simulations. (a) Overall view. (b) Frequency expansion on the veering region.

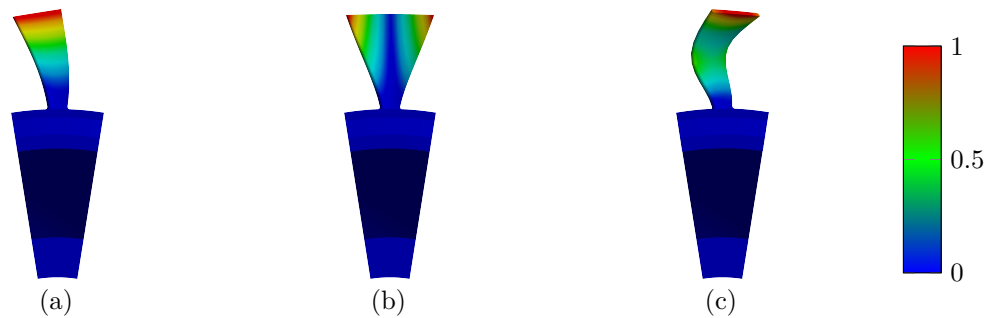


Figure IV.6 – Mode shapes of the three first blade-dominated mode families. (a) First flexural mode around 700 Hz. (b) First torsional mode around 2,000 Hz. (c) Second flexural mode around 2,500 Hz.

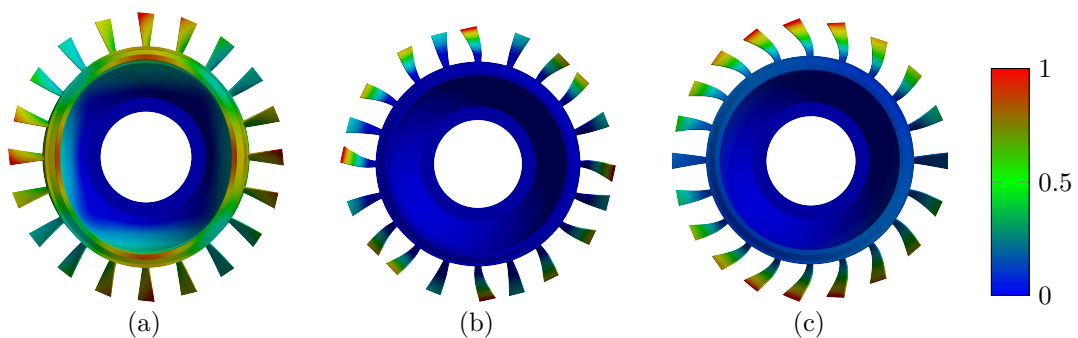


Figure IV.7 – Modal shape of three studied modes. (a) First mode: 2ND-FW 1. (b) Second mode: 6ND-FW 1. (c) Third mode: 1ND-BW 1

3.3 Free response

This subsection is devoted to validating the SNM, CMM and IMM ROMs for a free response. The numerical simulations investigating the interaction between the Coriolis effect and the mistuning will be in the frequencies around the first family modes and some modes of the

second family. For this reason, the validation will focus on the modes below 1,000 Hz for each method, which corresponds to the 26 first mistuned modes. As mentioned in the previous section, the mistuning is introduced by a mistuning parameter δ_n for each sector or blade depending on whether the mistuning is introduced on the whole sector or only on the blade Eq. (IV.37). The mistuning parameters for the validation simulations are generated using a normal distribution with zero mean and 2.5 % standard deviation. The mistuning pattern is summarised in Table IV.2.

Table IV.2 – Mistuning pattern introduced in the FEM using a normal distribution with zero mean and 2.5 % standard deviation.

Sector	1	2	3	4	5	6	7	8
δ_n	-0.00256	-0.00604	0.00798	0.00782	-0.02162	-0.00075	-0.00412	0.01569
Sector	9	10	11	12	13	14	15	16
δ_n	0.02733	0.02773	-0.02159	0.00193	-0.03035	-0.02784	-0.00017	0.03832
Sector	17	18	19	20				
δ_n	-0.01924	0.00928	-0.00564	0.02793				

3.3.1 Mode choice of the reduction basis

In Section IV.2, the tuned eigenvectors were determined from the system in Eq. (IV.30), which did not take into account the Coriolis matrix. With the Coriolis matrix, the system has to be recasted into the state-space representation, which doubles the size of the problem and increases the computational time. A very large system can increase very significantly the calculation of the tuned modes. As an example, for this FEM and using the cyclic symmetry with a MATLAB program, it takes 67.29 s to calculate the 60 first modes without the Coriolis matrix and 450.26 s to calculate the 60 first modes with the Coriolis matrix.

The tuned eigenvectors calculated with and without the Coriolis matrix have been compared using the Normalized Cross Orthogonality check (NCO) [113]. NCO is very similar to the Modal Assurance Criterion (MAC) but it also gives information about the orthogonality of the modes with regard to a matrix.

$$NCO(i, j) = \frac{|\phi_i^H \mathbf{B} \tilde{\phi}_j|^2}{|\phi_i^H \mathbf{B} \phi_j| |\tilde{\phi}_i^H \mathbf{B} \tilde{\phi}_j|}, \quad (\text{IV.51})$$

where ϕ_i is the mistuned mode of the FEM and $\tilde{\phi}_j$ is the mistuned mode of the ROM projected onto the FEM dofs using the subset of nominal mode basis. \mathbf{B} is the augmented matrix coming from the state-space representation of the full model [25]. The state-space representation, imposed by the Coriolis matrix, also applies to the modes ϕ_i and $\tilde{\phi}_j$.

$$\mathbf{B} = \begin{bmatrix} \mathbf{K} & \mathbf{0} \\ \mathbf{0} & \mathbf{M} \end{bmatrix} \quad (\text{IV.52})$$

If the NCO has a value near one, it indicates that the eigenvectors are very similar; on the contrary, a NCO near zero means that the eigenvectors are almost orthogonal with respect to the matrix \mathbf{B} . For the sake of clarity, Fig. IV.8 shows the NCO matrix for the eigenvectors of the two first tuned families, but the results are similar for the other families. ϕ_j are the modes calculated without the Coriolis matrix, and ψ_i the modes calculated with the Coriolis matrix.

There is an excellent accuracy between the modes calculated with and without the Coriolis matrix. On the diagonal, only five NCO indexes are below 0.95 -surrounded by squares in Fig.

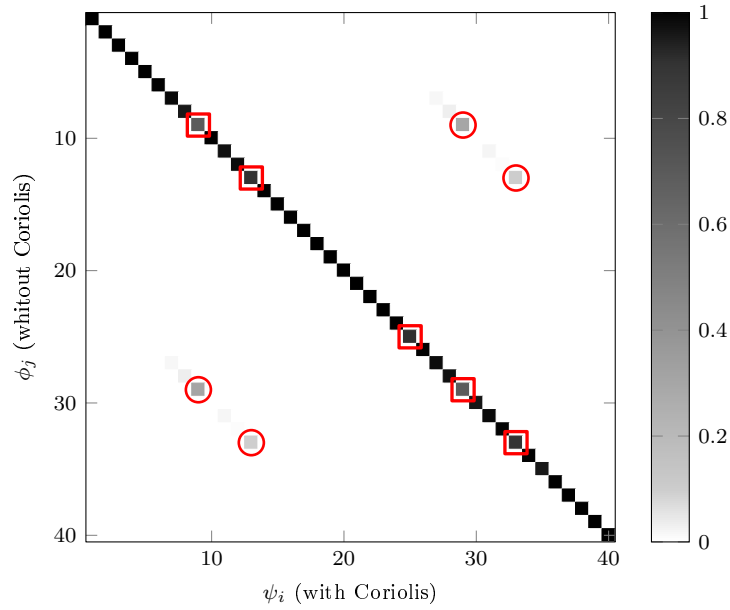


Figure IV.8 – Matrix of the Normalized Cross Orthogonality check (NCO) for the comparison between the eigenvectors calculated with Coriolis (ψ_i) and the eigenvectors calculated without Coriolis (ϕ_j) at 10,000 rpm. \circ NCO > 0.05 for the off-diagonal terms. \square NCO < 0.95 for the terms on the diagonal.

IV.8- and four indexes are above 0.05 NCO for the off-diagonal terms which are surrounded by circles in Fig. IV.8. These indexes correspond to the 1ND-BW and 3ND-FW modes of the first and second families and the 5ND-BW of the second family. All of these modes are in veering regions, as evidenced by Fig. IV.5a. This can be explained by the fact that because of the Coriolis matrix, the modes of two families near a veering region will be more or less close to each other in frequency and the shapes of the tuned modes evolve with the location in the veering region. For example, 1ND-BW modes of the first and second families are separated by 138.67 Hz without the Coriolis matrix, while with the Coriolis matrix, this frequency gap is reduced to 80.27 Hz (Fig. IV.5b). 1ND-FW and 1ND-BW modes of the first family have the same shape without Coriolis, but with Coriolis, 1ND-FW mode changes for a disc-dominated mode and 1ND-BW to a blade-dominated mode.

One of the hypotheses is that the shape of a tuned mode with the Coriolis effect in a veering region can be captured well by using a combination of tuned modes without considering the Coriolis effect. Therefore, it is possible to build the basis without the Coriolis matrix but still be able to accurately capture the Coriolis effect. For this reason, all the reductions carried out hereafter in this manuscript, are built without taking the Coriolis matrix into account, but the reduced Coriolis matrix is kept in the modelling using Eq. (IV.34).

With an equivalent mistuning pattern and the same reduction basis, the CMM ROM converges to the SNM ROM with the number of cantilevered blade modes. This can be better observed by examining the modal participation factors in Eq. (IV.39): if one takes all the cantilevered blade modes, the subset of nominal modes limited to the blade dofs Φ_n^b is the same as the one used in the SNM. The same can be done for the IMM ROM, which converges to the SNM ROM when increasing the number of free-interface sector modes using Eq. (IV.48). The choice was made to set the SNM as a reference for the CMM and IMM so that the choices of the tuned modes are made with the SNM and then one only needs to choose the number of cantilevered modes for the CMM and the number of free-interface modes for the IMM to

converge to the SNM ROM.

For this reason, there are two cases with the SNM. The first one is the introduction of a proportional stiffness mistuning on the blade equivalent to the CMM (Eq. (IV.37)), and the second one is a proportional stiffness mistuning on the whole sector equivalent to the IMM. Looking at the numbers of modal families taken into account in the reduction basis, it is possible to look at the maximum relative error of the first 26 modes where results are recorded in Table IV.3. To have a maximum relative error below 0.01 %, the tuned modes of the 25 first families' modes are selected to established the reduction basis, forming a final ROM of 500 dofs.

Table IV.3 – Relative error for different number of modal families in the reduction basis with the SNM.

Number of modal families	5	10	15	20	25
Relative error with sector mistuning	0.160%	0.118%	0.074%	0.041%	0.009%
Relative error with blade mistuning	0.050%	0.048%	0.029%	0.018%	0.009%

The three first cantilevered modes are, respectively, the first flexural mode, the first torsional mode and the second flexural mode, which are also the mode shapes of the blade-dominated modes of the three first families. These cantilevered modes are chosen to calculate the modal participation factors (Eq. (IV.41)) used in the CMM method and show a good convergence to the results calculated using the SNM as shown in Table IV.4. The number of cantilevered modes does not seem to have a great influence on the quality of the results and only the consideration of the three first cantilevered modes is sufficient to have a maximum relative error below 0.01 %. However, the first free-interface modal shapes have a dynamic quite different from that of the whole structure. It is therefore necessary to use the 200 first free-interface modes to compute the modal participation factors (Eq. (IV.49)) used in the IMM and have a good convergence to the SNM ROM results as shown in Table IV.5.

Table IV.4 – Relative error for different number of cantilevered modes with the CMM.

Number of cantilevered modes	1	3	10	50	100
Relative error	0.011%	0.009%	0.009%	0.009%	0.009%

Table IV.5 – Relative error for different number of free-interface modes with the IMM.

Number of free-interface modes	10	50	100	200	1,000
Relative error	0.068%	0.029%	0.011%	0.009%	0.009%

The computational cost to obtain each ROM is given in Table IV.6.

3.3.2 Comparison of the eigenvalues and eigenvectors of the ROMs with the FEM

The first criterion of validation is to calculate the relative error of the ROMs' natural frequencies versus the full mistuned model

$$\varepsilon = \frac{|f_{\text{ROM}} - f_{\text{FEM}}|}{f_{\text{FEM}}} . 100, \quad (\text{IV.53})$$

Table IV.6 – Computational cost to perform the SNM, CMM and IMM reductions. The simulations were run on an Intel(R) Core(TM) i7-10700K CPU @ 3.80GHz.

	SNM	CMM	IMM
Tuned modes	48 s	48 s	48 s
Cantilevered blade modes	-	<1 s	-
Free-interface sector modes	-	-	4 s
Matrices computing	16 s	8 s	4 s
Total	64 s	56 s	60 s

where f_{ROM} is the natural frequency of the mistuned ROM and f_{FEM} the natural frequency of the mistuned FEM.

The errors calculated with the mistuned frequencies for each ROM are plotted in Fig. IV.9. The values are all below 0.01 % for an average of around 0.007 % in the four cases. The NCO matrices represented in Fig. IV.10 show an excellent modelling of the mistuned mode shapes with a minimum NCO of 0.999 in the diagonal and a maximum of 0.001 for the off-diagonal terms, which demonstrates that the 25 first families are enough to estimate properly the 26 first natural frequencies and mode shapes using the SNM. Besides, the three first cantilevered modes using the CMM, and the 200 first free-interface modes using the IMM are sufficient to have a good convergence to the SNM ROM.

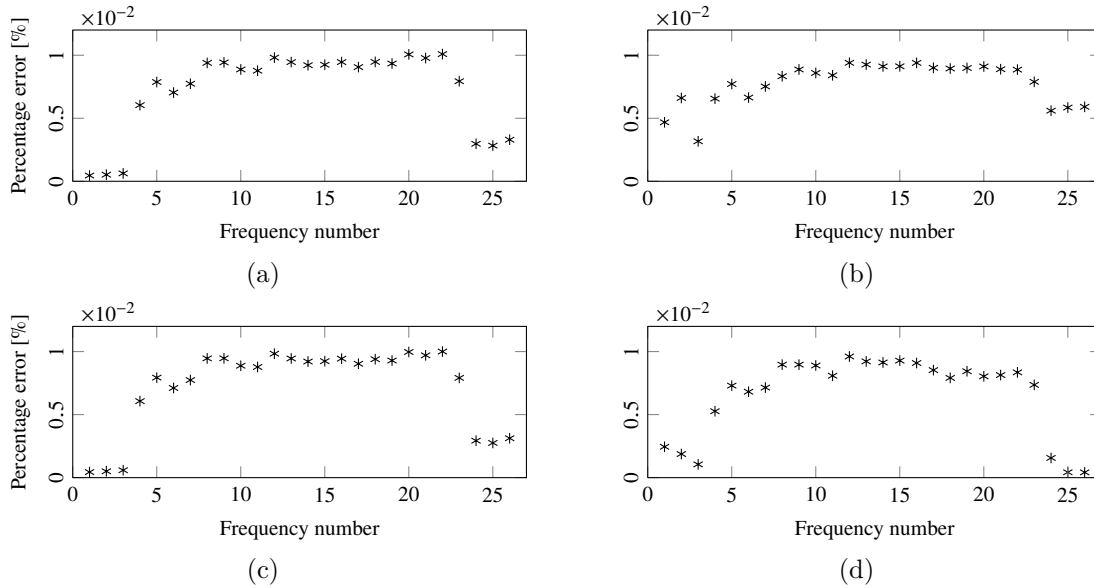


Figure IV.9 – Frequencies Error of the 26 first natural frequencies of the reduced order models versus the full mistuned model at 10,000 rpm. (a) The SNM reduction method with blade mistuning and (b) sector mistuning. (c) The CMM reduction method with blade mistuning and (d) the IMM reduction method with sector mistuning.

3.4 Forced response

Now that the ROMs have been validated for a free response, it is necessary to validate these same ROMs in forced response. The computing of the excitation force and damping matrix is explained in Section I.3.4 with a damping ratio of $\xi = 5e^{-4}$ and a natural frequency of $\omega_0 = 319.62$ Hz to calculate the damping coefficient α and β .

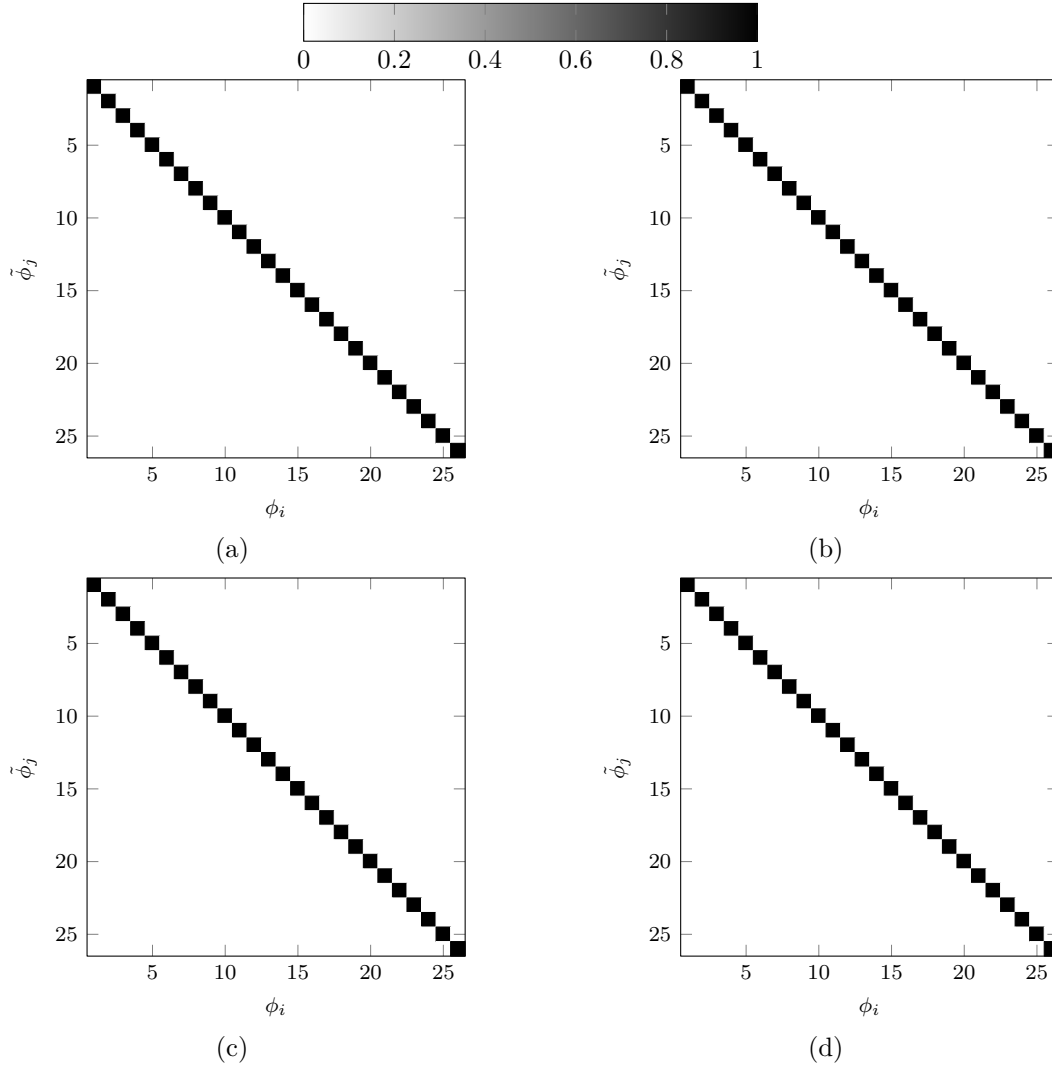


Figure IV.10 – NCO matrix for the comparison between the 26 first eigenvectors of the FEM (ϕ_i) and the eigenvectors of the ROMs ($\tilde{\phi}_j$) at 10,000 rpm. (a) The SNM reduction method with blade mistuning and (b) sector mistuning. (c) The CMM reduction method with blade mistuning and (d) the IMM reduction method with sector mistuning.

The validation has been focused on three different cases. The first region is around 320 Hz with a 2EO-FW excitation. It corresponds to the tuned 2ND-FW mode, which exhibits a strong Coriolis effect due to the split of the frequencies between the FW and BW modes and a disc-dominated shape. The second region is around 700 Hz with a 6EO-FW excitation. It is a high modal density region of blade-dominated modes. The third region, around 678 Hz with a 1EO-BW excitation, is related to the veering region surrounded in Fig. IV.5a between the 1ND-BW modes of the first and second families. These simulations are effective samples to test the ROMs because all of these regions have different dynamic behaviours regarding the Coriolis and mistuning effects.

The simulations are separated into two configurations: the blade mistuning configuration with the CMM and SNM ROMs, and the sector mistuning configuration with the IMM and SNM ROMs. The FEM simulations are set as the benchmark for the ROMs simulations. The maximum forced responses for the different cases are plotted in Fig. IV.11 for the blade mistuning and Fig. IV.12 for the sector mistuning.

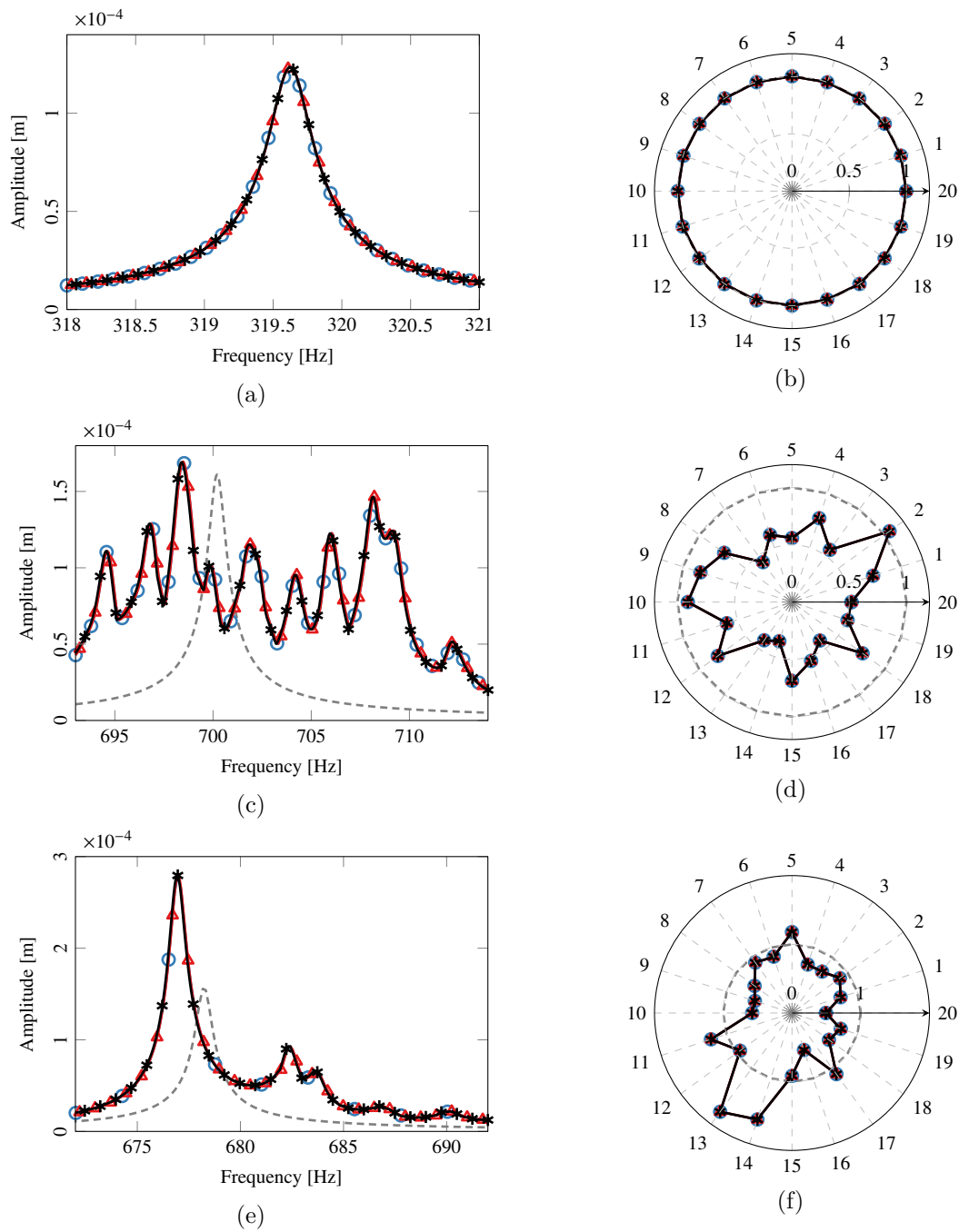


Figure IV.11 – Maximum forced response for a blade mistuning in different frequency regions and with different excitations at 10,000 rpm. [(a), (c), (e)] Maximum amplitude over the excitation frequency. [(b), (d), (f)] Maximum normalised amplitude over the blades. [(a), (b)] Low modal density region with a 2EO-FW excitation. [(c), (d)] High modal density region with a 6EO-FW excitation. [(e), (f)] Veering region with 1EO-BW excitation. [—○—]: SNM method. [—▲—]: CMM method. [—★—]: Mistuned FEM. [---]: Tuned FEM.

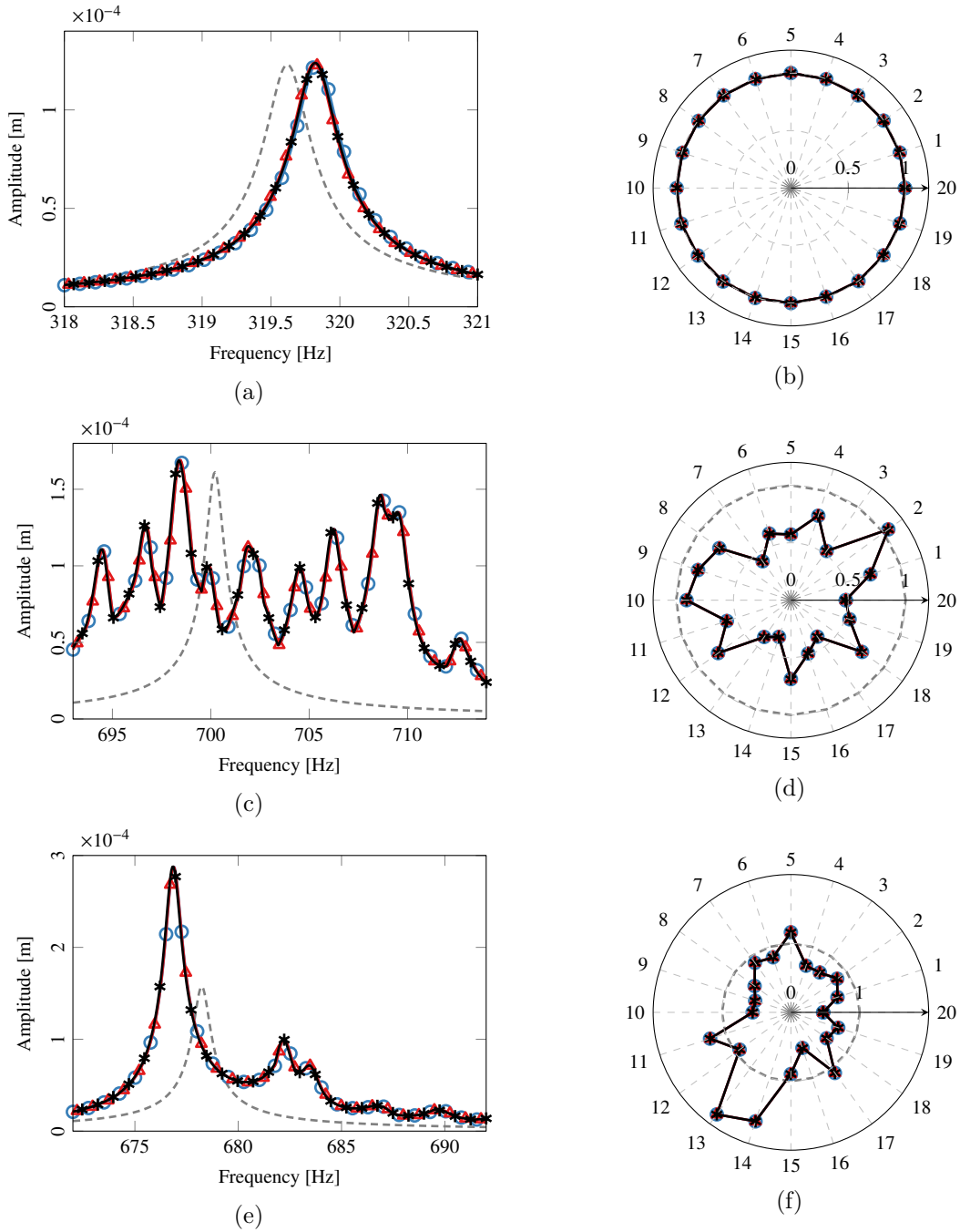


Figure IV.12 – Maximum forced response for a blade mistuning in different frequency regions and with different excitations at 10,000 rpm. [(a), (c), (e)] Maximum amplitude over the excitation frequency. [(b), (d), (f)] Maximum normalised amplitude over the blades. [(a), (b)] Low modal density region with a 2EO-FW excitation. [(c), (d)] High modal density region with a 6EO-FW excitation. [(e), (f)] Veering region with 1EO-BW excitation. [—○—]: SNM method. [—△—]: IMM method. [—*—]: Mistuned FEM. [---]: Tuned FEM.

The first observation that can be made is the similarity of the responses between the blade mistuning configuration and the sector mistuning configuration, the only difference being the offset of the peak in Fig. IV.12a, which does not appear in Fig. IV.11a. The sum of the stiffness perturbations listed in Table IV.2 is negative. Therefore, the mistuning of the disc has a softening effect that can be observed on the forced response.

In the first case, there is one peak corresponding to the only mode located in this region. The mistuned response is very close to the tuned response represented by the dashed line (Fig. IV.11a and Fig. IV.12a). It is almost a perfect 2ND-FW response with all sectors vibrating with the same amplitude (Fig. IV.11b and Fig. IV.12b), which is induced by a strong Coriolis as seen in Section II.4.2 for a frequency isolated mode. Even if the Coriolis matrix was not taken into account in the ROM construction bases, the Coriolis effect seems to be captured well, because all the ROM responses match perfectly with the full model responses.

The second case presents a strong mistuned behaviour due to the high modal density in this region with a lot of peaks compared to the tuned case (Fig. IV.11c and Fig. IV.12c), and different maximum amplitudes for all the sectors (Fig. IV.11d and Fig. IV.12d). Once again, the ROM results are very close to the benchmark, so the mistuning effect is well captured for the high modal density region with blade-dominated shapes.

Finally, for the third case, there are fewer peaks because it is not a high modal density although the amplification of the response against the tuned case is very strong (Fig. IV.11e and Fig. IV.12e). This phenomenon is known to occur in veering regions where there is a moderately weak blade-disc coupling which allows the possibility for the blades to exchange energy and to be located only on few blades, leading to a localisation response with a high amplitude on these few blades [152, 211] (Fig. IV.11f and Fig. IV.12f). These figures validate the use of the ROMs in the veering region where the Coriolis and mistuning effects coexist.

This section validates the use of the ROMs for the bladed drum model in both free and forced responses. The reduction bases can be calculated using the modes without the Coriolis effect as there are no significant changes in the mode shapes, which allows a faster computation of the ROMs. The computational cost to perform the forced responses are summarised in Table IV.7 which demonstrates the effectiveness of the reduction methods because the construction of the ROMs takes around one minute and the time saved on the forced responses is about several hours.

Table IV.7 – Computational cost to perform forced responses with the FEM and the ROMs from the SNM, CMM and IMM in the three different regions. The simulations were run on an Intel(R) Core(TM) i7-10700K CPU @ 3.80GHz except for the FEM (*) which required too much memory and was thus performed on a supercomputer with 40 cores and 400Go of RAM.

	FEM*	SNM	CMM	IMM
Low modal density region	21 h	17 s	17 s	17 s
High modal density region	190 h	17 s	17 s	17 s
Veering region	96 h	17 s	17 s	17 s

4 Reduction with variable rotational speeds

This section is dedicated to the estimation of the reduced matrices at different rotational speeds. When it is necessary to perform simulations at multiple speeds, the Coriolis and global stiffness matrices have to be calculated at every rotational speed, which involves a static non-linear resolution. This step can be very time consuming especially when a lot of rotational

speeds need to be considered.

4.1 Polynomial interpolation of the matrices

The first approach is to determine the full Coriolis and global stiffness matrices at different rotational speed using a finite number of determined matrices and the rotational speed variable Ω without the need to extract the matrices at each rotational speed.

4.1.1 Coriolis matrix

Assuming that the rotational speed is constant from one axis of rotation, it can be demonstrated that the Coriolis matrix is linearly dependent on the rotational speed Ω [144]. In Section I.2.2, it was shown that the Coriolis matrix can be written:

$$\mathbf{G} = 2 \int_{\mathcal{V}} \rho \mathbf{H}^T \boldsymbol{\Omega} \mathbf{H} \, d\mathcal{V}, \quad (\text{IV.54})$$

with

$$\boldsymbol{\Omega} = \begin{bmatrix} 0 & -\omega_z & \omega_y \\ \omega_z & 0 & -\omega_x \\ -\omega_y & \omega_x & 0 \end{bmatrix}. \quad (\text{IV.55})$$

Accordingly, if the rotational speed is constant from one axis of rotation the matrix $\boldsymbol{\Omega}$ can be rewritten as follows:

$$\boldsymbol{\Omega} = \Omega \mathbf{S}, \quad (\text{IV.56})$$

where Ω the rotational speed value and $\mathbf{S} = \begin{bmatrix} 0 & 0 & 0 \\ 0 & 0 & -1 \\ 0 & 1 & 0 \end{bmatrix}$, $\begin{bmatrix} 0 & 0 & 1 \\ 0 & 0 & 0 \\ -1 & 0 & 0 \end{bmatrix}$ or $\begin{bmatrix} 0 & -1 & 0 \\ 1 & 0 & 0 \\ 0 & 0 & 0 \end{bmatrix}$ if the rotation is along the x-axis, y-axis or z-axis, respectively. Then, all the Coriolis matrices for different rotational speeds can be determined from one Coriolis matrix \mathbf{G}_0 when injecting Eq. (IV.56) in (IV.54):

$$\mathbf{G} = \Omega \mathbf{G}_0, \quad (\text{IV.57})$$

with $\mathbf{G}_0 = 2 \int_{\mathcal{V}} \rho \mathbf{H}^T \mathbf{S} \mathbf{H} \, d\mathcal{V}$.

Modern finite element analysis software does not directly give the expression of the matrix \mathbf{G}_0 , but it is possible to calculate this matrix from any Coriolis matrix \mathbf{G}_i at a non-zero rotational speed Ω_i with $\mathbf{G}_0 = \frac{1}{\Omega_i} \mathbf{G}_i$.

It is also possible to express the matrix \mathbf{G}_0 in terms of the mass matrix \mathbf{M} . In a three-dimensional case with 3 dofs per node, the shape function matrix \mathbf{H} can be rewritten as follows:

$$\mathbf{H} = \mathbf{N} \otimes \mathbf{I}_3. \quad (\text{IV.58})$$

In order to carry out the demonstration it is necessary to use the following mixed-product property:

$$(\mathbf{A} \otimes \mathbf{B})(\mathbf{C} \otimes \mathbf{D}) = (\mathbf{AC}) \otimes (\mathbf{BD}), \quad (\text{IV.59})$$

where \mathbf{A} , \mathbf{B} , \mathbf{C} and \mathbf{D} have the correct matrix sizes to form the matrix products \mathbf{AC} and \mathbf{BD} .

Using this property and Eq. (IV.58), the expression $\mathbf{H}^T \mathbf{S}$ is equal to $(\mathbf{I}_n \otimes \mathbf{S}) \mathbf{H}^T$ because:

$$\begin{aligned}
\mathbf{H}^\top \mathbf{S} &= (\mathbf{N}^\top \otimes \mathbf{I}_3)(\mathbf{I}_1 \otimes \mathbf{S}) \\
&= \mathbf{N}^\top \otimes \mathbf{S} \\
&= (\mathbf{I}_n \otimes \mathbf{S})(\mathbf{N}^\top \otimes \mathbf{I}_3) \\
&= (\mathbf{I}_n \otimes \mathbf{S})\mathbf{H}^\top,
\end{aligned} \tag{IV.60}$$

where n is the number of nodes in the finite element model. Using this expression in Eq. (IV.54) gives:

$$\begin{aligned}
\mathbf{G} &= 2\Omega(\mathbf{I}_n \otimes \mathbf{S}) \int_{\mathcal{V}} \rho \mathbf{H}^\top \mathbf{H} \, d\mathcal{V} \\
&= 2\Omega(\mathbf{I}_n \otimes \mathbf{S})\mathbf{M}.
\end{aligned} \tag{IV.61}$$

This expression is convenient because it allows to determine the Coriolis matrix for any rotational speed simply by using the mass matrix, which can be very useful in case the Coriolis matrix could not be extracted from the finite element software. However, the disadvantage of this formulation is that it must be applied to the mass matrix without boundary conditions if the nodes are not clamped in all three directions as this becomes a problem of size for the matrix product between $\mathbf{I}_n \otimes \mathbf{S}$ (of size $3n \times 3n$) and \mathbf{M} (of size less than $3n \times 3n$). The boundary conditions must then be applied to the Coriolis matrix.

4.1.2 Global stiffness matrix

Using the non-linear static equation and expressing the inertial load as a linear dependence of the square rotational speed (Eq. (I.32)), it can be demonstrated that the global stiffness matrix can be approximated as a matrix polynomial in Ω^2 truncated at order P .

$$\mathbf{K}^g(\Omega) \approx \sum_{p=0}^P \Omega^{2p} \mathbf{K}_p \tag{IV.62}$$

Generally, an order $P = 2$ is sufficient to have a good interpolation of the global stiffness matrix [8, 73, 110, 111, 190]. As a consequence, all the global stiffness matrices can be determined between 0 and Ω_{\max} from three constant matrices (\mathbf{K}_0 , \mathbf{K}_1 , \mathbf{K}_2) which are calculated from three global stiffness matrices at different rotational speeds (0, $\Omega_{\max}/2$, Ω_{\max}).

$$\mathbf{K}_0 = \mathbf{K}(0), \tag{IV.63}$$

$$\mathbf{K}_1 = \frac{1}{3\Omega_{\max}^2} (16\mathbf{K}(\Omega_{\max}/2) - \mathbf{K}(\Omega_{\max}) - 15\mathbf{K}(0)), \tag{IV.64}$$

$$\mathbf{K}_2 = \frac{4}{3\Omega_{\max}^4} (\mathbf{K}(\Omega_{\max}) - 4\mathbf{K}(\Omega_{\max}/2) + 3\mathbf{K}(0)). \tag{IV.65}$$

This methodology performs correctly for the model presented in Fig. IV.3 as can be seen in Fig. IV.13 for the calculation of the frequency as a function of the rotational speed for the 3 modes studied in Section IV.3.4 and in Fig. IV.14 for the normalised amplitude of an observational dof.

When the model is very sensitive to geometric nonlinearity during centrifugal loading, an order of $P = 2$ is not necessarily sufficient and the order must be increased until a converged response is reached [94]. However, this method has a limit because the higher the degree, the more likely the Runge's phenomenon will occur [170].

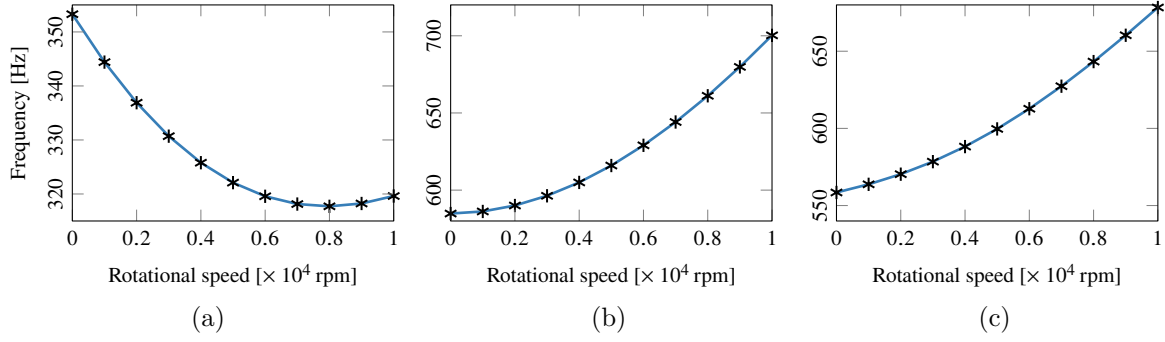


Figure IV.13 – Frequency versus rotational speed for different modes. (a) 2ND-FW mode. (b) 6ND-FW mode. (c) 1ND-BW mode. [—]: Interpolation method. [*]: Benchmark.

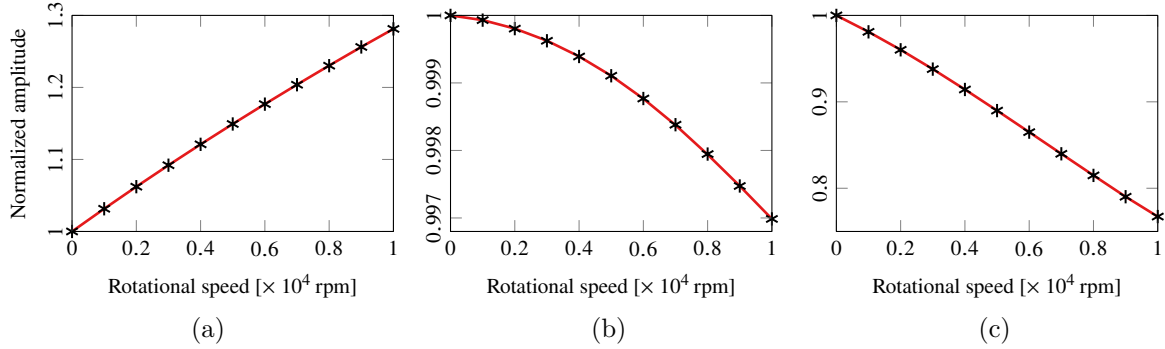


Figure IV.14 – Normalized amplitude versus rotational speed for different modes. (a) 2ND-FW mode. (b) 6ND-FW mode. (c) 1ND-BW mode. [—]: Interpolation method. [*]: Benchmark.

This phenomenon occurs because the interpolation curves must go exactly through the values given for the calculation of the interpolation coefficients. Another method that could avoid this problem would be to use B-Spline curves as the curve does not go through the control points [47].

Finally, if the study area is over a restricted range of rotational speeds, it is then possible to use a Taylor series expansion [76, 145, 226] of the global stiffness matrix around the rotational speeds studied Ω_0 .

$$\mathbf{K}^g(\Omega) \approx \sum_{p=0}^P \frac{1}{p!} \frac{\partial^p \mathbf{K}}{\partial^p \Omega} (\Omega - \Omega_0)^p \quad (\text{IV.66})$$

The derivatives $\frac{\partial^p \mathbf{K}}{\partial^p \Omega}$ are calculated at Ω_0 and approximated using the finite difference method,

which gives the following formulations for the first four derivatives:

$$\frac{\partial^0 \mathbf{K}}{\partial^0 \Omega} = \mathbf{K}(\Omega_0), \quad (\text{IV.67})$$

$$\frac{\partial^1 \mathbf{K}}{\partial^1 \Omega} \approx \frac{\mathbf{K}(\Omega_0 + \Delta\Omega) - \mathbf{K}(\Omega_0)}{\Delta\Omega}, \quad (\text{IV.68})$$

$$\frac{\partial^2 \mathbf{K}}{\partial^2 \Omega} \approx \frac{\mathbf{K}(\Omega_0 + \Delta\Omega) - 2\mathbf{K}(\Omega_0) + \mathbf{K}(\Omega_0 - \Delta\Omega)}{\Delta\Omega^2}, \quad (\text{IV.69})$$

$$\frac{\partial^3 \mathbf{K}}{\partial^3 \Omega} \approx \frac{\mathbf{K}(\Omega_0 + 2\Delta\Omega) - 3\mathbf{K}(\Omega_0 + \Delta\Omega) + 3\mathbf{K}(\Omega_0) - \mathbf{K}(\Omega_0 - \Delta\Omega)}{\Delta\Omega^3}, \quad (\text{IV.70})$$

$$\frac{\partial^4 \mathbf{K}}{\partial^4 \Omega} \approx \frac{\mathbf{K}(\Omega_0 + 2\Delta\Omega) - 4\mathbf{K}(\Omega_0 + \Delta\Omega) + 6\mathbf{K}(\Omega_0) - 4\mathbf{K}(\Omega_0 - \Delta\Omega) + \mathbf{K}(\Omega_0 - 2\Delta\Omega)}{\Delta\Omega^4}. \quad (\text{IV.71})$$

This method is often effective for a localised area around Ω_0 and without the Runge's phenomenon, the interpolation method is more effective and preferred. For example, the case studied in Section IV.3, the Taylor series approximation is not very effective as it can be observed in Fig. IV.15 for the eigenfrequencies and in Fig. IV.16 for the modal amplitudes. The study was done for different orders around $\Omega_0 = 5,000$ rpm but even with a fourth-order Taylor series, the approximation is far from the reference values. Moreover, for a fourth-order Taylor series, five global stiffness matrices have to be extracted to calculate the derivative $\frac{\partial^4 \mathbf{K}}{\partial^4 \Omega}$.

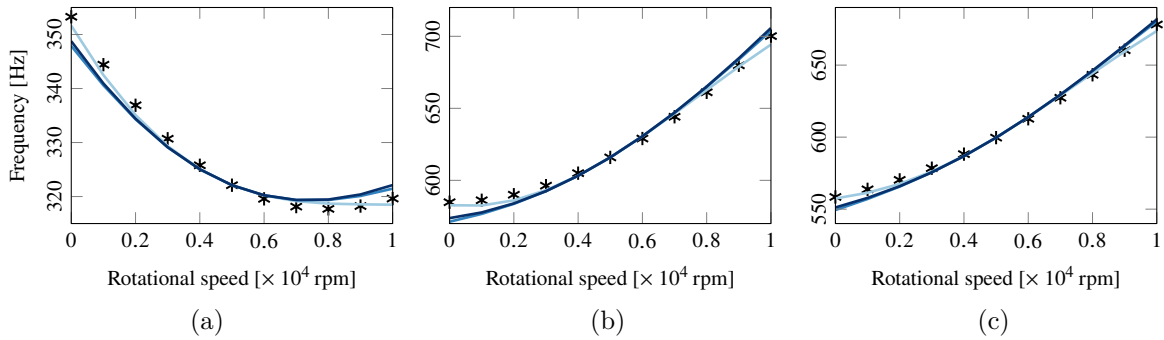


Figure IV.15 – Frequency versus rotational speed for different modes approximation of the Taylor series. (a) 2ND-FW mode. (b) 6ND-FW mode. (c) 1ND-BW mode. [—]: Second-order. [—]: Third-order. [—]: Fourth-order. [*]: Benchmark.

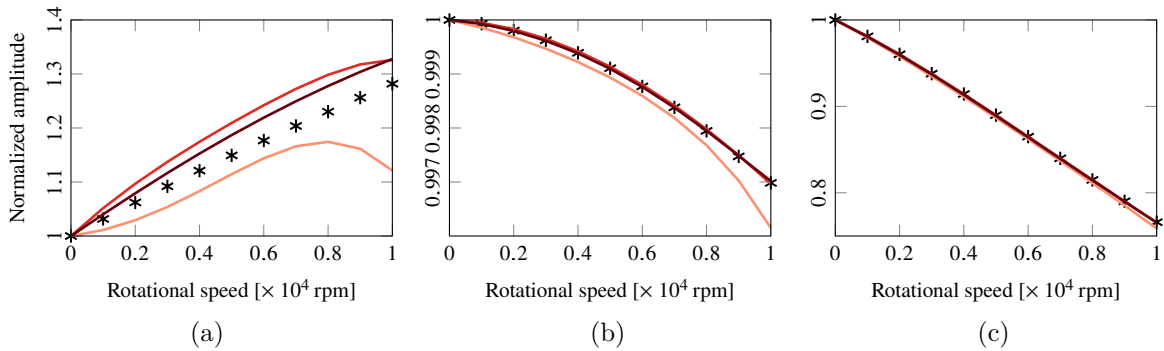


Figure IV.16 – Normalized amplitude versus rotational speed for different modes at different order approximation of the Taylor series. (a) 2ND-FW mode. (b) 6ND-FW mode. (c) 1ND-BW mode. [—]: Second-order. [—]: Third-order. [—]: Fourth-order. [*]: Benchmark.

4.2 Parametric Reduced Order Model methodology

The weak point in determining the full matrices by polynomial interpolation is that it is necessary to calculate the reduction basis at each rotational speed because the stiffness matrix used in the calculation of ROM depends on this rotational speed. The problem is solved by the Parametric Reduced Order Model (PROM) method, in which the goal is to apply the polynomial interpolation directly in the reduced space [76]. For this method, it is necessary to have a reduction basis common for all the rotational speeds. To construct this augmented reduction basis, it is necessary to combine the three reduction basis \mathbf{R}_0 , \mathbf{R}_1 , \mathbf{R}_2 calculated at 0, $\Omega_{\max}/2$ and Ω_{\max} , respectively

$$\mathbf{R}_{\text{aug}} = [\mathbf{R}_0 \ \mathbf{R}_1 \ \mathbf{R}_2]. \quad (\text{IV.72})$$

It is then necessary to perform a Singular Value Decomposition (SVD) [66] to form an orthogonal basis \mathbf{U} which is composed of the left singular vectors of \mathbf{R}_{aug} with singular values larger than 0.01 % of the maximum singular value. This value proposed by Hong [76] assumes that every left singular value lower than 0.01 % does not give significant additional information. Other methods of orthogonalisation can be used to create this orthogonal basis \mathbf{U} like the Gram-Schmidt methods [111, 176] or even the Independent Maximum Sequence (IMS) [6, 189].

Once the orthogonal basis \mathbf{U} has been formed, it is possible to determine all the matrices in this common reduced space

$$\mathbf{M}^{\text{PROM}} = \mathbf{U}^H \mathbf{M} \mathbf{U}, \quad (\text{IV.73})$$

$$\mathbf{C}^{\text{PROM}} = \mathbf{U}^H \mathbf{C} \mathbf{U}, \quad (\text{IV.74})$$

$$\mathbf{G}^{\text{PROM}}(\Omega) = \Omega \mathbf{U}^H \mathbf{G}_0 \mathbf{U}, \quad (\text{IV.75})$$

$$\mathbf{K}^{\text{PROM}}(\Omega) = \sum_{p=0}^2 \Omega^{2p} \mathbf{U}^H \mathbf{K}_p \mathbf{U}. \quad (\text{IV.76})$$

Note that the method is presented here using the second-order polynomial in Ω^2 whereas in the original method a third-order Taylor series approximation is used. This modification was made because it was seen in the previous section that the interpolation method is more efficient than the Taylor series, and the principle of the method remains the same.

The sub-structuring methods mentioned in Section IV.1 can be easily applied to the PROM methodology as well as the reduction methods for mistuned models. For the stiffness mistuning perturbation with the SNM, Eq. (IV.76) can be directly used for the mistuning projection. For the CMM and IMM, it is necessary to determine the modal participation factors. Developments of this method can be found in [102] for the CMM and can be used in a similar manner with the IMM.

In order to validate the effectiveness of the PROM on the SNM, the mistuning pattern presented in Table IV.2 has been applied on the model. The parametric reduced-order model was constructed from the reduction bases at 0 rpm, 5,000 rpm and 10,000 rpm with 500 tuned modes each, as in Section IV.3. After orthogonalisation and selection of the modes according to their singular values, the basis consists of 997 modes which gives a PROM with 997 dofs. The evolutions of the frequencies as a function of the rotational velocity of the M1, M4 and M10 modes located in the areas of low modal density, veering and high modal density respectively, have been plotted in Fig. IV.17.

More specifically, the frequency error and NCO for the 26 first modes were compared with the FEM at 8,000 rpm. The values of the frequency error are all below 0.1% for an average of 0.036% as seen in Fig. IV.18. With regard to the NCO criterion, the minimum value in the

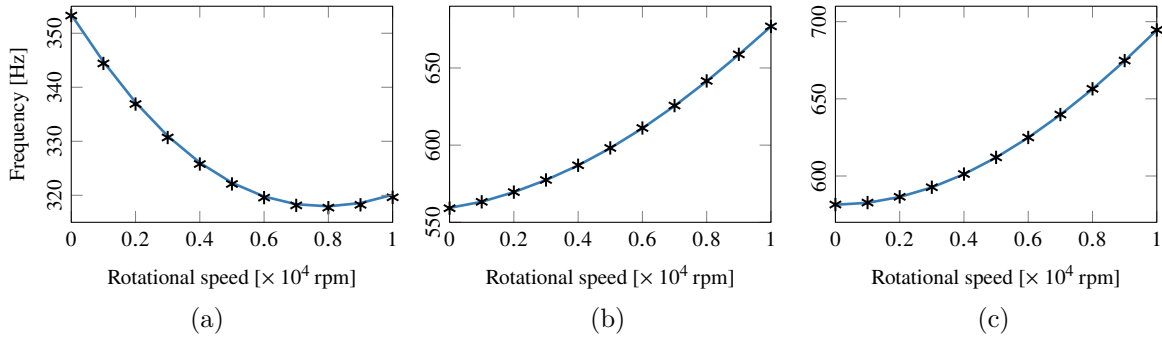


Figure IV.17 – Frequency versus rotational speed for different modes approximation of the PROM. (a) M1 mode. (b) M4 mode. (c) M10 mode. [—]: PROM. [*]: Benchmark.

diagonal is of 0.987 and the maximum for the off-diagonal terms is of 0.012. The NCO matrix is represented in Fig. IV.19. These results exhibit suitable predictions in free response using the PROM method, although the values are not as good as when SNM reduction is done at a specific rotational speed as seen in Section IV.3.3.

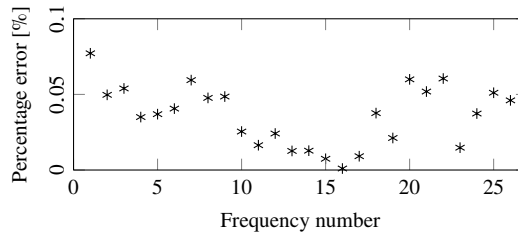


Figure IV.18 – Frequencies error of the 26 first natural frequencies of the PROM versus the full mistuned model at 8,000 rpm.

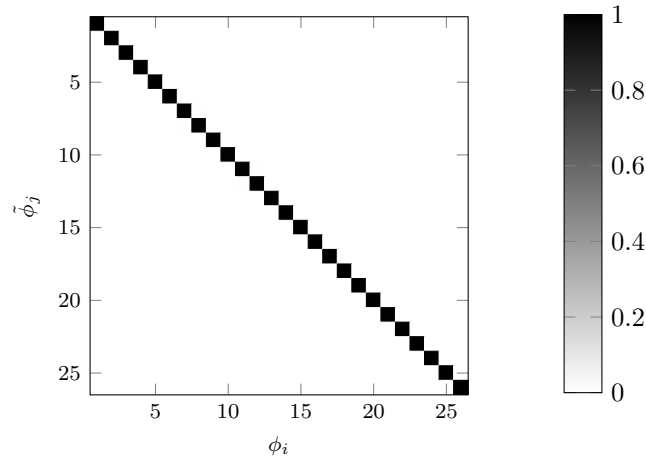


Figure IV.19 – NCO matrix for the comparison between the 26 first eigenvectors of the FEM (ϕ_i) and the eigenvectors of the PROM ($\tilde{\phi}_j$) at 8,000 rpm.

The validation was also realised in forced response in the same manner as in Section IV.3.4. The results are summarised in Fig. IV.20 and show a good correlation between the PROM method and the detuned FEM. Some slight offsets can still be observed but these are acceptable. To improve the PROM there are two possibilities: either increasing the number of modes in

the \mathbf{R}_0 , \mathbf{R}_1 , \mathbf{R}_2 bases which constitutes the augmented basis \mathbf{R}_{aug} or keeping more modes in the \mathbf{U} basis with a criterion on the singular value lower than 0.01%.

This method is interesting to perform a lot of calculation over different rotational speeds. For example, this method allows a significant gain of computing time to plot a Campbell diagram. Nevertheless, the weak point of the PROM is the increase of the size of the reduced system compared to the ROM due to the augmented subset of nominal modes. In the previous example, the size of the reduced model has been increased by a factor two and on top of that, the accuracy is poorer. To perform a Monte Carlos simulation, if the size of the PROM is two times larger than the ROM, the computing time gained during the reduction calculation will be lost during the simulation. This is why it is important to consider whether it is more interesting to use the PROM common to all rotational speeds or a classic ROM on each speed depending on the calculation time of a simulation, the number of simulations performed at each speed and the number of different speeds at which the simulations are performed. Either the reduction step is longer, thus it is better to use the PROM or the simulations are longer, thus it is better to use a classic ROM at each rotational speed.

Chapter summary

The classical sub-structuring methods were presented at the beginning of this chapter with the Craig-Bampton's method with fixed interfaces and the Craig-Chang's method with free interfaces. Guyan's static condensation and double modal synthesis were also discussed for interface reductions.

Secondly, the most popular reduction methods which are the SNM, CMM and IMM for mistuned models have been presented, adapted and validated to take into account the Coriolis effect. This validation was first performed in free response, then in forced response by comparing with the full FEM. This validation was done at 10,000 rpm, on a bladed drum sensitive to the Coriolis effect. The first case considered was for a disc-dominated mode in a low modal density region, the second for a blade-dominated mode in a high modal density region, and finally the third in a veering region where the behaviour is mixed with the participation of both the blades and the disc. This allows to define different ROM in the next chapter, which can take into account the Coriolis effect and reduce the calculation time.

The chapter ends with an opening on the multi-rotational speed evaluation of the dependent matrices, which are the Coriolis and the global stiffness matrices, with polynomial interpolation and Taylor series approximation. Then, the PROM method which allows to have a common reduction basis for all rotation speeds, has been merged with the polynomial interpolation and validated in free and forced responses. This allows to have a common reduction basis and to evaluate the reduced matrices for different rotational speeds.

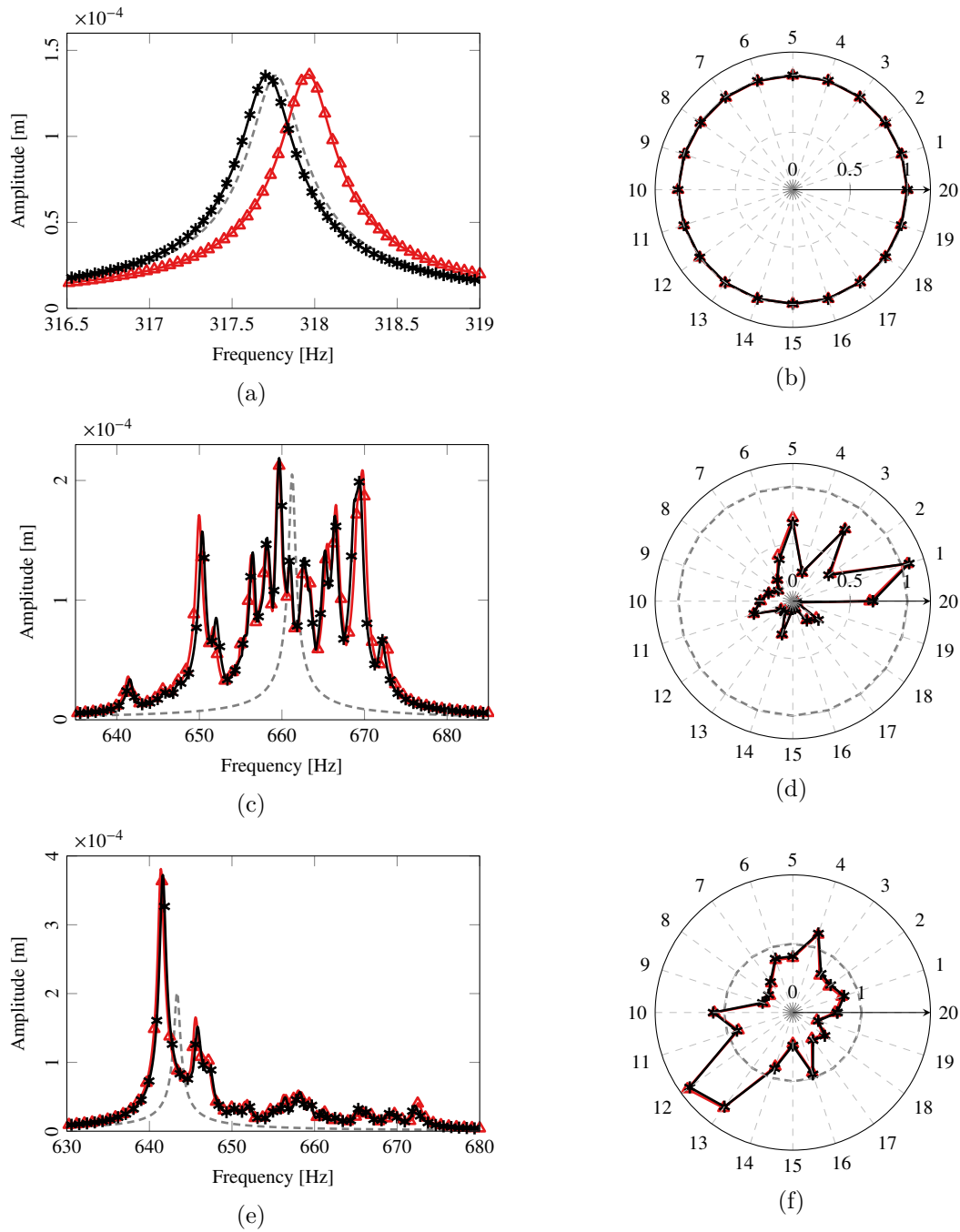


Figure IV.20 – Maximum forced response for a blade mistuning in different frequency regions and with different excitations at 8,000 rpm. [(a), (c), (e)] Maximum amplitude over the excitation frequency. [(b), (d), (f)] Maximum normalised amplitude over the blades. [(a), (b)] Low modal density region with a 2EO-FW excitation. [(c), (d)] High modal density region with a 6EO-FW excitation. [(e), (f)] Veering region with 1EO-BW excitation. [—▲]: PROM method. [—■]: Mistuned FEM. [---]: Tuned FEM.

Chapter V

Analysis of a finite element model of a rotating bladed drum

The analysis in Chapter II gave a better understanding of the interaction between the Coriolis and mistuning effects on a lumped mass-spring model and Chapter IV allowed to validate several reduction methods for finite element models taking into account both the Coriolis and mistuning effects. The main objective of this final chapter is to analyse the interaction between the Coriolis and mistuning effects on a reduced-order model of a bladed drum close to an industrial design using Monte Carlo simulations, which allows an estimation of the global behaviour of the system for different rotational speeds and mistuning levels. The analyses are focused on three different regions. The first region presents only one disc-dominated mode and a strong Coriolis effect. The second region presents a high density of blade-dominated modes with different nodal diameter numbers. The last region is a veering region where the maximum sensitivity to mistuning is known to arise.

The chapter is organised as follows. Section V.1 starts with the description of the finite element model and its reduced order model. Then the localisation of the mistuning on the model is investigated to show the best reduction method to use for this model, and, a focus on the behaviours with and without the Coriolis effect is provided. Finally, the evolution of mistuning with rotational speed in the three regions of interest is analysed.

Outline of the chapter

1 Introduction of the finite element model	122
1.1 Geometry and materials	122
1.2 Centrifugal loading and boundary conditions	123
1.3 Finite element mesh	123
1.4 Modal analysis	124
1.5 Reduced Order Model	126
2 Preliminary simulations	126
2.1 Influence of the mistuning locations in the bladed drum	127
2.2 Coriolis requirement in the simulations	129
3 Dynamics evolution with the rotational speed	131
3.1 Low modal density region	131
3.2 High modal density region	133
3.3 Veering region	135
Chapter summary	138

1 Introduction of the finite element model

This section is dedicated to the presentation of the finite element model that has been used for the simulations. This model has been realised with the help of the commercial software ANSYS and then exported as input data for the MATLAB computer programs developed in the present work.

1.1 Geometry and materials

The considered bladed drum is derived from an industrial low-pressure compressor mentioned in Section I.1.2 but neither the geometry nor the dimensions are those of a real existing structure. This type of structure is known to be strongly subjected to the Coriolis effect due to the flexibility of the disc and the strong interaction between the friction-welded blades and the disc [116, 155, 194, 195, 227, 228]. The model used has only one stage composed of 60 blades represented in Fig. V.1. The geometrical characteristics are broadly the same as those defined for the model in Chapter II, with a blade length $l^b = 0.080$ m, a disc radius $r = 0.320$ m, a chord length $c = 0.040$ m, and a stagger angle of the blade $\theta = 30^\circ$.

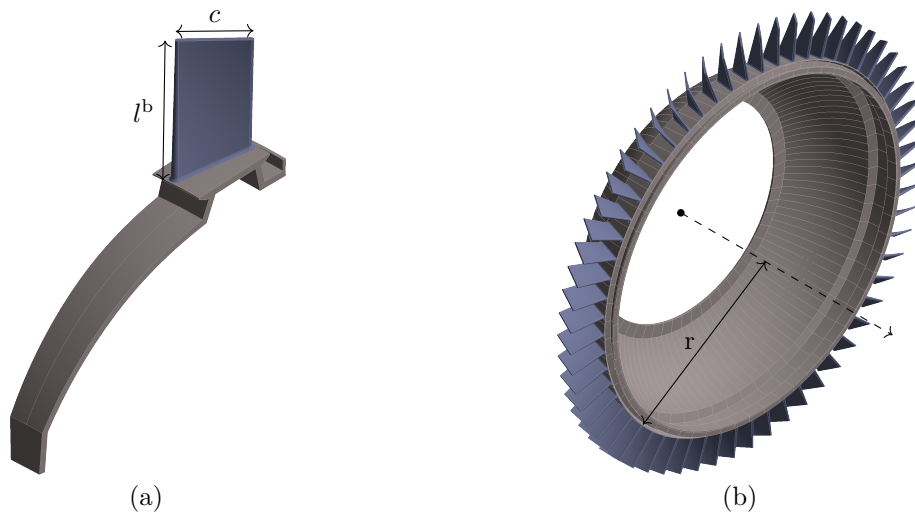


Figure V.1 – Geometry of the 60-sector bladed drum. (a) Reference sector. (b) Full assembly model.

This structure is supposed to be made of a Ti-6Al-4V titanium alloy whose properties are summarised in Tab. V.1. This material is one of the most used alloys in the aeronautics industry especially for its low density and excellent corrosion resistance [24, 53, 132].

Table V.1 – Material properties of the Ti-6Al-4V titanium alloy.

Material property	Value	Unit
Mass density (ρ)	4,368	kg/m ³
Young's modulus (E)	94	GPa
Poisson's ratio (ν)	0.323	-

1.2 Centrifugal loading and boundary conditions

The bladed drum will undergo different rotational speeds during the simulations from 0 to 10,000 rpm. For each rotational speed, a non-linear static analysis is conducted using a Newton-Raphson approach to iteratively converge to the equilibrium point of the system and determine the stiffening matrix. In addition, for each rotational speed, the extraction procedure described in Appendix D is used to compute the mass, Coriolis and global stiffening matrices.

Only the geometry of the reference sector is modelled and cyclic symmetry conditions to the left and right of this sector are applied to obtain the complete structure. The right cyclic symmetry section is highlighted in blue in Fig. V.2. A clamping at the base of the drum (shown in yellow in Fig. V.2) is applied to simulate the attachment of this part to the rest of the low-pressure rotor. Finally, for the forced response simulations, the excitation will be applied at the tip of the blade, represented as a red dot in Fig. V.2 with a vector excitation directed along the axis of rotation represented by a black arrow.

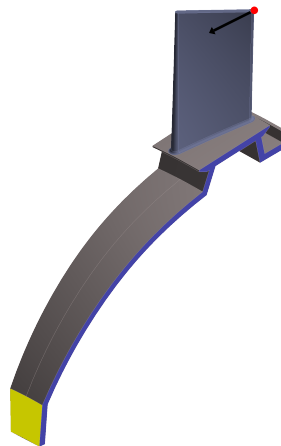


Figure V.2 – Boundary conditions of the bladed drum model. [■]: Clamped surface. [■]: Cyclic symmetric section. [●]: Excitation node. [→]: Excitation vector.

1.3 Finite element mesh

The mesh definition is a crucial step in the numerical study of a model because it must be as faithful as possible to the geometry while not being too refined in order to avoid long simulation times. One way of doing this is to match the frequency of the numerical model with the frequencies obtained experimentally, but in this case there is no experimental data available. The strategy adopted here is to assume that the more refined the mesh is, the more it will converge towards the real solution. Accordingly, a very refined mesh was taken as a benchmark and meshes with different size were made until the modes below 1,200 Hz were within 0.5% of the benchmark. This limit of 1,200 Hz was chosen because no mode above this value will be studied in what follows.

The mesh is defined only on the reference sector and duplicated for the others sectors using quadratic tetrahedral elements with 10 nodes. The refinement is chosen more important on the blade than on the disc because this part undergoes more stress and deformation than the disc. The benchmark sector is discretised using 140,603 elements which gives a total of 214,152 nodes and the tested meshes are of 1,189, 2,589, 4,338, 12,337 and 20,511 elements, respectively. The maximum relative error for each of these meshes has been recorded in Table V.2. The mesh with 12,337 elements is the one chosen because it is just below 0.5% error for a reasonable mesh size.

Table V.2 – Relative error for different mesh size.

Number of elements	1,189	2,589	4,338	12,337	20,511
Relative error	2.42%	0.71%	0.63%	0.49%	0.38%

Finally, the mesh model of the reference sector is shown in Fig. V.3a. It is discretised using 12,337 elements which gives a total of 21,890 nodes for the reference sector. The mesh sizing was performed by defining a maximum element size of 2.5 mm for the blades and 4 mm for the disc. Knowing that there are 199 clamped nodes and 432 nodes on a cyclic symmetry section, this represents a full assembly model with 1,275,540 nodes represented in Fig. V.3b. Each node has 3 dofs (one for each direction x , y and z), which gives a model of 3,826,620 dofs.

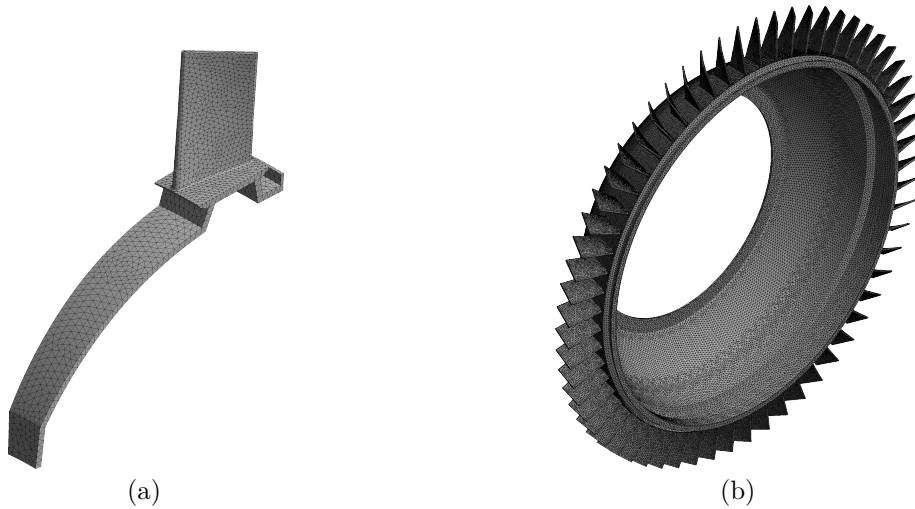


Figure V.3 – Finite element mesh for the 60-sector bladed drum. (a) Reference sector. (b) Full assembly model.

1.4 Modal analysis

This subsection presents the behaviour of the tuned model for different rotational speeds, in order to describe the different modes of interest and demonstrate their sensitivity to the Coriolis effect.

The evolution of the modes with the rotational speed can be summarised in a Campbell diagram (Fig. V.4). As observed previously in Fig. II.4, there are three identifiable regions. In the first one, the modes are disc-dominated modes except for the 5ND and 6ND mode of the first family, which are a blade-disc mode. The accumulation of modes in the second region are blade-dominated modes with a first flexural mode and different nodal diameter numbers from 7ND to 30ND. Finally, the third region is also composed of disc modes but from the second mode family, which have less tangential displacement and therefore leads to less pronounced Coriolis effect.

The modes of the tuned structure at 10,000 rpm are shown in Fig. V.5, representing their frequency versus their nodal diameter number. This graph is similar to the Fig. II.3 in Chapter II with the lumped mass-spring model. The study area is highlighted in grey between 200 Hz and 1,200 Hz, which is similar to the study area in Fig. II.3 with a region where the Coriolis effect is important between 1ND and 3ND, a veering region at 5ND and 6ND and a high modal density after 7ND with a predominant first flexural mode.

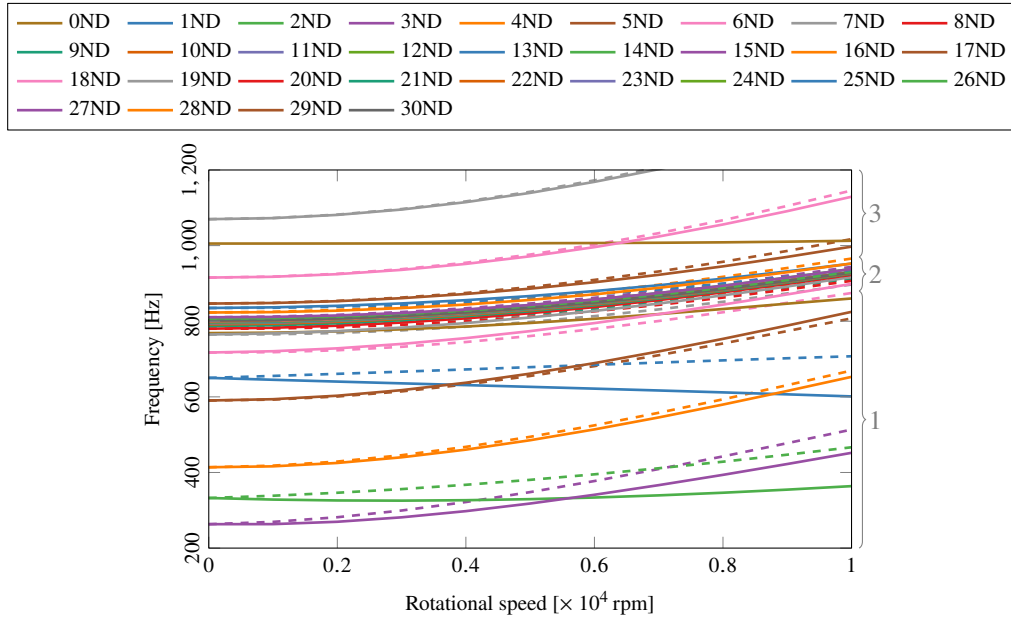


Figure V.4 – Campbell diagram of the tuned bladed drum between 200 Hz and 1,200 Hz. [—]: Forward wave modes. [--]: Backward wave modes.

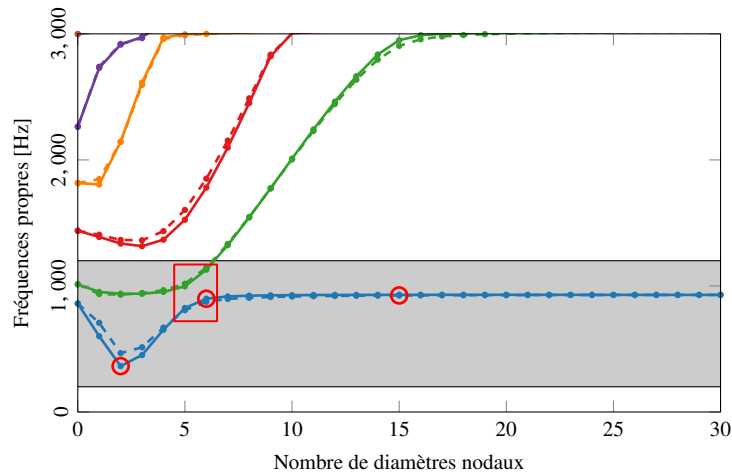


Figure V.5 – Natural frequencies versus number of nodal diameter at 10,000 rpm. All different modal families are represented with different colours. [—]: Forward wave modes. [--]: Backward wave modes. [□]: Veering regions. [■]: Studied region. [○]: Studied modes for the numerical simulations.

For the same reasons as in Section IV.3.2, there will be three modes of interest, circled in red on Fig. V.5. The first one is the 2ND-FW 1 represented in Fig. V.6a, with a strong participation of the disc, isolated in frequency and therefore a strong Coriolis effect. The second one is the 6ND-FW 1 represented in Fig. V.6b, which is in the veering region with both disc and blade participation. Finally, the third one is the 15ND-BW 1 represented in Fig. V.6c, which is in the high modal density region with a predominance of the first bending mode of the blades.

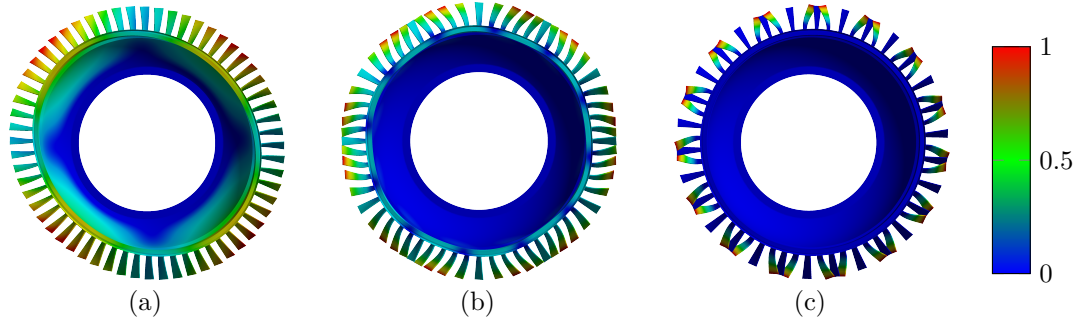


Figure V.6 – Modal shape of three studied modes. (a) First mode: 2ND-FW 1. (b) Second mode: 6ND-FW 1. (c) Third mode: 15ND-BW 1

1.5 Reduced Order Model

In this subsection, a convergence study is performed in order to validate the number of modes taken into account in the reduction bases of the different ROMs. The methodology adopted here will be the same as for the construction of ROMs in Section IV.3. Firstly, the number of tuned modes used for the SNM reduction bases is assigned. It has been shown that with the first 25 modal families, the relative error is less than 0.01% on the eigenvalues. For the current model, this represents a reduction basis of 1,500 modes, leading to ROMs of 1,500 dofs.

This large number of modes presents two problems. The first one is the size of the reduction basis, which is $3,826,620 \times 1,500$ and represents a storage of 56Go. Consequently, it takes a lot of time to record or load this basis and to make the reduction calculations for each rotational speed. The second problem is that a ROM size of 1500 dofs also slows down the computational time of the Monte Carlo simulations. Accordingly, it was decided to reduce the size of the basis by taking the case with 1,500 modes as a reference and remove modes until a maximum relative error of 0.5% is reached on the frequencies below 1,200 Hz. This criterion is achieved by taking the first three modal families, with a relative error of 0.34% which leads to a ROM with 180 dofs and a storage of the reduction basis of 6Go which is more reasonable for the following simulations. For the CMM, it is necessary to choose the number of cantilevered modes. The first bending mode is sufficient to have a relative error of 0.34%. Since it was shown in Section IV.3 that the number of cantilevered modes does not increase the size of the ROM and has small influence on the simulation times, 3 cantilevered modes were selected to further reduced the relative error.

For the IMM, 5 free–interface modes are enough to have a relative error of 0.36%. But for the same reasons as the CMM, 10 free–interface modes will be considered for the ROM construction with the IMM method.

2 Preliminary simulations

This section first considers which of the SNM, CMM and IMM reduction methods is most appropriate for studying the bladed drum. As the main difference between these methods is the implementation of mistuning on either the blade or the whole sector, it is needed to first look at the influence of the mistuning location on this model. Then, the importance of taking into account the Coriolis matrix for the study of the mistuned structure will be discussed.

2.1 Influence of the mistuning locations in the bladed drum

As mentioned above, the mistuning can be introduced on the blades or the sectors. In most publications, the mistuning is only introduced on the blades because it is the major contributor to the amplitude magnification [18, 19, 119, 222]. However, the impact of the interface mistuning [207] or the disc mistuning [178] can have a significant effect on the forced response when the modes have a large disc participation. As the bladed drum FEM has a significant disc participation in many of its modes, it is interesting to study the differences between a blade mistuning, a sector mistuning and a disc mistuning.

Blade, sector and disc mistuning have been investigated using the CMM, IMM, and the SNM techniques, respectively. The Monte Carlo simulations are performed for the three different cases defined previously, namely the low modal density region, the high modal density region and the veering region. As the aim is to compare behaviours between different mistuning localisation cases, there is no need to plot different values of the statistical response distributions: only the medians of the amplitude magnification factors are plotted in Fig. V.7 as a function of the mistuning level. The simulation for the low modal density region has been done at 0 rpm (Fig. V.7a) and 10,000 rpm (Fig. V.7b), while those for the two other regions have been performed only at 10,000 rpm.

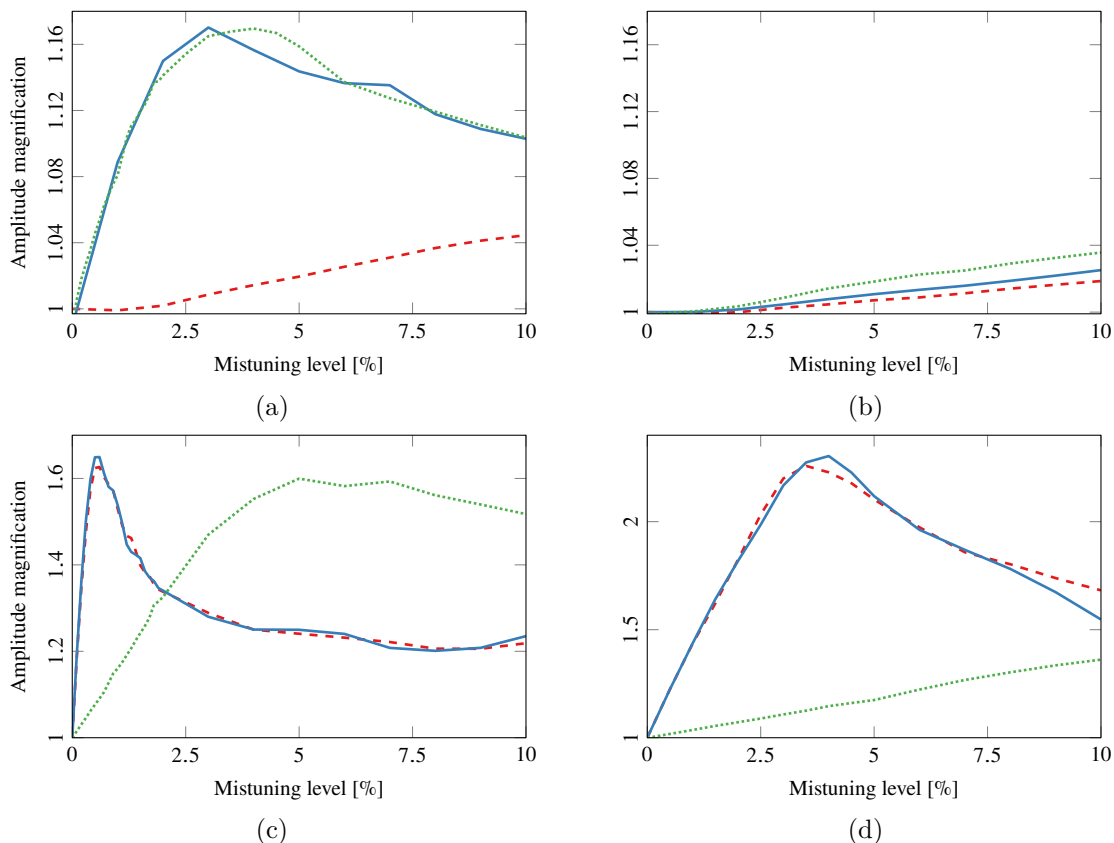


Figure V.7 – Comparison of the median amplitude magnification factor with the mistuning level. (a) Low modal density region with a 2EO-FW excitation at 0 rpm. (b) Low modal density region with a 2EO-FW excitation at 10,000 rpm. (c) High modal density region with a 15EO-BW excitation at 10,000 rpm. (d) Veering region with a 6EO-FW excitation at 10,000 rpm. [---]: Blade mistuning. [—]: Sector mistuning. [····]: Disc mistuning.

In the low modal density region, at 0 rpm (Fig. V.7a), there is an amplitude magnification

due to the mistuning. The behaviours of the disc and sector mistuning are similar while the behaviour of the blade mistuning is different. At 10,000 rpm (Fig. V.7b), the mistuning does not seem to have an impact on the amplitude magnification with a maximum amplitude response very close to that of the tuned case. Therefore, in this case, there is no particular difference between blade, sector and disc mistuning and this will not be studied further in the investigation of the mistuning location. The different trend between the case at 0 rpm and 10,000 rpm is mainly due to the Coriolis effect and will be further investigated and explained in the following section dedicated to the dynamic evolution of the system with the rotational speed. For both the high modal density region (Fig. V.7c) and the veering region (Fig. V.7d) at 10,000 rpm, the behaviours of the blade and sector mistuning are similar and the disc mistuning is different.

The above observations are not sufficient to determine if the mistuning effect is driven by the blade or the disc mistuning. For this reason, two additional Monte Carlo simulations were run for each region. In the first simulation, a pattern for the blade mistuning is given for a mistuning level at the local maximum of amplitude magnification, and the Monte Carlo is run for different disc mistuning levels. In the second simulation, the disc mistuning pattern is given for the disc mistuning local maximum, and the Monte Carlo simulation is run for different blade mistuning levels. The mistuning level values used for the patterns are summarised in Table V.3. These patterns are chosen in such a way that the mistuning amplitude magnification factors are around the median maximum values. All these simulations are run with the SNM reduction method because it allows to separate the disc and the blade mistuning. Finally, these simulations are compared to the Monte Carlo simulations of the blade and disc mistuning alone (Fig. V.8).

Table V.3 – Mistuning level values at the local maximum of amplitude magnification for the blade and disc mistuning.

	Blade mistuning	Disc mistuning
Low modal density region	10 %	4 %
High modal density region	0.6 %	5 %
Veering region	3.5 %	10 %

In the low modal density region (Fig. V.8a), the fixed disc mistuning with variable blade mistuning level does not seem to be affected by the blade mistuning, as the amplitude magnification factor does not substantially change with the mistuning level. However, the amplitude magnification of the fixed blade mistuning with variable disc mistuning increases with the mistuning level and follows the curve of the disc mistuning alone. For the high modal density region (Fig. V.8b) and the veering region (Fig. V.8c), the fixed blade mistuning with variable disc mistuning is not affected by the mistuning level and the disc mistuning with variable blade mistuning curves follow the blade mistuning curves.

These simulations exhibit two distinct situations. When there is a disc-dominated mode, it is the disc mistuning that drives the mistuning effect. When it is a blade-dominated mode or blade-disc mode like in the veering region, it is the blade mistuning that drives the mistuning effect. In both cases, the sector mistuning always follows the behaviour of the predominant mistuning effect. For this reason, the simulations presented later in this chapter are performed with a sector mistuning using the IMM reduction method.

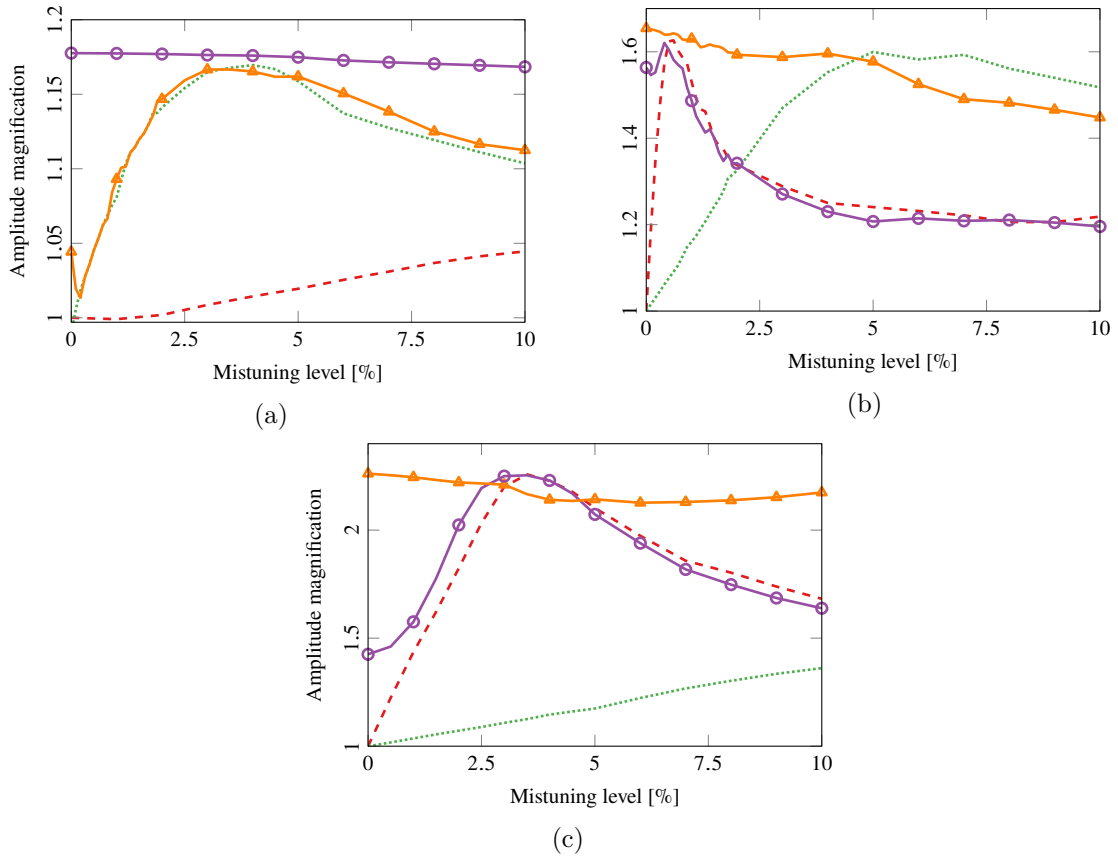


Figure V.8 – Comparison of the amplitude magnification factor with the mistuning level. (a) Low modal density region with a 2EO-FW excitation at 0 rpm. (b) High modal density region with a 15EO-BW excitation at 10,000 rpm. (c) Veering region with a 6EO-FW excitation at 10,000 rpm. [---]: Variable blade mistuning alone. [....]: Variable disc mistuning alone. [—▲]: Fixed blade mistuning with variable disc mistuning. [—○]: Fixed disc mistuning with variable blade mistuning.

2.2 Coriolis requirement in the simulations

As mentioned in Section I.4.1, the Coriolis effect is often neglected in bladed disc forced response. However, in the bladed drum model presently considered, the Coriolis effect is non-negligible, as can be observed with the presence of splits in the Campbell diagram of the tuned model (Fig. V.4). The dynamic behaviour of a mistuned model sensitive to the Coriolis effect can change with the rotational speed [166, 193]. More recently, Zhang [227] showed that the Coriolis force cannot be ignored in the analysis of the vibration localisation characteristics of a mistuned bladed disc FEM. For these reasons, Monte Carlo simulations with and without the Coriolis matrix were carried out at 10,000 rpm for the three different regions.

It is important to note that the simulations with and without the Coriolis matrix were not performed in the same frequency regions because the frequencies of the modes are changed by the Coriolis effect. The excitation regions for the different cases are summarised in Table V.4.

The evolution of the amplitude magnification factor with the mistuning level for the different regions are plotted in Fig. V.9. In the first case (Fig. V.9a), the magnification is greater without the Coriolis effect due to two modes that originate from the tuned double modes near the excitation region. These two modes are split in frequency by the mistuning, and there is an interaction between them that induces an amplitude magnification. With the Coriolis effect,

Table V.4 – Frequency regions for the different cases with and without the Coriolis effect.

	With the Coriolis effect	Without the Coriolis effect
Low modal density region	314 Hz-414 Hz	365 Hz-465 Hz
High modal density region	874 Hz-974 Hz	877 Hz-977 Hz
Veering region	848 Hz-948 Hz	840 Hz-940 Hz

there is only one mode that originates from the 2ND-FW tuned mode as the 2ND-BW mode is too far because of the frequency split. Therefore, there is no interaction and no amplitude magnification.

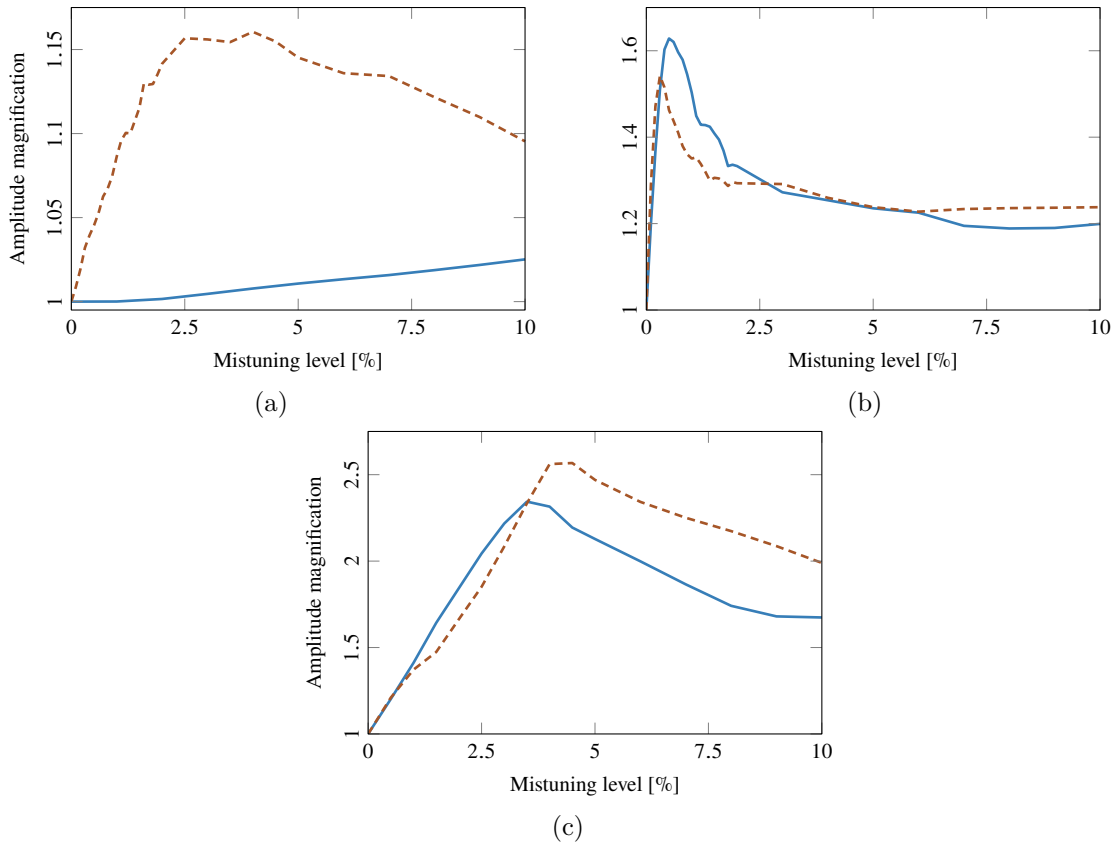


Figure V.9 – Variations in the amplitude magnification factor with the mistuning level at 10,000 rpm. (a) Low modal density region with a 2EO-FW excitation. (b) High modal density region with a 15EO-BW excitation. (c) Veering region with a 6EO-FW excitation. [—]: With the Coriolis effect. [--]: Without the Coriolis effect.

In the second case (Fig. V.9b), the Coriolis effect does not seem to have a real impact. The maximum magnification is slightly greater with the Coriolis effect, with an increase of 6% in the case of the Coriolis effect. This maximum is around the same level of mistuning and it can be observed in Table V.4 that the region of excitation is almost the same with and without Coriolis, which confirms that near blade-dominated modes, the Coriolis effect can be negligible, as reported in most previous papers investigating mistuning but this may result in a slight underestimation of the maximum magnification.

For the third case, the results are more mixed, (Fig. V.9c), between 0 and 3.5% of mistuning level, the behaviours with and without Coriolis effect are equivalent. After 3.5%, the case

without Coriolis gives a 9% higher magnification and the location of the maximum in terms of mistuning level is shifted by 1%. It can be noticed that compared to the study conducted in [194] for the veering region, the results are very different. This can be explained by the model geometry, which is the one presented in Section IV.3.1. The Coriolis effect is more pronounced there, with a very important frequency shift between the forward and backward wave as observed in Fig. IV.5a, whereas for the present model this shift is very weak.

This quick investigation shows that it is essential to take the Coriolis effect into account when there is disc participation in the response, especially for disc dominated modes where the behaviour can be completely different when the Coriolis effect is not taken into account.

3 Dynamics evolution with the rotational speed

The Coriolis effect depends on the rotational speed, which is not the case of mistuning. It is therefore expected that the interaction between the Coriolis and mistuning effects varies with the rotational speed. The forced response statistics will be investigated further under several rotational speeds in the three different regions and with the help of three criteria. The first criterion is the amplitude magnification induced by the mistuning. The second criterion is the average change of amplitude (ACA) given at the frequency of the maximum amplitude a_{\max} through all the sectors (Eq. (II.55)). This criterion is used to quantify the phenomenon of localisation as it measures the difference between the amplitude of each sector and the maximum sector amplitude. It is calculated for all the Monte Carlo simulations and the average of all these values is given. The third criterion is a discrete Fourier transform (DFT) (Eq. (II.56)) which gives information on the amplitude on the presence of travelling waves.

3.1 Low modal density region

In the low modal density region with a 2EO-FW excitation, the amplitude magnification curve shapes change a lot between 0 rpm and 1,000 rpm. From 0 rpm to 100 rpm, the shape evolves from a curve with a peak at 2.5 % of mistuning level -green curve in Fig. V.10- to a curve with a constant amplitude magnification increasing with the mistuning level -red curve in Fig. V.10. From 100 rpm to 1,000 rpm the amplitude magnification values decrease significantly -blue curve in Fig. V.10. After 1,000 rpm, these values remain almost constant (Fig. V.11) except for a slight increase at 6,000 rpm due to a crossing between the 2ND-FW 1 and 3ND-FW 1 modes as observed in Fig. V.4.

For the ACA criterion, the mistuning level (σ) has been fixed to 1 %, 5 %, and 10 %. The rotational speed range is zoomed between 0 rpm and 1,000 rpm as there is no significant change in behaviour after 1,000 rpm, except for the crossing of the modes at 6,000 rpm and the considered asymptotic value at 10,000 rpm. These values are indexed in Table V.5. The ACA are maximal at 0 rpm for every mistuning level and decrease quickly with an increasing rotational speed until 1,000 rpm, then decrease slowly to reach a minimum value at 10,000 rpm, except a small increase at 6,000 rpm, which shows that all the sectors vibrate with approximately the same amplitude at high speed, and that the minimum values reached depend on the mistuning level. The phenomenon of localisation is stronger with a high mistuning level and is more difficult to reduce at high speed.

For the sake of clarity, the mistuning levels for the DFT criterion have been fixed to 1 % (Fig. V.12a), 5 % (Fig. V.12b), and 10 % (Fig. V.12c). As for the ACA criterion, the rotational speed is zoomed between 0 rpm and 1,000 rpm. Only the 2ND-BW and 2ND-FW components can be observed in Fig. V.12, as they are the only two significant components, all the other components being close to zero. At rest, the 2ND-BW and 2ND-FW components are close

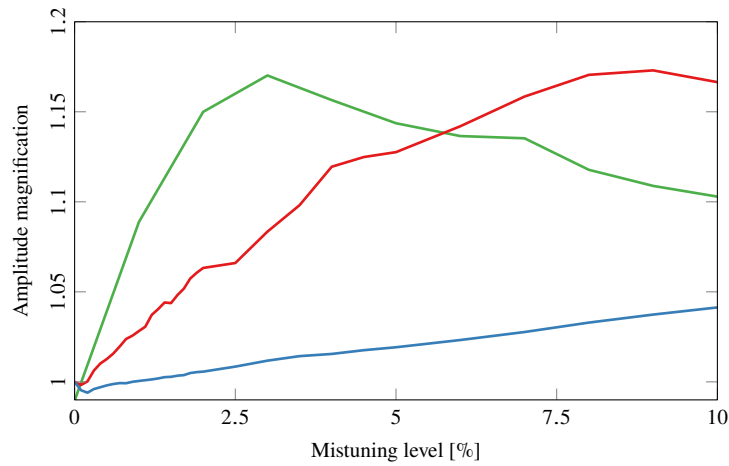


Figure V.10 – Variations in the amplitude magnification factor with mistuning in the low modal density region with a 2EO-FW excitation for different rotational speeds. [—]: 0 rpm. [—]: 100 rpm. [—]: 1,000 rpm.

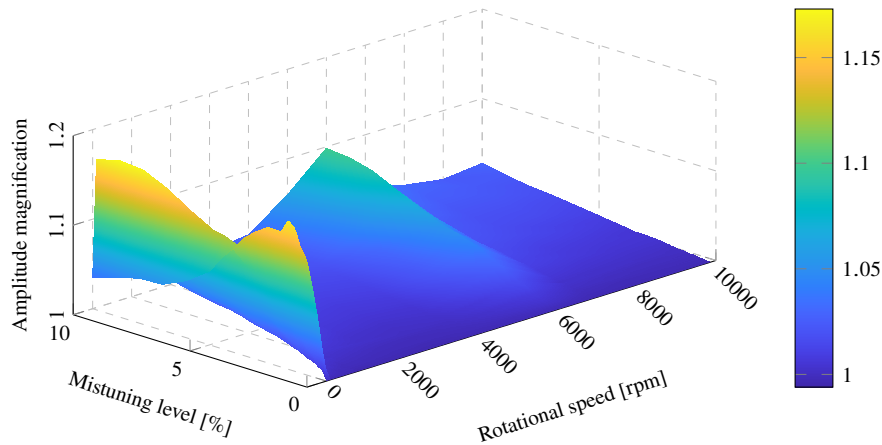


Figure V.11 – Variation in the amplitude magnification with the mistuning level and the rotational speed in the low modal density region with a 2EO-FW excitation.

Table V.5 – Average change of amplitude at different rotational speeds in the low modal density region with a 2EO-FW excitation and different mistuning levels.

σ	μ_0	μ_{200}	μ_{400}	μ_{600}	μ_{800}	$\mu_{1,000}$	$\mu_{6,000}$	$\mu_{10,000}$
1 %	15.84	1.88	1.1	0.71	0.62	0.49	1.24	0.28
5 %	33.41	8.65	5.00	4.00	3.06	2.58	6.32	1.35
10 %	35.7	14.31	9.01	7.24	4.87	4.90	10.39	3.22

to each other, whereas when the speed increases, the 2ND-BW component decreases until it becomes negligible while the 2ND-FW component increases. Therefore, at speeds around 1,000 rpm and above, a full forward travelling wave of 2 nodal diameters is developed except once again at 6,000 rpm where there is a slight appearance of the 3ND-FW wave.

As for the ACA criterion, the mistuning level does not change this behaviour, although it affects the values of the components. With a higher mistuning level, the values of the 2ND-BW component decrease more slowly with an asymptotic value further away from zero, and the

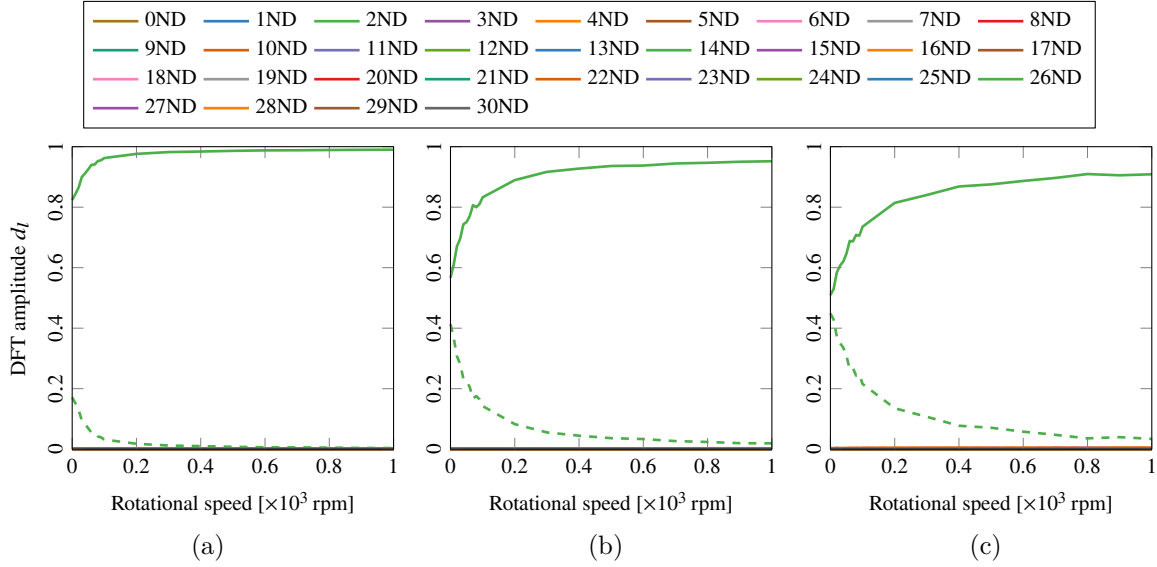


Figure V.12 – Evolution of the DFT components with speed in the low modal density region with a 2EO-FW excitation and different mistuning levels. (a) 1 % of mistuning level. (b) 5 % of mistuning level. (c) 10 % of mistuning level. [—]: Forward wave. [---]: Backward wave.

2ND-FW increases more slowly with an asymptotic value less close to one. This means that the contribution of the 2ND-FW shape at high speed is less developed with a high mistuning level.

This behaviour, previously observed with the lumped model in Chapter II and analytically explained in Section II.1 with the perturbation method, originates from the frequency isolation of modes due to the Coriolis effect. As there are no other nearby modes, the interaction of the tuned modes due to mistuning perturbation cannot develop, and therefore, the behaviour of the mistuned system is close to that of the tuned one. This also explains the small increase of mistuning at 6,000 rpm due to the crossover with the 3ND-FW 1 mode. However, this interaction is not strong enough to create a significant mistuning.

3.2 High modal density region

For the high modal density region with a 15EO-BW excitation, the amplitude magnification is not perturbed by the rotational speed: the peak is always found for a mistuning level between 0.5 % and 0.6 % with maximum values between 1.60 and 1.65 (Fig. V.13).

The ACA criterion has been evaluated at the peak of the mistuning level, i.e., at 0.5 % and at 1 %, 5 %, 10 %. These values are indexed in Table V.6 for different rotational speeds between 0 rpm and 10,000 rpm. As for the amplitude magnification, the ACA does not change significantly with the rotational speed. However, the localisation is not maximum at 0.5 % where the amplitude magnification is maximum. The localisation phenomenon is greater with a higher mistuning level.

In contrast to the DFT in the low modal density region, all the components have non-zero values in the high modal density region. Therefore, all the components are represented in Fig. V.14 for 1 %, 5 %, and 10 % of the mistuning level. All the component values are below 0.05 except for the 15ND-BW component, which is slightly above 0.1. The participation of all the components in the forced response means that there is no specific travelling wave, which is consistent with the ACA criterion, which suggests a strong localisation of the response because of the mistuning perturbation. With a stronger mistuning level, all the DFT components converge to a restricted zone below 0.04, which reveals a stronger interaction of the modes due

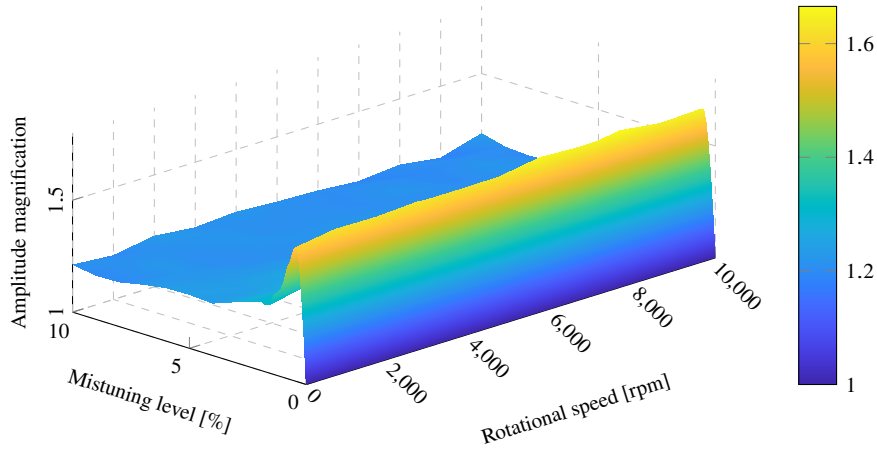


Figure V.13 – Variation in the amplitude magnification with the mistuning level and the rotational speed in the high modal density region with a 15EO-BW excitation.

Table V.6 – Average change of amplitude at different rotational speeds in the high modal density region with a 15EO-BW excitation and different mistuning levels.

σ	μ_0	$\mu_{2,000}$	$\mu_{4,000}$	$\mu_{6,000}$	$\mu_{8,000}$	$\mu_{10,000}$
0.5 %	60.94	58.74	56.99	58.44	58.17	57.17
1 %	70.23	71.14	70.80	70,13	70.69	70.68
5 %	85.16	85.02	84.61	84.77	84.16	84.44
10 %	87.90	87.26	87.41	87.41	86.83	87.20

to the mistuning.

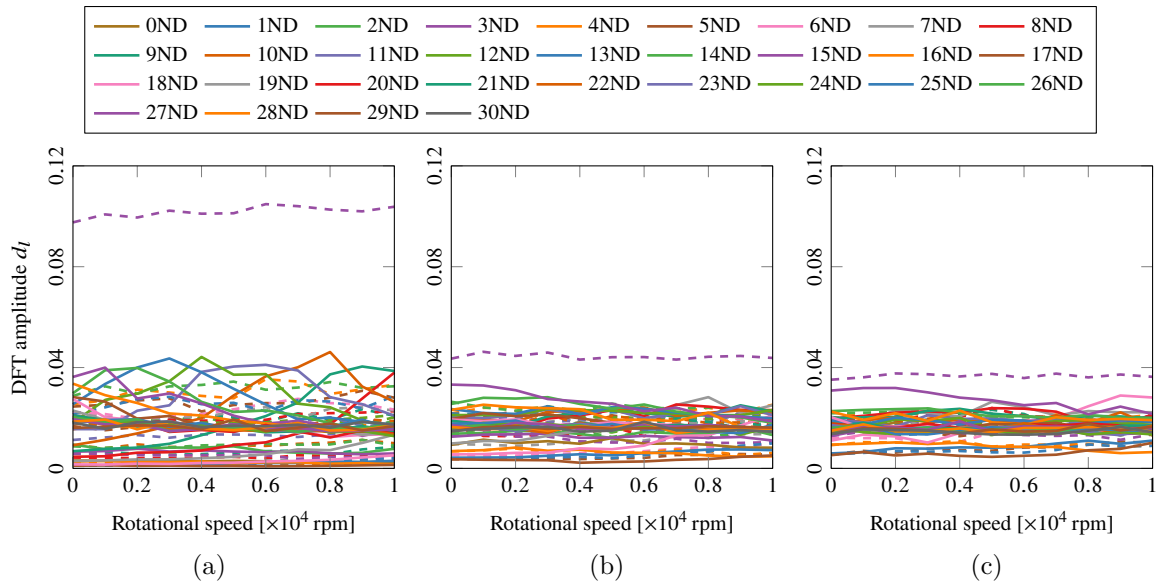


Figure V.14 – Evolution of the DFT components with speed in the high modal density region with a 15EO-BW excitation and different mistuning levels. (a) 1 % of mistuning level. (b) 5 % of mistuning level. (c) 10 % of mistuning level. [—]: Forward wave. [--]: Backward wave.

These results show that the Coriolis effect has no impact on the forced response in a high

modal density region. The localisation is stronger with a high mistuning level, even if the maximum amplitude magnification is at a lower mistuning level.

3.3 Veering region

The amplitude magnification versus the mistuning level and rotational speed is plotted in Fig. V.15 for the veering region with a 6EO-FW excitation. The mistuning level has been increased up to 20%, which is very large and therefore unrealistic, but it gives a better understanding of the general behaviour in this region by locating the maximum magnification response as a function of the rotational speed.

It is interesting to mention that the growth due to the mistuning in the veering region is much slower than in the high modal density region (Fig. V.14a). In the high modal density region, a small perturbation is enough to induce a strong interaction between the modes as well as an amplitude magnification. In contrast, in the veering region, the modes are further apart from each other, so there is a need for a stronger mistuning to have an interaction between the modes and a significant amplitude magnification.

At 0 rpm, the maximum amplitude magnification is of 3.24 at 14%. Then, with increasing rotational speed, the maximum amplitude magnification and its associated mistuning level decrease linearly until it reaches 2.3 at 3.5%. This trend is explained by the progressive convergence in frequency of the 6ND-FW 1 mode towards the high modal density region according to the rotational speed. At 0 rpm, the mode is 63 Hz away from the high modal density region, while at 10,000 rpm it is only 8 Hz away from this region.

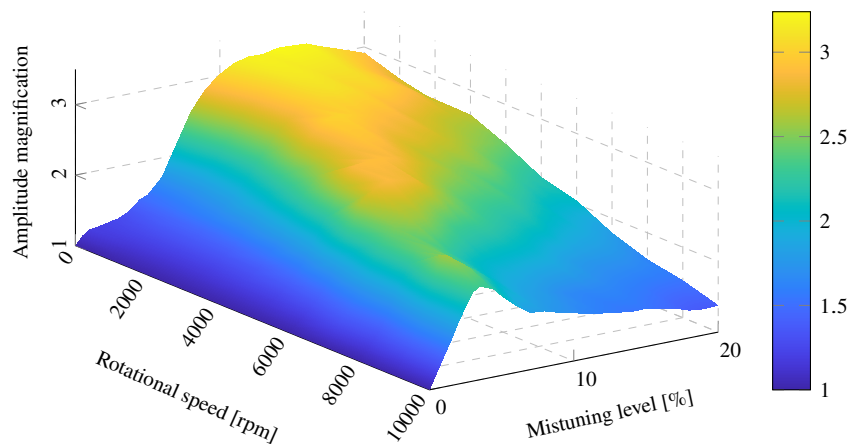


Figure V.15 – Variation in the amplitude magnification with the mistuning level and the rotational speed in the veering region with a 6EO-FW excitation.

The values of the ACA criterion are listed in Table V.7 for 1%, 5%, and 10% of the mistuning level. The values are lower at 2,000 rpm than at 0 rpm but increase again afterwards, which means that up to 2,000 rpm the localisation tends to decrease but becomes stronger afterwards. This phenomenon is less noticeable with increasing mistuning level.

The DFT components in the veering region, plotted in Fig. V.16, confirms the trend observed with the ACA criterion. At 0 rpm, the 6ND-FW and 6ND-BW components are equivalent and dominate compared to the other components, especially for a low mistuning level (Fig. V.16a). At 2,000 rpm, only the 6ND-FW component is predominant, which means that there is a diminution of the mistuning effect, in agreement with the ACA criterion, then this component decreases and all the others increase, especially the 0ND at 7,000 rpm and the 7ND-BW after 8,000 rpm due to crossings with these modes at these rotational speeds. For

Table V.7 – Average change of amplitude at different rotational speeds in the veering region with a 6EO-FW excitation and different mistuning levels.

σ	μ_0	$\mu_{2,000}$	$\mu_{4,000}$	$\mu_{6,000}$	$\mu_{8,000}$	$\mu_{10,000}$
1 %	27.76	9.31	10.18	14.85	20.18	33.97
5 %	55.50	44.38	52.73	65.12	75.54	82.76
10 %	82.96	79.79	83.05	86.34	84.89	85.88

higher mistuning levels (Fig. V.16b and Fig. V.16c), the 6ND-FW component values decrease and all the other components are present in the same range of values, below 0.2.

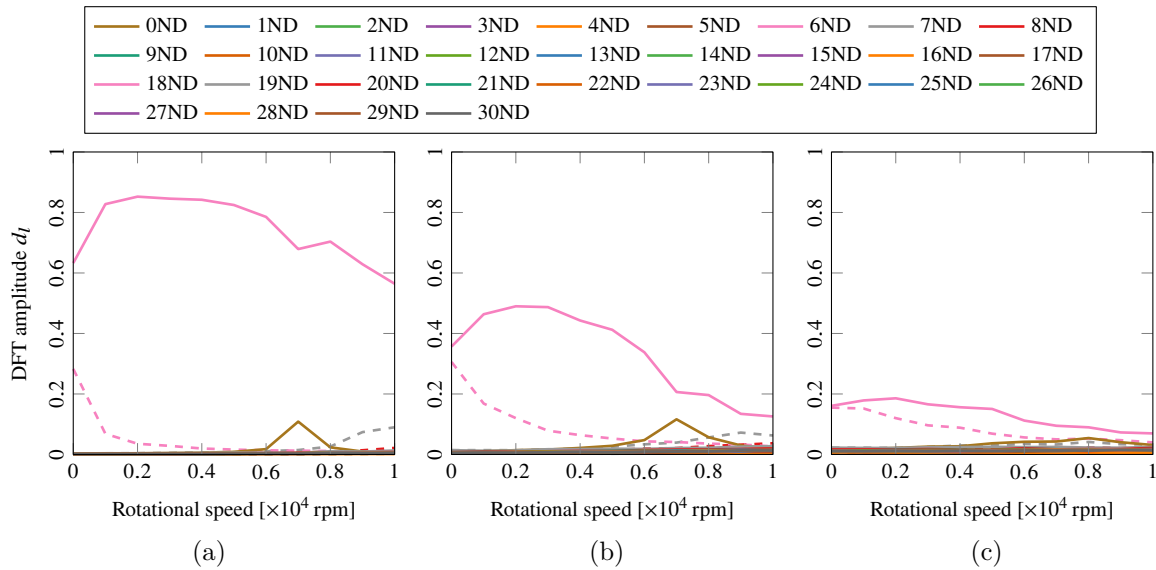


Figure V.16 – Evolution of the DFT components with speed in the veering region with a 6EO-FW excitation and different mistuning levels. (a) 1 % of mistuning level. (b) 5 % of mistuning level. (c) 10 % of mistuning level. [—]: Forward wave. [--]: Backward wave.

These results show that in the veering region with a 6EO-FW excitation, a full travelling wave cannot occur because of the proximity with the high modal density region and the interactions due to the mistuning. It can be noted that at low speeds, the mistuning effects have a lower influence, with a major contribution of the 6ND-FW travelling wave Fig. V.16a. There is a significant evolution of the dynamics with the rotational speed due to the proximity in frequency of the veering region with the high modal density region.

Conversely, the 6ND-FW 2 mode moves away with increasing rotational speed and becomes isolated in frequency. The amplification magnification versus the mistuning level and rotational speed is plotted in Fig. V.17. Here, the amplification magnification increases continually with the mistuning level, which means that the peak is above 20%. Looking more precisely at the curves for a given mistuning level in Fig. V.18, it can be observed a decrease of the amplitude magnification with the rotational speed increasing.

Here, the ACA criterion behaviour is like that of the low modal density region, with a decrease in the ACA values with the increasing rotational speed, and the values are higher with a higher mistuning level (Table V.8). However, in this case, the decrease is not as fast as in the first case and the values for a high mistuning level are still high, so a strong localisation is still present.

The DFT at 1 %, 5 % and 10 % of the mistuning level plotted in Fig. V.19 confirm the

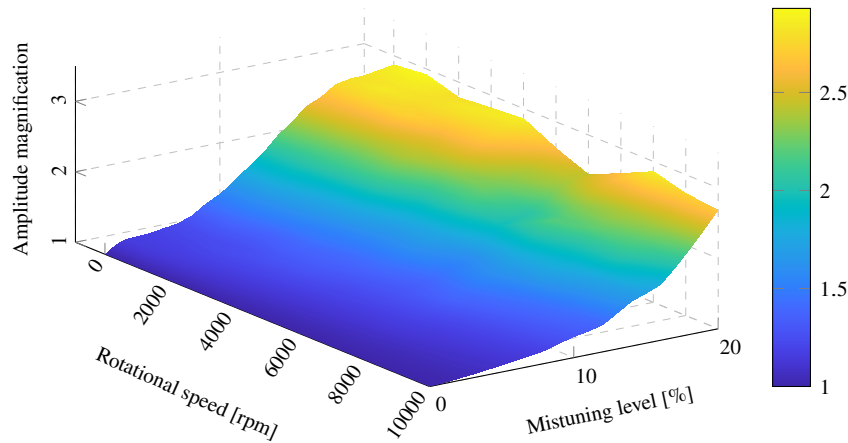


Figure V.17 – Variation in the amplitude magnification with the mistuning level and the rotational speed in the changing modal density region with a 6EO-FW excitation.

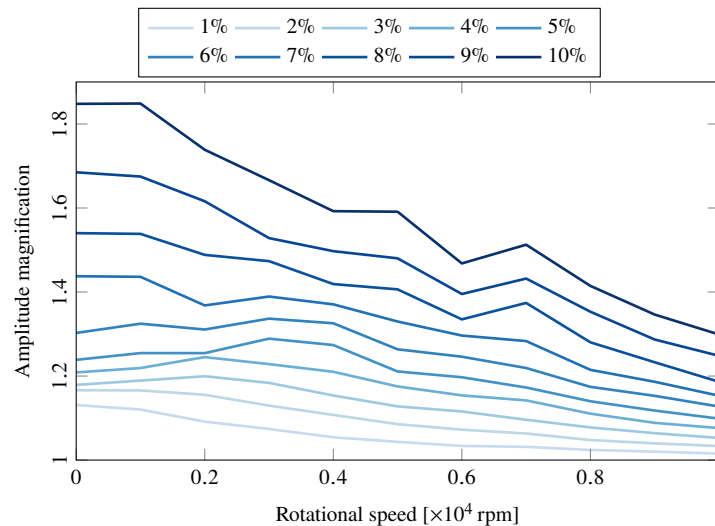


Figure V.18 – Variation in the amplitude magnification with the rotational speed for different mistuning level in the changing modal density region with a 6EO-FW excitation.

Table V.8 – Average change of amplitude at different rotational speeds in the changing modal density region with a 6EO-FW excitation and different mistuning levels.

σ	μ_0	$\mu_{2,000}$	$\mu_{4,000}$	$\mu_{6,000}$	$\mu_{8,000}$	$\mu_{10,000}$
1%	15.37	9.90	5.75	3.37	2.53	1.56
5%	38.47	31.40	24.74	17.56	12.81	9.36
10%	63.46	58.45	47.64	38.75	30.40	24.46

behaviour of the ACA criterion. At 0 rpm, all the components are non-negligible and the 6ND-FW and 6ND-BW components are predominant. Then the 6ND-FW component increases with the increasing rotational speed while the other components become almost negligible, which reveals the appearance of a distinct 6ND-FW shape response. With higher mistuning levels, the phenomenon becomes less pronounced.

From these results, it can be concluded that the large mistuning effects present in the veering region at rest can be reduced if the natural frequency moves away from the high modal

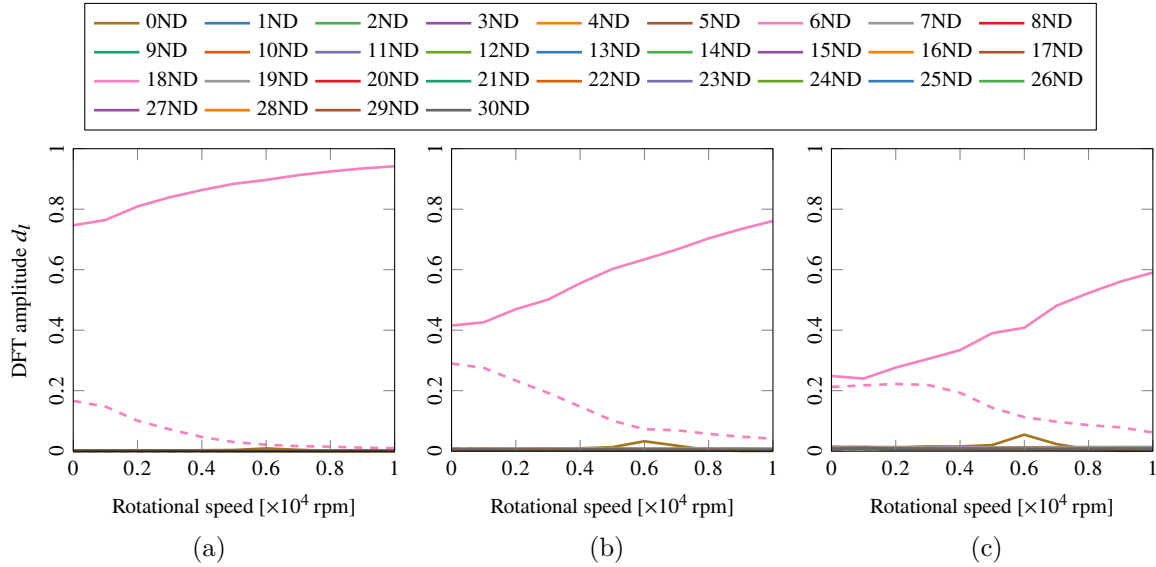


Figure V.19 – Evolution of the DFT components with speed in the changing modal density region with a 6EO-FW excitation and different mistuning levels. (a) 1 % of mistuning level. (b) 5 % of mistuning level. (c) 10 % of mistuning level. [—]: Forward wave. [---]: Backward wave.

density region with increased rotational speeds, due to the Coriolis and stiffening effects. In the mistuned case, a travelling wave response with a behaviour close to the tuned case can be observed, but the 6ND-FW response depends on the mistuning level. When the natural frequency stays close or gets closer to the high modal density region, there are no particular changes in the behaviour: the mistuning effect remains predominant.

Chapter summary

The main objective of this chapter was to investigate the interactions between the Coriolis and mistuning effects on bladed drums and the predominance of one effect over the other. A FEM of a simplified industrial bladed drum was used to carry out a forced response statistic analysis using Monte Carlo simulations at different mistuning levels and rotational speeds.

The blade mistuning is the main driver of the response behaviour, especially for blade-dominated modes but also for blade-disc modes in veering regions. The only exception is for disc-dominated modes for which the disc mistuning governs the response behaviour. In all cases, the sector mistuning always follows the dominant behaviour and therefore the IMM method is the most convenient for models with high disc participation.

The present work clearly shows that it is important to take the Coriolis effect into account when studying the disc modes or the veering regions since their behaviour is completely different when the Coriolis effect is not taken into account. The only case where it is almost possible to neglect the Coriolis matrix is with the blade-dominated modes for which the disc dynamics has a small impact on the global response. But even in this case, it can lead to an error in the estimation of the amplification level due to mistuning.

The interaction between the Coriolis and mistuning effects was investigated with the evolution of the rotational speed in three different regions. In the low modal density region, the mode quickly becomes isolated in frequency from the other modes because of the Coriolis effect, which results in a travelling wave and a behaviour similar to that of the tuned case. In the high modal density region, the localisation and amplitude magnification are strong and do

not change significantly with the rotational speed due to the lack of influence of the Coriolis effect. When the mode stays close to the veering region, the mistuning remains unaffected by the rotational speed, but when it moves away from the veering region and high modal density region, a travelling wave similar to that observed in the tuned behaviour appears.

Conclusion

This thesis work has provided a better understanding of the Coriolis effect occurring on new bladed disc architectures in the aeronautic field. In particular, the interaction between the Coriolis effect and mistuning has been studied in-depth to highlight the conditions of predominance of one phenomenon over the other. Finally, tools have also been developed to study the influence of the Coriolis effect on flutter instability, especially in the presence of detuning. The following section provides a summary of the main results obtained in this manuscript and the next one will focus on the perspectives for improving and completing this work.

Results

The dynamic behaviour of rotational cyclic symmetric structures was presented at the beginning of this manuscript, highlighting the appearance of the Coriolis effect. The use of cyclic symmetry theory shows that the standing wave double modes at rest are split in frequency into two travelling wave modes due to the Coriolis effect, one forward and the other backward. These consequences have been compared to mistuning which also splits the frequency into double modes but tends to create stationary modes.

The first objective was to investigate the interaction between the Coriolis and mistuning effects in cyclic symmetric structures using an analytical perturbation method. This method allowed expressing the eigenvalues and eigenvectors of the mistuned system as the sum of the tuned eigenvalues and eigenvectors multiplied by weight coefficients.

For a frequency isolated mode with small mistuning, the weight coefficients are negligible and therefore the mistuned mode shape is almost the same as the tuned mode shape. However, in veering zones, an asymptotic phenomenon occurred for the calculation of weight coefficients where two tuned modes have the same eigenvalue. Therefore, near these zones, two tuned mode shapes coexisted in the mistuned mode shape, which is reflected by a standing wave mode.

This phenomenon was then observed using a numerical approach on a lumped model representative of a 60-sector bladed disc. This model has been designed to take into account rotation-related effects including the Coriolis effect and frequency mistuning applied to the blades. For the frequency isolated modes, a standing wave mode was observed at rest before becoming a full travelling wave mode at high speeds due to the Coriolis effect. However, for veering zones or high modal density regions, two or more tuned mode shapes coexisted and a considerable change of amplitude occurred between each sector, interpreted as a localization phenomenon due to a standing wave. An amplitude magnification was also observed in the later case, which was not observed for frequency isolated modes.

The second objective was to study the influence of the Coriolis effect on flutter stability using the same parametric model. Aeroelastic forces were introduced using Whitehead's theory

for an incompressible flow on cascade blades. A recalibration of the parameters was then necessary to introduce flutter instability on some nodal diameter modes. At this stage, it was shown that without the presence of mistuning, the Coriolis effect had no effect on the aerodynamic stability of the structure.

Two strategies were used to optimise the detuning pattern to stabilise the aerodynamic system. The first one was the subspace optimisation strategy which can considerably reduce the number of detuning patterns to be tested by grouping blades and the second strategy was the genetic algorithm. The two methods showed fairly equivalent performance but with different strengths and weaknesses. The subspace optimisation strategy allows a shorter computation time than the genetic algorithm but does not allow an optimisation on the Young's modulus parameter whereas the second one does.

This optimisation was done without taking into account the Coriolis effect in order to clearly see the effect once it has been added to the system. The system, which was stable with the introduction of the detuning pattern, became unstable once the Coriolis effect was activated, demonstrating that the latter decreases the stabilising capacity of detuning on the flutter. Once the Coriolis effect was taken into account in the optimisation strategies, a detuning pattern with a higher level than the original could be found to stabilise the system.

In order to reduce computation time for large models simulations such as finite element models, reduction methods are essential. Accordingly, the third objective was to determine reduction methods that can take into account both mistuning and the Coriolis effect in order to study the interaction between these two phenomena on a finite element model more representative of an industrial structure. In that way, the SNM, CMM and IMM methods, which allow to take into account the frequency mistuning on finite element models of bladed discs, have been adapted and validated to effectively account for the Coriolis effect. Other methods involving reduction with variable rotational speeds were also mentioned but not subsequently used because they are less advantageous for a resolution of a few rotational speeds but can be very useful when simulations have to be done on a large number of different rotational speeds.

The fourth and last objective was to have an application on an industrial bladed drum model. This was to validate the observations already made on the lumped parameter model but also to go further in the understanding of the interaction between the Coriolis and mistuning effects. For this, instead of having the same single mistuning pattern for all simulations, a stochastic study was performed using the Monte Carlo method to capture the general behaviour of the mistuning according to the simulations.

First, the influence of the mistuning location was investigated. It was shown that this influence depends on whether the blades or disc motions are involved in the response. For a predominantly disc participation, the disc mistuning has a large influence while the one on the blades does not. In the opposite case, when the blades are predominantly involved, the blade mistuning has a significant influence on the response, whereas the mistuning of the disc does not. Finally, in the areas where the disc and blades motions are involved, it is the blades mistuning that influences the response behaviour. In any case, a uniform mistuning over the whole sector captures the predominant mistuning behaviour and thus the most general case.

Secondly, the influence of the Coriolis effect on the mistuned structure was examined by comparing the simulations with and without the Coriolis effect. The results showed that when the participation of the disc is important, the Coriolis effect modifies the results considerably, with a behaviour much closer to that of the tuned structure. On the other hand, for blade dominated modes, which are all very close in frequency, the Coriolis effect has a negligible impact on the response and can reasonably be omitted. Finally, for the veering regions, the

results are mixed, sometimes the Coriolis effect has a strong influence and sometimes it does not, depending on the frequency split between the forward and backward modes in these regions. In all cases when a structure is identified as sensitive to the Coriolis effect it is preferable to take it into account in the simulations in order to avoid unexpected behaviours.

Finally, the interaction between the Coriolis and mistuning effects was studied in-depth in three different regions by varying both the rotational speed and mistuning level. In the low modal density region, with disc dominated response, the mistuned system tend towards a tuned behaviour due to the Coriolis effect. In the high modal density region, with a blade dominated response, mistuning is always predominant and there is no noticeable evolution with the rotational speed. In the veering region, the results are again mixed, if the mode remains close to this region with the rotational speed then the mistuning behaviour remains predominant but if the mode moves away from this region then the Coriolis effect becomes predominant and a behaviour similar to the tuned case appears.

In any case, the higher the mistuning level the more apparent the localisation phenomenon. In contrast, the amplitude magnification always has a peak at a specific mistuning level, but its value depends on the modal density in frequency and their separation. The closer the modes are in frequency, the lower the mistuning level, but if the frequencies are further apart, then the peak appears at higher mistuning level.

Perspectives

In view of the work carried out during this thesis, many perspectives can be suggested in order to improve the numerical methods used but also to broaden the understanding of the phenomena studied and their interactions.

A first area of improvement could be the integration of non-linearities in the dynamic simulations. It has already been shown that the integration of frictional non-linearities on mistuned structures can lead to different behaviour from the linear system [84]. Accordingly, it can be considered that it also modifies the interaction between the Coriolis and mistuning effects. Even if the structures presenting an important Coriolis effect tend to be single-piece with a strong blades-disc coupling, it should not be forgotten that friction ring dampers can be added to these structures to limit the vibrations [107, 192] and thus modify the dynamic behaviour.

For geometrical non-linearities, a brief study in [193] shows that they have little impact on the studied model. It could still be necessary to carry out the same type of study on structures which are more sensitive to geometrical effects, such as open rotor blades [50]. Mabilia's work [121] has shown that the Coriolis effect interacts slightly with mistuning on LEAP blades, so a more slender structure could potentially allow more interaction between these phenomena, which should also interact with the friction non-linearity due to the blade root contact.

In this study, mistuning was only considered in terms of frequency, i.e. by changing the stiffness equivalent to Young's modulus. However, there are other ways of integrating mistuning, such as geometric mistuning, where the geometry from one blade to another can be different and thus the mass, Coriolis and stiffness matrices are all modified. There is also aerodynamic mistuning, where the blade loading is different between adjacent blades. It might then be interesting to see if the conclusions made in this manuscript will be the same with geometric or aerodynamic mistuning, which generally has higher mistuning level.

Geometric mistuning also requires the use of specific reduction methods because those

presented in this manuscript are not applicable. Many methods already exist on this subject, including the MMDA [185], Mbaye's method [129], PRIME [124], N-PRIME [196], PRISM [177]. The appropriateness of these methods should then be studied when integrating the Coriolis matrix. The same applies to the integration of non-linearities where methods such as CNCMS [85] or SNCR [158] have to be adapted to take into account the Coriolis effect.

The reduction methods used in this manuscript, SNM, CMM and IMM, can also be improved as the Coriolis matrix is not taken into account in the reduction basis. The development of these methods in a state-space representation to take the Coriolis effect directly into account in the reduction basis could be considered. The calculation time for the reduction basis may be much larger, as has already been shown in Chapter IV, but taking the Coriolis effect into account in the calculation of the tuned modes and free-interface sector modes may also potentially increase the accuracy of the forced response and allow one to decrease the size of the ROM. The time lost during the computation of the ROM may be made up by the Monte Carlo simulation.

As explained in Chapter I, in order to reduce mass and increase aerodynamic performance, some aircraft engine elements are made in one piece, and some components such as low pressure compressors can be multi-stage parts which makes the dynamics of each stage interdependent. Accordingly, multi-stage analysis strategies were developed [108] and reduction methods such as CMM were also adapted to this kind of structure [142] to take into account the mistuning. As these structures are potentially subject to the Coriolis effect, it would be necessary to adapt these methods to take this effect into account, and to look at the impact it can have.

Regarding the influence of the Coriolis effect on the flutter instability in Chapter III, the simulations were realised by adding only detuning in order to stabilise the system but it could be interesting to see the influence of random mistuning on the stability. In general, it is considered to stabilise the system [28, 97] but it is possible based on the observations made in this work that the Coriolis effect reduces this phenomenon.

The aerodynamic model presented in this thesis is convenient to quickly calculate aerodynamic coefficients according to different parameters and thus perform many simulations, but it also has some limitations. The fluid is considered to be incompressible, which is not a realistic case for turbomachinery. Accordingly, an aerodynamic model, which allows for fluid compressibility, could be considered to improve the simulations. The review made by Marshall and Imregun [125] presents a wide range of available methods that could be used in this regard.

Finally, to enable high fidelity simulations, it may be possible to use Computational Fluid Dynamics software [48, 153]. However, the calculation times are expensive with this method, so it is necessary to identify a specific geometry sensitive to the Coriolis effect, mistuning and flutter. Therefore, before using such software, it is preferable to use intermediate models to run simulations more quickly and to improve understanding of the phenomena.

A last interesting perspective would be to carry out experimental studies on the interactions between the Coriolis and mistuning effects as a first step and then with flutter in a second step as it is more complex to implement. All the numerical observations made in this thesis must be validated experimentally in order to further support them.

Some experimental studies [1, 64, 121, 166] are in agreement with the numerical observations made in this manuscript, however these have never been conducted specifically for the interaction between the Coriolis and mistuning effects and are therefore rather brief. More in-depth studies, especially in the veering and high modal density regions, should be considered. Finally, as far as the interaction between flutter and the Coriolis effect is concerned, no experimental studies

have yet been conducted.

List of Figures

I.1	Schematic diagram of an axial flow turbojet [Wikipedia].	8
I.2	Schematic diagram of a separated-flow turbofan [Wikipedia].	9
I.3	Schematic diagram of a double-spool turbofan [Wikipedia].	10
I.4	Schematic diagram of (a) compressor stage and (b) turbine stage.	10
I.5	Turbofan of CFM International; past, present and future. (a) CFM56. (b) LEAP. (c) RISE. [CFM]	11
I.6	Schematic representation of (a) a 3-stage low-pressure compressor and (b) a circumferential dovetail [JetX Engineering].	12
I.7	Schematic representation of (a) a dovetail root and (b) a fir tree root [JetX Engineering].	13
I.8	Single-piece technology. (a) Bladed disc [84]. (b) Bladed drum [Safran].	13
I.9	Wakes induced by stator vanes [183].	14
I.10	Configurations of a continuous system [63].	16
I.11	Example of a cyclic-symmetric structure. (a) Fully assembled structure composed of 60 sectors. (b) Reference sector.	23
I.12	Boundary conditions between each sector of a cyclic-symmetric structure.	26
I.13	Nondegenerate modes of a cyclic structure with 60 sectors : (a) 0ND and (b) 30ND.	28
I.14	Degenerate modes of a cyclic structure with 60 sectors : (a) 1ND and (b) 2ND.	29
I.15	Blades phase over one period for a degenerate mode with 2 nodal diameters. (a) Forward wave and (b) Backward wave.	29
I.16	In-plane motion of a blade tip with the action of the Coriolis force. (a) Forward local displacement and (b) Backward local displacement	33
I.17	Amplitude magnification factor versus the standard deviation of random mistuning [33].	34
I.18	Cumulative distribution function for the accelerated Monte Carlo simulation. [*] Set of 50 mistuning patterns. [—] The three-parameter Weibull distribution using Whitehead’s formula for λ . [—] The three-parameter Weibull distribution using the value 20% above the maximum for λ	36
I.19	Campbell diagram	37
I.20	ZZENF diagram.	38
I.21	Natural frequencies/nodal diameters diagram.	39
I.22	S-N curve.	39
I.23	Haigh diagram.	40
II.1	Cyclic symmetric lumped parameter model	48
II.2	Mistuning pattern using a normal distribution function with zero mean and $\pm 1\%$ standard deviation for each spring. (a) Blade spring k^b . (b) Radial spring k^r . (c) Coupling spring k^c . (d) Tangential spring k^t	53

II.3	Natural frequencies versus number of nodal diameter at 5,000 rpm. All different modal families are represented with different colours. [—]: Forward wave modes. [--]: Backward wave modes. [◻]: Veering regions. [■]: Studied region for the numerical simulations.	54
II.4	Campbell diagram of the tuned bladed disc between 750 Hz and 1,400 Hz. [—]: Forward wave modes. [--]: Backward wave modes.	54
II.5	Modal shape of three modes in each different regions. (a) First region: 2ND-FW 1. (b) Second region: 10ND-BW 1. (c) Third region: 3ND-BW 2	55
II.6	Campbell diagram of the mistuned bladed disc between 750 Hz and 1,400 Hz. . .	56
II.7	Zoom on the Campbell diagram of the mistuned bladed disc between 925 Hz and 1,025 Hz. [○]: Veering regions.	56
II.8	Evolution of the DFT components with speed for the modes; (a) M2, (b) M4 and (c) M21. The DFT components represent the participation of the different travelling waves on the dynamic response of the structure. The solid curves represent the forward wave [—] and the dashed curves represent the backward wave [--].	58
II.9	Comparison of the DFT components for the modes; (a) M4 at 3,500 rpm and (c) M21 at 5,000 rpm. [■]: Perturbation method. [■]: Benchmark.	61
II.10	FRF around the mode M2 at rest with a 1EO-FW excitation. [—]: FRF of one dof of each sector. [—]: Maximum amplitude response. [--]: Tuned case.	62
II.11	DFT around the mode M2 at rest with a 1EO-FW excitation. [—]: 1ND-FW. [--]: 1ND-BW.	62
II.12	FRF around the mode M21 at rest with a 10EO-BW excitation. [—]: FRF of one dof of each sector. [—]: Maximum amplitude response. [--]: Tuned case.	63
II.13	DFT around the mode M21 at rest with a 10EO-BW excitation. [—]: Forward wave. [--]: Backward wave.	63
II.14	FRF around the mode M2 at 5,000 rpm with a 1EO-FW excitation. [—]: FRF of one dof of each sector. [—]: Maximum amplitude response. [--]: Tuned case. . .	64
II.15	DFT around the mode M2 at 5,000 rpm with a 1EO-FW excitation. [—]: 1ND-FW.	65
II.16	FRF around the mode M21 at 5,000 rpm with a 10EO-BW excitation. [—]: FRF of one dof of each sector. [—]: Maximum amplitude response. [--]: Tuned case. .	65
II.17	DFT around the mode M21 at 5,000 rpm with a 10EO-BW excitation. [—]: Forward wave. [--]: Backward wave.	66
II.18	FRF around the mode M4 at (a) 2,500 rpm and (b) 3,500 rpm with a 2EO-FW excitation. [—]: FRF of one dof of each sector. [—]: Maximum amplitude response. [--]: Tuned case.	66
II.19	DFT around the mode M4 at (a) 2,500 rpm and (b) 3,500 rpm with a 2EO-FW excitation. [—]: 2ND-FW. [--]: 1ND-BW.	67
III.1	Blade geometry and aerodynamic model.	71
III.2	Aerodynamic damping versus the nodal diameter index for air inlet angle between -85° and 85° . (a) First modal family. (b) Second modal family.	77
III.3	Aerodynamic damping versus the nodal diameter index for air inlet angle between 70° and 80° . (a) First modal family. (b) Second modal family.	77
III.4	Aerodynamic damping versus the nodal diameter index. [○]: first modal family. [△]: second modal family. (a) With the Coriolis effect. (b) Without the Coriolis effect.	78
III.5	Best detuning patterns given by the subspace optimisation strategy for the eight subspace without the Coriolis effect. The eight letters correspond to the eight pairs of grouping.	80

III.6	Best detuning patterns given by the the genetic algorithm for different number of generation without the Coriolis effect. (a): $g_t = 100$. (b): $g_t = 500$. (c): $g_t = 2500$.	81
III.7	Convergence of the genetic algorithm for different number of generation without the Coriolis effect. (a): $g_t = 100$. (b): $g_t = 500$. (c): $g_t = 2500$. [—]: Maximum. [--]: Mean. [---]: Minimum.	82
III.8	Aerodynamic damping versus the model frequency without the Coriolis effect in the tuned case [○] and in the detuned case [✱]. The negative aerodynamic damping coefficients are represented in red and the positive ones in green.	83
III.9	Aerodynamic damping versus the frequency for the model with the Coriolis effect in the tuned case [○] and in the detuned case [✱]. The negative aerodynamic damping coefficients are represented in red and the positive ones in green.	84
III.10	Aerodynamic damping versus the continuation parameter (0 / 1: case without / with Coriolis). [—]: M6 mode. [—]: M8 mode. [—]: M67 mode. [—]: M71 mode. [—]: M73 mode.	84
III.11	Modal shape of the five unstable modes. (a) M6 mode. (b) M8 mode. (c) M67 mode. (d) M71 mode. (e) M73 mode.	85
III.12	Evolution of the DFT components with the continuation parameter in the tuned case (0 / 1: case without / with Coriolis). [—]: Forward waves. [--]: Backward waves. (a) M6 mode. (b) M8 mode. (c) M67 mode. (d) M71 mode. (e) M73 mode.	86
III.13	Campbell diagram of the mistuned bladed disc with the aerodynamic forces. (a) Zoom between 960 Hz and 1,040 Hz for the M6 and M8 modes. (b) Zoom between 1,250 Hz and 1,390 Hz for the M67, M71 and M73 modes. [○]: Crossing regions.	87
III.14	Campbell diagram of the mistuned bladed disc without the aerodynamic forces between 960 Hz and 1,040 Hz for the M6 and M8 modes. [○]: Veering regions.	88
III.15	Minimum damping coefficient of the best detuning pattern for different Young's modulus variation.	89
III.16	Best detuning pattern given by a genetic algorithm with the Coriolis effect.	89
III.17	Aerodynamic damping versus the frequency for the model with the Coriolis effect in the tuned case [○] and in the detuned case [✱]. The negative aerodynamic damping coefficients are represented in red and the positive ones in green.	89
IV.1	Representation of a cyclic structure with blade mistuning as introduced with the CMM method.	98
IV.2	Representation of a cyclic structure with sector mistuning as introduced with the IMM method.	100
IV.3	Finite element mesh for the 20-sector bladed drum. (a) Reference sector. (b) Full assembly model. [■]: Clamped surface. [■]: Cyclic symmetric section. [●]: Excitation node. [→]: Excitation vector.	102
IV.4	Campbell diagram of the tuned bladed drum between 200 Hz and 1,000 Hz. [—]: Forward wave modes. [--]: Backward wave modes.	102
IV.5	Natural frequencies versus number of nodal diameter at 10,000 rpm. All different modal families are represented with different colours. [—]: Forward wave modes. [--]: Backward wave modes. [□]: Veering regions. [○]: Studied modes for the numerical simulations. (a) Overall view. (b) Frequency expansion on the veering region.	103
IV.6	Mode shapes of the three first blade-dominated mode families. (a) First flexural mode around 700 Hz. (b) First torsional mode around 2,000 Hz. (c) Second flexural mode around 2,500 Hz.	103
IV.7	Modal shape of three studied modes. (a) First mode: 2ND-FW 1. (b) Second mode: 6ND-FW 1. (c) Third mode: 1ND-BW 1	103

IV.8	Matrix of the Normalized Cross Orthogonality check (NCO) for the comparison between the eigenvectors calculated with Coriolis (ψ_i) and the eigenvectors calculated without Coriolis (ϕ_j) at 10,000 rpm. [○] NCO>0.05 for the off-diagonal terms. [□] NCO<0.95 for the terms on the diagonal.	105
IV.9	Frequencies Error of the 26 first natural frequencies of the reduced order models versus the full mistuned model at 10,000 rpm. (a) The SNM reduction method with blade mistuning and (b) sector mistuning. (c) The CMM reduction method with blade mistuning and (d) the IMM reduction method with sector mistuning.	107
IV.10	NCO matrix for the comparison between the 26 first eigenvectors of the FEM (ϕ_i) and the eigenvectors of the ROMs ($\tilde{\phi}_j$) at 10,000 rpm. (a) The SNM reduction method with blade mistuning and (b) sector mistuning. (c) The CMM reduction method with blade mistuning and (d) the IMM reduction method with sector mistuning.	108
IV.11	Maximum forced response for a blade mistuning in different frequency regions and with different excitations at 10,000 rpm. [(a), (c), (e)] Maximum amplitude over the excitation frequency. [(b), (d), (f)] Maximum normalised amplitude over the blades. [(a), (b)] Low modal density region with a 2EO-FW excitation. [(c), (d)] High modal density region with a 6EO-FW excitation. [(e), (f)] Veering region with 1EO-BW excitation. [—○—]: SNM method. [—▲—]: CMM method. [—◆—]: Mistuned FEM. [—]: Tuned FEM.	109
IV.12	Maximum forced response for a blade mistuning in different frequency regions and with different excitations at 10,000 rpm. [(a), (c), (e)] Maximum amplitude over the excitation frequency. [(b), (d), (f)] Maximum normalised amplitude over the blades. [(a), (b)] Low modal density region with a 2EO-FW excitation. [(c), (d)] High modal density region with a 6EO-FW excitation. [(e), (f)] Veering region with 1EO-BW excitation. [—○—]: SNM method. [—▲—]: IMM method. [—◆—]: Mistuned FEM. [—]: Tuned FEM.	110
IV.13	Frequency versus rotational speed for different modes. (a) 2ND-FW mode. (b) 6ND-FW mode. (c) 1ND-BW mode. [—]: Interpolation method. [★]: Benchmark.	114
IV.14	Normalized amplitude versus rotational speed for different modes. (a) 2ND-FW mode. (b) 6ND-FW mode. (c) 1ND-BW mode. [—]: Interpolation method. [★]: Benchmark.	114
IV.15	Frequency versus rotational speed for different modes approximation of the Taylor series. (a) 2ND-FW mode. (b) 6ND-FW mode. (c) 1ND-BW mode. [—]: Second-order. [—]: Third-order. [—]: Fourth-order. [★]: Benchmark.	115
IV.16	Normalized amplitude versus rotational speed for different modes at different order approximation of the Taylor series. (a) 2ND-FW mode. (b) 6ND-FW mode. (c) 1ND-BW mode. [—]: Second-order. [—]: Third-order. [—]: Fourth-order. [★]: Benchmark.	115
IV.17	Frequency versus rotational speed for different modes approximation of the PROM. (a) M1 mode. (b) M4 mode. (c) M10 mode. [—]: PROM. [★]: Benchmark.	117
IV.18	Frequencies error of the 26 first natural frequencies of the PROM versus the full mistuned model at 8,000 rpm.	117
IV.19	NCO matrix for the comparison between the 26 first eigenvectors of the FEM (ϕ_i) and the eigenvectors of the PROM ($\tilde{\phi}_j$) at 8,000 rpm.	117

IV.20	Maximum forced response for a blade mistuning in different frequency regions and with different excitations at 8,000 rpm. [(a), (c), (e)] Maximum amplitude over the excitation frequency. [(b), (d), (f)] Maximum normalised amplitude over the blades. [(a), (b)] Low modal density region with a 2EO-FW excitation. [(c), (d)] High modal density region with a 6EO-FW excitation. [(e), (f)] Veering region with 1EO-BW excitation. [—▲—]: PROM method. [—◆—]: Mistuned FEM. [—]: Tuned FEM.	119
V.1	Geometry of the 60-sector bladed drum. (a) Reference sector. (b) Full assembly model.	122
V.2	Boundary conditions of the bladed drum model. [■]: Clamped surface. [■]: Cyclic symmetric section. [●]: Excitation node. [→]: Excitation vector.	123
V.3	Finite element mesh for the 60-sector bladed drum. (a) Reference sector. (b) Full assembly model.	124
V.4	Campbell diagram of the tuned bladed drum between 200 Hz and 1,200 Hz. [—]: Forward wave modes. [---]: Backward wave modes.	125
V.5	Natural frequencies versus number of nodal diameter at 10,000 rpm. All different modal families are represented with different colours. [—]: Forward wave modes. [---]: Backward wave modes. [□]: Veering regions. [■]: Studied region. [○]: Studied modes for the numerical simulations.	125
V.6	Modal shape of three studied modes. (a) First mode: 2ND-FW 1. (b) Second mode: 6ND-FW 1. (c) Third mode: 15ND-BW 1	126
V.7	Comparison of the median amplitude magnification factor with the mistuning level. (a) Low modal density region with a 2EO-FW excitation at 0 rpm. (b) Low modal density region with a 2EO-FW excitation at 10,000 rpm. (c) High modal density region with a 15EO-BW excitation at 10,000 rpm. (d) Veering region with a 6EO-FW excitation at 10,000 rpm. [---]: Blade mistuning. [—]: Sector mistuning. [---]: Disc mistuning.	127
V.8	Comparison of the amplitude magnification factor with the mistuning level. (a) Low modal density region with a 2EO-FW excitation at 0 rpm. (b) High modal density region with a 15EO-BW excitation at 10,000 rpm. (c) Veering region with a 6EO-FW excitation at 10,000 rpm. [---]: Variable blade mistuning alone. [---]: Variable disc mistuning alone. [—▲—]: Fixed blade mistuning with variable disc mistuning. [—◆—]: Fixed disc mistuning with variable blade mistuning.	129
V.9	Variations in the amplitude magnification factor with the mistuning level at 10,000 rpm. (a) Low modal density region with a 2EO-FW excitation. (b) High modal density region with a 15EO-BW excitation. (c) Veering region with a 6EO-FW excitation. [—]: With the Coriolis effect. [---]: Without the Coriolis effect.	130
V.10	Variations in the amplitude magnification factor with mistuning in the low modal density region with a 2EO-FW excitation for different rotational speeds. [—]: 0 rpm. [—]: 100 rpm. [—]: 1,000 rpm.	132
V.11	Variation in the amplitude magnification with the mistuning level and the rotational speed in the low modal density region with a 2EO-FW excitation.	132
V.12	Evolution of the DFT components with speed in the low modal density region with a 2EO-FW excitation and different mistuning levels. (a) 1 % of mistuning level. (b) 5 % of mistuning level. (c) 10 % of mistuning level. [—]: Forward wave. [---]: Backward wave.	133
V.13	Variation in the amplitude magnification with the mistuning level and the rotational speed in the high modal density region with a 15EO-BW excitation.	134

V.14	Evolution of the DFT components with speed in the high modal density region with a 15EO-BW excitation and different mistuning levels. (a) 1 % of mistuning level. (b) 5 % of mistuning level. (c) 10 % of mistuning level. [—]: Forward wave. [--]: Backward wave.	134
V.15	Variation in the amplitude magnification with the mistuning level and the rotational speed in the veering region with a 6EO-FW excitation.	135
V.16	Evolution of the DFT components with speed in the veering region with a 6EO-FW excitation and different mistuning levels. (a) 1 % of mistuning level. (b) 5 % of mistuning level. (c) 10 % of mistuning level. [—]: Forward wave. [--]: Backward wave.	136
V.17	Variation in the amplitude magnification with the mistuning level and the rotational speed in the changing modal density region with a 6EO-FW excitation.	137
V.18	Variation in the amplitude magnification with the rotational speed for different mistuning level in the changing modal density region with a 6EO-FW excitation.	137
V.19	Evolution of the DFT components with speed in the changing modal density region with a 6EO-FW excitation and different mistuning levels. (a) 1 % of mistuning level. (b) 5 % of mistuning level. (c) 10 % of mistuning level. [—]: Forward wave. [--]: Backward wave.	138
A.1	Principle of the AFT method	176
A.2	Polynomial interpolation	177
A.3	Tangential prediction	178
A.4	Sequential continuation	179
A.5	Arc-length continuation	179
A.6	Pseudo arc-length continuation	180
A.7	Bifurcation of periodic solutions and the location the characteristic multipliers on the complex plan	183
D.1	Procedures for the implementation of proportional mistuning. (a) Sector proportional mistuning. (b) Blade proportional mistuning.	194

List of Tables

II.1	Numerical values of the bladed disc	48
II.2	Average change of amplitude at different rotational speeds for different mistuned linear modes	58
II.3	Accuracy evaluation of the eigenvalues for different rotational speeds using the ACA criterion.	59
II.4	Accuracy evaluation of the eigenvectors for different rotational speeds using the MAC criterion.	60
II.5	Comparison of the average change of amplitude between the perturbation method (ACA P. M.) and the benchmark (ACA B.) for the M4 and M21 modes.	60
III.1	Numerical values for the aerodynamic model.	76
IV.1	Material properties of the standard steel.	101
IV.2	Mistuning pattern introduced in the FEM using a normal distribution with zero mean and 2.5 % standard deviation.	104
IV.3	Relative error for different number of modal families in the reduction basis with the SNM.	106
IV.4	Relative error for different number of cantilevered modes with the CMM.	106
IV.5	Relative error for different number of free-interface modes with the IMM.	106
IV.6	Computational cost to perform the SNM, CMM and IMM reductions. The simulations were run on an Intel(R) Core(TM) i7-10700K CPU @ 3.80GHz.	107
IV.7	Computational cost to perform forced responses with the FEM and the ROMs from the SNM, CMM and IMM in the three different regions. The simulations were run on an Intel(R) Core(TM) i7-10700K CPU @ 3.80GHz except for the FEM (*) which required too much memory and was thus performed on a supercomputer with 40 cores and 400Go of RAM.	111
V.1	Material properties of the Ti-6Al-4V titanium alloy.	122
V.2	Relative error for different mesh size.	124
V.3	Mistuning level values at the local maximum of amplitude magnification for the blade and disc mistuning.	128
V.4	Frequency regions for the different cases with and without the Coriolis effect.	130
V.5	Average change of amplitude at different rotational speeds in the low modal density region with a 2EO-FW excitation and different mistuning levels.	132
V.6	Average change of amplitude at different rotational speeds in the high modal density region with a 15EO-BW excitation and different mistuning levels.	134
V.7	Average change of amplitude at different rotational speeds in the veering region with a 6EO-FW excitation and different mistuning levels.	136
V.8	Average change of amplitude at different rotational speeds in the changing modal density region with a 6EO-FW excitation and different mistuning levels.	137

Bibliography

- [1] P. Almeida, C. Gibert, X. Leblanc, J.-P. Ousty, and F. Thouverez. “Experimental and numerical investigations on a rotating centrifugal compressor”. *ASME Turbo Expo 2012: Turbine Technical Conference and Exposition*. American Society of Mechanical Engineers. 2012, pp. 1133–1142. DOI: [10.1115/GT2012-69760](https://doi.org/10.1115/GT2012-69760) (cit. on pp. 35, 85, 144).
- [2] G. L. Anderson. “On the extensional and flexural vibrations of rotating bars”. *International Journal of Non-Linear Mechanics* 10.5 (1975), pp. 223–236. DOI: [10.1016/0020-7462\(75\)90014-1](https://doi.org/10.1016/0020-7462(75)90014-1) (cit. on p. 20).
- [3] J. Armand. “Nonlinear dynamics of jointed structures: a multiscale approach to predict fretting wear and its effects on the dynamic response”. PhD thesis. Imperial College London, 2017. DOI: [10.25560/59072](https://doi.org/10.25560/59072) (cit. on pp. 20, 174).
- [4] E. K. Armstrong. “An investigation into the coupling between turbine disk and blade vibrations”. PhD thesis. University of Cambridge, 1956 (cit. on p. 2).
- [5] K. E. Atkinson. *An introduction to numerical analysis*. 2008 (cit. on p. 174).
- [6] E. Balmes et al. “Orthogonal Maximum Sequence Sensor Placements Algorithms for modal tests, expansion and visibility”. *IMAC, January* 145 (2005), p. 146 (cit. on p. 116).
- [7] A. Batailly, M. Legrand, P. Cartraud, and C. Pierre. “Assessment of reduced models for the detection of modal interaction through rotor stator contacts”. *Journal of Sound and Vibration* 329.26 (2010), pp. 5546–5562. ISSN: 0022-460X. DOI: [10.1016/j.jsv.2010.07.018](https://doi.org/10.1016/j.jsv.2010.07.018) (cit. on p. 14).
- [8] A. Batailly, M. Legrand, A. Millecamps, and F. Garcin. “Numerical-Experimental Comparison in the Simulation of Rotor/Stator Interaction Through Blade-Tip/Abradable Coating Contact”. *Journal of Engineering for Gas Turbines and Power* 134.8 (June 2012). 082504. ISSN: 0742-4795. DOI: [10.1115/1.4006446](https://doi.org/10.1115/1.4006446) (cit. on pp. 14, 113).
- [9] A. Bedford. *Hamilton’s principle in continuum mechanics*. Vol. 139. 1985 (cit. on p. 16).
- [10] B. Beirow, A. Kühhorn, R. Weber, and F. Popig. “Vibration Analyses of an Axial Turbine Wheel With Intentional Mistuning”. *Journal of Engineering for Gas Turbines and Power* 143.6 (Mar. 2021). 061027. ISSN: 0742-4795. DOI: [10.1115/1.4049449](https://doi.org/10.1115/1.4049449) (cit. on p. 79).
- [11] T. Belytschko, W. K. Liu, B. Moran, and K. Elkhodary. *Nonlinear finite elements for continua and structures*. 2013. ISBN: 978-1-118-70008-2. DOI: [978-1-118-70008-2](https://doi.org/978-1-118-70008-2) (cit. on p. 17).
- [12] Y. Ben-Haim. *Info-gap decision theory: decisions under severe uncertainty*. 2006 (cit. on p. 37).
- [13] O. O. Bendiksen. “Flutter of Mistuned Turbomachinery Rotors”. *Journal of Engineering for Gas Turbines and Power* 106.1 (Jan. 1984), pp. 25–33. ISSN: 0742-4795. DOI: [10.1115/1.3239546](https://doi.org/10.1115/1.3239546) (cit. on pp. 3, 34).

- [14] T. Berthelon, A. Dugeai, J. Langridge, and F. Thouverez. “Analysis of Vortex Ingestion Impact on the Dynamic Response of the Fan in Resonance Condition”. Volume 7A: Structures and Dynamics. Turbo Expo: Power for Land, Sea, and Air. V07AT36A010. June 2019. DOI: [10.1115/GT2019-90939](https://doi.org/10.1115/GT2019-90939) (cit. on p. 74).
- [15] S. Besset and L. Jézéquel. “Dynamic Substructuring Based on a Double Modal Analysis”. *Journal of Vibration and Acoustics* 130.1 (Nov. 2007). 011008. ISSN: 1048-9002. DOI: [10.1115/1.2346698](https://doi.org/10.1115/1.2346698) (cit. on p. 96).
- [16] S. Biagiotti, L. Pinelli, F. Poli, F. Vanti, and R. Pacciani. “Numerical Study of Flutter Stabilization in Low Pressure Turbine Rotor with Intentional Mistuning”. *Energy Procedia* 148 (2018). ATI 2018 - 73rd Conference of the Italian Thermal Machines Engineering Association, pp. 98–105. ISSN: 1876-6102. DOI: [10.1016/j.egypro.2018.08.035](https://doi.org/10.1016/j.egypro.2018.08.035) (cit. on pp. 34, 78).
- [17] R. Bladh, M. P. Castanier, and C. Pierre. “Reduced Order Modeling and Vibration Analysis of Mistuned Bladed Disk Assemblies With Shrouds”. *Journal of Engineering for Gas Turbines and Power* 121.3 (July 1999), pp. 515–522. ISSN: 0742-4795. DOI: [10.1115/1.2818503](https://doi.org/10.1115/1.2818503) (cit. on p. 98).
- [18] R. Bladh, M. P. Castanier, and C. Pierre. “Component-Mode-Based Reduced Order Modeling Techniques for Mistuned Bladed Disks—Part I: Theoretical models”. *Journal of Engineering for Gas Turbines and Power* 123.1 (2001), pp. 89–99. DOI: [10.1115/1.1338947](https://doi.org/10.1115/1.1338947) (cit. on pp. 2, 52, 96 sq., 127).
- [19] R. Bladh, M. P. Castanier, and C. Pierre. “Component-Mode-Based Reduced Order Modeling Techniques for Mistuned Bladed Disks—Part II: Application ”. *Journal of Engineering for Gas Turbines and Power* 123.1 (Apr. 2001), pp. 100–108. ISSN: 0742-4795. DOI: [10.1115/1.1338948](https://doi.org/10.1115/1.1338948) (cit. on pp. 2, 96, 127).
- [20] R. Bladh, C. Pierre, M. P. Castanier, and M. J. Kruse. “Dynamic response predictions for a mistuned industrial turbomachinery rotor using reduced-order modeling”. *J. Eng. Gas Turbines Power* 124.2 (2002), pp. 311–324. DOI: [10.1115/1.1447236](https://doi.org/10.1115/1.1447236) (cit. on pp. 35, 102).
- [21] K. B. Blair, C. M. Krousgrill, and T. N. Farris. “Harmonic balance and continuation techniques in the dynamic analysis of Duffing’s equation”. *Journal of Sound and Vibration* 202.5 (1997), pp. 717–731. DOI: [10.1006/jsvi.1996.0863](https://doi.org/10.1006/jsvi.1996.0863) (cit. on p. 177).
- [22] N. N. Bogoliubov and Y. A. Mitropolski. “Asymptotic Methods in the Theory of Non-Linear Oscillations”. *Asymptotic Methods in the Theory of Non-Linear Oscillations, by NN Bogoliubov and YA Mitropolski. New York: Gordon and Breach, 1961.* (1961). DOI: [10.1063/1.3050754](https://doi.org/10.1063/1.3050754) (cit. on p. 174).
- [23] N. Bouhaddi and R. Fillod. “A method for selecting master DOF in dynamic substructuring using the Guyan condensation method”. *Computers & Structures* 45.5 (1992), pp. 941–946. ISSN: 0045-7949. DOI: [10.1016/0045-7949\(92\)90052-2](https://doi.org/10.1016/0045-7949(92)90052-2) (cit. on p. 95).
- [24] R. R. Boyer and R. D. Briggs. “The use of β titanium alloys in the aerospace industry”. *Journal of Materials Engineering and Performance* 14.6 (2005), pp. 681–685 (cit. on p. 122).
- [25] I. Bucher and D. J. Ewins. “Modal analysis and testing of rotating structures”. *Philosophical Transactions of the Royal Society of London. Series A: Mathematical, Physical and Engineering Sciences* 359.1778 (2001), pp. 61–96. DOI: [10.1098/rsta.2000.0714](https://doi.org/10.1098/rsta.2000.0714) (cit. on pp. 32, 104).

- [26] J. Butcher. “Runge-kutta methods”. *Scholarpedia* 2.9 (2007), p. 3147. DOI: [10.4249/scholarpedia.3147](https://doi.org/10.4249/scholarpedia.3147) (cit. on p. 172).
- [27] T. M. Cameron and J. H. Griffin. “An Alternating Frequency/Time Domain Method for Calculating the Steady-State Response of Nonlinear Dynamic Systems”. *Journal of Applied Mechanics* 56.1 (Mar. 1989), pp. 149–154. ISSN: 0021-8936. DOI: [10.1115/1.3176036](https://doi.org/10.1115/1.3176036) (cit. on p. 175).
- [28] M. S. Campobasso and M. Giles. “Flutter and forced response of mistuned turbomachinery” (2000) (cit. on p. 144).
- [29] E. Capiez-Lernout and C. Soize. “Nonparametric Modeling of Random Uncertainties for Dynamic Response of Mistuned Bladed Disks”. *Journal of Engineering for Gas Turbines and Power* 126.3 (Aug. 2004), pp. 610–618. ISSN: 0742-4795. DOI: [10.1115/1.1760527](https://doi.org/10.1115/1.1760527) (cit. on p. 2).
- [30] E. Capiez-Lernout, C. Soize, and M. Mbaye. “Mistuning analysis and uncertainty quantification of an industrial bladed disk with geometrical nonlinearity”. *Journal of Sound and Vibration* 356 (2015), pp. 124–143. ISSN: 0022-460X. DOI: <https://doi.org/10.1016/j.jsv.2015.07.006> (cit. on p. 2).
- [31] M. Castanier and C. Pierre. “Investigation of the combined effects of intentional and random mistuning on the forced response of bladed disks”. *34th AIAA/ASME/SAE/ASEE Joint Propulsion Conference and Exhibit*. 1998, p. 3720. DOI: [10.2514/6.1998-3720](https://doi.org/10.2514/6.1998-3720) (cit. on pp. 39, 102).
- [32] M. P. Castanier and C. Pierre. “Using intentional mistuning in the design of turbomachinery rotors”. *AIAA journal* 40.10 (2002), pp. 2077–2086. DOI: [10.2514/2.1542](https://doi.org/10.2514/2.1542) (cit. on pp. 2, 34).
- [33] M. P. Castanier and C. Pierre. “Modeling and Analysis of Mistuned Bladed Disk Vibration: Current Status and Emerging Directions”. *Journal of Propulsion and Power* 22.2 (2006), pp. 384–396. DOI: [10.2514/1.16345](https://doi.org/10.2514/1.16345) (cit. on pp. 2, 34, 38).
- [34] D. Chen, J. Zhang, J. Xiao, and Y. Chen. “Rubbing Of a Bladed Disk Considering Coriolis Effect: A Reduced Model Based on Complex Modal Analysis”. Volume 9B: Structures and Dynamics — Fatigue, Fracture, and Life Prediction; Probabilistic Methods; Rotordynamics; Structural Mechanics and Vibration. Turbo Expo: Power for Land, Sea, and Air. V09BT29A014. June 2021. DOI: [10.1115/GT2021-59008](https://doi.org/10.1115/GT2021-59008) (cit. on p. 93).
- [35] S. H. Chen, X. W. Yang, and H. D. Lian. “Comparison of several eigenvalue reanalysis methods for modified structures”. *Structural and Multidisciplinary optimization* 20.4 (2000), pp. 253–259. DOI: [10.1007/s001580050171](https://doi.org/10.1007/s001580050171) (cit. on p. 44).
- [36] Y. K. Cheung, S. H. Chen, and S. L. Lau. “Application of the incremental harmonic balance method to cubic non-linearity systems”. *Journal of Sound and Vibration* 140.2 (1990), pp. 273–286. DOI: [10.1016/0022-460x\(90\)90528-8](https://doi.org/10.1016/0022-460x(90)90528-8) (cit. on p. 177).
- [37] B.-K. Choi, J. Lentz, A. J. Rivas-Guerra, and M. P. Mignolet. “Optimization of Intentional Mistuning Patterns for the Reduction of the Forced Response Effects of Unintentional Mistuning: Formulation and Assessment”. *Journal of Engineering for Gas Turbines and Power* 125.1 (Dec. 2002), pp. 131–140. ISSN: 0742-4795. DOI: [10.1115/1.1498270](https://doi.org/10.1115/1.1498270) (cit. on pp. 2, 34, 79, 81).
- [38] Y. Colaïtis. “Stratégie numérique pour l’analyse qualitative des interactions aube/carter”. Theses. École Polytechnique de Montréal, July 2021 (cit. on p. 20).

- [39] A. R. Collar. “The Expanding Domain of Aeroelasticity”. *The Journal of the Royal Aeronautical Society* 50.428 (1946), 613–636. DOI: [10.1017/S0368393100120358](https://doi.org/10.1017/S0368393100120358) (cit. on p. 14).
- [40] R. Corral, J. Beloki, P. Calza, and R. Elliott. “Flutter Generation and Control Using Mistuning in a Turbine Rotating Rig”. *AIAA Journal* 57.2 (2019), pp. 782–795. DOI: [10.2514/1.J056943](https://doi.org/10.2514/1.J056943) (cit. on pp. 3, 34).
- [41] R. Corral, O. Khemiri, and C. Martel. “Design of mistuning patterns to control the vibration amplitude of unstable rotor blades”. *Aerospace Science and Technology* 80 (2018), pp. 20–28. ISSN: 1270-9638. DOI: [10.1016/j.ast.2018.06.034](https://doi.org/10.1016/j.ast.2018.06.034) (cit. on p. 3).
- [42] R. R. Craig and C.-J. Chang. “Free-interface methods of substructure coupling for dynamic analysis”. *AIAA Journal* 14.11 (1976), pp. 1633–1635. DOI: [10.2514/3.7264](https://doi.org/10.2514/3.7264) (cit. on pp. 2, 91 sqq.).
- [43] R. R. Craig Jr. and M. C. C. Bampton. “Coupling of substructures for dynamic analyses.” *AIAA journal* 6.7 (1968), pp. 1313–1319. DOI: [10.2514/3.4741](https://doi.org/10.2514/3.4741) (cit. on pp. 2, 91 sq., 98).
- [44] R. R. Craig Jr and C.-J. Chang. *Substructure coupling for dynamic analysis and testing*. Tech. rep. NASA, 1977 (cit. on p. 95).
- [45] E. F. Crawley and K. C. Hall. “Optimization and mechanisms of mistuning in cascades”. *Journal of Engineering for Gas Turbines and Power* 107.2 (1985), pp. 418–426. DOI: [10.1115/1.3239742](https://doi.org/10.1115/1.3239742) (cit. on pp. 34, 78).
- [46] C. Darwin. *On the origin of species*. 1859 (cit. on p. 79).
- [47] C. De Boor. “On calculating with B-splines”. *Journal of Approximation theory* 6.1 (1972), pp. 50–62 (cit. on p. 114).
- [48] J. D. Denton and W. N. Dawes. “Computational fluid dynamics for turbomachinery design”. *Proceedings of the Institution of Mechanical Engineers, Part C: Journal of Mechanical Engineering Science* 213.2 (1998), pp. 107–124. DOI: [10.1243/0954406991522211](https://doi.org/10.1243/0954406991522211) (cit. on p. 144).
- [49] O. Dessombz, F. Thouverez, J.-P. Laine, and L. Jézéquel. “Analysis Of Mechanical Systems Using Interval Computations Applied To Finite Element Methods”. *Journal of Sound and Vibration* 239.5 (2001), pp. 949–968. ISSN: 0022-460X. DOI: <https://doi.org/10.1006/jsvi.2000.3191> (cit. on p. 36).
- [50] N. Di Palma. “Dynamique non-linéaire des aubages : comportement multi-hamornique avec couplage torsion-flexion”. PhD thesis. École Centrale de Lyon, 2022 (cit. on pp. 21, 143, 174).
- [51] R. C. F. Dye and T. A. Henry. “Vibration Amplitudes of Compressor Blades Resulting From Scatter in Blade Natural Frequencies”. *Journal of Engineering for Power* 91.3 (July 1969), pp. 182–187. ISSN: 0022-0825. DOI: [10.1115/1.3574726](https://doi.org/10.1115/1.3574726) (cit. on p. 2).
- [52] L. E. El-Bayoumy and A. V. Srinivasan. “Influence of mistuning on rotor-blade vibrations”. *AIAA Journal* 13.4 (1975), pp. 460–464. DOI: [10.2514/3.49731](https://doi.org/10.2514/3.49731) (cit. on p. 33).
- [53] J. Escaffre, Y. Lefaux, and A. Lenain. “The orbital friction welding process for engines components in aeronautic”. *MATEC Web of Conferences*. 321. EDP Sciences. 2020, p. 04024 (cit. on pp. 12, 122).
- [54] D. J. Ewins. “The effects of detuning upon the forced vibrations of bladed disks”. *Journal of Sound and Vibration* 9.1 (1969), pp. 65–79. ISSN: 0022-460X. DOI: [10.1016/0022-460X\(69\)90264-8](https://doi.org/10.1016/0022-460X(69)90264-8) (cit. on p. 2).

- [55] D. J. Ewins. “Vibration Characteristics of Bladed Disc Assemblies”. *Journal of Mechanical Engineering Science* 15.3 (1973), pp. 165–186 (cit. on p. 2).
- [56] D. J. Ewins. “Vibration Modes of Mistuned Bladed Disks”. *Journal of Engineering for Power* 98.3 (July 1976), pp. 349–355. ISSN: 0022-0825. DOI: [10.1115/1.3446180](https://doi.org/10.1115/1.3446180) (cit. on p. 2).
- [57] D. M. Feiner and J. H. Griffin. “A fundamental model of mistuning for a single family of modes”. *J. Turbomach.* 124.4 (2002), pp. 597–605. DOI: [10.1115/1.1508384](https://doi.org/10.1115/1.1508384) (cit. on pp. 2, 96).
- [58] F. Figaschewsky, A. Kühhorn, B. Beirow, J. Nipkau, T. Giersch, and B. Power. “Design and Analysis of an Intentional Mistuning Experiment Reducing Flutter Susceptibility and Minimizing Forced Response of a Jet Engine Fan”. Volume 7B: Structures and Dynamics. Turbo Expo: Power for Land, Sea, and Air. V07BT36A020. June 2017. DOI: [10.1115/GT2017-64621](https://doi.org/10.1115/GT2017-64621) (cit. on p. 79).
- [59] C. Fitzner, B. I. Epureanu, and S. Filippi. “Nodal energy weighted transformation: A mistuning projection and its application to FLADE™ turbines”. *Mechanical Systems and Signal Processing* 42.1-2 (2014), pp. 167–180. DOI: [10.1016/j.ymsp.2013.08.027](https://doi.org/10.1016/j.ymsp.2013.08.027) (cit. on pp. 2, 96).
- [60] S. Fleeter and D. Hoyniak. “Aeroelastic Detuning for Stability Enhancement of Unstalled Supersonic Flutter”. *International Journal of Turbo and Jet Engines* 6.1 (1989), pp. 17–26. DOI: [doi:10.1515/TJJ.1989.6.1.17](https://doi.org/10.1515/TJJ.1989.6.1.17) (cit. on p. 78).
- [61] R. A. Frazer. “The flutter of aeroplane wings”. *The Aeronautical Journal* 33.222 (1929), pp. 407–454 (cit. on p. 3).
- [62] I. E. Garrick and W. H. Reed. “Historical Development of Aircraft Flutter”. *Journal of Aircraft* 18.11 (1981), pp. 897–912. DOI: [10.2514/3.57579](https://doi.org/10.2514/3.57579) (cit. on p. 3).
- [63] M. Géradin and D. J. Rixen. *Mechanical vibrations: theory and application to structural dynamics*. 2014. ISBN: 978-1-118-90019-2. DOI: [978-1-118-90019-2](https://doi.org/978-1-118-90019-2) (cit. on pp. 15 sq., 92).
- [64] C. Gibert, V. Kharyton, F. Thouverez, and P. Jean. “On forced response of a rotating integrally bladed disk: Predictions and experiments”. *ASME turbo expo 2010: Power for land, sea, and air*. ASME. 2010. DOI: [10.1115/GT2010-23610](https://doi.org/10.1115/GT2010-23610) (cit. on pp. 2, 32, 144).
- [65] T. Gmür. *Dynamique des structures: analyse modale numérique*. 1997. DOI: [9782880748135](https://doi.org/9782880748135) (cit. on pp. 15, 23, 173).
- [66] G. H. Golub and C. F. Van Loan. *Matrix computations*. 2013 (cit. on p. 116).
- [67] A. Grolet. “Dynamique non-linéaire des structures mécaniques: application aux systèmes à symétrie cyclique”. PhD thesis. École Centrale de Lyon, 2013 (cit. on pp. 21, 174, 178, 180).
- [68] M. Gruin. “Dynamique non-linéaire d’une roue de turbine Basse Pression soumise à des excitations structurales d’un turboréacteur”. PhD thesis. École Centrale de Lyon, 2012 (cit. on p. 176).
- [69] M. Guskov. “Dynamique non-linéaire des systèmes multirotors. Etudes numérique et expérimentale”. PhD thesis. École Centrale de Lyon, 2007 (cit. on p. 183).
- [70] R. J. Guyan. “Reduction of stiffness and mass matrices”. *AIAA Journal* 3.2 (1965), pp. 380–380. DOI: [10.2514/3.2874](https://doi.org/10.2514/3.2874) (cit. on p. 95).

- [71] Y. Han, R. Murthy, M. P. Mignolet, and J. Lentz. “Optimization of Intentional Mistuning Patterns for the Mitigation of the Effects of Random Mistuning”. *Journal of Engineering for Gas Turbines and Power* 136.6 (Feb. 2014). 062505. ISSN: 0742-4795. DOI: [10.1115/1.4026141](https://doi.org/10.1115/1.4026141) (cit. on pp. 2, 34, 78).
- [72] P. Hartman. “A lemma in the theory of structural stability of differential equations”. *Proceedings of the American Mathematical Society* 11.4 (1960), pp. 610–620. DOI: [10.1090/s0002-9939-1960-0121542-7](https://doi.org/10.1090/s0002-9939-1960-0121542-7) (cit. on p. 181).
- [73] T. Heinze, L. Panning-von Scheidt, J. Wallaschek, and A. Hartung. “A Taylor Series Expansion Approach for Nonlinear Blade Forced Response Prediction Considering Variable Rotational Speed”. *Journal of Engineering for Gas Turbines and Power* 139.6 (Jan. 2017). 062503. ISSN: 0742-4795. DOI: [10.1115/1.4035286](https://doi.org/10.1115/1.4035286) (cit. on p. 113).
- [74] D. Hemberger, D. Filsinger, and H.-J. Bauer. “Investigations on maximum amplitude amplification factor of real mistuned bladed structures”. *Turbo Expo: Power for Land, Sea, and Air*. 44731. American Society of Mechanical Engineers. 2012, pp. 1041–1052. DOI: [10.1115/gt2012-68084](https://doi.org/10.1115/gt2012-68084) (cit. on p. 36).
- [75] G. W. Hill. “On the part of the motion of the lunar perigee which is a function of the mean motions of the sun and moon”. *Acta mathematica* 8.1 (1886), pp. 1–36. DOI: [10.1007/bf02417081](https://doi.org/10.1007/bf02417081) (cit. on p. 183).
- [76] S.-K. Hong, B. I. Epureanu, M. P. Castanier, and D. J. Gorsich. “Parametric reduced-order models for predicting the vibration response of complex structures with component damage and uncertainties”. *Journal of sound and vibration* 330.6 (2011), pp. 1091–1110. DOI: [10.1016/j.jsv.2010.09.022](https://doi.org/10.1016/j.jsv.2010.09.022) (cit. on pp. 114, 116).
- [77] A. Hot, S. Cogan, E. Foltête, G. Kerschen, F. Buffe, J. Buffe, and S. Behar. “Design of Uncertain Prestressed Space Structures: An Info-Gap Approach”. *Topics in Model Validation and Uncertainty Quantification, Volume 4*. Ed. by T. Simmermacher, S. Cogan, L. Horta, and R. Barthorpe. New York, NY, 2012, pp. 13–20. ISBN: 978-1-4614-2431-4 (cit. on p. 37).
- [78] S. N. Hou. “Review of modal synthesis techniques and a new approach”. *Shock Vibration Bulletin* (1969) (cit. on pp. 92, 95).
- [79] D. Hoyniak and S. Fleeter. “The Effect of Circumferential Aerodynamic Detuning on Coupled Bending-Torsion Unstalled Supersonic Flutter”. *Journal of Turbomachinery* 108.2 (Oct. 1986), pp. 253–260. ISSN: 0889-504X. DOI: [10.1115/1.3262045](https://doi.org/10.1115/1.3262045) (cit. on pp. 34, 78).
- [80] B. W. Huang and J. H. Kuang. “Mode localization in a rotating mistuned turbo disk with Coriolis effect”. *International journal of mechanical sciences* 43.7 (2001), pp. 1643–1660. DOI: [10.1016/S0020-7403\(00\)00096-5](https://doi.org/10.1016/S0020-7403(00)00096-5) (cit. on pp. 3, 34).
- [81] W. C. Hurty. “Dynamic analysis of structural systems using component modes”. *AIAA Journal* 3.4 (1965), pp. 678–685. DOI: [10.2514/3.2947](https://doi.org/10.2514/3.2947) (cit. on p. 92).
- [82] M. I. Hussein, M. P. Castanier, and C. Pierre. *Examination of the relationship between tuned free vibration characteristics and mistuning sensitivity for an industrial turbomachinery rotor*. Tech. rep. The University of Michigan, 2001 (cit. on p. 102).
- [83] L. Jezequel. “A hybrid method of modal synthesis using vibration tests”. *Journal of Sound and Vibration* 100.2 (1985), pp. 191–210. ISSN: 0022-460X. DOI: [10.1016/0022-460X\(85\)90415-8](https://doi.org/10.1016/0022-460X(85)90415-8) (cit. on p. 96).

- [84] C. Joannin. “Réduction de modèle par sous-structuration et modes non-linéaires- Application à la dynamique des roues aubagées”. PhD thesis. École Centrale de Lyon, 2017 (cit. on pp. 12 sq., 20, 143, 174).
- [85] C. Joannin, B. Chouvion, F. Thouverez, J.-P. Ousty, and M. Mbaye. “A nonlinear component mode synthesis method for the computation of steady-state vibrations in non-conservative systems”. *Mechanical Systems and Signal Processing* 83 (2017), pp. 75–92. DOI: [10.1016/j.ymssp.2016.05.044](https://doi.org/10.1016/j.ymssp.2016.05.044) (cit. on p. 144).
- [86] X. Kan and Z. Xu. “Vibration localization for a rotating mistuning bladed disk with the Coriolis effect by a state-space decoupling method”. *Proceedings of the Institution of Mechanical Engineers, Part G: Journal of Aerospace Engineering* 233.3 (2017), pp. 1011–1020. DOI: [10.1177/0954410017744238](https://doi.org/10.1177/0954410017744238) (cit. on pp. 3, 35).
- [87] X. Kan, Z. Xu, B. Zhao, and J. Zhong. “Effect of Coriolis force on forced response magnification of intentionally mistuned bladed disk”. *Journal of Sound and Vibration* 399 (2017), pp. 124–136. ISSN: 0022-460X. DOI: [10.1016/j.jsv.2017.03.002](https://doi.org/10.1016/j.jsv.2017.03.002) (cit. on pp. 3, 35).
- [88] X. Kan and B. Zhao. “Vibration characteristics of a mistuned bladed disk considering the effect of Coriolis forces”. *Shock and Vibration* 2016 (2016). DOI: [10.1155/2016/4656032](https://doi.org/10.1155/2016/4656032) (cit. on pp. 3, 35).
- [89] H. Ç. Karataş, E. Cığeroğlu, and H. N. Özgüven. “Possibilistic Interpretation of Mistuning in Bladed Disks by Fuzzy Algebra”. *Topics in Model Validation and Uncertainty Quantification, Volume 4*. Ed. by T. Simmermacher, S. Cogan, L. Horta, and R. Barthorpe. New York, NY, 2012, pp. 109–116. ISBN: 978-1-4614-2431-4 (cit. on p. 37).
- [90] K. R. V. Kaza and R. E. Kielb. “Flutter and Response of a Mistuned Cascade in Incompressible Flow”. *AIAA Journal* 20.8 (1982), pp. 1120–1127. DOI: [10.2514/3.51172](https://doi.org/10.2514/3.51172) (cit. on pp. 3, 34).
- [91] K. R. V. Kaza and R. E. Kielb. “Vibration and flutter of mistuned bladed-disk assemblies”. *Journal of Propulsion and Power* 1.5 (1985), pp. 336–344 (cit. on p. 3).
- [92] H. B. Keller. “Lectures on numerical methods in bifurcation problems”. *Applied Mathematics* 217 (1987), p. 50 (cit. on p. 173).
- [93] J. A. Kenyon, J. H. Griffin, and N. E. Kim. “Sensitivity of Tuned Bladed Disk Response to Frequency Veering”. *Journal of Engineering for Gas Turbines and Power* 127.4 (Mar. 2004), pp. 835–842. ISSN: 0742-4795. DOI: [10.1115/1.1924486](https://doi.org/10.1115/1.1924486) (cit. on p. 36).
- [94] E. Khalifeh, E. Piollet, A. Millecamps, and A. Batailly. “Non-Linear Modeling of Centrifugal Stiffening Effects for Accurate Bladed Component Reduced-Order Models”. Volume 7B: Structures and Dynamics. Turbo Expo: Power for Land, Sea, and Air. V07BT35A009. June 2017. DOI: [10.1115/GT2017-63629](https://doi.org/10.1115/GT2017-63629) (cit. on p. 113).
- [95] O. Khemiri, C. Martel, and R. Corral. “Quantitative Validation of the Asymptotic Mistuning Model Using a High Fidelity Bladed Disk Model”. Volume 6: Structures and Dynamics, Parts A and B. Turbo Expo: Power for Land, Sea, and Air. June 2010, pp. 889–898. DOI: [10.1115/GT2010-22498](https://doi.org/10.1115/GT2010-22498) (cit. on p. 95).
- [96] R. E. Kielb, D. M. Feiner, J. H. Griffin, and T. Miyakozawa. “Flutter of Mistuned Bladed Disks and Blisks With Aerodynamic and FMM Structural Coupling”. Volume 6: Turbo Expo 2004. Turbo Expo: Power for Land, Sea, and Air. June 2004, pp. 573–579. DOI: [10.1115/GT2004-54315](https://doi.org/10.1115/GT2004-54315) (cit. on pp. 34, 78).

- [97] R. E. Kielb, K. C. Hall, E. Hong, and S. S. Pai. “Probabilistic Flutter Analysis of a Mistuned Bladed Disks”. Volume 5: Marine; Microturbines and Small Turbomachinery; Oil and Gas Applications; Structures and Dynamics, Parts A and B. Turbo Expo: Power for Land, Sea, and Air. May 2006, pp. 1145–1150. DOI: [10.1115/GT2006-90847](https://doi.org/10.1115/GT2006-90847) (cit. on p. 144).
- [98] G. J. Klir. “Generalized information theory”. *Fuzzy Sets and Systems* 40.1 (1991), pp. 127–142. ISSN: 0165-0114. DOI: [https://doi.org/10.1016/0165-0114\(91\)90049-V](https://doi.org/10.1016/0165-0114(91)90049-V) (cit. on p. 36).
- [99] A. de Kraker. “Generalization of the Craig-Bampton CMS procedure for general damping”. *DCT rapporten* 1993 (1993) (cit. on p. 93).
- [100] B. de Kraker and D. H. van Campen. “Modification of the Craig-Bampton CMS Procedure for General Systems”. Volume 1C: 16th Biennial Conference on Mechanical Vibration and Noise. International Design Engineering Technical Conferences and Computers and Information in Engineering Conference. V01CT12A012. Sept. 1997. DOI: [10.1115/DETC97/VIB-4030](https://doi.org/10.1115/DETC97/VIB-4030) (cit. on p. 93).
- [101] N. M. Krylov and N. N. Bogoliubov. *Introduction to non-linear mechanics*. 11. 1949. DOI: [10.1515/9781400882274](https://doi.org/10.1515/9781400882274) (cit. on p. 174).
- [102] E. Kurstak, R. Wilber, and K. D’Souza. “Parametric reduced order models for bladed disks with mistuning and varying operational speed”. *Journal of Engineering for Gas Turbines and Power* 141.5 (2019). DOI: [10.1115/1.4041204](https://doi.org/10.1115/1.4041204) (cit. on pp. 99, 116).
- [103] W. Kutta. “Beitrag zur naherungsweise integration totaler differentialgleichungen”. *Z. Math. Phys.* 46 (1901), pp. 435–453 (cit. on p. 172).
- [104] F. Lane. “System Mode Shapes in the Flutter of Compressor Blade Rows”. *Journal of the Aeronautical Sciences* 23.1 (1956), pp. 54–66. DOI: [10.2514/8.3502](https://doi.org/10.2514/8.3502) (cit. on pp. 3, 15).
- [105] F. Lane and M. Friedman. *Theoretical investigation of subsonic oscillatory blade-row aerodynamics*. Tech. rep. 1958 (cit. on p. 3).
- [106] F. Lane and C.-t. Wang. *A Theoretical Investigation of the Flutter Characteristics of Compressor and Turbine Blade Systems*. Tech. rep. NEW YORK UNIV BRONX SCHOOL OF ENGINEERING and SCIENCE, 1954 (cit. on p. 3).
- [107] D. Laxalde, F. Thouverez, J.-J. Sinou, and J.-P. Lombard. “Qualitative analysis of forced response of blisks with friction ring dampers”. *European Journal of Mechanics - A/Solids* 26.4 (2007), pp. 676–687. ISSN: 0997-7538. DOI: [10.1016/j.euromechsol.2006.10.002](https://doi.org/10.1016/j.euromechsol.2006.10.002) (cit. on pp. 12, 143).
- [108] D. Laxalde. “Étude d’amortisseurs non-linéaires appliqués aux roues aubagées et aux systèmes multi-étages”. PhD thesis. École Centrale de Lyon, 2007 (cit. on pp. 20, 144, 174).
- [109] A. Lazarus and O. Thomas. “A harmonic-based method for computing the stability of periodic solutions of dynamical systems”. *Comptes Rendus Mécanique* 338.9 (2010), pp. 510–517. DOI: [10.1016/j.crme.2010.07.020](https://doi.org/10.1016/j.crme.2010.07.020) (cit. on p. 183).
- [110] M. Legrand, A. Batailly, and C. Pierre. “Numerical Investigation of Abradable Coating Removal in Aircraft Engines Through Plastic Constitutive Law”. *Journal of Computational and Nonlinear Dynamics* 7.1 (Sept. 2011). 011010. ISSN: 1555-1415. DOI: [10.1115/1.4004951](https://doi.org/10.1115/1.4004951) (cit. on pp. 14, 113).

- [111] M. Legrand, A. Batailly, B. Magnain, P. Cartraud, and C. Pierre. “Full three-dimensional investigation of structural contact interactions in turbomachines”. *Journal of Sound and Vibration* 331.11 (2012), pp. 2578–2601. ISSN: 0022-460X. DOI: [10.1016/j.jsv.2012.01.017](https://doi.org/10.1016/j.jsv.2012.01.017) (cit. on pp. 113, 116).
- [112] M. Legrand, C. Pierre, P. Cartraud, and J.-P. Lombard. “Two-dimensional modeling of an aircraft engine structural bladed disk-casing modal interaction”. *Journal of Sound and Vibration* 319.1 (2009), pp. 366–391. ISSN: 0022-460X. DOI: [10.1016/j.jsv.2008.06.019](https://doi.org/10.1016/j.jsv.2008.06.019) (cit. on p. 14).
- [113] C. Lein and M. Beitelschmidt. “Comparative study of model correlation methods with application to model order reduction”. *Proceedings 26th ISMA (International Conference on Noise and Vibration Engineering)*. 2014, pp. 2683–2700 (cit. on p. 104).
- [114] E. Lemoine. “Approche couplée pour l’étude du contact sous chargement dynamique vibratoire: application à l’usure par fretting du contact aube-disque”. PhD thesis. École Centrale de Lyon, 2021 (cit. on pp. 12, 20, 174).
- [115] N. Lesaffre. “Stabilité et analyse non-linéaire du contact rotor-stator”. Theses. École Centrale de Lyon, Sept. 2007 (cit. on p. 20).
- [116] C. Li, Q. Tang, C. Xi, B. Zhong, and B. Wen. “Coupling vibration behaviors of drum-disk-shaft structures with elastic connection”. *International Journal of Mechanical Sciences* 155 (2019), pp. 392–404. DOI: [10.1016/j.ijmecsci.2019.03.014](https://doi.org/10.1016/j.ijmecsci.2019.03.014) (cit. on pp. 2, 122).
- [117] A. Liapounoff. “Problème général de la stabilité du mouvement”. *Annales de la Faculté des sciences de Toulouse: Mathématiques*. 9. 1907, pp. 203–474. DOI: [10.5802/afst.246](https://doi.org/10.5802/afst.246) (cit. on p. 181).
- [118] G. M. Lilley. “An investigation of the flexure-torsion flutter characteristics of aerofoils in cascade.” (1952) (cit. on p. 3).
- [119] S.-H. Lim, R. Bladh, M. P. Castanier, and C. Pierre. “Compact, generalized component mode mistuning representation for modeling bladed disk vibration”. *AIAA journal* 45.9 (2007), pp. 2285–2298. DOI: [10.2514/1.13172](https://doi.org/10.2514/1.13172) (cit. on pp. 2, 52, 91, 96 sq., 99, 127).
- [120] M. Maalekian. “Friction welding—critical assessment of literature”. *Science and technology of welding and joining* 12.8 (2007), pp. 738–759 (cit. on p. 12).
- [121] A. Mabilia. “Dynamique non-linéaire d’une soufflante en rotation”. PhD thesis. École Centrale de Lyon, 2020 (cit. on pp. 143 sq.).
- [122] R. H. MacNeal, R. L. Harder, and J. B. Mason. “NASTRAN cyclic symmetry capability”. *NASTRAN: Users’ Experiences* (1973) (cit. on p. 24).
- [123] R. H. MacNeal. “A hybrid method of component mode synthesis”. *Computers & Structures* 1.4 (1971). Special Issue on Structural Dynamics, pp. 581–601. ISSN: 0045-7949. DOI: [10.1016/0045-7949\(71\)90031-9](https://doi.org/10.1016/0045-7949(71)90031-9) (cit. on pp. 94 sq.).
- [124] A. Madden, B. I. Epureanu, and S. Filippi. “Reduced-order modeling approach for blisks with large mass, stiffness, and geometric mistuning”. *AIAA journal* 50.2 (2012), pp. 366–374. DOI: [10.2514/1.j051140](https://doi.org/10.2514/1.j051140) (cit. on p. 144).
- [125] J. G. Marshall and M. Imregun. “A Review Of Aeroelasticity Methods With Emphasis On Turbomachinery Applications”. *Journal of Fluids and Structures* 10.3 (1996), pp. 237–267. ISSN: 0889-9746. DOI: [10.1006/jfls.1996.0015](https://doi.org/10.1006/jfls.1996.0015) (cit. on pp. 15, 144).
- [126] C. Martel, R. Corral, and J. M. Llorens. “Stability Increase of Aerodynamically Unstable Rotors Using Intentional Mistuning”. *Journal of Turbomachinery* 130.1 (Dec. 2007). 011006. ISSN: 0889-504X. DOI: [10.1115/1.2720503](https://doi.org/10.1115/1.2720503) (cit. on pp. 2 sq., 96).

- [127] C. Martel and S. Rodríguez. “Mistuning Effects on the Nonlinear Friction Saturation of Flutter Vibration Amplitude”. Volume 10A: Structures and Dynamics. Turbo Expo: Power for Land, Sea, and Air. V10AT24A018. Sept. 2020. DOI: [10.1115/GT2020-15442](https://doi.org/10.1115/GT2020-15442) (cit. on p. 3).
- [128] A. Martin. “Réduction en dynamique non-linéaire géométrique: Application au cas des structures à symétrie cyclique”. PhD thesis. École Centrale de Lyon, 2019 (cit. on pp. 21, 174).
- [129] M. Mbaye, C. Soize, and J.-P. Ousty. “A reduced-order model of detuned cyclic dynamical systems with geometric modifications using a basis of cyclic modes”. *Journal of engineering for gas turbines and power* 132.11 (2010). DOI: [10.1115/1.4000805](https://doi.org/10.1115/1.4000805) (cit. on p. 144).
- [130] L. Meirovitch. “A new method of solution of the eigenvalue problem for gyroscopic systems”. *AiAA Journal* 12.10 (1974), pp. 1337–1342. DOI: [10.2514/3.49486](https://doi.org/10.2514/3.49486) (cit. on p. 22).
- [131] A. Mendelson. “Aerodynamic hysteresis as a factor in critical flutter speed of compressor blades at stalling conditions”. *Journal of the Aeronautical Sciences* 16.11 (1949), pp. 645–652 (cit. on p. 3).
- [132] M. Y. Mendoza, M. J. Quintana, and P. C. Collins. “Microstructure Characterization and Mechanical Properties in Individual Zones of Linear Friction Welded Ti-6Al-4V Alloy”. *Metallurgical and Materials Transactions A* 51.12 (2020), pp. 6294–6306 (cit. on p. 122).
- [133] N. Minorsky. *Introduction to non-linear mechanics. part II. Analytical methods of non-linear mechanics*. Tech. rep. DAVID TAYLOR MODEL BASIN WASHINGTON DC, 1945 (cit. on pp. 174 sq.).
- [134] T. Miura, N. Sakai, N. Kanazawa, and K. Nakayama. “Forced Response Excitation Due to the Stator Vanes of Two and Three Compressor Stages Away”. *Journal of Engineering for Gas Turbines and Power* 143.11 (Oct. 2021). 111018. ISSN: 0742-4795. DOI: [10.1115/1.4051918](https://doi.org/10.1115/1.4051918) (cit. on p. 14).
- [135] R. E. Moore. *Methods and applications of interval analysis*. 1979 (cit. on p. 36).
- [136] J. J. Moré, B. S. Garbow, and K. E. Hillstrom. *User guide for MINPACK-1*. Tech. rep. CM-P00068642, 1980. DOI: [10.2172/6997568](https://doi.org/10.2172/6997568) (cit. on p. 53).
- [137] A. H. Nayfeh and B. Balachandran. *Applied nonlinear dynamics: analytical, computational, and experimental methods*. 2008. DOI: [10.1002/9783527617548](https://doi.org/10.1002/9783527617548) (cit. on pp. 181 sqq.).
- [138] N. M. Newmark. “A method of computation for structural dynamics”. *Journal of the engineering mechanics division* 85.3 (1959), pp. 67–94. DOI: [10.1061/taceat.0008448](https://doi.org/10.1061/taceat.0008448) (cit. on p. 173).
- [139] M. Nikolic, E. P. Petrov, and D. J. Ewins. “Coriolis forces in forced response analysis of mistuned bladed disks”. *Journal of turbomachinery* 129.4 (2007), pp. 730–739. DOI: [10.1115/1.2720866](https://doi.org/10.1115/1.2720866) (cit. on pp. 2 sq., 32, 35).
- [140] M. Nikolic. “New insights into the blade mistuning problem”. PhD thesis. Imperial College London, 2006. DOI: [uk.bl.ethos.443784](https://doi.org/uk.bl.ethos.443784) (cit. on pp. 3, 34).
- [141] F. Nyssen and J.-C. Golinval. “Identification of mistuning and model updating of an academic blisk based on geometry and vibration measurements”. *Mechanical Systems and Signal Processing* 68-69 (2016), pp. 252–264. ISSN: 0888-3270. DOI: <https://doi.org/10.1016/j.ymssp.2015.08.006> (cit. on p. 99).

- [142] F. Nyssen. “Numerical Modeling and Experimental Identification of Mistuned Multi-Stage Bladed Assemblies”. PhD thesis. Université de Liège, 2016 (cit. on p. 144).
- [143] G. S. Ottarsson. “Dynamic modeling and vibration analysis of mistuned bladed disks”. PhD thesis. University of Michigan, 1994 (cit. on p. 95).
- [144] J. Paltrinieri, F. Nyssen, M.-O. Parent, and A. Batailly. “Towards Full 3D Numerical Simulation of Whirl Motions Stemming From Unilateral Contact Constraints in Aircraft Engines”. *Turbo Expo: Power for Land, Sea, and Air*. 50930. American Society of Mechanical Engineers. 2017, V07BT35A007. DOI: [10.1115/gt2017-63488](https://doi.org/10.1115/gt2017-63488) (cit. on p. 112).
- [145] K. Park. “Component-based vibration modeling methods for fast reanalysis and design of complex structures.” PhD thesis. 2008 (cit. on p. 114).
- [146] L. Peletan. “Stratégie de modélisation simplifiée et de résolution accélérée en dynamique non linéaire des machines tournantes : Application au contact rotor-stator”. Theses. INSA de Lyon, Dec. 2012 (cit. on p. 21).
- [147] L. Peletan, S. Baguet, M. Torkhani, and G. Jacquet-Richardet. “Quasi-periodic harmonic balance method for rubbing self-induced vibrations in rotor–stator dynamics”. *Nonlinear Dynamics* 78.4 (2014), pp. 2501–2515. DOI: [10.1007/s11071-014-1606-8](https://doi.org/10.1007/s11071-014-1606-8) (cit. on p. 178).
- [148] E. Pesheck. “Reduced order modeling of nonlinear structural systems using nonlinear normal modes and invariant manifolds”. PhD thesis. University of Michigan, 2000 (cit. on p. 185).
- [149] E. Pesheck, C. Pierre, and S. Shaw. “A new Galerkin-based approach for accurate non-linear normal modes through invariant manifolds”. *Journal of Sound and Vibration* (2002). DOI: [10.1006/jsvi.2001.3914](https://doi.org/10.1006/jsvi.2001.3914) (cit. on p. 185).
- [150] E. P. Petrov, K. Y. Sanliturk, and D. J. Ewins. “A new method for dynamic analysis of mistuned bladed disks based on the exact relationship between tuned and mistuned systems”. *J. Eng. Gas Turbines Power* 124.3 (2002), pp. 586–597. DOI: [10.1115/1.1451753](https://doi.org/10.1115/1.1451753) (cit. on pp. 2, 52, 96).
- [151] H. M. Phan and L. He. “Investigation of Mistuned Oscillating Cascade Using Fully-Coupled Method”. Volume 9A: Structures and Dynamics — Aerodynamics Excitation and Damping; Bearing and Seal Dynamics; Emerging Methods in Design and Engineering. *Turbo Expo: Power for Land, Sea, and Air*. V09AT23A009. June 2021. DOI: [10.1115/GT2021-59124](https://doi.org/10.1115/GT2021-59124) (cit. on pp. 34, 78).
- [152] C. Pierre. “Mode localization and eigenvalue loci veering phenomena in disordered structures”. *Journal of Sound and Vibration* 126.3 (1988), pp. 485–502. DOI: [10.1016/0022-460x\(88\)90226-x](https://doi.org/10.1016/0022-460x(88)90226-x) (cit. on pp. 39, 102, 111).
- [153] R. N. Pinto, A. Afzal, L. V. D’Souza, Z. Ansari, and A. Mohammed Samee. “Computational fluid dynamics in turbomachinery: a review of state of the art”. *Archives of Computational Methods in Engineering* 24.3 (2017), pp. 467–479 (cit. on p. 144).
- [154] M. J. D. Powell. *A FORTRAN subroutine for solving systems of nonlinear algebraic equations*. Tech. rep. Atomic Energy Research Establishment, Harwell (England), 1968. DOI: [NSA-23-028645](https://doi.org/10.1016/0022-460x(68)90226-x) (cit. on p. 53).
- [155] Z. Qin, Z. Yang, J. Zu, and F. Chu. “Free vibration analysis of rotating cylindrical shells coupled with moderately thick annular plates”. *International Journal of Mechanical Sciences* 142 (2018), pp. 127–139. DOI: [10.1016/j.ijmecsci.2018.04.044](https://doi.org/10.1016/j.ijmecsci.2018.04.044) (cit. on pp. 2, 122).
- [156] S. Quaegebeur. “Prévision de la réponse forcée de roues aubagées désaccordées en présence de non-linéarités de frottement”. PhD thesis. École Centrale de Lyon, 2021 (cit. on pp. 12, 20, 28, 174).

- [157] S. Quaegebeur, B. Chouvion, and F. Thouverez. “Impact of Mistuned Underplatform Dampers on the Nonlinear Vibration of Bladed Disks”. *Journal of Engineering for Gas Turbines and Power* 143.12 (Oct. 2021). 121023. ISSN: 0742-4795. DOI: [10.1115/1.4051868](https://doi.org/10.1115/1.4051868) (cit. on p. 34).
- [158] S. Quaegebeur, B. Chouvion, and F. Thouverez. “Nonlinear cyclic reduction for the analysis of mistuned cyclic systems”. *Journal of Sound and Vibration* 499 (2021), p. 116002. DOI: [10.1016/j.jsv.2021.116002](https://doi.org/10.1016/j.jsv.2021.116002) (cit. on p. 144).
- [159] J. S. Rao. *History of rotating machinery dynamics*. Vol. 20. 2011. DOI: [10.1007/978-94-007-1165-5](https://doi.org/10.1007/978-94-007-1165-5) (cit. on p. 19).
- [160] A. J. Rivas-Guerra and M. P. Mignolet. “Local/Global Effects of Mistuning on the Forced Response of Bladed Disks”. *Journal of Engineering for Gas Turbines and Power* 126.1 (Mar. 2004), pp. 131–141. ISSN: 0742-4795. DOI: [10.1115/1.1581898](https://doi.org/10.1115/1.1581898) (cit. on p. 79).
- [161] S. Rodríguez and C. Martel. “Analysis of experimental results of turbomachinery flutter using an asymptotic reduced order model”. *Journal of Sound and Vibration* 509 (2021), p. 116225. ISSN: 0022-460X. DOI: [10.1016/j.jsv.2021.116225](https://doi.org/10.1016/j.jsv.2021.116225) (cit. on p. 3).
- [162] R. M. Rosenberg and J. K. Kuo. “Nonsimilar normal mode vibrations of nonlinear systems having two degrees of freedom”. *Advances in applied mechanics* (1964). DOI: [10.1115/1.3629599](https://doi.org/10.1115/1.3629599) (cit. on p. 184).
- [163] R. M. Rosenberg. “The normal modes of nonlinear n-degree-of-freedom systems”. *Advances in applied mechanics* (1962). DOI: [10.1115/1.3636501](https://doi.org/10.1115/1.3636501) (cit. on p. 184).
- [164] R. Rosenberg. “On Nonlinear Vibrations of Systems with Many Degrees of Freedom”. *Advances in Applied Mechanics* 9 (1966). Ed. by G. Chernyi, H. Dryden, P. Germain, L. Howarth, W. Olszak, W. Prager, R. Probstein, and H. Ziegler, pp. 155–242. ISSN: 0065-2156. DOI: [10.1016/S0065-2156\(08\)70008-5](https://doi.org/10.1016/S0065-2156(08)70008-5) (cit. on p. 184).
- [165] V. Ruffini. “Coriolis effects in bladed discs”. PhD thesis. Imperial College London, 2016. DOI: [10.25560/61825](https://doi.org/10.25560/61825) (cit. on pp. 2, 34).
- [166] V. Ruffini, J. S. Green, and C. W. Schwingshackl. “The Influence of Mistuning and Coriolis Effects on the Modal Parameters of Bladed Discs: An Experimental Study”. *ASME Turbo Expo 2017: Turbomachinery Technical Conference and Exposition*. American Society of Mechanical Engineers. 2017. DOI: [10.1115/GT2017-63437](https://doi.org/10.1115/GT2017-63437) (cit. on pp. 2, 35, 85, 129, 144).
- [167] V. Ruffini, C. Schwingshackl, and J. Green. “Experimental and analytical study of Coriolis effects in bladed disk”. *ASME 2015 international design engineering technical conferences and computers and information in engineering conference*. American Society of Mechanical Engineers. 2015. DOI: [10.1115/DETC2015-46621](https://doi.org/10.1115/DETC2015-46621) (cit. on p. 2).
- [168] V. Ruffini, C. W. Schwingshackl, and J. S. Green. “Prediction capabilities of Coriolis and gyroscopic effects in current finite element software”. *Proceedings of the 9th IFToMM International Conference on Rotor Dynamics*. Springer. 2015, pp. 1853–1862 (cit. on p. 2).
- [169] C. Runge. “Über die numerische Auflösung von Differentialgleichungen”. *Mathematische Annalen* 46.2 (1895), pp. 167–178. DOI: [10.1007/bf01446807](https://doi.org/10.1007/bf01446807) (cit. on p. 172).
- [170] C. Runge. “Über empirische Funktionen und die Interpolation zwischen äquidistanten Ordinaten”. *Zeitschrift für Mathematik und Physik* 46.224-243 (1901), p. 20 (cit. on p. 113).

- [171] M. Sadeghi and F. Liu. “Computation of Mistuning Effects on Cascade Flutter”. *AIAA Journal* 39.1 (2001), pp. 22–28. DOI: [10.2514/2.1297](https://doi.org/10.2514/2.1297) (cit. on p. 78).
- [172] M. Sadeghi and F. Liu. “Investigation of Mistuning Effects on Cascade Flutter Using a Coupled Method”. *Journal of Propulsion and Power* 23.2 (2007), pp. 266–272. DOI: [10.2514/1.18876](https://doi.org/10.2514/1.18876) (cit. on p. 78).
- [173] L. Salles and M. Vahdati. “Comparison of Two Numerical Algorithms for Computing the Effects of Mistuning of Fan Flutter”. Volume 7B: Structures and Dynamics. Turbo Expo: Power for Land, Sea, and Air. V07BT34A018. June 2016. DOI: [10.1115/GT2016-57324](https://doi.org/10.1115/GT2016-57324) (cit. on p. 78).
- [174] L. Salles. “Etude de l’usure par fretting sous chargements dynamiques dans les interfaces frottantes: Application aux pieds d’aubes de turbomachines”. PhD thesis. École Centrale de Lyon, 2010 (cit. on pp. 20, 174).
- [175] S. Sawyer and S. Fleeter. “Flutter stability of a detuned cascade in subsonic compressible flow”. *Journal of Propulsion and Power* 11.5 (1995), pp. 923–930. DOI: [10.2514/3.23918](https://doi.org/10.2514/3.23918) (cit. on pp. 34, 78).
- [176] E. Schmidt. “Über die Auflösung linearer Gleichungen mit unendlich vielen Unbekannten”. *Rendiconti del Circolo Matematico di Palermo (1884-1940)* 25.1 (1908), pp. 53–77 (cit. on p. 116).
- [177] L. Schwerdt, L. Panning-von Scheidt, and J. Wallaschek. “A Model Reduction Method for Bladed Disks With Large Geometric Mistuning Using a Partially Reduced Intermediate System Model”. *Journal of Engineering for Gas Turbines and Power* (2020). DOI: [10.1115/gt2020-14199](https://doi.org/10.1115/gt2020-14199) (cit. on p. 144).
- [178] L. Schwerdt, S. Willeke, L. P.-v. Scheidt, and J. Wallaschek. “Reduced-order modeling of bladed disks considering small mistuning of the disk sectors”. *Journal of Engineering for Gas Turbines and Power* 141.5 (2019). DOI: [10.1115/1.4041071](https://doi.org/10.1115/1.4041071) (cit. on p. 127).
- [179] A. Shanmugam and C. Padmanabhan. “A fixed–free interface component mode synthesis method for rotordynamic analysis”. *Journal of Sound and Vibration* 297.3 (2006), pp. 664–679. ISSN: 0022-460X. DOI: [10.1016/j.jsv.2006.04.011](https://doi.org/10.1016/j.jsv.2006.04.011) (cit. on p. 93).
- [180] S. Shaw and C. Pierre. “Non-linear normal modes and invariant manifolds”. *Journal of sound and vibration* (1991). DOI: [10.1016/0022-460x\(91\)90412-d](https://doi.org/10.1016/0022-460x(91)90412-d) (cit. on p. 184).
- [181] S. W. Shaw and C. Pierre. “Normal modes for non-linear vibratory systems”. *Journal of sound and vibration* 164.1 (1993), pp. 85–124. DOI: [10.1006/jsvi.1993.1198](https://doi.org/10.1006/jsvi.1993.1198) (cit. on p. 184).
- [182] S. W. Shaw and C. Pierre. “Normal modes of vibration for non-linear continuous systems”. *Journal of sound and vibration* 169.3 (1994), pp. 319–347. DOI: [10.1006/jsvi.1994.1021](https://doi.org/10.1006/jsvi.1994.1021) (cit. on p. 184).
- [183] F. Sicot. “Simulation efficace des écoulements instationnaires périodiques en turbomachines”. PhD thesis. École Centrale de Lyon, 2009 (cit. on p. 14).
- [184] C. Siewert, O. Pütz, and J. Eigemann. “Analysis of Intentional Mistuning on the Aeroelastic Stability of Freestanding Last Stage Blade Rows in Steam Turbines”. Volume 9: Oil and Gas Applications; Organic Rankine Cycle Power Systems; Steam Turbine. Turbo Expo: Power for Land, Sea, and Air. V009T23A010. Sept. 2020. DOI: [10.1115/GT2020-14656](https://doi.org/10.1115/GT2020-14656) (cit. on pp. 3, 34).
- [185] A. Sinha. “Reduced-order model of a bladed rotor with geometric mistuning”. *Journal of Turbomachinery* 131.3 (2009). DOI: [10.1115/1.2987237](https://doi.org/10.1115/1.2987237) (cit. on p. 144).

- [186] G. Sliva, A. Brézillon, J.-M. Cadou, and L. Duigou. “A study of the eigenvalue sensitivity by homotopy and perturbation methods”. *Journal of computational and applied mathematics* 234.7 (2010), pp. 2297–2302. DOI: [10.1016/j.cam.2009.08.086](https://doi.org/10.1016/j.cam.2009.08.086) (cit. on p. 44).
- [187] C. Soize. “A nonparametric model of random uncertainties for reduced matrix models in structural dynamics”. *Probabilistic Engineering Mechanics* 15.3 (2000), pp. 277–294. ISSN: 0266-8920. DOI: [https://doi.org/10.1016/S0266-8920\(99\)00028-4](https://doi.org/10.1016/S0266-8920(99)00028-4) (cit. on p. 2).
- [188] C. Soize. “A comprehensive overview of a non-parametric probabilistic approach of model uncertainties for predictive models in structural dynamics”. *Journal of Sound and Vibration* 288.3 (2005). Uncertainty in structural dynamics, pp. 623–652. ISSN: 0022-460X. DOI: <https://doi.org/10.1016/j.jsv.2005.07.009> (cit. on p. 2).
- [189] A. Sternchüss. “Multi-level parametric reduced models of rotating bladed disk assemblies”. PhD thesis. Châtenay-Malabry, Ecole centrale de Paris, 2009 (cit. on p. 116).
- [190] A. Sternchüss and E. Balmes. “On the reduction of quasi-cyclic disk models with variable rotation speeds”. *ISMA*. 2006, isma2006_0397–pdf (cit. on p. 113).
- [191] K. B. Subrahmanyam and K. R. V. Kaza. “Non-linear flap-lag-extensional vibrations of rotating, pretwisted, precone beams including Coriolis effects”. *International journal of mechanical sciences* 29.1 (1987), pp. 29–43. DOI: [10.1016/0020-7403\(87\)90072-5](https://doi.org/10.1016/0020-7403(87)90072-5) (cit. on pp. 2, 32).
- [192] Y. Sun, J. Yuan, E. Denimal, and L. Salles. “Nonlinear Modal Analysis of Frictional Ring Damper for Compressor Blisk”. *Journal of Engineering for Gas Turbines and Power* 143.3 (Feb. 2021). 031008. ISSN: 0742-4795. DOI: [10.1115/1.4049761](https://doi.org/10.1115/1.4049761) (cit. on pp. 12, 143).
- [193] A. Tacher, F. Thouverez, and J. Armand. “Interaction Between Coriolis Forces and Mistuning on a Cyclic Symmetric Structure With Geometrical Nonlinearity”. *Journal of Engineering for Gas Turbines and Power* 143.5 (Mar. 2021). 051006. ISSN: 0742-4795. DOI: [10.1115/1.4048844](https://doi.org/10.1115/1.4048844) (cit. on pp. 52, 85, 129, 143, 185).
- [194] A. Tacher, F. Thouverez, and J. Armand. “Modelling and analysis of a bladed drum subject to the Coriolis and mistuning effects”. *International Journal of Mechanical Sciences* 218 (2022), p. 106994. ISSN: 0020-7403. DOI: [10.1016/j.ijmecsci.2021.106994](https://doi.org/10.1016/j.ijmecsci.2021.106994) (cit. on pp. 85, 122, 131).
- [195] Q. Tang, C. Li, H. She, and B. Wen. “Analysis of frequency and mode shape of rotating-flexible disk-drum coupled structure with non-continuous connections”. *International Journal of Mechanical Sciences* 190 (2021), p. 106004. DOI: [10.1016/j.ijmecsci.2020.106004](https://doi.org/10.1016/j.ijmecsci.2020.106004) (cit. on pp. 2, 101, 122).
- [196] W. Tang, B. I. Epureanu, and S. Filippi. “Models for blisks with large blends and small mistuning”. *Mechanical Systems and Signal Processing* 87 (2017), pp. 161–179. DOI: [10.1016/j.ymssp.2016.10.019](https://doi.org/10.1016/j.ymssp.2016.10.019) (cit. on p. 144).
- [197] T. Theodorsen and W. H. Mutchler. “General theory of aerodynamic instability and the mechanism of flutter” (1935) (cit. on pp. 3, 15, 70).
- [198] D. L. Thomas. “Dynamics of rotationally periodic structures”. *International Journal for Numerical Methods in Engineering* 14.1 (1979), pp. 81–102. DOI: [10.1002/nme.1620140107](https://doi.org/10.1002/nme.1620140107) (cit. on pp. 2, 23).
- [199] S. A. Tobias and R. N. Arnold. “The Influence of Dynamical Imperfection on the Vibration of Rotating Disks”. *Proceedings of the Institution of Mechanical Engineers* 171.1 (1957), pp. 669–690. DOI: [10.1243/PIME\PROC\1957\171\056\02](https://doi.org/10.1243/PIME\PROC\1957\171\056\02) (cit. on p. 2).

- [200] D.-M. Tran. “Component mode synthesis methods using interface modes. Application to structures with cyclic symmetry”. *Computers & Structures* 79.2 (2001), pp. 209–222. ISSN: 0045-7949. DOI: [10.1016/S0045-7949\(00\)00121-8](https://doi.org/10.1016/S0045-7949(00)00121-8) (cit. on p. 96).
- [201] D.-M. Tran. “Component mode synthesis methods using partial interface modes: Application to tuned and mistuned structures with cyclic symmetry”. *Computers & Structures* 87.17 (2009), pp. 1141–1153. ISSN: 0045-7949. DOI: [10.1016/j.compstruc.2009.04.009](https://doi.org/10.1016/j.compstruc.2009.04.009) (cit. on p. 96).
- [202] M. Turner and J. B. Duke. “Propeller Flutter”. *Journal of the Aeronautical Sciences* 16.6 (1949), pp. 323–336 (cit. on p. 3).
- [203] P. Vacher, B. Jacquier, and A. Bucharles. “Extensions of the MAC criterion to complex modes”. *Proceedings of the international conference on noise and vibration engineering*. 2010, pp. 2713–2726 (cit. on p. 59).
- [204] A. F. Vakakis. “Dynamics of a nonlinear periodic structure with cyclic symmetry”. *Acta Mechanica* 95.1 (1992), pp. 197–226 (cit. on p. 24).
- [205] R. Valid and R. Ohayon. “Théorie et calcul statique et dynamique des structures à symétries cycliques”. *La recherche aérospatiale* 4 (1985), pp. 251–263 (cit. on pp. 23 sq.).
- [206] J. M. Vance, F. Y. Zeidan, and B. G. Murphy. *Machinery vibration and rotordynamics*. 2010 (cit. on p. 13).
- [207] P. Vargiu, C. M. Firrone, S. Zucca, and M. M. Gola. “A reduced order model based on sector mistuning for the dynamic analysis of mistuned bladed disks”. *International Journal of Mechanical Sciences* 53.8 (2011), pp. 639–646. DOI: [10.1016/j.ijmecsci.2011.05.010](https://doi.org/10.1016/j.ijmecsci.2011.05.010) (cit. on pp. 2, 91, 96, 99, 127).
- [208] A. G. Von Baumhauer and C. Koning. *On the stability of oscillations of an airplane wing*. Tech. rep. 1923 (cit. on p. 3).
- [209] G. Von Groll and D. J. Ewins. “The harmonic balance method with arc-length continuation in rotor/stator contact problems”. *Journal of sound and vibration* 241.2 (2001), pp. 223–233. DOI: [10.1006/jsvi.2000.3298](https://doi.org/10.1006/jsvi.2000.3298) (cit. on p. 183).
- [210] J. T. Wagner. “Coupling of Turbomachine Blade Vibrations Through the Rotor”. *Journal of Engineering for Power* 89.4 (Oct. 1967), pp. 502–512. ISSN: 0022-0825. DOI: [10.1115/1.3616718](https://doi.org/10.1115/1.3616718) (cit. on p. 2).
- [211] S.-T. Wei and C. Pierre. “Localization phenomena in mistuned assemblies with cyclic symmetry part I: free vibrations”. *Journal of Vibration, Acoustics, Stress, and Reliability in Design* 110.4 (1988), pp. 429–438. DOI: [10.1115/1.3269547](https://doi.org/10.1115/1.3269547) (cit. on pp. 33, 111).
- [212] S.-T. Wei and C. Pierre. “Localization phenomena in mistuned assemblies with cyclic symmetry part ii: Forced vibrations”. *Journal of Vibration, Acoustics, Stress, and Reliability in Design* 110.4 (1988), pp. 439–449. DOI: [10.1115/1.3269548](https://doi.org/10.1115/1.3269548) (cit. on p. 33).
- [213] D. S. Whitehead. “Effect of mistuning on the vibration of turbo-machine blades induced by wakes”. *Journal of mechanical engineering science* 8.1 (1966), pp. 15–21 (cit. on pp. 2 sq., 36).
- [214] D. S. Whitehead. “The Maximum Factor by Which Forced Vibration of Blades Can Increase Due to Mistuning”. *Journal of Engineering for Gas Turbines and Power* 120.1 (Jan. 1998), pp. 115–119. ISSN: 0742-4795. DOI: [10.1115/1.2818061](https://doi.org/10.1115/1.2818061) (cit. on p. 52).
- [215] D. S. Whitehead. “Force and moment coefficients for vibrating aerofoils in cascade”. *Aeronautical Research Council Reports and Memoranda* (1960) (cit. on pp. 3, 15, 70, 73, 76).

- [216] D. S. Whitehead. “Bending flutter of unstalled cascade blades at finite deflection”. *Aeronautical Research Council Reports and Memoranda* (1962) (cit. on pp. 69 sq., 76, 187).
- [217] J. Wildheim. “Excitation of rotationally periodic structures”. *Journal of Applied Mechanics* (1979). DOI: [10.1115/1.3424671](https://doi.org/10.1115/1.3424671) (cit. on pp. 23, 38).
- [218] J. Wildheim. “Excitation of rotating circumferentially periodic structures”. *Journal of Sound and Vibration* 75.3 (1981), pp. 397–416. DOI: [10.1016/0022-460x\(81\)90386-2](https://doi.org/10.1016/0022-460x(81)90386-2) (cit. on pp. 23, 38).
- [219] B. Xiao, A. J. Rivas-Guerra, and M. P. Mignolet. “Maximum amplification of blade response due to mistuning in multi-degree-of-freedom blade models”. *Turbo Expo: Power for Land, Sea, and Air*. 41715. 2004, pp. 427–438. DOI: [10.1115/gt2004-54030](https://doi.org/10.1115/gt2004-54030) (cit. on p. 36).
- [220] J. Xin and J. Wang. “Investigation of coriolis effect on vibration characteristics of a realistic mistuned bladed disk”. *ASME 2011 turbo expo: Turbine technical conference and exposition*. American Society of Mechanical Engineers. 2011, pp. 993–1005. DOI: [10.1115/1.2720866](https://doi.org/10.1115/1.2720866) (cit. on pp. 3, 35).
- [221] M.-T. Yang and J. H. Griffin. “A Reduced Order Approach for the Vibration of Mistuned Bladed Disk Assemblies”. *Journal of Engineering for Gas Turbines and Power* 119.1 (Jan. 1997), pp. 161–167. ISSN: 0742-4795. DOI: [10.1115/1.2815542](https://doi.org/10.1115/1.2815542) (cit. on pp. 2, 96).
- [222] M.-T. Yang and J. H. Griffin. “A reduced-order model of mistuning using a subset of nominal system modes”. *J. Eng. Gas Turbines Power* 123.4 (2001), pp. 893–900. DOI: [10.1115/1.1385197](https://doi.org/10.1115/1.1385197) (cit. on pp. 2, 52, 91, 96, 127).
- [223] J. Yuan, F. Scarpa, G. Allegri, B. Titurus, S. Patsias, and R. Rajasekaran. “Efficient computational techniques for mistuning analysis of bladed discs: A review”. *Mechanical Systems and Signal Processing* 87 (2017), pp. 71–90. ISSN: 0888-3270. DOI: [10.1016/j.ymsp.2016.09.041](https://doi.org/10.1016/j.ymsp.2016.09.041) (cit. on pp. 2, 34).
- [224] L. A. Zadeh. “Fuzzy sets as a basis for a theory of possibility”. *Fuzzy Sets and Systems* 1.1 (1978), pp. 3–28. ISSN: 0165-0114. DOI: [https://doi.org/10.1016/0165-0114\(78\)90029-5](https://doi.org/10.1016/0165-0114(78)90029-5) (cit. on p. 36).
- [225] J. Zeng, C. Zhao, H. Ma, K. Yu, and B. Wen. “Rubbing dynamic characteristics of the blisk-casing system with elastic supports”. *Aerospace Science and Technology* 95 (2019), p. 105481. ISSN: 1270-9638. DOI: [10.1016/j.ast.2019.105481](https://doi.org/10.1016/j.ast.2019.105481) (cit. on p. 93).
- [226] G. Zhang. *Component-based and parametric reduced-order modeling methods for vibration analysis of complex structures*. 2005 (cit. on p. 114).
- [227] H. Zhang, H. Yuan, and H. Sun. “Effect of Coriolis force on vibration localization characteristics of mistuned bladed disk”. *Journal of Vibroengineering* 22.5 (2020), pp. 1069–1083. DOI: [10.21595/jve.2020.21237](https://doi.org/10.21595/jve.2020.21237) (cit. on pp. 93, 122, 129).
- [228] H. Zhang, H. Yuan, and H. Sun. “Vibration reduction optimization for mistuned bladed disk based on reduced order modeling technique”. *Journal of Vibroengineering* 23.2 (2021), pp. 385–399. DOI: [10.21595/jve.2020.21381](https://doi.org/10.21595/jve.2020.21381) (cit. on pp. 93, 122).
- [229] B. Zhou, F. Thouverez, and D. Lenoir. “Vibration Reduction of Mistuned Bladed Disks by Passive Piezoelectric Shunt Damping Techniques”. *AIAA Journal* 52.6 (2014), pp. 1194–1206. DOI: [10.2514/1.J052202](https://doi.org/10.2514/1.J052202) (cit. on p. 34).
- [230] L. Zoghaib and P.-O. Mattei. “Time and frequency response of structures with frequency dependent, non-proportional linear damping”. *Journal of Sound and Vibration* 333.3 (2014), pp. 887–900. ISSN: 0022-460X. DOI: [10.1016/j.jsv.2013.09.044](https://doi.org/10.1016/j.jsv.2013.09.044) (cit. on p. 76).

Appendix A

Nonlinear aspects and frequency analysis

This appendix is focused on the search of periodic solutions for nonlinear systems. The time integration methods are first introduced, then the search of periodic solutions in the frequency domain with the harmonic balance method is presented and is completed with different tools like the prediction and continuation methods or the alternating time frequency method. Finally, the phenomenology of nonlinear system is discussed with the concept of stability and nonlinear normal modes.

In Section 1.2.2, the equations of motion have been written for an elastic rotational body with the assumption of nonlinear static deformation and linear dynamics. The resolution of these linear systems is well controlled by industrial computing codes. However, turbomachinery are complex rotating systems with a lot of nonlinear effects like contact or friction between the different elements or even large dynamic displacements. These nonlinear effects lead to the inclusion of a nonlinear term \mathbf{f}^{nl} in Eq. (1.37)

$$\mathbf{M}\ddot{\mathbf{q}}_d(t) + (\mathbf{C} + \mathbf{G})\dot{\mathbf{q}}_d(t) + \mathbf{K}^t\mathbf{q}_d(t) + \mathbf{f}^{\text{nl}}(\dot{\mathbf{q}}_d(t), \mathbf{q}_d(t)) = \mathbf{f}^{\text{ext}}(t). \quad (\text{A.1})$$

The resolution of this kind of system is more complex and requests the development of appropriate methods. In what follows, the resolution is only focused on the search of periodic solutions i.e. in the steady-state regime.

1 Time methods

This section presents some classical approaches to solve time dependent differential equations with a temporal approach of the search for periodic solutions. These reminders allow to introduce the relevance of the frequency-domain methods which will be presented afterwards.

1.1 Temporal integration methods

The temporal integrations methods consists in a discretization in n_t elements of the studied time interval $[t_0, t_{n_t-1}]$ such as:

$$t_0 < \dots < t_n < \dots < t_f, \quad (\text{A.2})$$

and with a time increment h_n such as $t_{n+1} = t_n + h_n$. The principle is to verify Eq. (A.1) at these consecutive times t_n depending on the previous moment in an explicit time integration method or depending on the same moment in an implicit time integration method.

1.1.1 First order differential equations

The most common time integration methods are based on first order differential equation method so it is necessary to substitute the system of n second order differential equations (Eq. (A.1)) by a system of $2n$ first order differential equations such as:

$$\dot{\mathbf{g}}(t) = \mathbf{f}(t, \mathbf{g}(t)), \quad (\text{A.3})$$

with

$$\mathbf{g}(t) = \begin{bmatrix} \mathbf{q}_d(t) \\ \dot{\mathbf{q}}_d(t) \end{bmatrix} \quad (\text{A.4})$$

$$\mathbf{f}(t, \mathbf{g}(t)) = \begin{bmatrix} \dot{\mathbf{q}}_d(t) \\ -\mathbf{M}^{-1} \left[(\mathbf{C} + \mathbf{G})\dot{\mathbf{q}}_d(t) + \mathbf{K}^t \mathbf{q}_d(t) + \mathbf{f}^{nl}(\dot{\mathbf{q}}_d(t), \mathbf{q}_d(t)) - \mathbf{f}^{\text{ext}}(t) \right] \end{bmatrix}. \quad (\text{A.5})$$

The initial point $\mathbf{g}(t_0) = \mathbf{g}_0$ is given.

Using the Taylor's theorem for $\mathbf{g}(t_{n+1}) = \mathbf{g}_{n+1}$ at the point t_n with the integral form of the remainder gives:

$$\begin{aligned} \mathbf{g}_{n+1} &= \mathbf{g}(t_n) + \int_{t_n}^{t_{n+1}} \dot{\mathbf{g}}(t) dt \\ &= \mathbf{g}_n + \int_{t_n}^{t_{n+1}} \mathbf{f}(t, \mathbf{g}(t)) dt \\ &= \mathbf{g}_n + h_n \int_0^1 \mathbf{f}(t_n + uh_n, \mathbf{g}(t_n + uh_n)) du. \end{aligned} \quad (\text{A.6})$$

The integral can be approached with a Gaussian quadrature such as:

$$\mathbf{g}_{n+1} = \mathbf{g}_n + h_n \sum_{i=1}^s b_i \mathbf{k}_i. \quad (\text{A.7})$$

This expression is the generalised expression of the Runge-Kutta method [103, 169] where s defines the order, b_i are the weights and \mathbf{k}_i are the increment based on the slope which can be found using the Butcher tableau [26]. The more s is important the more the stability and the accuracy are high because it takes $s - 1$ intermediate points between t_n and t_{n+1} in the evaluation of \mathbf{g}_{n+1} .

- **Forward Euler method** : For $s = 1$, Eq. (A.7) is known as the forward Euler method, it is the most basic method but its stability and accuracy are weak.

$$\mathbf{g}_{n+1} = \mathbf{g}_n + h_n \mathbf{f}(t_n, \mathbf{g}_n) \quad (\text{A.8})$$

- **Fourth-order Runge-Kutta method** : The fourth-order Runge-Kutta method is the classic Runge-Kutta method because it is the most widely known member of the

Runge-Kutta family.

$$\begin{aligned}
\mathbf{g}_{n+1} &= \mathbf{g}_n + \frac{h_n}{6}(\mathbf{k}_1 + 2\mathbf{k}_2 + 2\mathbf{k}_3 + \mathbf{k}_4) \\
\mathbf{k}_1 &= \mathbf{f}(t_n, \mathbf{g}_n) \\
\mathbf{k}_2 &= \mathbf{f}\left(t_n + \frac{h_n}{2}, \mathbf{g}_n + \frac{h_n}{2}\mathbf{k}_1\right) \\
\mathbf{k}_3 &= \mathbf{f}\left(t_n + \frac{h_n}{2}, \mathbf{g}_n + \frac{h_n}{2}\mathbf{k}_2\right) \\
\mathbf{k}_4 &= \mathbf{f}(t_n + h_n, \mathbf{g}_n + h_n\mathbf{k}_3)
\end{aligned} \tag{A.9}$$

1.2 Other time integration methods

The previous methods are robust and can be a good baseline, however due to the state space representation the number of unknowns is doubled and this can affect the time of calculation. The Newmark method [138] allows to resolve the problem directly with the second order differential equations:

$$\begin{aligned}
\dot{\mathbf{q}}_{n+1} &= \dot{\mathbf{q}}_n + (1 - \gamma)h_n\ddot{\mathbf{q}}_n + \gamma h_n\ddot{\mathbf{q}}_{n+1}, \\
\mathbf{q}_{n+1} &= \mathbf{q}_n + h_n\dot{\mathbf{q}}_n + \frac{h_n^2}{2}(1 - 2\beta)\ddot{\mathbf{q}}_n + h_n^2\beta\ddot{\mathbf{q}}_{n+1}.
\end{aligned} \tag{A.10}$$

Where γ and β are the characteristics parameters of the integration schema. More information can be found in [65].

With these methods, if the initial point g_0 is too far from the periodic solution of Eq. (A.1) the calculation of the transition period can be long and the converged solution may not be the one initially desired. To avoid these weak points, methods with a direct research of the periodic solution in the time domain have been developed such as the shooting method [92]. This method consists in finding a initial condition \mathbf{g}_0 and a period T such as the solution $\mathbf{g}(t, \mathbf{g}_0)$ realised a periodic motion of period T . The shooting function is defined as follows:

$$\mathbf{H}(T, \mathbf{g}_0) = (T, \mathbf{g}_0) - g_0 = 0. \tag{A.11}$$

The couple of solutions (T, \mathbf{q}_0) is determined in an iterative way with the help of the following equation:

$$\frac{\partial \mathbf{H}}{\partial \mathbf{g}_0}(\mathbf{g}_0^k, T^k)\Delta \mathbf{g}_0^k + \frac{\partial \mathbf{H}}{\partial T}(\mathbf{g}_0^k, T^k)\Delta T^k = -\mathbf{H}(\mathbf{g}_0^k, T^k). \tag{A.12}$$

The shooting function is evaluated with a time integration and Eq. (A.12) combined with a phase condition allow to find $\Delta \mathbf{g}_0^k$ and ΔT^k such as:

$$\mathbf{g}_0^{k+1} = \mathbf{g}_0^k + \Delta \mathbf{g}_0^k, \tag{A.13}$$

$$T^{k+1} = T^k + \Delta T^k. \tag{A.14}$$

A good point with this method is the determination of the monodromy matrix at the last evaluation of the shooting function because it allows to determine the stability of the system without additional computation as will be explained later in Section A.4.1.1.

2 Harmonic Balance Method

The time integration methods allow to find periodic solution in a robust way but the time of calculation to find the periodic solution can be very long especially if the transient period is important. A faster method of searching the periodic solution is to be in the Fourier space i.e. in the frequency domain. The Harmonic Balance Method (HBM) [22, 101, 133] is an analytical method based on the Galerkin method in which the periodic property of the solution is directly imposed in the shape of the searched solution in the frequency domain. Indeed the solution is written as a Fourier series of fundamental periodicity $T = 2\pi/\omega$

$$\mathbf{q}_d(t) = \frac{1}{2} \left(\sum_{k=0}^{\infty} \mathbf{c}_k e^{ik\omega t} + c.c. \right). \quad (\text{A.15})$$

This method has been widely used over the past few years in the nonlinear dynamics study of turbomachinery with friction [84, 108, 156], wear [3, 114, 174] or geometrical nonlinearity [50, 67, 128].

2.1 Theoretical principle

Due to the numerical use of the HBM, the Fourier series in Eq. (A.15) has to be truncated to an order H such as:

$$\mathbf{q}_d(t) \approx \frac{1}{2} \left(\sum_{k=0}^H \mathbf{c}_k e^{ik\omega t} + c.c. \right), \quad (\text{A.16})$$

where H is the number of harmonics kept, \mathbf{c}_k , the Fourier coefficient for the k^{th} harmonic.

This approximation leads to the apparition of a residue $\mathbf{r}(t)$ in the substitution of Eq. (A.16) in Eq. (A.1). This residue is then orthogonalised using the harmonic exponential function basis and the scalar product (Eq. (I.43)). Thanks to the orthogonality properties of the harmonic exponential function, the system can be decomposed in H decoupled expressions:

$$\langle \mathbf{r} | e^{-ik\omega t} \rangle = [-(k\omega)^2 \mathbf{M} + ik\omega(\mathbf{G} + \mathbf{C}) + \mathbf{K}^t] \mathbf{c}_k + \langle \mathbf{f}^{\text{nl}} | e^{-ik\omega t} \rangle - \langle \mathbf{f}^{\text{ext}} | e^{-ik\omega t} \rangle = \mathbf{0}, \quad (\text{A.17})$$

with $k \in \llbracket 0, H \rrbracket$.

This leads to the general matrix equation:

$$\mathbf{Z}(\omega) \mathbf{q}_h + \mathbf{f}_h^{\text{nl}}(\mathbf{q}_h, \omega) - \mathbf{f}_h^{\text{ext}}(\omega) = \mathbf{0}, \quad (\text{A.18})$$

where \mathbf{q}_h , \mathbf{f}_h^{nl} and $\mathbf{f}_h^{\text{ext}}$ are the Fourier coefficients of \mathbf{q}_d , \mathbf{f}^{nl} and \mathbf{f}^{ext} , respectively, in the shape $\mathbf{a}_h = [\mathbf{a}_0, \dots, \mathbf{a}_k, \dots, \mathbf{a}_H]^T$, whereas \mathbf{Z} is the dynamics stiffness matrix expressed as:

$$\mathbf{Z} = \begin{bmatrix} \mathbf{Z}_0 & & \\ & \ddots & \\ & & \mathbf{Z}_H \end{bmatrix} \quad (\text{A.19})$$

and where each block \mathbf{Z}_k has for expression:

$$\mathbf{Z}_k = -(k\omega)^2 \mathbf{M} + ik\omega(\mathbf{G} + \mathbf{C}) + \mathbf{K}^t. \quad (\text{A.20})$$

This nonlinear algebraic system in Eq. (A.18) can be solved numerically using a Newton-Raphson method [5] but the number of unknowns is multiplied by the number of harmonic chosen and because of the complex writing of the system the size of the problem is double.

Indeed, there is one resolution for the real part and one resolution for the imaginary part. It must be emphasised that the use of the HBM in the real domain have the same problem of doubling size because in this case for each harmonic there is two harmonic coefficients, one for the cosine function and one for the sine function [133].

2.2 Nonlinear terms calculation

The vector of Fourier coefficients of the nonlinear efforts $\mathbf{f}_h^{\text{ext}}$ depends on the frequency harmonic variables \mathbf{q}_h and ω but the law connecting these terms is in most of the cases unknown, only the law connecting the nonlinear forces $\mathbf{f}_h^{\text{ext}}$ to the time domain variables \mathbf{q}_d and $\dot{\mathbf{q}}_d$ is known. To circumvent the problem, it is possible to use the Alternating Frequency/Time domain method (AFT) [27]. This method consists in rebuilding the time domain variables \mathbf{q}_d and $\dot{\mathbf{q}}_d$ from the harmonic variables \mathbf{q}_h , then evaluate the nonlinear forces expressions in the time domain and projecting in the frequency domain after for each iteration of the nonlinear solver.

The transition from the frequency harmonics variables \mathbf{q}_h to the time domain variables \mathbf{q}_d and $\dot{\mathbf{q}}_d$ can be done with the help of a discretization of the time on one period T in n_t elements and the inverse Discrete Transform Fourier matrix (iDFT) $\bar{\mathbf{F}}$ such as:

$$\mathbf{q}_d = \bar{\mathbf{F}}\mathbf{q}_h, \quad (\text{A.21})$$

$$\dot{\mathbf{q}}_d = \bar{\mathbf{F}}\nabla\mathbf{q}_h, \quad (\text{A.22})$$

with

$$\bar{\mathbf{F}} = \begin{bmatrix} 1 & e^{i\omega t_1} & \dots & e^{iH\omega t_1} \\ \vdots & \vdots & & \vdots \\ 1 & e^{i\omega t_{n_t}} & \dots & e^{iH\omega t_{n_t}} \end{bmatrix} \otimes \mathbf{I}_n, \quad (\text{A.23})$$

$$\nabla = \begin{bmatrix} 0 & & \\ & \ddots & \\ & & iH\omega \end{bmatrix} \otimes \mathbf{I}_n, \quad (\text{A.24})$$

where n is the number of physical unknowns.

The time elements t_k can be written as $t_k = kn_t/T$ and knowing that $\omega = 2\pi/T$ gives:

$$\omega t_k = k \frac{2\pi}{n_t}. \quad (\text{A.25})$$

This expression allows to write the iDFT matrix as independent of ω , so the matrices do not need to be recalculated at each frequency iteration. Due to the discretization of time the number of unknowns of the problem is multiplied by n_t so finally the size of the problem is $(n(H+1))$ in the frequency domain and (nn_t) in the time domain. It is important to choose H and n_t high enough to have a converged solution but not too much either because it would necessitate a lot of memory and time of calculation.

Once the nonlinear efforts are evaluated in the time domain, they are projected in the frequency domain using the following DFT matrix:

$$\mathbf{F} = \frac{1}{n_t} \begin{bmatrix} 1 & \dots & 1 \\ e^{i\omega t_1} & \dots & e^{i\omega t_{n_t}} \\ \vdots & & \vdots \\ e^{iH\omega t_1} & \dots & e^{iH\omega t_{n_t}} \end{bmatrix}. \quad (\text{A.26})$$

As the iDFT, the DFT can be calculated independently of the pulsation ω using Eq. (A.25). Finally the vector \mathbf{f}_h^{nl} can be directly expressed as follows:

$$\mathbf{f}_h^{\text{nl}} = \mathbf{F}\mathbf{f}^{\text{nl}}(\bar{\mathbf{F}}\nabla\mathbf{q}_h, \bar{\mathbf{F}}\mathbf{q}_h). \quad (\text{A.27})$$

This method can also be represented with the diagram shown in A.1.

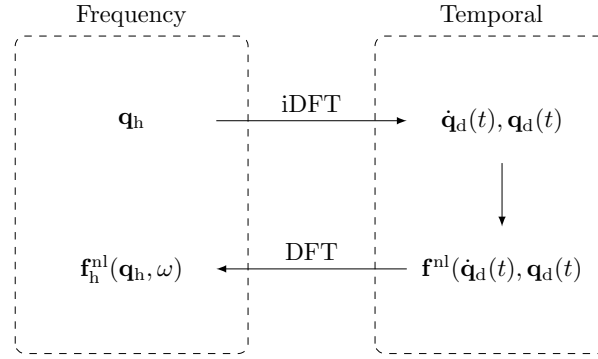


Figure A.1 – Principle of the AFT method

3 Continuation methods

The time and frequency methods presented previously allow to calculate the periodic solutions for a set of fixed parameters. But in general dynamics analysis, the study is realised for a data range of one parameter like the excitation frequency to find the forced response function. For a nonlinear system the solutions for one set excitation frequency can be multiple with the observation of turning point and bifurcation point. The continuation methods consist in following a particular solution with the evolution of one parameter. This methods are based on 3 principles : the parametrisation, the prediction and the correction [68].

The system used to apply the methods presented in the rest of this section is the HBM system in Eq. (A.18) with ω taken as the continuation parameter

$$\mathbf{r}(\mathbf{q}_h, \omega) = \mathbf{Z}(\omega)\mathbf{q}_h + \mathbf{f}_h^{\text{nl}}(\mathbf{q}_h, \omega) - \mathbf{f}_h^{\text{ext}}(\omega) = \mathbf{0}. \quad (\text{A.28})$$

3.1 Parametrisation methods

3.1.1 Sequential continuation

The system in Eq. (A.28) is composed of $N = (2H + 1)n$ equations and $N + 1$ unknowns with the inclusion of ω . The system to solve is therefore underdetermined so the most simple and famous technique is to fix ω for a set of values included in a data range $[\omega_1, \omega_2]$. This method is called sequential method and has the disadvantage not to follow the response curve in the presence of a turning point and leads to amplitude jump phenomenon. It is possible to rectify this with a selective parametrisation or a curvilinear parametrisation [68].

3.1.2 Parametrisation by arc-length

In this method the continuation is parametrised by its curvilinear abscissa s such as the unknowns are dependant on this curvilinear abscissa $(\mathbf{q}_h(s), \omega(s))$. Because the curvilinear abscissa can not be determined precisely, it is approximated by length of broken lines from

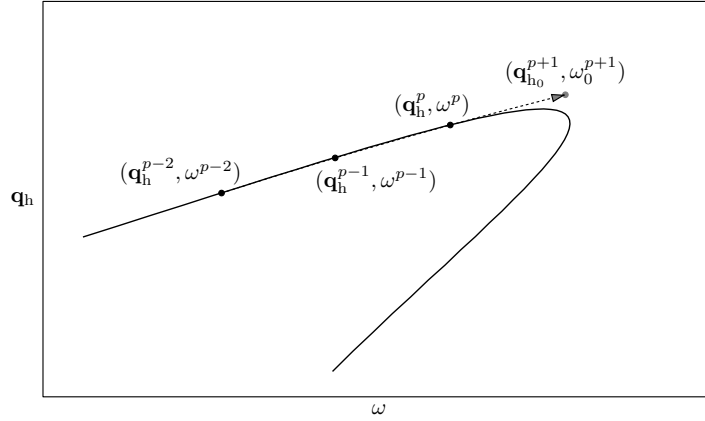


Figure A.2 – Polynomial interpolation

the previous calculated points. The curvilinear abscissa parameter s is calculated step by step such as $s^{p+1} = s^p + \Delta s^p$ and that the spacing between two successive points Δs^p is given by

$$\Delta s^p = \sqrt{\|\mathbf{q}_h^{p+1} - \mathbf{q}_h^p\|^2 + (\omega^{p+1} - \omega^p)^2}, \quad (\text{A.29})$$

where $(\mathbf{q}_h^p, \omega^p)$ is the p^{th} solution point.

After defining the parametrisation used, there remains to define the predictor method that allows to obtain an estimation of the system solution from the previous calculated points and the corrector method to obtain the converged solution of the system from the predicted point.

3.2 Prediction methods

3.2.1 Higher-order method

The higher-order method is based on the polynomial interpolation of order d and uses the $d + 1$ last calculated points of the system. The prediction's point $(\mathbf{q}_{h_0}^{p+1}, \omega_0^{p+1})$ is expressed with the help of the Lagrange polynomials as follows:

$$\begin{cases} \mathbf{q}_{h_0}^{p+1} = \sum_{i=0}^d \prod_{j=0, j \neq i}^d \frac{s^{p+1} - s^{p-d+j}}{s^{p-d+i} - s^{p-d+j}} \mathbf{q}_h^{p-d+i} \\ \omega_0^{p+1} = \sum_{i=0}^d \prod_{j=0, j \neq i}^d \frac{s^{p+1} - s^{p-d+j}}{s^{p-d+i} - s^{p-d+j}} \omega^{p-d+i} \end{cases}. \quad (\text{A.30})$$

The method is presented in figure A.2. The more the polynomial order is high the more it requires points. To avoid bad estimation, the method is usually restricted to a quadratic or cubic interpolation as in [36]. Note that a prediction at the first order is called secant method [21] but even if this method is simple and robust, the prediction can be far from the real solution and the number of required iterations of the solver to converge may be significant.

3.2.2 Tangential method

The tangent predictor evaluates the prediction with the help of the tangent matrix at the last point calculated. The tangent equation at the point $(\mathbf{q}_h^p, \omega^p)$ is obtained by differentiation of Eq. (A.28):

$$\mathbf{J}_{\mathbf{q}_h}(\mathbf{q}_h^p, \omega^p) \Delta \mathbf{q}_h^p + \mathbf{J}_{\omega}(\mathbf{q}_h^p, \omega^p) \Delta \omega^p = 0, \quad (\text{A.31})$$

with $\mathbf{J}_{\mathbf{q}_h} = \frac{\partial r}{\partial \mathbf{q}_h}$ and $\mathbf{J}_\omega = \frac{\partial r}{\partial \omega}$ the Jacobian matrices of the system with respect to $\partial \mathbf{q}_h$ and ω respectively. $\Delta \mathbf{q}_h^p$ and $\Delta \omega^p$ are the increments defining the tangent. Imposing the norm of the tangent equal to the continuation step Δs^p gives:

$$\|(\Delta \mathbf{q}_h^p)\|^2 + (\Delta \omega^p)^2 = \Delta s^p. \quad (\text{A.32})$$

The previous expressions in Eq. (A.31) and Eq. (A.32) give:

$$\Delta \mathbf{q}_h^p = -\mathbf{J}_{\mathbf{q}_h}^{-1} \mathbf{J}_\omega \Delta \omega^p, \quad (\text{A.33})$$

$$\Delta \omega^p = \frac{\pm \Delta s^p}{\sqrt{-\mathbf{J}_{\mathbf{q}_h}^{-1} \mathbf{J}_\omega + 1}}. \quad (\text{A.34})$$

A solution to determine the sign of $\Delta \omega$ is to perform the scalar product of the two last successive tangent vectors. If the product is positive the sign remains the same but if the product is negative, $\Delta \omega$ changes sign [67, 147].

The predictions are expressed in function of the previous obtained variables and the tangent vector such as:

$$\begin{cases} \mathbf{q}_{h_0}^{p+1} = \mathbf{q}_h^p + \Delta \mathbf{q}_h^p \\ \omega_0^{p+1} = \omega^p + \Delta \omega^p \end{cases}. \quad (\text{A.35})$$

The tangential prediction is presented in figure A.3. This method is an effective and robust tool for prediction of solutions especially in the presence of turning point. However the calculation of the tangent may be a problem if the matrix $\mathbf{J}_{\mathbf{q}_h}$ is not invertible. In this case a prediction of higher-order is preferred.

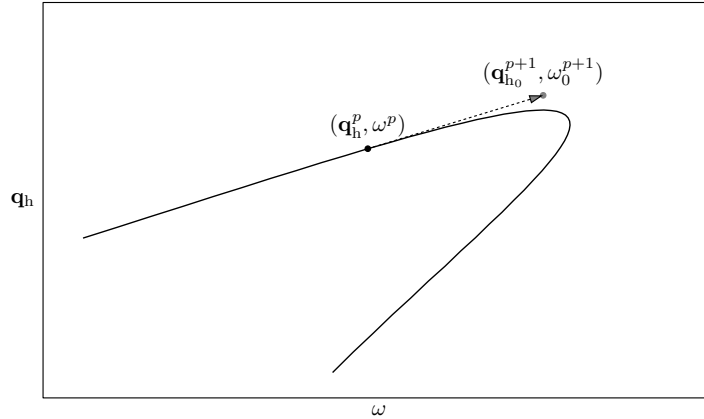


Figure A.3 – Tangential prediction

3.3 Correction methods

The estimation given by a predictor does not satisfy Eq. (A.28), so a correction procedure is needed from the predicted point $(\mathbf{q}_{h_0}^{p+1}, \omega_0^{p+1})$ to obtain the converged point $(\mathbf{q}_h^{p+1}, \omega^{p+1})$ which satisfies Eq. (A.28). As previously mentioned, the system is underdetermined with N equations and $N + 1$ unknowns so the correction method to use depends on the chosen parametrisation method. The system can be directly solved by fixing a parameter like the sequential method which is represented in figure A.4 or by increasing the system with an additional equation characterising the chosen continuation method.

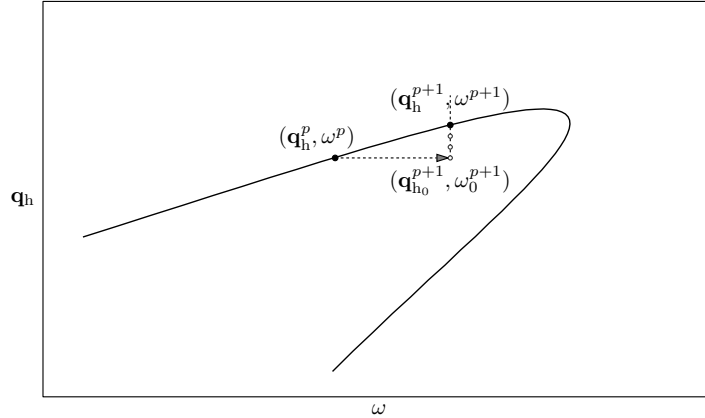


Figure A.4 – Sequential continuation

3.3.1 Arc-length continuation

The idea of the arc-length method is that the solution is on the curve defined by $\mathbf{r}(\mathbf{q}_h, \omega) = \mathbf{0}$ and on a hypersphere of radius Δs^p also called arc-length, centred on the last converged solution $(\mathbf{q}_h^p, \omega^p)$. This last condition gives an additional equation to the system:

$$c(\mathbf{q}_h, \omega) = \|\mathbf{q}_h - \mathbf{q}_h^p\|^2 + (\omega - \omega^p)^2 - (\Delta s^p)^2 = 0. \quad (\text{A.36})$$

The solution $(\mathbf{q}_h^{p+1}, \omega^{p+1})$ of the new increased system is an intersection between the curve of solutions and the hypersphere. This method has the advantage to always have a solution because there is always an intersection between the curve of solutions and the hypersphere. Numerically, this system can be solved with a Newton-Raphson process where the correction increments can be expressed as

$$\begin{bmatrix} \Delta \mathbf{q}_{h_i}^{p+1} \\ \Delta \omega_i^{p+1} \end{bmatrix} = \begin{bmatrix} \mathbf{J}_{\mathbf{q}_h}(\mathbf{q}_{h_i}^{p+1}, \omega_i^{p+1}) & \mathbf{J}_{\omega}(\mathbf{q}_{h_i}^{p+1}, \omega_i^{p+1}) \\ \frac{\partial c}{\partial \mathbf{q}_h}(\mathbf{q}_{h_i}^{p+1}, \omega_i^{p+1}) & \frac{\partial c}{\partial \omega}(\mathbf{q}_{h_i}^{p+1}, \omega_i^{p+1}) \end{bmatrix}^{-1} \begin{bmatrix} \mathbf{r}(\mathbf{q}_{h_i}^{p+1}, \omega_i^{p+1}) \\ c(\mathbf{q}_{h_i}^{p+1}, \omega_i^{p+1}) \end{bmatrix}, \quad (\text{A.37})$$

where i is the iteration number of the Newton-Raphson method and the solution point $(\mathbf{q}_h^{p+1}, \omega^{p+1})$ is obtained at the end of the iterations when the stopping criterion is achieved. The arc-length method is illustrated in figure A.5.

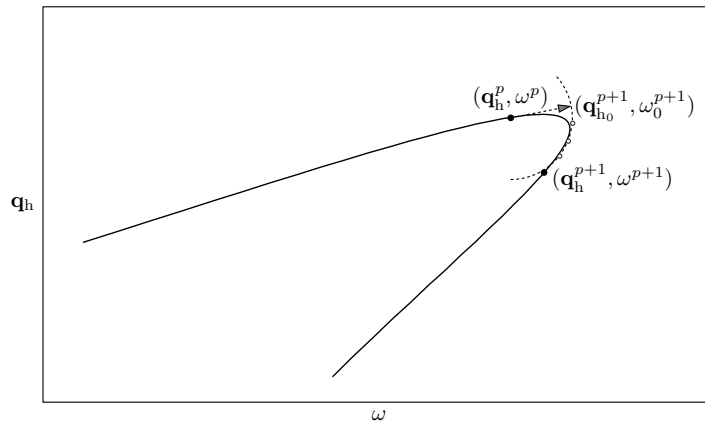


Figure A.5 – Arc-length continuation

This method is very efficient to deal with the turning points, however the augmented system always has two possible converged points, the one desired downstream the curve and the second upstream the curve where solutions have been already found. If the second point is more attractive than the first point this can lead to a parasitic reversing of the running direction of the curve. This weakness can be addressed using the pseudo arc length method.

3.3.2 Pseudo arc-length continuation

In this method, the solution desired is at the intersection between the curve of solutions and an hyperplane orthogonal to the tangent of the last obtained point $(\mathbf{q}_h^p, \omega^p)$ and at a distance Δs^p from this last point. The tangent equation is given with the help of Eq. (A.31) so it is convenient to use this method with the tangential prediction to directly have the expression of $\Delta \mathbf{q}_h^p$ with Eq. (A.33) and $\Delta \omega^p$ with Eq. (A.34). This condition gives the following additional equation to the system:

$$c(\mathbf{q}_h, \omega) = (\Delta \mathbf{q}_h^p)^\top (\mathbf{q}_h - \mathbf{q}_h^p) + \Delta \omega^p (\omega - \omega^p) - (\Delta s^p)^2 = 0. \quad (\text{A.38})$$

This method has the advantage to have a unique intersection between the curve of solutions and the hyperplane and to avoid the parasitic reversing mentioned above. However if the distance Δs^p is oversized, it is possible to not have an intersection point. To avoid this specific case it is necessary to choose a distance Δs^p small enough especially at the turning point. An adaptive continuation step method can for example be used to prevent this problem. Finally, the pseudo arc-length method is illustrated in figure A.6.

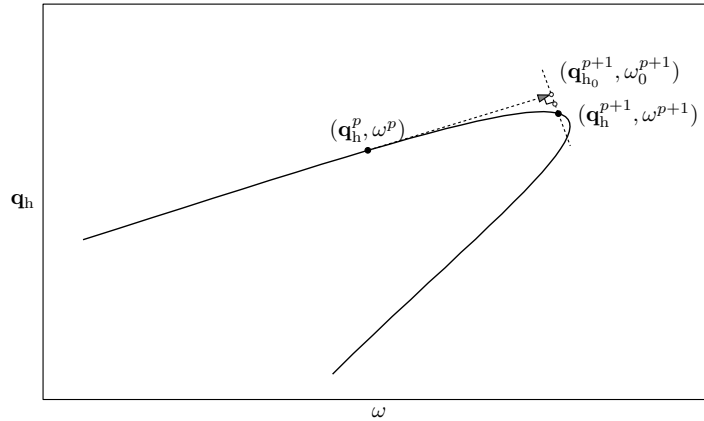


Figure A.6 – Pseudo arc-length continuation

3.3.3 Adaptive continuation step

The continuation step is an important parameter of the continuation methods because it plays a role in both the correction and the prediction methods. In one case, the larger the step, the further the prediction will be from the real solution, accordingly the number of iterations in the Newton-Raphson method will increase. However, the smaller the step, the larger number of points describing the solution curve, which will contribute to the increase of the computation time. The best solution is a compromise between these two cases which can be achieved using an adaptive continuation step based upon the number of iterations of the Newton-Raphson method.

The method chosen here consists in fixing a maximum number of iterations N_{\max} and a minimum number of iterations N_{\min} [67] in such a way that if the number of iterations of

the Newton-Raphson method exceeds N_{\max} , the correction is stopped and the continuation step is reduced. Otherwise, if the number of iterations is below N_{\min} , the continuation step is increased for the next point. Finally, if the number of iterations is between N_{\min} and N_{\max} , the length Δs of the continuation step is unchanged. In general, N_{\min} and N_{\max} are chosen lower than 20.

The calculation of the new continuation step can be done in different ways. The reduction can be done by multiplying the previous continuation step by a coefficient $\alpha < 1$ such that $\Delta s^{p+1} = \alpha \Delta s^p$. To increase the continuation step, the previous one can be multiplied by a coefficient $\beta > 1$ but a more interesting way is to take into account the number of iterations N_{it} in the Newton-Raphson method of the previous solution point to calculate the new continuation step. For example with $\Delta s^{p+1} = (N_{\max}/N_{\text{it}})\Delta s^p$, the faster the convergence the higher the increase of the continuation step.

An upper limit continuation step Δs_{\max} can be fixed to avoid a discretization too coarse and a lower limit Δs_{\min} to avoid a high computational cost or a problem of convergence of the solver if the program does not find a solution with N_{\max} iterations.

4 Nonlinear phenomenology

This section is focused on the particular phenomena that occur in nonlinear dynamics. It allows to show the differences between the nonlinear systems and their associated linear systems. Moreover, the weak and strong points of using the HBM in the study of these phenomenon will be discussed. Firstly, the concept of stability of the periodic solutions of such system will be addressed with the Floquet theory [137]. Then the notion of nonlinear normal mode is introduced with different definitions and the principle of the numerical determination with the harmonic balance.

4.1 Concept of stability

The periodic solutions found for a nonlinear dynamics system can be unstable which means that the solution is not physically observable. Indeed, with the integral method the solution can only converge to a stabilised solution because the stabilisation to an equilibrium state is the transition phase of a response. However with the frequency method all periodic solutions are found but it is not possible to determine the stability of the solution directly with the frequency method. This is why it is important to use a specific tool to analyse the stability of nonlinear periodic solutions.

The notion of stability is characterised by the capacity of a solution to return to its equilibrium state when it is subjected to a perturbation. The most popular definitions are from the work of Liapounov [117] and Poincaré. These definitions are very general and not really applicable to the systems studied here. Other methods allow to determine the local stability of a solution with the study of a linearised system around a perturbed solution thanks to the Hartman-Grobman theorem [72]. This theorem justifies that the behaviour of the nonlinear system at the neighbourhood of the perturbed solution is similar to the one of the linear system.

4.1.1 Floquet theory

The Floquet theory allows to study the stability of linear systems with periodic coefficients. Noting $\mathbf{g}_p(t)$ as a periodic solution of Eq. (A.3) with a period T and $\mathbf{g}(t)$ the perturbed solution with a perturbation $\mathbf{z}(t)$ such as:

$$\mathbf{g} = \mathbf{g}_p(t) + \mathbf{z}(t). \quad (\text{A.39})$$

Injecting Eq. (A.39) in Eq. (A.3) and performing a Taylor development at the first order around $\mathbf{g}_p(t)$ gives the following linear system:

$$\dot{\mathbf{z}}(t) = \frac{\partial \mathbf{f}}{\partial \mathbf{g}}(t, \mathbf{g}_p) \mathbf{z}(t) = \mathbf{A}(t) \mathbf{z}(t), \quad (\text{A.40})$$

with

$$\mathbf{A}(t) = \begin{bmatrix} \mathbf{0} & \mathbf{I} \\ -\mathbf{M}^{-1} \left[\mathbf{K}^t + \frac{\partial \mathbf{f}^{\text{nl}}}{\partial \mathbf{q}_p}(\dot{\mathbf{q}}_p, \mathbf{q}_p) \right] & -\mathbf{M}^{-1} \left[(\mathbf{C} + \mathbf{G}) + \frac{\partial \mathbf{f}^{\text{nl}}}{\partial \dot{\mathbf{q}}_p}(\dot{\mathbf{q}}_p, \mathbf{q}_p) \right] \end{bmatrix}, \quad (\text{A.41})$$

the jacobian matrix which is periodic thanks to the periodic solution \mathbf{g}_p such as $\mathbf{A}(t+T) = \mathbf{A}(t)$. The differential system in Eq. (A.39) is a linear system with periodic coefficient so it is possible to solve the system with the Floquet theory [137]. This theory postulates that there are $2n$ solutions \mathbf{z}_i which produce a basis of the set of solutions and which can be expressed as a fundamental matrix $\mathbf{Z}(t)$ such as:

$$\mathbf{Z}(t) = [\mathbf{z}_1 \dots \mathbf{z}_i \dots \mathbf{z}_{2n}] \quad (\text{A.42})$$

\mathbf{Z} is solution of the following differential system:

$$\dot{\mathbf{Z}}(t) = \mathbf{A}(t) \mathbf{Z}(t). \quad (\text{A.43})$$

Moreover, $\dot{\mathbf{Z}}(t+T)$ is also a solution of Eq. (A.43) thanks to the periodicity of the matrix $\mathbf{A}(t)$ so $\dot{\mathbf{Z}}(t+T)$ can be expressed as a linear combination of the set of \mathbf{z}_i ,

$$\mathbf{Z}(t+T) = \mathbf{Z}(t) \mathbf{\Phi}, \quad (\text{A.44})$$

where $\mathbf{\Phi}$ is the monodromy matrix of the system, which is constant and supposed to be diagonalizable such as:

$$\mathbf{\Phi} = \mathbf{P} \mathbf{C} \mathbf{P}^{-1}, \quad (\text{A.45})$$

with

$$\mathbf{C} = \begin{bmatrix} \rho_1 & & & & \\ & \ddots & & & \\ & & \rho_i & & \\ & & & \ddots & \\ & & & & \rho_{2n} \end{bmatrix}, \quad (\text{A.46})$$

the matrix of the eigenvalues and \mathbf{P} , the matrix of the eigenvectors of $\mathbf{\Phi}$. Using Eq. (A.44) and Eq. (A.45), it is possible to write:

$$\mathbf{Z}(t+mT) = \mathbf{Z}(t) \mathbf{\Phi}^m = \mathbf{P} \mathbf{C}^m \mathbf{P}^{-1}, \quad m \in \mathbb{N}. \quad (\text{A.47})$$

Imposing $\mathbf{V}(t) = \mathbf{Z}(t) \mathbf{P}$ and multiplying Eq. (A.47) at the left by \mathbf{P} gives:

$$\mathbf{V}(t+mT) = \mathbf{V} \mathbf{C}^m = [\mathbf{v}_1(t) \rho_1^m \dots \mathbf{v}_i(t) \rho_i^m \dots \mathbf{v}_{2n}(t) \rho_{2n}^m]. \quad (\text{A.48})$$

As a consequence, the evolution of the perturbation is deduced from the eigenvalues ρ_i also called characteristic multiplier. There is three specific cases:

- $\max_i |\rho_i| < 1$: the perturbation amplitude decreases and tends to 0, the solution is

asymptotically stable

- $\max_i |\rho_i| > 1$: there is one or more direction in which the amplitude of the perturbation diverges, the solution is unstable
- $\max_i |\rho_i| = 1$: the perturbation is periodic and the analysis at the first order is not enough to conclude

The target to determine the stability of a dynamics system with the Floquet theory is to find the monodromy matrix to calculate its eigenvalues. By imposing an initial condition $\mathbf{Z}(0) = \mathbf{I}_{2n}$, the monodromy matrix is equal to $\mathbf{Z}(T)$ thanks to Eq. (A.44). The matrix $\mathbf{Z}(T)$ is obtained by a time integration over one period T of Eq. (A.40). The determination due to the Floquet theory is easy to execute and robust but has an important computational cost with the time integration and increases with the number of unknowns. A solution to this weak point is the Hill method which studies the stability of periodic solution directly in the frequency domain so the method used with the HBM can be very efficient. However, due to the lack of robustness of this method, it will not be developed in this manuscript because it has not been chosen as reference method to study the stability. However, more informations about this method can found in [69, 75, 109, 209].

4.1.2 Bifurcation

Using the Floquet theory, it is possible to determine the stability of each solution found with the continuation methods and the HBM. In some cases the solutions curve can switch between a stable solution and an unstable solution which is known as a bifurcation point [137]. A bifurcation point can also refer to a change of number of solutions but in this case an additional procedure is needed during the continuation method to find all the bifurcation branches. The different sorts of bifurcation can be detected by the way the characteristic multipliers of the Floquet theory leave the unit circle on the complex plan. There are three different cases summarized in figure A.7:

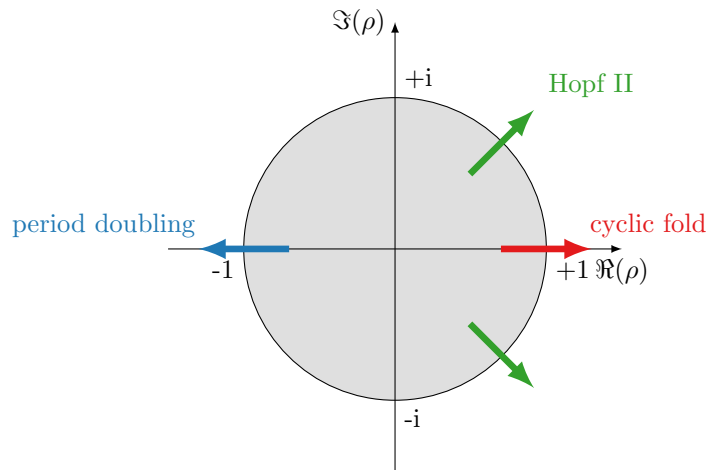


Figure A.7 – Bifurcation of periodic solutions and the location the characteristic multipliers on the complex plan

- The characteristic multipliers cut across the unit circle following the real axis and through the value $+1$, represented with the red arrow in figure A.7. This is a cyclic fold bifurcation also called turning point which is the most common case in nonlinear dynamics and coincides with coalescence of two branches, one stable and the other unstable. In general,

there is no other stable solution near this point and this can lead to a strong discontinuity of the solution also called jump phenomenon which can be very dangerous for the integrity of the structure.

- The characteristic multipliers cut across the unit circle following the real axis and through the value -1, represented with the blue arrow in figure A.7. This is a period doubling bifurcation also called flip. The stable T -periodic solution becomes unstable at the bifurcation point and a second branch of solution is created with a period $2T$. The second branch is stable in the supercritical case and unstable in the subcritical case. In the second case of subcritical bifurcation this creates a jump phenomenon as in the cyclic fold instability.
- A pair of complex conjugate characteristic multipliers cut across the unit circle simultaneously, representing with the green arrows in figure A.7. This is a Hopf II bifurcation also called Neimark bifurcation. In this case the bifurcation can be supercritical or subcritical, with the creation or the destruction of a quasi-periodic solution.

4.2 Nonlinear normal mode

In linear dynamic analysis, the notion of mode is very powerful and allows to determine the eigenvalues and eigenvectors of a system. These components describe the solution space of the linear system with two proprieties . If the motion is initiated on a mode, the motion remains on this mode, this is the invariance property. The second property is the modal superposition principle which says that the free and forced oscillations can be expressed as a linear combination of the eigenvectors. The extension of this notion to the nonlinear system is problematic due to the dependency between eigenvalue and eigenvector amplitude. In this section, the definition of nonlinear normal mode proposed by Rosenberg [162–164] and Shaw and Pierre [180–182] will be discussed and the determination by the HBM will be explained.

4.2.1 Rosenberg definition

Rosenberg defined the nonlinear normal mode as vibrations-in-unison for the case of undamped nonlinear free system. This vibrations-in-unison is composed of three criteria:

1. All degree of freedoms vibrate at the same frequency.
2. All degree of freedoms reach their extremum and go to zero at the same time.
3. The motion of every degree of freedom is configurable in function of the motion of a single unspecified degree of freedom such as:

$$\mathbf{x}_i(t) = g_i(\mathbf{x}_k(t)) \quad \forall i \in \llbracket 1, n \rrbracket \setminus k, \quad (\text{A.49})$$

k is the index of the component kept for the settings and g_i are the functions representing the link between the motion of the coordinate i and the coordinate of reference k .

The functions g_i are determined by solving the differential system of $n - 1$ unknowns. In general, the expressions g_i are approximated with a polynomial development because it is rarely possible to directly find the analytical expressions of these functions. Injecting the expressions g_i in the equation of motion gives the modal equation. This equation allows to determine the time evolution of the component \mathbf{x}_k and shows the dependency between the amplitude and the frequency of vibration. There is two different cases, if the frequency of the oscillation reduces with amplitude, it is a softening nonlinearity. In the other case, if the oscillation increases with the amplitude, it is a stiffening nonlinearity.

Equation (A.49) allows to define the nonlinear normal mode in the configuration space as a curve called modal line. If this curve is a straight line (ie $g_i = \alpha_i \mathbf{x}_k$ with α_i constant) the NNM is called similar normal-mode, in this case the modal shape does not depend on the amplitude of vibration and is identical to the linear normal mode. In the other case, the relations g_i are not linear and the modal shape changes with the amplitude, the NNM is called nonsimilar normal-mode.

The definition of the nonlinear normal mode of Rosenberg is restrictive because it cannot be applied to non-conservative or gyroscopic systems. Indeed, it has been demonstrated in Section I.3.3, that for linear rotational cyclic-symmetric structure, there is travelling wave mode, therefore all degree of freedoms can not reach their extremum and go to zero at the same time, which does not respect the second criteria of the Rosenberg definition.

4.2.2 Shaw and Pierre definition

The works of Shaw and Pierre offer to generalise the Rosenberg's definition for damped and gyroscopic system. The nonlinear normal mode is defined as a nonlinear invariant manifold, namely every pair $(\mathbf{x}_i, \dot{\mathbf{x}}_i)$ is configured by a unique unspecified pair $(\mathbf{x}_k, \dot{\mathbf{x}}_k)$ such as:

$$\mathbf{x}_i(t) = g_i(\mathbf{x}_k(t), \dot{\mathbf{x}}_k), \quad \dot{\mathbf{x}}_i(t) = h_i(\mathbf{x}_k(t), \dot{\mathbf{x}}_k) \quad \forall i \in \llbracket 1, n \rrbracket \setminus k. \quad (\text{A.50})$$

As for the Rosenberg's method, the determination of the functions g_i and h_i is realised by resolving the differential system of $n - 2$ unknowns. For the same reason as previously the expressions g_i and h_i are generally approximated with a polynomial development. These analytical methods are limited by the acceptability of the approximation which decreases with the increase of the amplitude motion and are not easily applicable. Numerical methods are more interesting to solve large size and complex problem. In this way, Pescheck adapted the Shaw and Pierre definition with a numerical approach [148, 149].

4.2.3 Harmonic balance determination

The numerical approach used in [193] to find the nonlinear normal mode is the harmonic balance method described in Section A.2. The nonlinear normal mode is the periodic solution of the following free conservative system:

$$\mathbf{M}\ddot{\mathbf{q}}_d(t) + \mathbf{G}\dot{\mathbf{q}}_d(t) + \mathbf{K}^t\mathbf{q}_d(t) + \mathbf{f}^{nl}(\dot{\mathbf{q}}_d(t), \mathbf{q}_d(t)) = \mathbf{0}. \quad (\text{A.51})$$

Using the Fourier series and following the Galerkin procedure leads to the general matrix equation:

$$\mathbf{Z}(\omega)\mathbf{q}_h + \mathbf{f}_h^{nl}(\mathbf{q}_h, \omega) = \mathbf{0}, \quad (\text{A.52})$$

where \mathbf{Z} is the dynamics stiffness matrix expressed as:

$$\mathbf{Z} = \begin{bmatrix} \mathbf{Z}_0 & & \\ & \ddots & \\ & & \mathbf{Z}_H \end{bmatrix}, \quad (\text{A.53})$$

and where each block \mathbf{Z}_k has for expression:

$$\mathbf{Z}_k = -(k\omega)^2\mathbf{M} + ik\omega\mathbf{G} + \mathbf{K}^t. \quad (\text{A.54})$$

The system contains $(n(H + 1))$ equations and $(n(H + 1)) + 1$ unknowns because ω is also an unknown in the free response, consequently the system is underdetermined. It is possible to

close the system with the addition of a phase equation by imposing an initial zero velocity to a given degree of freedom p such as:

$$\dot{q}_d^p(0) = \omega \sum_{k=1}^H k \Im(c_k^p) = 0. \quad (\text{A.55})$$

An other solution is to include a continuation equation for which the pulsation is not fixed, as for the forced response presented previously. The initialisation of the continuation method can be done at low amplitude, where the nonlinear terms are negligible. In order to do this, the initial pulsation is fixed on the one of the linear mode and the coefficients in the vector \mathbf{c}_1 of the first harmonic are equal to the modal shape of the linear mode with a low weighting factor to be at low amplitude, the others harmonics being set to zero.

Appendix B

Expressions used in the calculation of the aerodynamic forces

More details about the developments of the following components and functions can be found in [216] from Section 2.1 to 2.8.

Variable used to specify the incidence of the steady flow τ :

$$\tau = \frac{\tan(\alpha) - \tan(\theta)}{\sec^2(\theta)}. \quad (\text{B.1})$$

Frequency parameter λ :

$$\lambda = \frac{\omega c}{U}. \quad (\text{B.2})$$

Steady parameter ζ_0 :

$$\zeta_0(x'/c) = -\frac{\zeta(x')}{\tau U}. \quad (\text{B.3})$$

Geometric parameter a :

$$a = \frac{c}{s} \cos(\theta). \quad (\text{B.4})$$

Geometric parameter b :

$$b = \frac{c}{s} \sin(\theta). \quad (\text{B.5})$$

The unknown bound vorticity γ can be decomposed in two components, one independent of τ noted γ_p and one proportional to τ noted γ_τ as follows:

$$\gamma(x') = i\omega p_j \gamma_p(x'/c) + i\omega p_j \tau \gamma_\tau(x'/c). \quad (\text{B.6})$$

Free vorticity ϵ at the point x'_1 on the chord axis x' :

$$\epsilon(x'_1) = -\frac{i\omega}{U} \int_0^{x'_1} e^{\frac{i\omega}{U}(x'-x'_1)} \gamma(x') dx'. \quad (\text{B.7})$$

As for the bound vorticity γ in Eq. (B.6), the free vorticity ϵ can be decomposed in two components, one independent of τ noted ϵ_p and one proportional to τ noted ϵ_τ

$$\epsilon(x') = i\omega p_j \epsilon_p(x'/c) + i\omega p_j \tau \epsilon_\tau(x'/c). \quad (\text{B.8})$$

Deriving the previous equation by x'_1 gives the following relationship:

$$\frac{d\epsilon}{dx'_1} + \frac{i\omega}{U}(\gamma(x'_1) + \epsilon(x'_1)) = 0. \quad (\text{B.9})$$

$U_0(z)$ function:

$$U_0(z) = \frac{c}{4s} \left(e^{-i\theta} \cot(-i\pi z(c/s)e^{-i\theta}) + e^{i\theta} \cot(i\pi z(c/s)e^{i\theta}) \right). \quad (\text{B.10})$$

$U(z)$ function:

$$U(z) = \frac{c}{4s} \left(e^{z(c/s)(\pi-\beta)e^{-i\theta}-i\theta} \operatorname{cosec}(-i\pi z(c/s)e^{-i\theta}) + e^{-z(c/s)(\pi-\beta)e^{i\theta}+i\theta} \operatorname{cosec}(i\pi z(c/s)e^{i\theta}) \right). \quad (\text{B.11})$$

$V_0(z)$ function:

$$V_0(z) = \frac{c}{4is} \left(e^{-i\theta} \cot(-i\pi z(c/s)e^{-i\theta}) - e^{i\theta} \cot(i\pi z(c/s)e^{i\theta}) \right). \quad (\text{B.12})$$

$V(z)$ function:

$$V(z) = \frac{c}{4is} \left(e^{z(c/s)(\pi-\beta)e^{-i\theta}-i\theta} \operatorname{cosec}(-i\pi z(c/s)e^{-i\theta}) - e^{-z(c/s)(\pi-\beta)e^{i\theta}+i\theta} \operatorname{cosec}(i\pi z(c/s)e^{i\theta}) \right). \quad (\text{B.13})$$

$K(z)$ function:

$$K(z) = V(z) + i\lambda e^{-i\lambda z} \left(\int_z^{-1} \left(e^{i\lambda z_1} V(z_1) - \frac{1}{2\pi z_1} \right) dz_1 - \frac{1}{2\pi} \log |z| + \frac{1}{2}(a+ib) \sum_{r=0}^{+\infty} \frac{e^{-(2\pi r+\beta)(a+ib)-i\lambda}}{(2\pi r+\beta)(a+ib)+i\lambda} + \frac{1}{2}(a-ib) \sum_{r=1}^{+\infty} \frac{e^{-(2\pi r-\beta)(a-ib)-i\lambda}}{(2\pi r-\beta)(a-ib)+i\lambda} \right). \quad (\text{B.14})$$

$J(z)$ function:

$$J(z) = U(z) + i\lambda e^{-i\lambda z} \left(\int_z^{-1} e^{i\lambda z_1} U(z_1) dz_1 - \frac{i}{2}(a+ib) \sum_{r=0}^{+\infty} \frac{e^{-(2\pi r+\beta)(a+ib)-i\lambda}}{(2\pi r+\beta)(a+ib)+i\lambda} + \frac{i}{2}(a-ib) \sum_{r=1}^{+\infty} \frac{e^{-(2\pi r-\beta)(a-ib)-i\lambda}}{(2\pi r-\beta)(a-ib)+i\lambda} \right). \quad (\text{B.15})$$

$M(z)$ function:

$$\begin{aligned}
M(z) = & \frac{i}{4\pi\lambda} \left(\frac{c}{s}\right)^2 \left\{ e^{-2i\theta} \pi^2 \operatorname{cosec}^2(-i\pi z(c/s)e^{-i\theta}) \left[\left(1 - \frac{\beta}{2\pi}\right) e^{-\beta z(c/s)e^{-i\theta}} \right. \right. \\
& + \frac{\beta}{2\pi} e^{z(c/s)(2\pi-\beta)e^{-i\theta}} - 1 \left. \right] + e^{2i\theta} \pi^2 \operatorname{cosec}^2(i\pi z(c/s)e^{i\theta}) \left[\left(1 - \frac{\beta}{2\pi}\right) e^{\beta z(c/s)e^{i\theta}} \right. \\
& \left. \left. + \frac{\beta}{2\pi} e^{-z(c/s)(2\pi-\beta)e^{i\theta}} - 1 \right] \right\}. \quad (\text{B.16})
\end{aligned}$$

$N(z)$ function:

$$\begin{aligned}
N(z) = & \frac{1}{4\pi\lambda} \left(\frac{c}{s}\right)^2 \left\{ e^{-2i\theta} \pi^2 \operatorname{cosec}^2(-i\pi z(c/s)e^{-i\theta}) \left[\left(1 - \frac{\beta}{2\pi}\right) e^{-\beta z(c/s)e^{-i\theta}} \right. \right. \\
& + \frac{\beta}{2\pi} e^{z(c/s)(2\pi-\beta)e^{-i\theta}} - 1 \left. \right] - e^{2i\theta} \pi^2 \operatorname{cosec}^2(i\pi z(c/s)e^{i\theta}) \left[\left(1 - \frac{\beta}{2\pi}\right) e^{\beta z(c/s)e^{i\theta}} \right. \\
& \left. \left. + \frac{\beta}{2\pi} e^{-z(c/s)(2\pi-\beta)e^{i\theta}} - 1 \right] \right\}. \quad (\text{B.17})
\end{aligned}$$

The steady parameter ζ_0 is the solution of the following integral:

$$\int_0^1 (V_0(\eta - x') - V_0(-\infty)) \zeta_0(x') dx' = 1. \quad (\text{B.18})$$

The component γ_p is the solution of the following integral:

$$\int_0^1 K(\eta - x') \gamma_p(x') dx' = 1. \quad (\text{B.19})$$

The component γ_τ is the solution of the following integral:

$$\int_0^1 K(\eta - x') \gamma_\tau(x') dx' = \int_0^1 N(\eta - x') \zeta_0(x') dx'. \quad (\text{B.20})$$

Component ϵ_p at the point η on the reference blade:

$$\epsilon_p(x'_1) = -i\lambda \int_0^{x'_1} e^{i\lambda(x'-x'_1)} \gamma_p(x') dx'. \quad (\text{B.21})$$

Component ϵ_τ at the point η on the reference blade:

$$\epsilon_\tau(x'_1) = -i\lambda \int_0^{x'_1} e^{i\lambda(x'-x'_1)} \gamma_\tau(x') dx'. \quad (\text{B.22})$$

Component u_0 at the point η on the reference blade:

$$u_0 = \tan(\theta) - \int_0^1 (U_0(\eta - x') - U_0(-\infty)) \zeta_0(x') dx'. \quad (\text{B.23})$$

Component u_p at the point η on the reference blade:

$$u_p = \int_0^1 J(\eta - x') \gamma_p(x') dx'. \quad (\text{B.24})$$

Component u_τ at the point η on the reference blade:

$$u_\tau = \int_0^1 J(\eta - x') \gamma_p(x') dx' - \int_0^1 M(\eta - x') \zeta_0(x') dx'. \quad (\text{B.25})$$

Appendix C

Matrices and vectors used to calculate the aerodynamic coefficient C_f

In order to minimize the expression of the matrices, only the element of the $(m + 1)^{\text{th}}$ row and $(l + 1)^{\text{th}}$ column is given where m and l are integers between 0 and $n - 1$. The matrices are of size n by n and the element of the $(m + 1)^{\text{th}}$ row and $(l + 1)^{\text{th}}$ column is noted $\mathbf{A}(m + 1, l + 1)$, in the same way the vectors are of size n and are noted $\mathbf{A}(m + 1, 1)$.

$$\mathbf{D}(m + 1, 1) = 1, \quad (\text{C.1})$$

$$\mathbf{Z}_p(m + 1, 1) = \frac{\pi}{2n} \zeta_0 \left(\frac{\pi m}{n} \right) \sin \left(\frac{\pi m}{n} \right), \quad (\text{C.2})$$

$$\mathbf{\Gamma}_p(m + 1, 1) = \frac{\pi}{2n} \gamma_p \left(\frac{\pi m}{n} \right) \sin \left(\frac{\pi m}{n} \right), \quad (\text{C.3})$$

$$\mathbf{\Gamma}_\tau(m + 1, 1) = \frac{\pi}{2n} \gamma_\tau \left(\frac{\pi m}{n} \right) \sin \left(\frac{\pi m}{n} \right), \quad (\text{C.4})$$

$$\mathbf{E}_p(m + 1, 1) = \frac{\pi}{2n} \epsilon_p \left(\frac{\pi m}{n} \right) \sin \left(\frac{\pi m}{n} \right), \quad (\text{C.5})$$

$$\mathbf{E}_\tau(m + 1, 1) = \frac{\pi}{2n} \epsilon_\tau \left(\frac{\pi m}{n} \right) \sin \left(\frac{\pi m}{n} \right), \quad (\text{C.6})$$

$$\mathbf{Y}_0(m + 1, 1) = u_0 \left(\frac{\pi m}{n} \right), \quad (\text{C.7})$$

$$\mathbf{Y}_p(m + 1, 1) = u_p \left(\frac{\pi m}{n} \right), \quad (\text{C.8})$$

$$\mathbf{Y}_\tau(m + 1, 1) = u_\tau \left(\frac{\pi m}{n} \right). \quad (\text{C.9})$$

$$(\text{C.10})$$

$$\mathbf{A}_0(m+1, l+1) = V_0(z) - V_0(-\infty), \quad (\text{C.11})$$

$$\mathbf{B}_0(m+1, l+1) = U_0(z) - U_0(-\infty), \quad (\text{C.12})$$

$$\mathbf{A}(m+1, l+1) = K(z) + i\lambda e^{-i\lambda z} \left(\frac{1}{\pi} \log(2) + \frac{1}{\pi} \sum_{r=1}^n \frac{1}{r} \cos\left(\frac{\pi r(2m+1)}{2n}\right) \cos\left(\frac{\pi r l}{n}\right) \right), \quad (\text{C.13})$$

$$\mathbf{B}(m+1, l+1) = J(z), \quad (\text{C.14})$$

$$\mathbf{H}(m+1, l+1) = -\frac{i\lambda}{2n} e^{-\lambda z} \sin\left(\frac{\pi m}{n}\right) \left(\frac{\pi m}{n} + 2 \sum_{r=1}^{n-1} \frac{1}{r} \sin\left(\frac{\pi r m}{n}\right) \cos\left(\frac{\pi r l}{n}\right) \right), \quad (\text{C.15})$$

$$\mathbf{P}(m+1, l+1) = M(z), \quad (\text{C.16})$$

$$\mathbf{Q}(m+1, l+1) = N(z), \quad (\text{C.17})$$

where $z = \frac{1}{2} \cos\left(\frac{\pi l}{n}\right) - \frac{1}{2} \cos\left(\frac{\pi(2m+1)}{2n}\right)$.

Appendix D

Procedure for the matrices extraction

This section is devoted to the explanation of the method used to extract the mass, Coriolis and global stiffness matrices. The geometry, finite-element mesh and matrices have been generated using the ANSYS software. The non-linear static equation due to the centrifugal force is directly solved in ANSYS. Therefore, the global stiffness matrix extracted from ANSYS is composed of the stiffness, softening and stiffening matrices.

The mistuning is introduced directly in the MATLAB codes so that the static simulations in the ANSYS software are only made on a single tuned reference sector for different rotational speeds and using the cyclic symmetry properties. For the mistuning introduction, there are two different cases.

- The mistuning is proportionally introduced into the whole sector. Here, it is only necessary to extract the mass, Coriolis and global stiffness matrices of the whole sector.
- The mistuning is proportionally introduced on the blade only. Here, it is necessary to extract separately the mass, Coriolis and global stiffness of the blade and disc sector to be re-assembled after introducing the mistuning within a MATLAB code.

In the first case, the procedure is very simple, the mass, Coriolis and global stiffness of the whole tuned sector are extracted from ANSYS after the static analysis and the proportional mistuning is introduced on the global stiffness matrix of the whole sector. This procedure is depicted in Fig. [D.1a](#).

The procedure to introduce different proportional mistuning between the blades and the disc is more complex. First, a static analysis is performed on the whole tuned sector to extract the displacement of the dofs at the blade/disc interface. Then two other static analyses are performed, one for the blade and the other for the disc sector with the displacement imposed at the disc/blade interface, which allows to extract the mass, Coriolis and global stiffness matrices of the tuned blade and tuned disc sector from ANSYS with the correct preload due to the centrifugal force and finally, the disc and blade are reassembled to form the mass, Coriolis and global stiffness matrices of the full prestressed sector. This procedure is depicted in Fig. [D.1b](#).

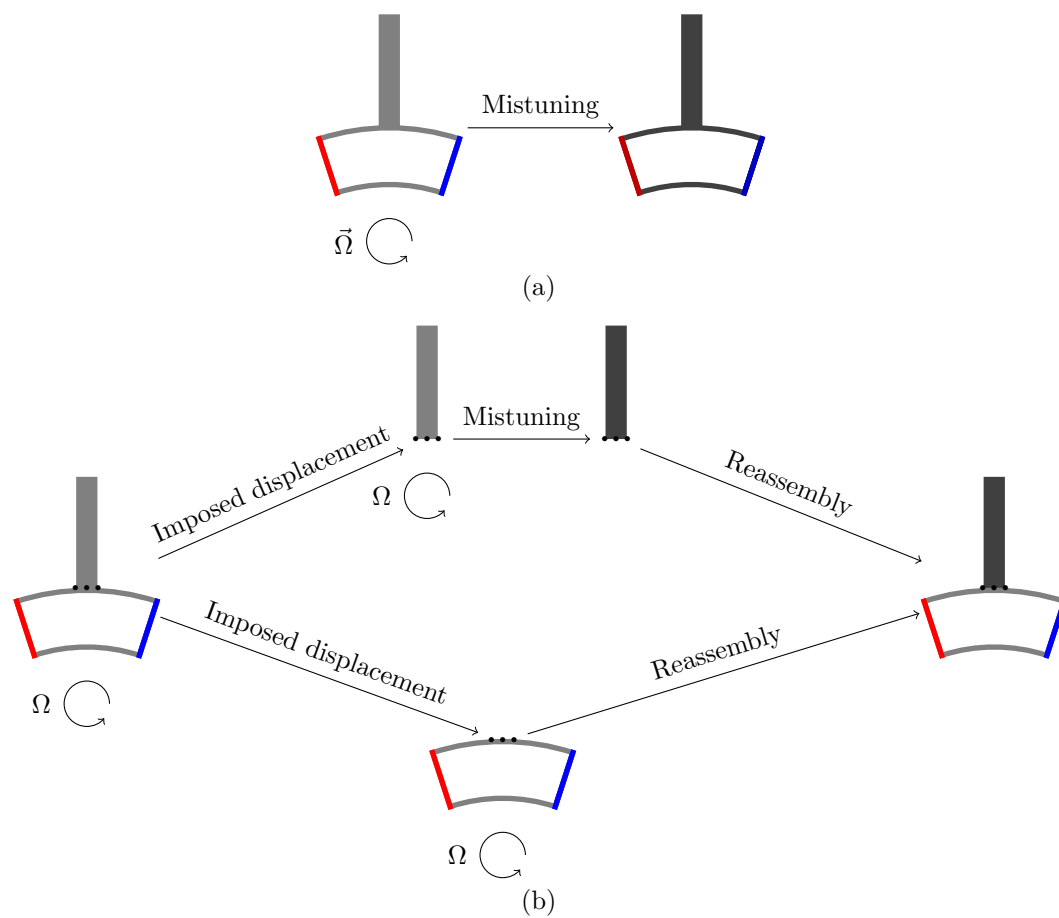


Figure D.1 – Procedures for the implementation of proportional mistuning. (a) Sector proportional mistuning. (b) Blade proportional mistuning.

List of personal publications

Peer-reviewed international journals

- Anthony Tacher, Fabrice Thouverez, Jason Armand. "Interaction Between Coriolis Forces and Mistuning on a Cyclic Symmetric Structure With Geometrical Nonlinearity". *Journal of Engineering for Gas Turbines and Power*, Vol. 143, No. 5, 2021. DOI : [10.1115/1.4048844](https://doi.org/10.1115/1.4048844)
- Anthony Tacher, Fabrice Thouverez, Jason Armand. "Modelling and analysis of a bladed drum subject to the Coriolis and mistuning effects". *International Journal of Mechanical Sciences* Vol. 218, 2022, p. 106994. DOI : [10.1016/j.ijmecsci.2021.106994](https://doi.org/10.1016/j.ijmecsci.2021.106994)
- Anthony Tacher, Fabrice Thouverez, Jason Armand. "The Flutter Stability of Mistuned Bladed Disks Subjected to the Coriolis effect". *Journal of Engineering for Gas Turbines and Power*, October 20, 2022. DOI : [10.1115/1.4056020](https://doi.org/10.1115/1.4056020)

International conferences with published proceedings

- Anthony Tacher, Fabrice Thouverez, Jason Armand. "Interaction Between Coriolis Forces and Mistuning on a Cyclic Symmetric Structure With Geometrical Nonlinearity". *ASME Turbo Expo 2020: Turbomachinery Technical Conference and Exposition*, Sep. 2020, Virtual, Online. DOI : [10.1115/GT2020-15343](https://doi.org/10.1115/GT2020-15343)

AUTORISATION DE SOUTENANCE

Vu les dispositions de l'arrêté du 25 mai 2016,

Vu la demande du directeur de thèse

Monsieur F. THOUVEREZ

et les rapports de

M. S. COGAN

Chargé de Recherche HDR - FEMTO-ST - Département Mécanique appliquée
24 chemin de l'Epitaphe - 25000 BESANSON

et de

M. F. SCARPA

Professeur - University of BRISTOL - Department of Aerospace Engineering Cabot Institute for
the Environment - The Bristol Centre for Nanoscience and Quantum Information
Composites University Technology Centre (UTC)

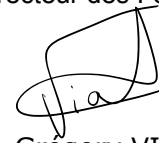
Monsieur TACHER Anthony

est autorisé à soutenir une thèse pour l'obtention du grade de **DOCTEUR**

Ecole doctorale Mécanique, Energétique, Génie civil, Acoustique

Fait à Ecully, le 2 septembre 2022

Pour le directeur de l'Ecole centrale de Lyon
Le directeur des Formations



Grégory VIAL